Université de Montréal

Applications of finite reflection groups in Fourier analysis and symmetry breaking of polytopes

par

Mariia Myronova

Département de physique
Faculté des arts et des sciences

Thèse présentée en vue de l'obtention du grade de
Philosophiæ Doctor (Ph.D.)
en physique

Mai 2021

© Mariia Myronova, 2021

Université de Montréal

Faculté des arts et des sciences

Cette thèse intitulée

Applications of finite reflection groups in Fourier analysis and symmetry breaking of polytopes

présentée par

Mariia Myronova

a été évaluée par un jury composé des personnes suivantes :

Luc Vinet
(président-rapporteur)

Jiří Patera
(directeur de recherche)

Marzena Szajewska
(codirecteur)

Yvan Saint–Aubin
(membre du jury)

Pierre–Philippe Dechant
(examinateur externe)

Iosif Polterovich
(représentant du doyen de la FESP)

Thèse acceptée le :
10 Mai 2021

Résumé

Cette thèse présente une étude des applications des groupes de réflexion finis aux problèmes liés aux réseaux bidimensionnels et aux polytopes tridimensionnels. Plusieurs familles de fonctions orbitales, appelées fonctions orbitales de Weyl, sont associées aux groupes de réflexion cristallographique. Les propriétés exceptionnelles de ces fonctions, telles que l'orthogonalité continue et discrète, permettent une analyse de type Fourier sur le domaine fondamental d'un groupe de Weyl affine correspondant. Dans cette considération, les fonctions d'orbite de Weyl constituent des outils efficaces pour les transformées discrètes de type Fourier correspondantes connues sous le nom de transformées de Fourier–Weyl. Cette recherche limite notre attention aux fonctions d'orbite de Weyl symétriques et antisymétriques à deux variables du groupe de réflexion cristallographique A_2. L'objectif principal est de décomposer deux types de transformations de Fourier–Weyl du réseau de poids correspondant en transformées plus petites en utilisant la technique de division centrale. Pour les cas non cristallographiques, nous définissons les indices de degré pair et impair pour les orbites des groupes de réflexion non cristallographique avec une symétrie quintuple en utilisant un remplacement de représentation-orbite. De plus, nous formulons l'algorithme qui permet de déterminer les structures de polytopes imbriquées. Par ailleurs, compte tenu de la pertinence de la symétrie icosaédrique pour la description de diverses molécules sphériques et virus, nous étudions la brisure de symétrie des polytopes doubles de type non cristallographique et des structures tubulaires associées. De plus, nous appliquons une procédure de stellation à la famille des polytopes considérés. Puisque cette recherche se concentre en partie sur les fullerènes icosaédriques, nous présentons la construction des nanotubes de carbone correspondants. De plus, l'approche considérée pour les cas non cristallographiques est appliquée aux structures cristallographiques. Nous considérons un mécanisme de brisure de symétrie appliqué aux polytopes obtenus en utilisant les groupes Weyl tridimensionnels pour déterminer leurs extensions structurelles possibles en nanotubes.

Mots clès : groupe de Coxeter, fonction d'orbite de Weyl, transformée de Fourier discrète, polytope imbriqué, polytope convexe, décomposition d'orbite, brisure de symétrie, fullerène, nanotube

Abstract

This thesis presents a study of applications of finite reflection groups to the problems related to two-dimensional lattices and three-dimensional polytopes. Several families of orbit functions, known as Weyl orbit functions, are associated with the crystallographic reflection groups. The exceptional properties of these functions, such as continuous and discrete orthogonality, permit Fourier-like analysis on the fundamental domain of a corresponding affine Weyl group. In this consideration, Weyl orbit functions constitute efficient tools for corresponding Fourier-like discrete transforms known as Fourier–Weyl transforms. This research restricts our attention to the two-variable symmetric and antisymmetric Weyl orbit functions of the crystallographic reflection group A_2. The main goal is to decompose two types of the corresponding weight lattice Fourier-Weyl transforms into smaller transforms using the central splitting technique. For the non-crystallographic cases, we define the even- and odd-degree indices for orbits of the non-crystallographic reflection groups with 5-fold symmetry by using a representation-orbit replacement. Besides, we formulate the algorithm that allows determining the structures of nested polytopes. Moreover, in light of the relevance of the icosahedral symmetry to the description of various spherical molecules and viruses, we study symmetry breaking of the dual polytopes of non-crystallographic type and related tube-like structures. As well, we apply a stellation procedure to the family of considered polytopes. Since this research partly focuses on the icosahedral fullerenes, we present the construction of the corresponding carbon nanotubes. Furthermore, the approach considered for the non-crystallographic cases is applied to crystallographic structures. We consider a symmetry-breaking mechanism applied to the polytopes obtained using the three-dimensional Weyl groups to determine their possible structural extensions into nanotubes.

Keywords: Coxeter group, Weyl orbit function, discrete Fourier transform, nested polytope, convex polytope, orbit decomposition, symmetry breaking, fullerene, nanotube

Contents

Résumé 5

Abstract 7

List of tables 13

List of figures 17

Acknowledgments 27

Introduction 29

Chapter 1. Preliminaries 33

- 1.1. Root systems 33
- 1.2. Finite reflection groups 36
- 1.3. Coxeter graphs and Dynkin diagrams 37
- 1.4. Dual bases and corresponding lattices 39
- 1.5. Affine Weyl group and fundamental region 42
- 1.6. Grids F_M and Λ_M 43
- 1.7. Orbits of finite reflection groups 45
- 1.8. Weyl orbit functions 46
- 1.9. Applications of finite reflection groups in the modelling of nanostructures 47

Chapter 2. Central splitting of A_2 discrete Fourier–Weyl transforms 51

- 2.1. Introduction 52
- 2.2. Splitting weight and point sets 55
  - 2.2.1. Root and weight lattices 55
  - 2.2.2. Splitting weight sets 57
  - 2.2.3. Splitting point sets 59

2.3. Weight lattice Fourier–Weyl transforms 64
2.3.1. $C-$ and $S-$functions 64
2.3.2. Discrete orthogonality 66
2.3.3. Splitting transforms 68

2.4. Central splitting 72
2.4.1. Central splitting of discrete transforms 72
2.4.2. Decompositions of unitary transform matrices 74
2.4.3. Decompositions of transform matrices $\mathbb{I}_3$ and $\widetilde{\mathbb{I}}_6$ 77

2.5. Concluding remarks 80
Acknowledgments 81

Chapter 3. Nested polyhedra and indices of orbits of Coxeter groups of non-crystallographic type 83

3.1. Introduction 84

3.2. Even-degree indices for orbits 86

3.3. Odd-degree indices for orbits 91

3.4. Embedding index 94

3.5. Lower orbits of H_2 and H_3 96

3.6. Concluding remarks 102
Acknowledgments 102

Chapter 4. On symmetry breaking of dual polyhedra of the non-crystallographic group H_3 103

4.1. Introduction 105

4.2. Bases of the icosahedral group H_3 108
4.2.1. The $\alpha-$ and $\omega-$bases 108
4.2.2. The orthonormal bases 111
4.2.3. The mixed bases 111
4.2.4. The $\omega'-$basis 112

4.3. Reflections and reflection graphs 113
4.3.1. Reflections of the Coxeter group H_3 113
4.3.2. The fundamental region of H_3 114

4.3.3. Reflection graphs 114

4.4. Decoration of the Coxeter–Dynkin diagram 117

4.5. Faces of dual polytopes 118

4.6. Orbits of $\mathcal{V}_{H_3}(\lambda)-$polytopes 124

4.7. Stellations of dual polyhedra of H_3 127

4.8. Orbit decompositions of $\mathcal{V}_{H_3}(\lambda)-$polytopes 128

4.9. Symmetry breaking of $\mathcal{V}_{H_3}(\lambda)$ and related tubes 132
4.9.1. The $\mathcal{V}_{H_3}(1,0,0)-$polytope 134
4.9.2. The $\mathcal{V}_{H_3}(0,0,1)-$polytope 136
4.9.3. The $\mathcal{V}_{H_3}(0,1,0)-$polytope 138

4.10. Symmetry breaking of the fullerene C_{20} 139

4.11. Concluding remarks 145
Acknowledgments 147

Chapter 5. Symmetry breaking of dual polyhedra of crystallographic type 149

5.1. Bases associated with the crystallographic reflection groups in $\mathbb{R}^3$ 149
5.1.1. The $\alpha-$ and $\omega-$bases 149
5.1.2. The orthonormal bases 153
5.1.3. The mixed bases 153
5.1.4. The $\omega'-$basis 154

5.2. The reflections of a crystallographic group W 156

5.3. Dual polytopes of the crystallographic groups A_3, B_3 and C_3 156

5.4. The orbits of $\mathcal{V}_W(\lambda)-$polytopes 159

5.5. Orbit decompositions 160
5.5.1. Orbit decompositions of the $\mathcal{V}_{A_3}(\lambda)-$polytopes 162
5.5.2. Orbit decompositions of the $\mathcal{V}_{B_3}(\lambda)-$polytopes 165
5.5.3. Orbit decompositions of the $\mathcal{V}_{C_3}(\lambda)-$polytopes 168

5.6. Symmetry breaking of $\mathcal{V}_W(\lambda)$ and related tubes 171

Conclusion 175

References 177

Appendix A. The ‘pancake’-structures of $\mathcal{V}_{H_3}(\lambda)-$polytopes 185

Appendix B. Tables of orbit decompositions of $\mathcal{V}_{H_3}(\lambda)-$polytopes 189

Appendix C. The ‘pancake’-structures of $\mathcal{V}_{A_3}(\lambda)-$polytopes 195

Appendix D. The ‘pancake’-structures of $\mathcal{V}_{B_3}(\lambda)-$polytopes 199

Appendix E. Interpolation by splitting transforms (Mathematica code) . . . 203

List of tables

1.1 The numbers of elements of Φ and the orders of finite reflection groups G are presented. 37

1.2 Relations for the simple root of the crystallographic root systems. 39

2.1 The integral error estimates of the interpolations $\mathrm{I}[f]^{(0)}_M$, $\mathrm{I}[f]^{(1)}_M$, $\widetilde{\mathrm{I}}[f]^{(0)}_M$ and $\widetilde{\mathrm{I}}[f]^{(1)}_M$ are tabulated for $M = 10, 12, 14, 16$ and 18. 72

3.1 The sizes of orbits $O_\lambda(H_n)$ of the non-crystallographic groups H_n, $n \in \{2, 3, 4\}$ provided for each type of dominant point λ with the coefficients $a, b, c, d \in \mathbb{R}^{>0}$. . 88

3.2 The Cartan matrices and their inverses for the non-crystallographic groups H_2, H_3 and H_4. 88

3.3 The embedding index γ provided for the non-crystallographic groups H_n, $n \in \{2, 3, 4\}$ and their maximal subgroups G'. 95

3.4 Dominant points for lower orbits obtained by subtraction of the simple roots $\alpha_1, \alpha_2, \alpha_3$ of H_3 are listed for any type of a dominant point of the initial orbit: $(a, 0, 0)$, $(0, a, 0)$, $(0, 0, a)$, $(a, a, 0)$, $(0, a, a)$, $(a, 0, a)$. The coefficients are provided by the values $a \in \{1, 2, \ldots, 9\}$. 99

4.1 The two-dimensional subgroups of the Coxeter group H_3. 112

4.2 Scaling coefficients c_k, $k \in \{1, 2, 3\}$ for the vectors of the $\omega-$basis. 113

4.3 The orbits of a polytope $\mathcal{V}_{H_3}(\lambda)$ are presented for each type of dominant point λ. The scaled orbits $(a', 0, 0), (0, b', 0)$ and $(0, 0, c')$ are presented by means of the corresponding decorated Coxeter–Dynkin diagrams. The generic orbits within the structure of a $\mathcal{V}_{H_3}(\lambda)-$polytope are marked by ✓. 119

4.4 The seed points λ of $\mathcal{D}_{H_3}(\lambda)$ and λ' of its dual $\mathcal{V}_{H_3}(\lambda)$. The first column indicates a dominant point λ in the coordinate form, the second column provides λ as a linear combination of the fundamental weights ω_k, and the third column provides λ' as the vectors ω'_k, $k \in \{1, 2, 3\}$. 122

4.5 The faces v_2 of $\mathcal{V}_{H_3}(\lambda)$ are presented for each type of dominant point λ (see Figure 4.7). The faces v_0 are generated by the corresponding reflections applied to λ' indicated in Table 4.4. The approximate lengths of the edges v_1 are denoted by a, b, c, and the relative angles are denoted by α, β, γ. 123

4.6 The types and the numbers of faces d_k and v_{2-k} of $\mathcal{D}_{H_3}(a,0,0)$ and $\mathcal{V}_{H_3}(a,0,0)$, respectively, are provided for each decorated Coxeter–Dynkin diagram of H_3. The polygon-polygon notation corresponds to the types of edges shared by the two-dimensional faces of a polytope. The number of faces $N(d_k)$ and $N(v_{2-k})$ is denoted by N. 124

4.7 Decorations of the Coxeter–Dynkin diagram of H_3 are presented for dominant points λ, namely $(0,b,0)$, $(a,b,0)$, $(a,0,c)$, $(0,b,c)$ and (a,b,c). The faces d_k and v_{2-k}, $k \in \{0,1,2\}$ correspond to the faces of $\mathcal{D}(\lambda)$ and $\mathcal{V}(\lambda)$. The polygon-polygon notation corresponds to the types of edges shared by the two-dimensional faces of a polytope. The number of faces $N(d_k)$ and $N(v_{2-k})$ is denoted by N. 125

4.8 The numerical values of the squared radii $R^2_{H_3}(\lambda')$ of the orbits $O_{H_3}(\lambda')$ of $\mathcal{V}_{H_3}(\lambda)-$polytopes. 127

4.9 The numbers of orbits and ‘pancakes’ are provided for each two-dimensional subgroup $G' \subset H_3$ by the orbit decompositions of $\mathcal{V}_{H_3}(\lambda)-$polytopes. The dominant points λ with $a = b = c$ are considered. 133

4.10 The symmetries and number of faces of the fullerenes C_{20}, C_{24}, C_{26}, $C_{28:m}$, $C_{30:m}$ are presented. 142

5.1 The Cartan matrices and their inverses are listed for the crystallographic reflection groups A_3, B_3 and C_3. 152

5.2 The two-dimensional subgroups of the crystallographic groups A_3, B_3 and C_3 and the corresponding mixed bases. 154

5.3 Scaling coefficients c_k, $k \in \{1,2,3\}$ for the vectors of the $\omega-$basis of the A_3, B_3 and C_3 groups. 155

5.4 Decorations of the Coxeter–Dynkin diagram of A_3 are presented for dominant points λ, namely $(0,b,0)$, $(a,b,0)$, $(a,0,c)$, $(0,b,c)$ and (a,b,c). The faces d_k and v_{2-k}, $k \in \{0,1,2\}$ correspond to the faces of $\mathcal{D}(\lambda)$ and $\mathcal{V}(\lambda)$. The polygon-polygon notation corresponds to the types of edges shared by the two-dimensional faces of a polytope. The number of faces $N(d_k)$ and $N(v_{2-k})$ is denoted by N. 157

5.5 Decorations of the Coxeter–Dynkin diagrams of B_3 and C_3 are presented for dominant points λ, namely $(0,b,0)$, $(a,b,0)$, $(a,0,c)$, $(0,b,c)$ and (a,b,c). The faces d_k and v_{2-k}, $k \in \{0,1,2\}$ correspond to the faces of $\mathcal{D}(\lambda)$ and $\mathcal{V}(\lambda)$, respectively. The polygon-polygon notation corresponds to the types of edges shared by the two-dimensional faces of a polytope. The number of faces $N(d_k)$ and $N(v_{2-k})$ is denoted by N. 158

5.6 The sizes of two-dimensional orbits of the crystallographic reflection groups A_2, B_2, C_2 and $A_1 \times A_1$ are provided for each type of dominant point λ with $a,b \in \mathbb{R}^{>0}$. 162

5.7 The numbers of orbits and 'pancakes' are provided for $\mathcal{V}_{A_3}(\lambda)-$polytopes. The dominant points λ with the coordinates $a = b = c$ are considered. 165

5.8 The numbers of orbits and 'pancakes' are provided for $\mathcal{V}_{B_3}(\lambda)-$polytopes. The dominant points λ with the coordinates $a = b = c$ are considered. 168

5.9 The numbers of orbits and 'pancakes' are provided for $\mathcal{V}_{C_3}(\lambda)-$polytopes. The dominant points λ with the coordinates $a = b = c$ are considered. 171

B.1 The orbit decomposition of the polytope $\mathcal{V}_{H_3}(1,0,0)$. 189

B.2 The orbit decomposition of the polytope $\mathcal{V}_{H_3}(0,0,1)$. 190

B.3 The orbit decomposition of the polytope $\mathcal{V}_{H_3}(0,1,0)$. 190

B.4 The orbit decomposition of the polytope $\mathcal{V}_{H_3}(1,1,0)$. 191

B.5 The orbit decomposition of the polytope $\mathcal{V}_{H_3}(0,1,1)$. 191

B.6 The orbit decomposition of the polytope $\mathcal{V}_{H_3}(1,0,1)$. 192

B.7 The orbit decomposition of the polytope $\mathcal{V}_{H_3}(1,1,1)$. 193

List of figures

1.1 Crystallographic root systems of rank 1 and 2 and the non-crystallographic root system H_2 are presented. The labels correspond to the positive roots of the considered root systems. The simple roots are labeled by α_1 and α_2. 35

1.2 The root systems of crystallographic reflection groups of rank 3 are presented. The simple roots are labeled by α_k, $k \in \{1, 2, 3\}$. 36

1.3 The complete classification of all connected Coxeter diagrams. 40

1.4 The complete classification of all connected Dynkin diagrams. 40

1.5 The fundamental region of the Weyl group A_3 is shown. The vectors ω_1, ω_2 and ω_3 correspond to the fundamental weights of A_3. For $M = 2, 3$ and 5, the points of the grid F_M are depicted by black color. 44

1.6 The structure of the triplet is presented. (a) For simplicity, the bonds of tetrahedral atoms are depicted by orange edges; (b) The angles depicted by blue, orange, pink and green colors correspond to the values 109.47°, 101.02°, 100.67° and 117.58°, respectively.
(c) The top-view of the triplet. 49

2.1 (a) The magnified fundamental region $6F_Q$ is depicted as the equilateral triangle which contains 28 points corresponding to the elements of the weight set Λ_6. The weight sets $\Lambda_6^{(0)}$, $\Lambda_6^{(1)}$ and $\Lambda_6^{(2)}$ are depicted by 10 light blue, 9 yellow and 9 magenta points, respectively. Omitting the dotted nodes on the boundary, the weight set $\widetilde{\Lambda}_6$ contains 10 points. The weight sets $\widetilde{\Lambda}_6^{(0)}$, $\widetilde{\Lambda}_6^{(1)}$ and $\widetilde{\Lambda}_6^{(2)}$ contain 4 light blue, 3 yellow and 3 magenta points. The blue numbers correspond to the values of the discrete $h-$function. (b) The fundamental domain F_Q of A_2, depicted by the equilateral triangle, contains 10 yellow nodes in the kite-shaped domain F_P that form the point set $F_6^{(0)}$. Excluding the point in center of F_Q, the sets $F_6^{(1)}$ and $F_6^{(2)}$ are depicted as 9 yellow nodes. The yellow nodes without the dotted ones on the boundary of F_Q correspond to the set $\widetilde{F}_6^{(0)}$. Omitting the central point of F_Q and the points on its boundary, 3 yellow nodes correspond to the point set $\widetilde{F}_6^{(1)}$,

$\widetilde{F}_6^{(2)}$. The blue and red numbers correspond to the values of the discrete $\varepsilon-$ and $d-$functions, respectively. 60

2.2 The fundamental region F_Q is depicted by the blue triangle. The simple roots and fundamental weights are marked by α_i, ω_i, $i \in \{1,2\}$. The reflections r_i orthogonal to α_i pass through the origin. The points $x+\omega_1$ and $x+\omega_2$ are obtained by shifting of $x \in F_Q$ by the vectors ω_1 and ω_2. The affine reflections r_{α_i} are orthogonal to α_i, and they pass through $\frac{1}{2}\alpha_i$; the affine reflection r_0 passes through the middle of the highest root ξ. The points reflected back into F_Q coincide with the points obtained by the action of the elements γ_i of the cyclic group Γ. 61

2.3 The model function f plotted over the region F_P. 70

2.4 The interpolating functions $\mathrm{I}[f]_M^{(0)}$ are for $M = 10,14,18$ plotted over the region F_P. The sampling point sets $F_M^{(0)}$ of the interpolation are marked by the blue dots. . 70

2.5 The interpolating functions $\mathrm{I}[f]_M^{(1)}$ are for $M = 10,14,18$ plotted over the region F_P. The sampling point sets $F_M^{(1)}$ of the interpolation are marked by the blue dots. . 71

2.6 The interpolating functions $\widetilde{\mathrm{I}}[f]_M^{(0)}$ are for $M = 10,14,18$ plotted over the region F_P. The sampling point sets $\widetilde{F}_M^{(0)}$ of the interpolation are marked by the blue dots. . 71

2.7 The interpolating functions $\widetilde{\mathrm{I}}[f]_M^{(1)}$ are for $M = 10,14,18$ plotted over the region F_P. The sampling point sets $\widetilde{F}_M^{(1)}$ of the interpolation are marked by the blue dots. . 72

3.1 The Coxeter–Dynkin diagrams of the non-crystallographic groups H_n, $n \in \{2,3,4\}$. The nodes correspond to the simple roots α_k, $k \in \{1,\dots,n\}$. 92

3.2 The root system of the Coxeter group H_2. The dashed lines r_1 and r_2 correspond to the reflecting hyperplanes orthogonal to the simple roots α_1 and α_2, respectively. The root ξ denotes the highest root of H_2. The coordinates of the points of an orbit with a dominant point $\lambda = (a,b)$ of H_2 are listed. The orbits of the reflection group A_1 are depicted by green segments. 93

3.3 The tree-diagram for the orbits of H_2. (*a*) $O_{(1,0)}(H_2)$; (*b*) $O_{(0,1)}(H_2)$; (*c*) $O_{(1,1)}(H_2)$. The dominant points are displayed in boxes. The points that do not belong to $O_{(1,1)}(H_2)$ are depicted by blue color. 98

3.4 The tree-diagram for the orbit $O_{(\tau,1)}(H_2)$. The dominant points are displayed in boxes. The points that do not belong to $O_{(\tau,1)}(H_2)$ are depicted by blue color. . . . 100

3.5 The tree-diagrams constructed for the orbits of H_3. (*a*) $O_{(1,0,0)}(H_3)$; (*b*) $O_{(0,0,1)}(H_3)$. The subtraction paths that yield already existing points are marked by blue color. 100

3.6 (a) The tree-diagram for the orbit $O_{(2,0,0)}(H_3)$; (b) the corresponding nested polytopes. The orbits $O_{(2,0,0)}(H_3)$, $O_{(0,1,0)}(H_3)$ and $O_{(0,-\tau',0)}(H_3)$ are presented in green, black and bold colors, respectively. 101

3.7 The nested polytopes provided by the algorithm of root-subtraction. (a) $O_{(3,1,0)}(H_3)$; (b) $O_{(0,1,3)}(H_3)$. 101

4.1 The dual pairs of polytopes of the Coxeter group H_3 are constructed for each type of dominant point λ. 109

4.2 The Coxeter–Dynkin diagram of the non-crystallographic group H_3. The nodes of the diagram are labeled by the simple roots α_k, $k \in \{1,2,3\}$. The links between the nodes provide the relative angles between the simple roots: $\angle(\alpha_1,\alpha_2) = \frac{2\pi}{3}$, $\angle(\alpha_2,\alpha_3) = \frac{4\pi}{5}$, $\angle(\alpha_1,\alpha_3) = \frac{\pi}{2}$. 110

4.3 The 15 positive roots of the non-crystallographic group H_3 are presented. The simple roots α_k, $k \in \{1,2,3\}$ are depicted by green color. The root $\xi = \tau\alpha_1 + 2\tau\alpha_2 + \tau^2\alpha_3$ stands for the highest root. The values of the angles between the simple roots α_k are provided. 111

4.4 The spherical and Euclidean polytopes are provided by the structure of the icosahedron $\mathcal{D}_{H_3}(1,0,0)$. The vectors ω_k, $k = \{1,2,3\}$ label the fundamental weights. The fundamental region F is provided by the vertices $\{0,\omega_1,\omega_2,\omega_3\}$. . . . 114

4.5 (a) The icosahedron $\mathcal{D}_{H_3}(1,0,0)$ is presented. The directed edges corresponding to the reflections r_1, r_2 and r_3 are depicted by blue, orange and green colors, respectively. The orange and blue points indicate the vertices providing branching and rejoining of the reflection graph. (b) The planar reflection graph. 115

4.6 (a) The polytope $\mathcal{D}_{H_3}(1,1,1)$. (b) The vertex of $\mathcal{D}_{H_3}(1,1,1)$. The dominant point $\lambda = (1,1,1)$ is depicted by an empty node. The actions of reflections r_1, r_2 and r_3 are illustrated by blue, orange and green arrows, respectively. 117

4.7 The vertices of polytopes $\mathcal{D}_{H_3}(\lambda)$ and the corresponding two-dimensional faces of $\mathcal{V}_{H_3}(\lambda)$ (indicated by green color) are presented for each type of λ (marked by black rhombus node). The coordinates are provided in the $\omega-$ and $\omega'-$basis for $\mathcal{D}_{H_3}(\lambda)$ and $\mathcal{V}_{H_3}(\lambda)$, respectively. 120

4.8 The decoration method applied to the diagram of $\mathcal{D}_{H_3}(0,1,0)$. The orbits of $\mathcal{V}_{H_3}(0,1,0)$ are presented at the last step of the decoration procedure. 121

4.9 On the left, the vertices of $\mathcal{D}_{H_3}(a,0,0)$ and $\mathcal{V}_{H_3}(a,0,0)$ are found on the surface of a sphere $\mathcal{S}$. The green tile corresponds to the fundamental region F of H_3. The points provided by the vectors ω_1, ω_2 and ω_3 are depicted by orange, green and black colors, respectively. On the right, the recursive decoration rules are applied to the Coxeter–Dynkin diagram of H_3. 124

4.10 The polytopes $\mathcal{V}_{H_3}(0,b,0)$ and $\mathcal{V}_{H_3}(a,b,0)$ are shown in (a) and (b). The fundamental region F is depicted by the orange triangle. The stellations of $\mathcal{V}_{H_3}(0,b,0)$ and $\mathcal{V}_{H_3}(a,b,0)$ are provided with respect to the scaling factors x and z by (c) the small stellated dodecahedron and (d) the excavated dodecahedron. . . 129

4.11 (a) The polytope $\mathcal{V}_{H_3}(0,b,c)$ is shown. The fundamental region F is depicted by the orange triangle. The stellations of $\mathcal{V}_{H_3}(0,b,c)$ are provided with respect to the scaling factors x and z by (b) the great dodecahedron, (c) the great stellated dodecahedron. 129

4.12 The polytopes $\mathcal{V}_{H_3}(a,0,c)$ and $\mathcal{V}_{H_3}(a,b,c)$ are shown. The fundamental region F is depicted by the orange triangle. 130

4.13 Depending on the scaling factors x, y, z, the twelve different types of stellations of $\mathcal{V}_{H_3}(a,b,c)$ are presented. 131

4.14 On the left, the polytope $\mathcal{V}_{H_3}(1,0,0)$ is viewed from the direction orthogonal to the simple root (a) α_1, (b) α_2, (c) α_3. The values of the squared radii are listed on the right for each ‘pancake’. 134

4.15 For $\mathcal{V}_{H_3}(a,0,0)$ viewed from the direction orthogonal to the simple root α_1, the inserts and the corresponding tubes are presented in the columns (a) and (b). . . . 135

4.16 For $\mathcal{V}_{H_3}(a,0,0)$ viewed from the direction orthogonal to the simple root α_2, the inserts and the corresponding tubes are presented in the columns (a) and (b). . . . 135

4.17 For $\mathcal{V}_{H_3}(a,0,0)$ viewed from the direction orthogonal to the simple root α_3, the inserts and the corresponding tubes are presented in the columns (a) and (b). . . . 136

4.18 On the left, the polytope $\mathcal{V}_{H_3}(0,0,1)$ is viewed from the direction orthogonal to the simple root (a) α_1, (b) α_2, (c) α_3. The values of the squared radii are listed on the right for each ‘pancake’. 136

4.19 For $\mathcal{V}_{H_3}(0,0,c)$ viewed from the direction orthogonal to the simple roots α_1 and α_3, the inserts and the corresponding tubes are presented in the columns (a) and (b), respectively. 137

4.20 For $\mathcal{V}_{H_3}(0,0,c)$ viewed from the directions orthogonal to the simple root α_2, the inserts and the corresponding tubes are presented in the columns (a) and (b). . . . 137

4.21 On the left, the polytope $\mathcal{V}_{H_3}(0,1,0)$ is viewed from the direction orthogonal to the simple root (*a*) α_1, (*b*) α_2, (*c*) α_3. The values of squared radii are listed on the right for each 'pancake'. 138

4.22 For $\mathcal{V}_{H_3}(0,b,0)$ viewed from the direction orthogonal to the simple root α_1, the inserts and the corresponding tubes are presented in the columns (*a*) and (*b*). . . . 138

4.23 For $\mathcal{V}_{H_3}(0,b,0)$ viewed from the directions orthogonal to the simple root α_2 and α_3, the inserts and the corresponding tubes are presented in the columns (*a*) and (*b*), respectively. In (*a*) the same tube is viewed from a different angle. 139

4.24 The possible inserts are presented in columns for the polytopes (*a*) $\mathcal{V}_{H_3}(a,b,0)$, (*b*) $\mathcal{V}_{H_3}(a,0,c)$, (*c*) $\mathcal{V}_{H_3}(0,b,c)$, (*d*) $\mathcal{V}_{H_3}(a,b,c)$, and they are ordered for the directions of the simple roots α_1, α_2, α_3 from top to bottom. 140

4.25 (*a*) The fullerene C_{20} is oriented in the direction of the simple root α_1. The edges depicted by bold segments correspond to the symmetry-breaking path. (*b*) The net of C_{20}. 141

4.26 (*a*) The fullerene C_{20} is viewed from the direction orthogonal to the simple root α_1. The faces depicted by gray color are kept after the symmetry of C_{20} is broken. (*b*) The fullerene C_{24}. (*c*) The fullerene $C_{30:1}$. (*d*) The structure of $C_{30:1}$ is extended into the nanotube C_{50}. 143

4.27 (*a*) The fullerene C_{20} is viewed from the direction orthogonal to the simple root α_1. The faces depicted by gray color are kept after the symmetry of C_{20} is broken. (*b*) The fullerene $C_{30:2}$. 143

4.28 (*a*) The fullerene C_{20} is viewed from the direction orthogonal to the simple root α_2. The faces depicted by gray color are kept after the symmetry of C_{20} is broken. (*b*) The fullerene $C_{28:2}$. 144

4.29 (*a*) The fullerene C_{20} is viewed from the direction orthogonal to the simple root α_2. The faces depicted by gray color are kept after the symmetry of C_{20} is broken. (*b*) The fullerene $C_{30:3}$. 144

4.30 (*a*) The fullerene C_{20} is viewed from the direction orthogonal to the simple root α_3. The faces depicted by gray color are kept after the symmetry of C_{20} is broken. (*b*) The fullerene $C_{28:1}$. 144

4.31 (*a*) The fullerene C_{20} is viewed from the direction orthogonal to the simple root α_3. The faces depicted by gray color are kept after the symmetry of C_{20} is broken. (*b*) The fullerene C_{26}. (*c*) The structure of C_{26} is extended into the nanotube C_{50}. 145

4.32 The two-dimensional nets of the fullerenes C_{24}, C_{26}, $C_{28:m}$, $C_{30:m}$ are presented. The bold edges are in one-to-one correspondence with the edges chosen at the start of the symmetry breaking procedure. The faces depicted by green color are inserted whenever the symmetry of C_{20} is broken. The empty and filled nodes indicate an overlap as the net is folded onto a cylinder.......................... 146

5.1 The dual pairs of polytopes of the crystallographic group A_3 are constructed for each type of dominant point λ.. 150

5.2 The dual pairs of polytopes of the crystallographic group B_3 and C_3 are constructed for each type of dominant point λ.. 151

5.3 The Dynkin diagrams associated with the crystallographic groups A_3, B_3 and C_3. The nodes of the diagrams correspond either to the vectors of the $\alpha-$basis, or to the basis vectors of the $\omega-$basis, or to the reflections r_k in the reflecting hyperplanes m_k, $k \in \{1, 2, 3\}$.. 152

5.4 (a) The polytope $\mathcal{V}_{B_3}(0,0,1)$ is oriented in the α_1-direction. The symmetry-breaking path is indicated by bold black edges. (b) The insert for $\mathcal{V}_{B_3}(0,0,1)$. (c) The nanotube obtained by inserting four extra orbits into the structure of $\mathcal{V}_{B_3}(0,0,1)$.. 172

5.5 (a) The polytope $\mathcal{V}_{B_3}(1,0,0)$ is oriented in the α_3-direction. The symmetry-breaking path is indicated by bold black edges. (b) The insert for $\mathcal{V}_{B_3}(1,0,0)$. (c) The nanotube obtained by inserting four extra orbits into the structure of $\mathcal{V}_{B_3}(1,0,0)$.. 172

5.6 (a) The polytope $\mathcal{V}_{A_3}(1,0,1)$ is oriented in the α_1-direction. The symmetry-breaking path is indicated by bold black edges. (b) The insert for $\mathcal{V}_{A_3}(1,0,1)$. (c) The nanotube obtained by inserting four extra orbits into the structure of $\mathcal{V}_{A_3}(1,0,1)$.. 172

5.7 (a) The polytope $\mathcal{V}_{B_3}(0,1,1)$ is oriented in the α_3-direction. The symmetry-breaking path is indicated by bold black edges. (b) The insert for $\mathcal{V}_{B_3}(0,1,1)$. (c) The nanotube obtained by inserting six extra orbits into the structure of $\mathcal{V}_{B_3}(0,1,1)$.. 173

5.8 (a) The polytope $\mathcal{V}_{A_3}(1,0,1)$ is oriented in the α_2-direction. The symmetry-breaking path is indicated by bold black edges. (b) The insert for $\mathcal{V}_{A_3}(1,0,1)$. (c) The nanotube obtained by inserting six extra orbits into the structure of $\mathcal{V}_{A_3}(1,0,1)$.. 173

5.9 (a) The polytope $\mathcal{V}_{A_3}(1,1,1)$ is oriented in the α_2-direction. The symmetry-breaking path is indicated by bold black edges. (b) The insert for $\mathcal{V}_{A_3}(1,1,1)$. (c) The nanotube obtained by inserting six extra orbit into the structure of $\mathcal{V}_{A_3}(1,1,1)$. 173

5.10 (a) The structure of Zeolite A is constituted by the polytopes $\mathcal{D}_{A_3}(1,1,1)$ (truncated octahedron) and $\mathcal{D}_{B_3}(1,0,0)$ (cube). (b) The structure of faujasite-type zeolites X and Y is constituted by the polytopes $\mathcal{D}_{A_3}(1,1,1)$ (truncated octahedron) and $\mathcal{D}_{A_2\times A_1}(1,1,1)$ (hexagonal prism). 176

A.1 The polytope $\mathcal{V}_{H_3}(1,0,0)$ is oriented in the direction of the simple roots α_1, α_2 and α_3. The points of the orbits $O_{H_3}(0,0,c')$ are depicted by black color. 185

A.2 The polytope $\mathcal{V}_{H_3}(0,0,1)$ is oriented in the direction of the simple roots α_1, α_2 and α_3. The points of the orbits $O_{H_3}(a',0,0)$ are depicted by black color. 186

A.3 The polytope $\mathcal{V}_{H_3}(0,1,0)$ is oriented in the direction of the simple roots α_1, α_2 and α_3. The points of the orbits $O_{H_3}(a',0,0)$ and $O_{H_3}(0,0,c')$ are depicted by green and black colors, respectively. 186

A.4 The polytope $\mathcal{V}_{H_3}(1,1,0)$ is oriented in the direction of the simple roots α_1, α_2 and α_3. The points of the orbits $O_{H_3}(a',0,0)$ and $O_{H_3}(0,0,c')$ are depicted by green and black colors, respectively. 187

A.5 The polytope $\mathcal{V}_{H_3}(0,1,1)$ is oriented in the direction of the simple roots α_1, α_2 and α_3. The points of the orbits $O_{H_3}(a',0,0)$ and $O_{H_3}(0,0,c')$ are depicted by green and black colors, respectively. 187

A.6 The polytope $\mathcal{V}_{H_3}(1,0,1)$ is oriented in the direction of the simple roots α_1, α_2 and α_3. The points of the orbits $O_{H_3}(a',0,0)$, $O_{H_3}(0,b',0)$ and $O_{H_3}(0,0,c')$ are depicted by orange, black and green colors, respectively. 188

A.7 The polytope $\mathcal{V}_{H_3}(1,1,1)$ is oriented in the direction of the simple roots α_1, α_2 and α_3. The points of the orbits $O_{H_3}(a',0,0)$, $O_{H_3}(0,b',0)$ and $O_{H_3}(0,0,c')$ are depicted by orange, black and green colors, respectively. 188

C.1 The polytope $\mathcal{V}_{A_3}(1,0,0)$ is oriented in the direction of the simple roots α_1, α_2 and α_3. The points of the orbit $O_{A_3}(0,0,c')$ are depicted by black color. 195

C.2 The polytope $\mathcal{V}_{A_3}(0,0,1)$ is oriented in the direction of the simple roots α_1, α_2 and α_3. The points of the orbit $O_{A_3}(a',0,0)$ are depicted by black color. 196

C.3 The polytope $\mathcal{V}_{A_3}(0,1,0)$ is oriented in the direction of the simple roots α_1, α_2 and α_3. The points of the orbits $O_{A_3}(a',0,0)$ and $O_{A_3}(0,0,c')$ are depicted by green and black colors, respectively. 196

C.4 The polytope $\mathcal{V}_{A_3}(1,1,0)$ is oriented in the direction of the simple roots α_1, α_2 and α_3. The points of the orbits $O_{A_3}(a',0,0)$ and $O_{A_3}(0,0,c')$ are depicted by green and black colors, respectively. 197

C.5 The polytope $\mathcal{V}_{A_3}(0,1,1)$ is oriented in the direction of the simple roots α_1, α_2 and α_3. The points of the orbits $O_{A_3}(a',0,0)$ and $O_{A_3}(0,0,c')$ are depicted by green and black colors, respectively. 197

C.6 The polytope $\mathcal{V}_{A_3}(1,0,1)$ is oriented in the direction of the simple roots α_1, α_2 and α_3. The points of the orbits $O_{A_3}(a',0,0)$, $O_{A_3}(0,b',0)$ and $O_{A_3}(0,0,c')$ are depicted by green, orange and black colors, respectively. 198

C.7 The polytope $\mathcal{V}_{A_3}(1,1,1)$ is oriented in the direction of the simple roots α_1, α_2 and α_3. The points of the orbits $O_{A_3}(a',0,0)$, $O_{A_3}(0,b',0)$ and $O_{A_3}(0,0,c')$ are depicted by green, orange and black colors, respectively. 198

D.1 The polytope $\mathcal{V}_{B_3}(1,0,0)$ is oriented in the direction of the simple roots α_1, α_2 and α_3. The points of the orbit $O_{B_3}(c',0,0)$ are depicted by black color. 199

D.2 The polytope $\mathcal{V}_{B_3}(0,0,1)$ is oriented in the direction of the simple roots α_1, α_2 and α_3. The points of the orbit $O_{B_3}(0,0,a')$ are depicted by black color. 200

D.3 The polytope $\mathcal{V}_{B_3}(0,1,0)$ is oriented in the direction of the simple roots α_1, α_2 and α_3. The points of the orbits $O_{B_3}(a',0,0)$ and $O_{B_3}(0,0,c')$ are depicted by black and green colors, respectively. 200

D.4 The polytope $\mathcal{V}_{B_3}(1,1,0)$ is oriented in the direction of the simple roots α_1, α_2 and α_3. The points of the orbits $O_{B_3}(a',0,0)$ and $O_{B_3}(0,0,c')$ are depicted by black and green colors, respectively. 201

D.5 The polytope $\mathcal{V}_{B_3}(0,1,1)$ is oriented in the direction of the simple roots α_1, α_2 and α_3. The points of the orbits $O_{B_3}(a',0,0)$ and $O_{B_3}(0,0,c')$ are depicted by black and green colors, respectively. 201

D.6 The polytope $\mathcal{V}_{B_3}(1,0,1)$ is oriented in the direction of the simple roots α_1, α_2 and α_3. The points of the orbits $O_{B_3}(a',0,0)$, $O_{B_3}(0,b',0)$ and $O_{B_3}(0,0,c')$ are depicted by green, orange and black colors, respectively. 202

D.7 The polytope $\mathcal{V}_{B_3}(1,1,1)$ is oriented in the direction of the simple roots α_1, α_2 and α_3. The points of the orbits $O_{B_3}(a',0,0)$, $O_{B_3}(0,b',0)$ and $O_{B_3}(0,0,c')$ are depicted by green, orange and black colors, respectively. 202

Acknowledgments

Foremost, I would like to express my deepest gratitude to my research director, Professor Jiří Patera, for giving me the opportunity to study under his supervision. I am grateful to him for his constant guidance, enthusiasm, patience and great support throughout my Ph.D. studies. This thesis would never have been possible without his help.

I would like to sincerely thank my co-director, Dr. Marzena Szajewska, to whom I am indebted for her collaboration, encouragement and invaluable support. I am also extremely grateful to Professor Jiří Hrivnák for his enormous help and for answering my questions with great patience. This thesis work would not have been possible without their support.

I would also like to thank Professor Robert V. Moody for his many stimulating discussions and valuable comments. A great thanks to Dr. Maryna Nesterenko for her collaboration and many helpful insights. Special thanks to Dr. Alexandra Patera for her invaluable help with the text editing of this work. I am grateful to my colleague Emmanuel Bourret for his collaboration and help with the computer code for calculations related to polytopes. I also thank my colleagues, Vojtech Teska and Xavier Pelletier, for their help and many interesting, thought-provoking conversations.

I would like to express my gratitude to the committee members, with special thanks to Dr. Pierre–Philippe Dechant and Professor Yvan Saint–Aubin for their insightful comments and helpful suggestions to improve this thesis.

I would like to gratefully acknowledge the Département de Physique (bourse d'admission) and the Faculté des Études Supérieures et Postdoctorales (bourse d'exemption des droits supplémentaires de scolarité pour les étudiants internationaux) for their hospitality and financial support that allowed me to fully concentrate on my studies.

Finally, I would like to express my sincere gratitude to my beloved family and friends for their endless love, patience and support that have always been accompanying me in my life journey. I am deeply grateful to my parents for supporting, inspiring and encouraging me every step of the way.

Introduction

The purpose of this work is to study the role of finite reflection groups in Fourier analysis related to the two-dimensional digital data processing, symmetry breaking of three-dimensional polytopes and their structural extension into nanotubes, as well as the construction of stellated and nested polytopes of non-crystallographic type.

Finite reflection groups, which are widely known as Coxeter groups (Coxeter [**31**]), are relevant to the description of many structural phenomena found in nature. The classification of such groups was one of the major achievements of the 20th century. The finite Coxeter groups are generated by the set of reflections across the reflecting hyperplanes that are orthogonal to the simple roots and passing through the origin (Humphreys [**67**]; Kane [**72**]). There are two types of finite Coxeter groups: crystallographic groups (Weyl groups) and non-crystallographic ones. The terminology and pertinent information about crystallographic root systems stem from Lie theory, and any finite Weyl group is uniquely associated with a Lie algebra (Bourbaki [**17**]; Humphreys [**66**]). Although there are infinitely many finite reflection groups of non-crystallographic type that are not related to Lie theory (Humphreys [**67**]). In this work, we focus only on those that possess 5-fold symmetry: the dihedral group H_2 of order 10, the icosahedral group H_3 of order 120 and the H_4 group of order 14400 (Chen *et al.* [**28**]).

The symmetries of non-crystallographic finite reflection groups are relevant to the description of aperiodic point sets and quasi-crystals (Moody and Patera [**104**]; Baake and Grimm [**10**]), as well as polytope structures (Atiyah and Sutcliffe [**7**]). In recent years, due to the broad interest in mathematical virology and biophysics, the icosahedral symmetry of the non-crystallographic group H_3 has been extensively utilized to provide a blueprint of the structural assembly of spherical viruses (Dechant *et al.* [**36, 37**]; Twarock [**142**]; Twarock and Luque [**143**]; Zappa [**149**]; Salthouse *et al.* [**130**]). The relevance of the icosahedral symmetry to the description of density maps of macromolecules has been explored in (Terwilliger [**138**]). In physics and chemistry, the H_3-symmetry is used to determine the architecture of various icosahedral molecules, such as fullerenes (Fowler and Manolopoulos [**52**]) and carbon multi-shell nanostructures (Diudea *et al.* [**45**]). Moreover, the connections between the structures of fullerene molecules and icosahedral viruses have been investigated in (Dechant *et al.* [**38**]).

The discovery of the icosahedral fullerene C_{60} (Kroto *et al.* [**84**]) and graphene (Geim and Novoselov [**53**]) have influenced the progress in carbon nanotechnology and led to the further development of new carbon nanomaterials, such as carbon nanofibers (Tzeng *et al.* [**144**]; Yadav *et al.* [**146**]) and carbon-based nanocomposites (Lin *et al.* [**92**]). Due to their remarkable mechanical, physical and chemical properties (Balandin [**11**]; Eletskii and Smirnov [**49**]; Eletskii [**50**]; Knupfer [**82**]), the carbon nanostructures remain promising materials for numerous specialized applications, including carbon-based supercapacitors (Dirican *et al.* [**44**]), nanomedical biosensors (Devi *et al.* [**43**]), nanobiomaterials for hard tissue engineering (Ravanbakhsh *et al.* [**129**]) and drug delivery (Bianco *et al.* [**12**]).

The structural extension of the molecule C_{60} into carbon nanotubes using a group theoretical approach has been described in detail in (Bodner *et al.* [**13, 14, 15**]). The structure of the fullerene C_{60} is provided by the truncated icosahedron, whose orbit is obtained by the action of the H_3 group on a dominant point $(a, b, 0)$, for $a, b > 0$ and $a = b$. Recently, the structures of two polytopes, whose orbits also have 60 vertices, namely those obtained by the action of the icosahedral group on the points $(a, 0, c)$ and $(0, b, c)$, for $a, b, c > 0$ and $a = b = c$, have been investigated to determine their possible extension into nanotubes (Bourret and Grabowiecka [**18**]). Inspired by the work done for C_{60}, we study a symmetry-breaking technique applied to the family of dual polytopes with the H_3-symmetry.

The crystallographic reflection groups found numerous applications in mathematics and theoretical physics. However, we focus only on the relevance of such groups to the Fourier analysis. There are three families of Weyl orbit functions associated with the Weyl groups, i.e., $C-$, $S-$ and $E-$functions, that constitute efficient tools for the Fourier transforms. The Weyl orbit functions have been formulated for semisimple Lie algebras (Klimyk and Patera [**78**], [**79**], [**80**]), and their seven hybrid versions have been studied in detail (Moody *et al.* [**99**]; Hrivnák *et al.* [**59**]; Hrivnák and Juránek [**60**]). The orthogonality property of Weyl orbit functions is crucial, as it permits the Fourier-like analysis on the fundamental region of the infinite extension of a considered Weyl group.

The uniform tori discretization of semisimple Lie groups (Moody and Patera [**101, 102, 105**]; Hrivnák and Patera [**63**]; Hrivnák *et al.* [**59**]) led to the discrete Fourier transforms on lattices. The continuous and discrete two-variable cosine and sine transforms together with their continuous interpolations have been formulated in (Patera and Zaratsyan [**117, 118, 119**]). Later, the family of $C-$, $S-$ and $E-$transforms has been extensively studied for simple and semisimple Lie groups in (Moody *et al.* [**98**]). Such transforms allow the data sampled on the lattice points comprised within the fundamental region to be Fourier-analyzed. Since then, the discrete Fourier calculus of (anti)symmetric Weyl orbit functions has been formulated on the points of the refined dual root (Hrivnák and Motlochová [**62**];

Czyżycki *et al.* [**34**]), weight (Hrivnák and Walton [**65**]), and dual weight lattices (Hrivnák and Patera [**63**]; Hrivnák *et al.* [**59**]). In this work, we focus on the central splitting of the original weight Fourier-Weyl transforms into smaller weight lattice splitting transforms governed by the number of the elements of the center of the Weyl group A_2. In this consideration, the central splitting decomposition of the original transform can be considered as a first step to the recursive two-dimensional digital data processing.

This work comprises Chapters 1–5, and it is organized as follows. In Chapter 1, we recall some useful information about the finite Coxeter groups and the corresponding crystallographic and non-crystallographic root systems, as well as the Weyl orbit functions and their pertinent properties. Chapters 2 and 3 correspond to the articles (Hrivnák *et al.* [**1**]) and (Myronova *et al.* [**2**]), respectively. Chapter 4, together with Appendices A and B, corresponds to the article (Myronova [**3**]). Chapter 5, together with Appendices C and D, corresponds to a paper currently in preparation. More precisely,

- In Chapter 2, using the central splitting mechanism (Moody and Patera [**105**]), we extend the family of the discrete Fourier-like transforms based on the (anti)symmetric Weyl orbit functions of the crystallographic reflection group A_2. The two-variable (anti)symmetric Weyl orbit functions constitute the kernels of the considered discrete Fourier–Weyl transforms. Since the crystallographic group A_2 has three elements of the center, any function f sampled on the points of the weight lattice comprised within the fundamental region decomposes into a sum of three components f_0, f_1 and f_2 each associated to one congruence class of the weight lattice labels. Therefore, employing the central splitting decomposition, we reduce the original weight lattice Fourier-Weyl transforms into the smaller weight lattice splitting transforms that provide the framework for more efficient digital data processing.

  In the interest of open science and reproducibility, in Appendix E, we share the code used to produce the figures in Example 6 (Interpolation by splitting transforms).

- In Chapter 3, using the definition of indices of irreducible representations of simple Lie algebras (Patera *et al.* [**116**]; Okubo and Patera [**110, 111**]) as a foundation to our approach, we determine the even- and odd-order indices of orbits of the non-crystallographic groups H_n, $n \in \{2,3,4\}$. Replacing irreducible representations by orbits of non-crystallographic type, we examine the higher-order indices together with the indices of the tensor product decompositions. Using the branching rules described in (Grabowiecka *et al.* [**54**]), we determine the embedding index for each considered non-crystallographic group. In addition, similarly to the weight systems of representations (Bremner [**20**]; Bremner *et al.* [**21**]), we formulate the algorithm allowing to find the orbits of smaller radii that are contained within the structure of initial polytope, i.e., provides the structures of nested polytopes of non-crystallographic type.

- In Chapter 4, we examine the structural extension of the non-crystallographic dual polyhedra $\mathcal{V}_{H_3}(\lambda)$ to carbon nanotubes and tube-like structures. The choice of the considered polytopes is motivated by the structures of various spherical icosahedral viruses and fullerenes. Using the approach proposed in (Bodner *et al.* [**13, 14, 15**]), we apply a symmetry-breaking mechanism to the family of dual polyhedra of the finite Coxeter group H_3. Using the reduction of the icosahedral symmetry to its two-dimensional subgroups H_2, A_2 and $A_1 \times A_1$, we decompose the orbit points corresponding to the vertices of a polytope into the two-dimensional circular/polygonal orbits known as the 'pancake'-structure of a polytope. We expand the structure of each considered polytope into a nanotube by duplicating the two-dimensional orbits involved in the symmetry-breaking procedure and inserting them into the 'pancake'-structure while preserving the spacing between them. Since a polytope of the $\mathcal{V}_{H_3}(\lambda)-$family may contain up to three orbits within its structure, we introduce the construction of stellated polytopes by scaling the radii of such orbits.
- In Chapter 5, we consider the orbit decompositions of the families of dual polytopes of crystallographic type, i.e., the polytopes obtained by the action of the Weyl groups A_3, B_3 and C_3 on a single point in the three-dimensional real Euclidean space. Since the actions of the B_3 and C_3 groups on seed points in $\mathbb{R}^3$ yield the same polytopes, we demonstrate the 'pancake'-structures for the polytopes obtained only by the actions of the A_3 and B_3 groups (see Appendices C and D, respectively). As well, for some of the considered cases, we present examples of related nanotubes.

In this thesis, all the calculations have been performed using Wolfram Mathematica. All figures have been produced using Wolfram Mathematica and GeoGebra.

Chapter 1

Preliminaries

1.1. Root systems

Let E be a real n-dimensional Euclidean space over $\mathbb{R}$ endowed with the standard scalar product denoted by $\langle \cdot, \cdot \rangle$. For any non-zero vector $\alpha \in E$, a reflection r_α across the reflecting hyperplane $P_\alpha = \{\beta \in E \mid \langle \beta, \alpha \rangle = 0\}$ passing through the origin and orthogonal to α determines a linear transformation

$$r_\alpha(\beta) = \beta - \frac{2\langle \beta, \alpha \rangle}{\langle \alpha, \alpha \rangle}\alpha. \tag{1.1.1}$$

A reflection r_α fixes the corresponding mirror P_α point-wise, and its action sends any vector orthogonal to P_α to its negative. A reflection r_α has the following properties:

- (i) r_α is orthogonal, and it preserves the scalar product as $\langle x, y \rangle = \langle r_\alpha x, r_\alpha y \rangle$, for any $x, y \in E$;
- (ii) non-zero vectors proportional to α yield the same reflection, i.e., $r_\alpha = r_{c\alpha}$, $c \neq 0$;
- (iii) for a zero-vector, it holds that $r_\alpha 0 = 0$.

It is convenient to introduce the notation for the scalar product $(\cdot, \cdot)$, that is linear only in first variable,

$$(\beta, \alpha) = \frac{2\langle \beta, \alpha \rangle}{\langle \alpha, \alpha \rangle}. \tag{1.1.2}$$

Hence, reflection formula (1.1.1) takes the simplified form

$$r_\alpha(\beta) = \beta - (\beta, \alpha)\alpha. \tag{1.1.3}$$

Let $\Phi = \{\alpha_j \mid j = 1, 2, \dots, n\}$ be a subset of a real Euclidean space E. A subset Φ is called a root system if it satisfies the following conditions:

1. Φ is finite, spans E and $0 \notin \Phi$;
2. if $\alpha \in \Phi$, then the only multiples of α in Φ are $\pm\alpha$;
3. if $\alpha \in \Phi$ and r_α permutes the elements of Φ, then Φ is invariant under a reflection r_α.

The root systems of crystallographic type satisfy an extra condition:

(4) if $\alpha, \beta \in \Phi$, then $(\beta, \alpha) \in \mathbb{Z}$.

The elements of a root system Φ are called roots. From the conditions (2) and (3), it follows that $\Phi = -\Phi$. If (2) is omitted, then Φ becomes a reduced root system.

A subset Δ of a root system Φ is called a base, if it satisfies the properties:

(i) Δ forms a basis in E;

(ii) each root β can be expressed as a linear combination of the elements $\alpha \in \Delta$ with all non-negative or all non-positive integers as coefficients k_α,

$$\beta = \sum_{\alpha \in \Delta} k_\alpha \alpha. \tag{1.1.4}$$

A base Δ comprises the elements $\{\alpha_1, \ldots, \alpha_n\}$ that are called the simple roots. Such elements are orthogonal to the reflecting hyperplanes, and they form the $\alpha-$basis of a root system Φ. Since Δ is not unique, the invariant information contained in the simple roots is better explained using the Coxeter–Dynkin diagrams (Section 1.3).

A root system is called irreducible if it cannot be written as a union of two subsets, such that each root from the first set is orthogonal to each root of the second set. Otherwise, the root system is called reducible.

Let Φ be an irreducible root system of crystallographic type. In this case, the simple roots are at most of two different lengths, and they are called long and short roots. If all roots have equal lengths, they are conventionally called long roots. The latter also applies to non-crystallographic roots systems. For any long root $\alpha \in \Phi$, the standard normalization $\langle \alpha_{\text{long}}, \alpha_{\text{long}} \rangle = 2$ is utilized.

The height of the root β is provided by the formula

$$\mathrm{ht}(\beta) = \sum_{\alpha \in \Delta} k_\alpha. \tag{1.1.5}$$

From formula (1.1.5), if all $k_\alpha \geq 0$ ($k_\alpha \leq 0$), then a root β is called a positive (negative) root. However, if all $k_\alpha > 0$, then β is called the highest root. Every root system, that contains the roots of two different lengths, has the unique highest long root ξ and the unique highest short root ξ_s.

Let Φ^+ and Φ^- be a collections of positive and negative roots, respectively, such that $\Phi^- = -\Phi^+$. For any non-zero vector $\gamma \in E$, a set of roots lying on the "positive" side of a reflecting hyperplane orthogonal to γ is denoted by

$$\Phi^+(\gamma) = \{\alpha \in \Phi \mid \langle \gamma, \alpha \rangle > 0\}. \tag{1.1.6}$$

A vector γ is called regular, if $\gamma \in E - \bigcup_{\alpha \in \Phi} P_\alpha$, and it is called singular, otherwise. If γ is regular, i.e., it is not lying on a reflecting hyperplane, then a root system Φ is provided by the union $\Phi^+(\gamma) \cup \Phi^-(\gamma)$. Furthermore, if $\alpha = \beta_1 + \beta_2$ for any $\beta_i \in \Phi^+(\gamma)$, $i \in \{1, 2\}$, then

$\alpha \in \Phi^+(\gamma)$ is called decomposable, and it is indecomposable otherwise. If $\beta \in \Phi^+$, then it can be expressed as a linear combination of the simple roots $\{\alpha_1, \ldots, \alpha_n\}$, for $\alpha_i \in \Delta$, that are not necessarily distinct.

Since reflecting hyperplanes P_α partition E into a finite number of regions, the components $E - \bigcup_\alpha P_\alpha$ are called the Weyl chambers of E. We denote the Weyl chambers by D, as in this consideration, each regular $\gamma \in E$ belongs to only one Weyl chamber. For $\alpha \in \Delta$, the open convex set D^+, that contains all $\gamma \in E$ satisfying the condition $\langle \alpha, \gamma \rangle > 0$, is called the fundamental Weyl chamber relative to Δ.

Let $n = \dim E$ be the rank of a root system. For $n = 1$, there exists only one root system denoted as A_1. However, for $n = 2$, there are four irreducible (A_2, $B_2 \cong C_2$, G_2) and one reducible ($A_1 \times A_1$) crystallographic, as well as the infinite family of non-crystallographic root systems. The one- and two-dimensional root systems are shown in Figure 1.1. For $n = 3$, the crystallographic root systems A_3, B_3 and C_3 are depicted in Figures 1.2, and the positive roots Φ^+ of the root system of H_3 are shown in Figure 4.3.

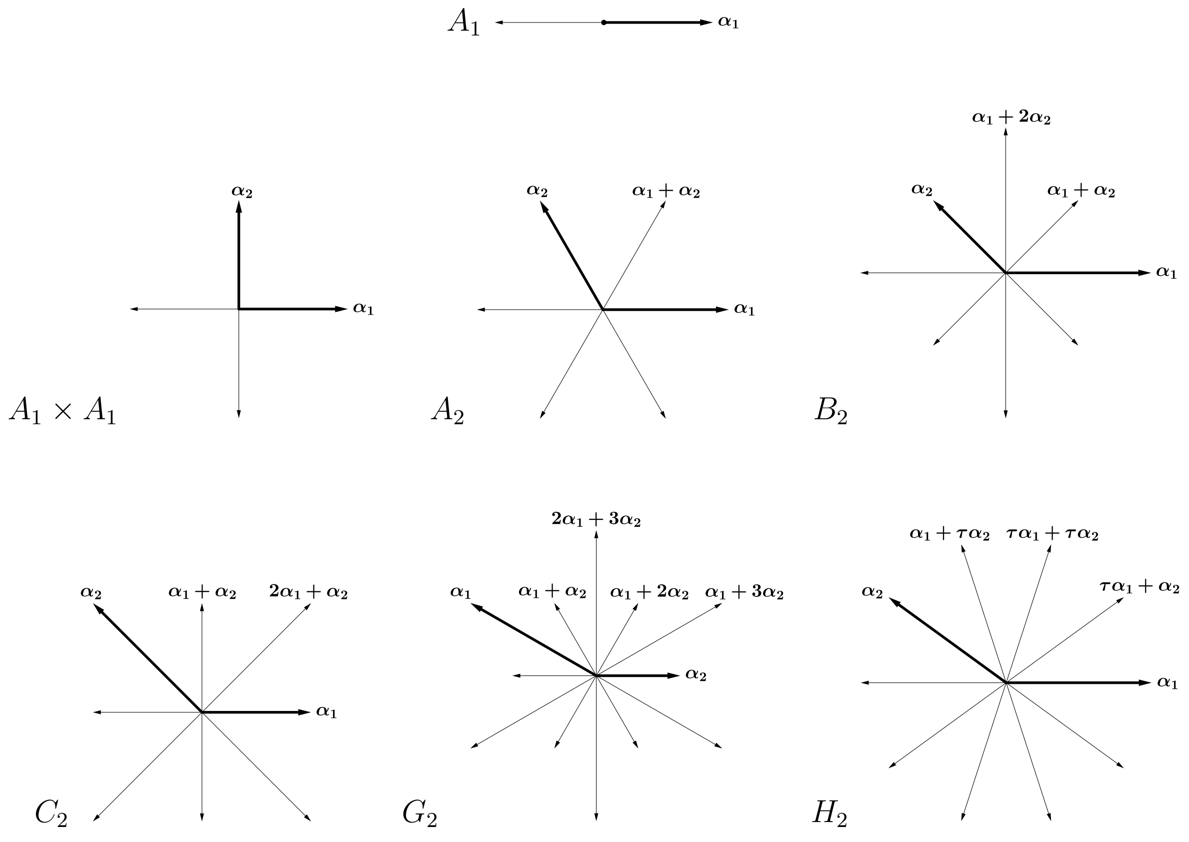
A_1
α_1
α_2
α_1
$A_1 \times A_1$
α_2
$\alpha_1 + \alpha_2$
α_1
A_2
$\alpha_1 + 2\alpha_2$
α_2
$\alpha_1 + \alpha_2$
α_1
B_2
α_2
$\alpha_1 + \alpha_2$
$2\alpha_1 + \alpha_2$
α_1
C_2
$2\alpha_1 + 3\alpha_2$
α_1
$\alpha_1 + \alpha_2$
$\alpha_1 + 2\alpha_2$
$\alpha_1 + 3\alpha_2$
α_2
G_2
$\alpha_1 + \tau\alpha_2$
$\tau\alpha_1 + \tau\alpha_2$
α_2
$\tau\alpha_1 + \alpha_2$
α_1
H_2

Fig. 1.1. Crystallographic root systems of rank 1 and 2 and the non-crystallographic root system H_2 are presented. The labels correspond to the positive roots of the considered root systems. The simple roots are labeled by α_1 and α_2.

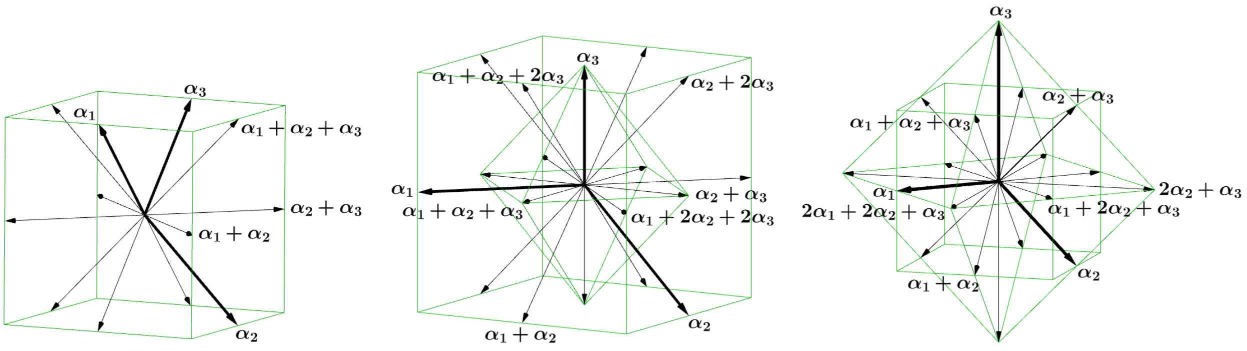
α_1
α_3
$\alpha_1+\alpha_2+\alpha_3$
$\alpha_2+\alpha_3$
$\alpha_1+\alpha_2$
α_2
$\alpha_1+\alpha_2+2\alpha_3$
α_3
$\alpha_2+2\alpha_3$
α_1
$\alpha_1+\alpha_2+\alpha_3$
$\alpha_2+\alpha_3$
$\alpha_1+2\alpha_2+2\alpha_3$
$\alpha_1+\alpha_2$
α_2
α_3
$\alpha_2+\alpha_3$
$\alpha_1+\alpha_2+\alpha_3$
α_1
$2\alpha_2+\alpha_3$
$2\alpha_1+2\alpha_2+\alpha_3$
$\alpha_1+2\alpha_2+\alpha_3$
$\alpha_1+\alpha_2$
α_2

A_3 B_3 C_3

Fig. 1.2. The root systems of crystallographic reflection groups of rank 3 are presented. The simple roots are labeled by α_k, $k \in \{1,2,3\}$.

1.2. Finite reflection groups

For any reflection r_{α_i} defined by (1.1.1), we introduce the notation $r_{\alpha_i} := r_i$. For simple roots $\alpha_i, \alpha_j \in \Delta$, we consider the positive integers,

$$m(\alpha_i, \alpha_j) := m_{ij}, \quad i,j \in \{1,\dots,n\}, \tag{1.2.1}$$

which provide the entries of the Coxeter matrix denoted by M_{ij}. The values of m_{ij} are related to the angles between the simple roots as

$$\theta_{ij} = \angle(\alpha_i, \alpha_j) = \pi(1 - m_{ij}^{-1}), \quad i,j \in \{1,\dots,n\}. \tag{1.2.2}$$

Then, the angles between the reflecting hyperplanes corresponding to r_i and r_j are given by the values πm_{ij}^{-1}.

Let $\Delta = \{\alpha_1, \dots, \alpha_n\}$ be a base of a root system Φ. A reflection group G is a subgroup of the general linear group $GL(E)$ generated by the set of reflections $\{r_1, \dots, r_n\}$ as

$$G = \{r_i \mid \alpha_i \in \Delta\}, \quad i \in \{1,\dots,n\}. \tag{1.2.3}$$

A reflection group G is also a Coxeter group, and its generators satisfy the following relations

$$(r_i r_j)^{m_{ij}} = 1, \quad i,j \in \{1,\dots,n\}, \tag{1.2.4}$$

where m_{ij} denotes the order of $r_i r_j$ in G, if it satisfies the conditions:

(i) $m_{ii} = 1$ (so that $r_i^2 = 1$);

(ii) $m_{ij} = m_{ji} \geq 2$, for $i \neq j$.

There are three families of Coxeter groups: finite, affine and hyperbolic. In general, the finite reflection groups are also the finite Coxeter groups. However, the finite reflection

G	$\lvert\Phi\rvert$	$\lvert G\rvert$	G	$\lvert\Phi\rvert$	$\lvert G\rvert$
$A_n, n \geq 1$	$n(n+1)$	$(n+1)!$	F_4	48	$2^7 \cdot 3^2$
$B_n, n \geq 2$	$2n^2$	$n! \cdot 2^n$	E_6	72	$2^7 \cdot 3^4 \cdot 5$
$C_n, n \geq 2$	$2n^2$	$n! \cdot 2^n$	E_7	126	$2^{10} \cdot 3^4 \cdot 5 \cdot 7$
$D_n, n \geq 4$	$2n^2 - 2n$	$n! \cdot 2^{n-1}$	E_8	240	$2^{14} \cdot 3^5 \cdot 5^2 \cdot 7$
G_2	12	12			
$I_2(m), m \geq 3$	$2m$	$2m$	H_3	30	120
H_2	10	10	H_4	120	120^2

Table 1.1. The numbers of elements of Φ and the orders of finite reflection groups G are presented.

groups arising from the crystallographic root systems are also known as the Weyl groups from a Lie theoretic perspective, and we denote them by W. Unlike the non-crystallographic cases, the Weyl groups have associated Lie algebras.

The classification of finite reflection groups relative to irreducible root systems has been done for all crystallographic groups in (Bourbaki [**17**]; Humphreys [**67**]), and for the non-crystallographic cases with 5-fold symmetry have been described in (Chen *et al.* [**28**]). For the finite reflection groups, the numbers of roots $|\Phi|$ and the orders of finite reflection groups $|G|$ are listed in Table 1.1.

There are three non-crystallographic reflection groups with 5-fold symmetry, namely H_2, H_3 and H_4. However, the dihedral group $I_2(m)$, $m \geq 3$, determines an infinite number of finite reflection groups. For instance, the crystallographic reflection groups A_2, $B_2 \cong C_2$, G_2 are provided by the values $m = 3, 4, 6$, respectively. For $m = 5$, the corresponding reflection group is H_2. For $m \geq 7$, the reflection groups are of non-crystallographic type.

1.3. Coxeter graphs and Dynkin diagrams

Let $\Delta = \{\alpha_1, \dots, \alpha_n\}$ be a set of the simple roots with a fixed ordering. A Cartan matrix corresponding to a finite reflection group G generated by $\{r_1, \dots, r_n\}$ is denoted by

$$C_G = (C(G))_{ij} = \left(\frac{2\langle \alpha_i, \alpha_j \rangle}{\langle \alpha_j, \alpha_j \rangle} \right) = (c_{ij}), \quad i, j \in \{1, \dots, n\}, \tag{1.3.1}$$

where its entries c_{ij} satisfiy the following properties:

(*i*) if $i = j$, then $c_{ij} = 2$;
(*ii*) if $i \neq j$, then $c_{ij} \leq 0$;
(*iii*) $c_{ij} = 0$ implies $c_{ji} = 0$.

Cartan matrices are independent from a choice of Δ; however, the ordering of the simple roots is important. For the crystallographic root systems, the elements of a Cartan matrix are called Cartan integers. However, the entries of the Cartan matrices of the non-crystallographic reflection groups H_2, H_3 and H_4 are not necessarily integers, and they can take values from the extension ring $\mathbb{Z}[\tau] := \{a + \tau b \,|\, a, b \in \mathbb{Z}\}$, where $\tau = \frac{1+\sqrt{5}}{2}$ is the positive root of $x^2 = x + 1$ called the golden ratio.

Let us consider a root system Φ with a base $\Delta = \{\alpha_1, \ldots, \alpha_n\}$. Then, the Coxeter graph of Φ is a finite undirected graph with

- n vertices, which are in one-to-one correspondence with the elements of Δ, depicted by white nodes;
- edges connecting two distinct vertices corresponding to α_i and α_j, if $m_{ij} > 2$.

Furthermore, if $m_{ij} = 2$, then an edge between two vertices is omitted, indicating that the corresponding simple roots are orthogonal. For $m_{ij} > 3$, an edge is labelled by m_{ij}. By convention, since an edge corresponding to $m_{ij} = 3$ occurs often, we do not label it. Thus, a Coxeter graph is equivalent to a Coxeter matrix, and it encodes information about the angles between the simple roots. A Coxeter graph is also referred to as a Coxeter diagram or a Coxeter–Dynkin diagram. For irreducible root systems, the connected Coxeter diagrams are presented in Figure 1.3.

For root systems, which contain the roots with equal lengths, it is convenient to use a Coxeter diagram to recover the corresponding Cartan integers. However, for crystallographic root systems, which contain the roots with two different lengths, Coxeter diagrams fail to provide correct values c_{ij}. Therefore, it is convenient to consider a modification of the Coxeter graph called a Dynkin diagram, which can encode not only the angles between the simple roots, but also their relative lengths. Since the latter determines a root system up to isomorphism, it can be used interchangeably with a corresponding Cartan matrix.

Let us consider a crystallographic root system Φ with a base $\Delta = \{\alpha_1, \ldots, \alpha_n\}$. Then, the Dynkin diagram is a graph with

- n vertices, which are in one-to-one correspondence with the elements of Δ, depicted by white (black) nodes in the case of long (short) simple roots;
- edges connecting two distinct vertices corresponding to α_i and α_j, if $c_{ij} \neq 0$ (1.3.1); the number of edges between any two nodes is determined by

  $$(\alpha_i, \alpha_j)(\alpha_j, \alpha_i) = 4\cos^2\theta_{ij},$$

  where θ_{ij} is provided by (1.2.2).

Let us recall that crystallographic root systems satisfy an extra condition $(\alpha_i, \alpha_j) \in \mathbb{Z}$. Since $0 \leq \cos^2\theta_{ij} \leq 1$, we have that $(\alpha_i, \alpha_j)(\alpha_j, \alpha_i) \in \{0, 1, 2, 3, 4\}$. However, as the simple roots α_i and α_j are linearly independent, the relation $\cos\theta_{ij} = \pm 1$ providing the angles $\theta_{ij} \in \{0, \pi\}$ between the simple roots is omitted. Therefore,

$$(\alpha_i, \alpha_j)(\alpha_j, \alpha_i) \in \{0, 1, 2, 3\}.$$

$\langle\alpha_i, \alpha_j\rangle$	$\langle\alpha_j, \alpha_i\rangle$	θ_{ij}	$\lVert\alpha_i\rVert^2 \,/\, \lVert\alpha_j\rVert^2$
0	0	$\pi/2$	undetermined
-1	-1	$2\pi/3$	1
-1	-2	$3\pi/4$	2
-1	-3	$5\pi/6$	3

Table 1.2. Relations for the simple root of the crystallographic root systems.

Let us recall that for any two vectors $\alpha, \beta \in E$, the standard scalar product is given by

$$\langle\alpha, \beta\rangle = \lVert\alpha\rVert \, \lVert\beta\rVert \cos\theta_{\alpha\beta}.$$

Then, the scalar product (1.1.2) can be explicitly written as

$$(\alpha_i, \alpha_j) = \frac{2\langle\alpha_i, \alpha_j\rangle}{\langle\alpha_j, \alpha_j\rangle} = 2\frac{\lVert\alpha_i\rVert}{\lVert\alpha_j\rVert}\cos\theta_{ij}. \tag{1.3.2}$$

From property *(ii)* of a Cartan matrix (1.3.1), we notice that $\langle\alpha_i, \alpha_j\rangle < 0$ and $\langle\alpha_j, \alpha_i\rangle < 0$. Therefore, the angle between two distinct simple roots α_i and α_j is not acute, which implies that $\cos\theta_{ij} \leq 0$. The corresponding angles together with the length ratios are provided in Table 1.2.

Similarly to Coxeter diagrams, the absence of a link between the nodes indicates that the corresponding simple roots are orthogonal. A single, double and triple links corresponds to the angles $2\pi/3$, $3\pi/4$, $5\pi/6$ between the simple roots α_i and α_j, or the angles $\pi/3$, $\pi/4$, $\pi/6$ between the corresponding reflecting hyperplanes P_{α_i} and P_{α_j}, respectively. For the crystallographic root systems A_n, B_n, C_n, D_n and the exceptional cases G_2, F_4, E_6, E_7, E_8, the Dynkin diagrams are presented in Figure. 1.4.

1.4. Dual bases and corresponding lattices

Let Φ be a root system with a base Δ. The elements of the set $\Omega = \{\omega_i \mid i = 1, \ldots, n\}$, are called the fundamental weights (relative to Δ), and they form the $\omega-$basis,

$$(\omega_i, \alpha_j) = \frac{2\langle\omega_i, \alpha_j\rangle}{\langle\alpha_j, \alpha_j\rangle} = \delta_{ij}. \tag{1.4.1}$$

where δ_{ij} denotes the Kronecker delta.

The lengths of the fundamental weights and the relative angles between them are provided by a quadratic form matrix (Bremner *et al.* [**21**]) as

$$C^q_G = (C(G))^q_{ij} = (\langle\omega_i, \omega_j\rangle), \quad i, j \in \{1, \ldots, n\}. \tag{1.4.2}$$

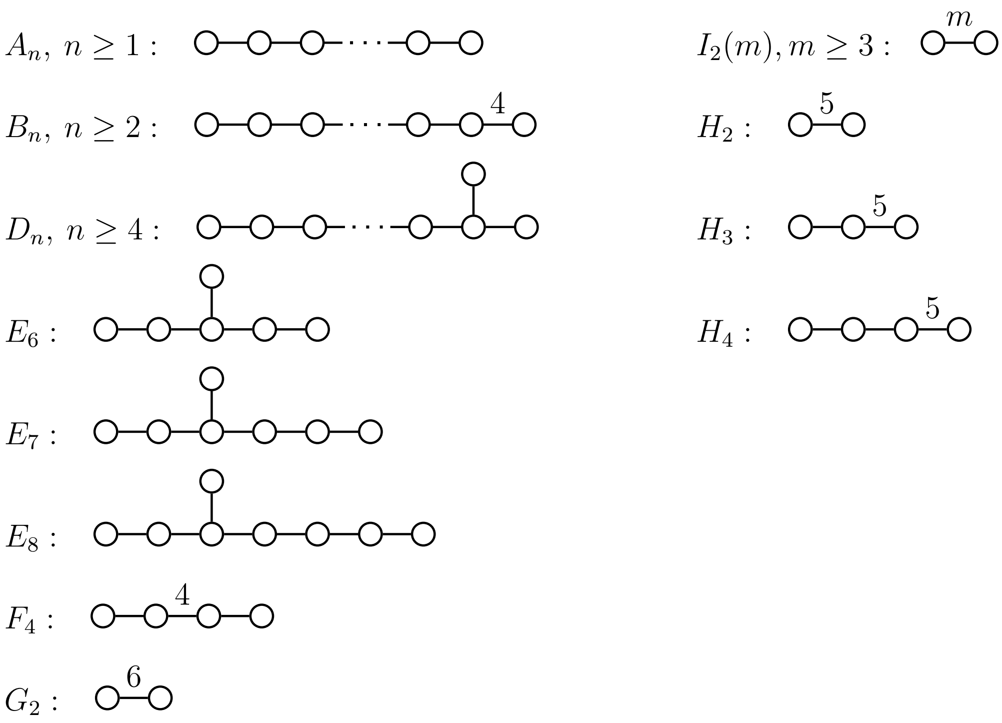
$A_n,\ n \geq 1:$
$B_n,\ n \geq 2:$
4
$D_n,\ n \geq 4:$
$E_6:$
$E_7:$
$E_8:$
$F_4:$
4
$G_2:$
6
$I_2(m), m \geq 3:$
m
$H_2:$
5
$H_3:$
5
$H_4:$
5

Fig. 1.3. The complete classification of all connected Coxeter diagrams.

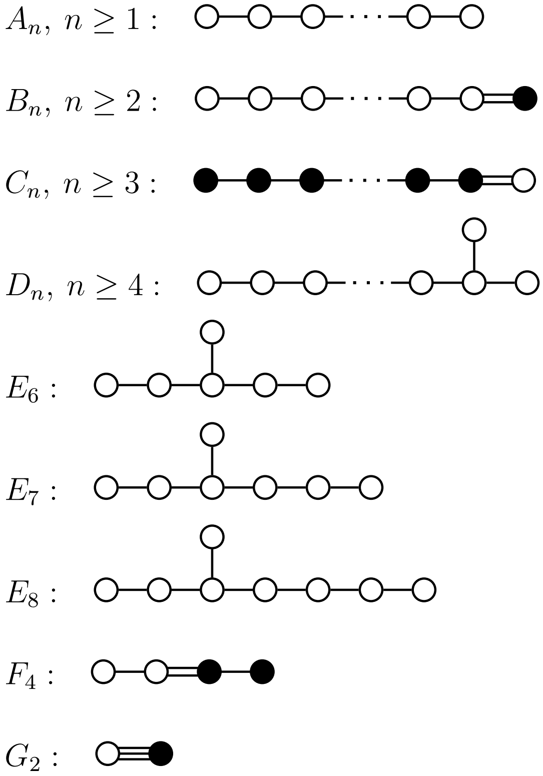
$A_n,\ n \geq 1:$
$B_n,\ n \geq 2:$
$C_n,\ n \geq 3:$
$D_n,\ n \geq 4:$
$E_6:$
$E_7:$
$E_8:$
$F_4:$
$G_2:$

Fig. 1.4. The complete classification of all connected Dynkin diagrams.

For root systems with equal root lengths, the matrix (1.4.2) coincides with the inverse of a Cartan matrix denoted by C_G^{-1},

$$C_G^q = C_G^{-1} = (C(G))_{ij}^{-1}.$$

The link between $\alpha-$ and $\omega-$bases is provided by a Cartan matrix (1.3.1) and its inverse as

$$\alpha_i = \sum_{j=1}^{n} C_G \omega_j, \quad \omega_i = \sum_{j=1}^{n} C_G^{-1} \alpha_j, \quad i, j \in \{1, \dots, n\}.$$

Using formulas (1.1.3) and (1.4.3), the action of a reflection r_i on ω_j is provided by

$$r_i(\omega_j) = \omega_j - \frac{2\langle \alpha_i, \omega_j \rangle}{\langle \alpha_i, \alpha_i \rangle} \alpha_i = \omega_j - \delta_{ij} \alpha_i, \quad i, j \in \{1, \dots, n\}.$$

Let $\Phi^\vee$ be a root system in E, whose crystallographic group is canonically isomorphic to W. Then, $\Phi^\vee = \{\alpha_1^\vee, \dots, \alpha_n^\vee\}$ is the inverse of $\Phi = \{\alpha_1, \dots, \alpha_n\}$ called a coroot system. For any $\alpha_i \in \Phi$, a dual root (coroot) $\alpha_i^\vee$ is determined by

$$\alpha_i^\vee = \frac{2\alpha_i}{\langle \alpha_i, \alpha_i \rangle}, \quad i \in \{1, \dots, n\}.$$

Similarly to a coroot, dual weights (coweights) are expressed as

$$\omega_i^\vee = \frac{2\omega_i}{\langle \alpha_i, \alpha_i \rangle}, \quad i \in \{1, \dots, n\}.$$

The duality relations between (co)root and (co)weight bases are provided by

$$\frac{2\langle \alpha_i, \omega_j \rangle}{\langle \alpha_i, \alpha_i \rangle} \equiv \langle \alpha_i^\vee, \omega_j \rangle = \delta_{ij}, \quad \frac{2\langle \alpha_i, \omega_j \rangle}{\langle \alpha_j, \alpha_j \rangle} \equiv \langle \alpha_i, \omega_j^\vee \rangle = \delta_{ij}, \quad i, j \in \{1, \dots, n\}. \tag{1.4.3}$$

The set of all linear combinations of the simple roots (coroots) forms a root (coroot) lattice in E as

$$Q = \mathbb{Z}\alpha_1 + \dots + \mathbb{Z}\alpha_n, \quad Q^\vee = \mathbb{Z}\alpha_1^\vee + \dots + \mathbb{Z}\alpha_n^\vee.$$

The set of all linear combinations of the fundamental weights (coweights) forms a weight (coweight) lattice in E as

$$P = \mathbb{Z}\omega_1 + \dots + \mathbb{Z}\omega_n, \quad P^\vee = \mathbb{Z}\omega_1^\vee + \dots + \mathbb{Z}\omega_n^\vee.$$

The relations between the lattices and the bases of (co)roots and (co)weights are determined by the following diagram

$$\begin{array}{ccccccc} \{\alpha_1, \dots, \alpha_n\} & \subset & Q & & Q^\vee & \supset & \{\alpha_1^\vee, \dots, \alpha_n^\vee\} \\ & & \cap & \times & \cap & & \\ \{\omega_1, \dots, \omega_n\} & \subset & P & & P^\vee & \supset & \{\omega_1^\vee, \dots, \omega_n^\vee\} \end{array}$$

The symbol "×" indicates that the lattices Q and $P^\vee$, as well as the lattices $Q^\vee$ and P, are $\mathbb{Z}$–dual to each other, as required by relations (1.4.3).

1.5. Affine Weyl group and fundamental region

Let us consider crystallographic reflection groups. Let us recall that for any root system Φ, whose roots have equal lengths, there is a unique highest long root denoted by ξ. The highest root ξ and the highest coroot, denoted by η, are defined by linear combinations of the simple roots $\alpha_i \in \Delta$, $i \in \{1, \ldots, n\}$ and coroots $\alpha_j^\vee \in \Delta^\vee$, $j \in \{1, \ldots, n\}$, respectively,

$$\xi = m_1\alpha_1 + \cdots + m_n\alpha_n, \quad \eta = m_1^\vee \alpha_1^\vee + \cdots + m_n^\vee \alpha_n^\vee,$$

where m_i and $m_i^\vee$ are called marks and dual marks (comarks), respectively.

Let $\Delta = \{\alpha_1, \ldots, \alpha_n\}$ be a set of simple roots of a crystallographic root system, and let W be a corresponding Weyl group. For the highest root ξ, the reflection across the reflecting hyperplane $P_\xi = \{x \in E \mid \langle x, \xi\rangle = 0\}$ passing through the origin is given by the formula,

$$r_\xi x = x - \frac{2\langle x, \xi\rangle}{\langle \xi, \xi\rangle}\xi.$$

The affine reflection across the reflecting hyperplane P_ξ passing through $\xi/2$ is provided by

$$r_0 x = r_\xi x + \frac{2\xi}{\langle \xi, \xi\rangle}.$$

The affine Weyl group, which is denoted by W^{aff}, is generated by reflections r_i, $i \in \{0, 1, \ldots, n\}$. Equivalently, W^{aff} is defined as the semidirect product of the group of shifts $Q^\vee$ and Weyl group W,

$$W^{\text{aff}} = Q^\vee \rtimes W.$$

The fundamental region of W^{aff}, which is denoted by F, is provided by the convex hull of the points $\left\{0, \frac{\omega_1^\vee}{m_1}, \ldots, \frac{\omega_n^\vee}{m_n}\right\}$,

$$\begin{aligned} F &= \left\{ \sum_{i=1}^n a_i \omega_i^\vee \mid a_0 + \sum_{i=1}^n a_i m_i = 1,\ a_0, \ldots, a_n \in \mathbb{R}^{\geq 0} \right\} \\ &= \Big\{ x \in E \mid \langle x, \alpha\rangle \geq 0, \forall \alpha \in \Delta, \langle x, \xi\rangle \leq 1 \Big\}, \end{aligned}$$

and it has the property that $W^{\text{aff}} F = E$.

The points contained within the fundamental region F satisfy the following properties:

(*i*) For any $x \in E$, there exists $x' \in F$, $w \in W$, $q^\vee \in Q^\vee$, such that the relation $x = wx' + q^\vee$ holds.

(*ii*) For any $x, x' \in F$, such that $x' = w^{\text{aff}} x$, where $w^{\text{aff}} \in W^{\text{aff}}$, it holds that $x = x'$.

(*iii*) For any point $x = a_1\omega_1 + \cdots + a_n\omega_n \in F$, such that $a_0 + a_1\omega_1 + \cdots + \alpha_n\omega_n = 1$, the stabilizer of a point x is given by

$$\operatorname{Stab}_{W^{\text{aff}}}(x) = \left\{ w^{\text{aff}} \in W^{\text{aff}} \mid w^{\text{aff}} x = x \right\}. \tag{1.5.1}$$

For $x \in \operatorname{int}(F)$, i.e., $a_i > 0$, $i \in \{1, \dots, n\}$, we have that $\operatorname{Stab}_{W^{\mathrm{aff}}}(x) = 1$. Otherwise, the isotropy group $\operatorname{Stab}_{W^{\mathrm{aff}}}(x)$ is generated by r_i, for which $a_i = 0$, $i = \{1, \dots, n\}$.

The dual affine Weyl group, which is denoted by $\widehat{W}^{\mathrm{aff}}$, is generated by reflections r_i, $i \in \{1, \dots, n\}$ and a reflection $r_0^\vee$,

$$r_0^\vee x = r_\eta x + \frac{2\eta}{\langle \eta, \eta \rangle}, \quad r_\eta^\vee x = x - \frac{2\langle x, \eta \rangle}{\langle \eta, \eta \rangle}, \quad x \in E.$$

Equivalently, $\widehat{W}^{\mathrm{aff}}$ is defined as the semidirect product of the group of shifts Q and Weyl group W,

$$\widehat{W}^{\mathrm{aff}} = Q \rtimes W.$$

The fundamental region of $\widehat{W}^{\mathrm{aff}}$, which is denoted by $F^\vee$, is provided by the convex hull of the points $\left\{0, \frac{\omega_1}{m_1^\vee}, \dots, \frac{\omega_n}{m_n^\vee}\right\}$ as

$$\begin{aligned} F^\vee &= \left\{ \sum_{i=1}^{n} b_i \omega_i \mid b_0 + \sum_{i=1}^{n} b_i m_i^\vee = 1,\ b_0, \dots, b_n \in \mathbb{R}^{\geq 0} \right\} \\ &= \left\{ x \in E \mid \langle x, \alpha^\vee \rangle \geq 0, \forall \alpha^\vee \in \Delta^\vee, \langle x, \eta \rangle \leq 1 \right\}, \end{aligned}$$

and it has the property that $\widehat{W}^{\mathrm{aff}} F^\vee = E$.

The properties of the fundamental region $F^\vee$ are similar to the properties of F, and they can be found in (Hrivnák and Patera [**63**]).

1.6. Grids F_M and Λ_M

The grids F_M and Λ_M are pertinent for the definition of the Weyl-orbit functions and the corresponding discrete Fourier-Weyl transforms, as they provide the sampling point sets and label sets, respectively (see Chapter 2). In this case, M is considered as the scaling factor.

For any fixed $M \in \mathbb{N}$, the order of the $W-$invariant quotient group $\frac{1}{M} P^\vee / Q^\vee$ is given by

$$\left| \frac{1}{M} P^\vee / Q^\vee \right| = c M^n,$$

where

$$c = |P/Q| = |P^\vee / Q^\vee| = \det C_G. \tag{1.6.1}$$

The grid F_M comprises cosets from the $W-$invariant group $\frac{1}{M} P^\vee / Q^\vee$, which have representative elements in F. More precisely,

$$F_M \equiv \frac{1}{M} P^\vee / Q^\vee \cap F.$$

The points of F_M can be written explicitly as

$$F_M = \left\{ \sum_{i=1}^{n} \frac{s_n}{M} \omega_n^\vee \mid s_0 + \sum_{i=1}^{n} s_n m_n = M,\ s_0, s_1, \dots, s_n \in \mathbb{Z}^{\geq 0} \right\}. \tag{1.6.2}$$

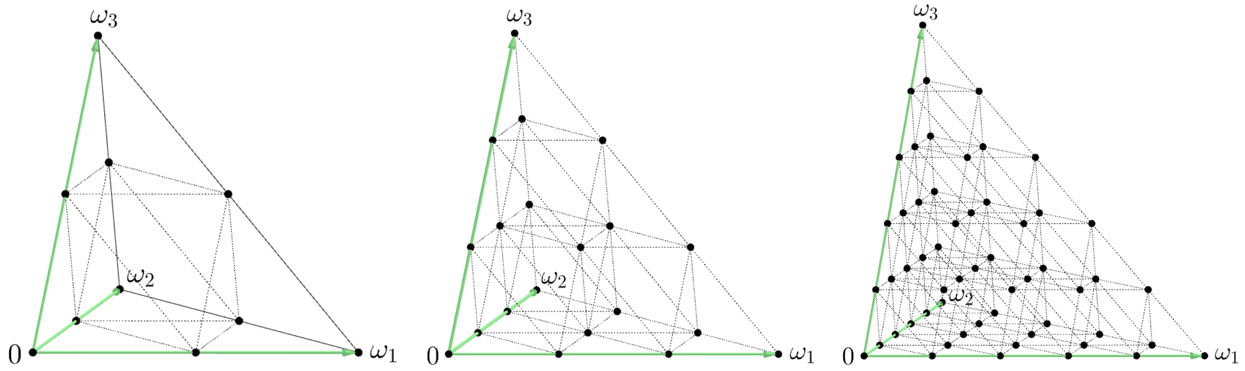

$M = 2$ $M = 3$ $M = 5$

Fig. 1.5. The fundamental region of the Weyl group A_3 is shown. The vectors ω_1, ω_2 and ω_3 correspond to the fundamental weights of A_3. For $M = 2, 3$ and 5, the points of the grid F_M are depicted by black color.

Excluding the points of the grid F_M found on the boundary of the fundamental region F, we obtain the points corresponding to the interior of F. Thus,

$$\widetilde{F}_M \equiv \frac{1}{M} P^\vee / Q^\vee \cap \operatorname{int}(F).$$

The points of $\widetilde{F}_M$ are explicitly written as

$$\widetilde{F}_M = \left\{ \sum_{i=1}^{n} \frac{s'_n}{M} \omega_n^\vee \mid s'_0 + \sum_{i=1}^{n} s'_n m_n = M,\ s'_0, s'_1, \dots, s'_n \in \mathbb{N} \right\}. \tag{1.6.3}$$

The grid Λ_M is defined as cosets from the $W-$invariant group P/MQ, which have representative elements in $MF^\vee$,

$$\Lambda_M \equiv P/MQ \cap MF^\vee.$$

The points of Λ_M can be explicitly written as

$$\Lambda_M = \left\{ \sum_{i=1}^{n} \lambda_n \omega_n \mid \lambda_0 + \sum_{i=1}^{n} \lambda_n m_n^\vee = M, \lambda_0, \dots, \lambda_n \in \mathbb{Z}^{\geq 0} \right\}. \tag{1.6.4}$$

Excluding the points of the grid Λ_M found on the boundary of the magnified fundamental region $MF^\vee$, we obtain the points corresponding to the interior of $MF^\vee$. Thus,

$$\widetilde{\Lambda}_M \equiv P/MQ \cap \operatorname{int}(MF^\vee).$$

The points of $\widetilde{\Lambda}_M$ are explicitly written as

$$\widetilde{\Lambda}_M = \left\{ \sum_{i=1}^{n} \lambda'_n \omega_n \mid \lambda'_0 + \sum_{i=1}^{n} \lambda'_n m_n^\vee = M, \lambda'_0, \dots, \lambda'_n \in \mathbb{N} \right\}. \tag{1.6.5}$$

For irreducible crystallographic groups, the n-tuple of marks $(m_1, \dots, m_n)$ is a permutation of the n-tuple of comarks $(m_1^\vee, \dots, m_n^\vee)$. Therefore, the cardinalities of (1.6.2) and

(1.6.4), as well as (1.6.3) and (1.6.5), are equal,

$$|F_M| = |\Lambda_M|, \quad |\widetilde{F}_M| = |\widetilde{\Lambda}_M|.$$

The formulas providing the numbers of points of F_M and $\widetilde{F}_M$ have been derived for irreducible crystallographic groups in (Hrivnák and Patera [**63**]). For example, for the crystallographic group A_3, whose dual root and dual weight lattices coincide, the fundamental region F is given by the convex hull of the points $\{0, \omega_1, \omega_2, \omega_3\}$. The grids F_M contained within the fundamental region F are presented for $M = 2, 3$ and 5 in Figure 1.5.

1.7. Orbits of finite reflection groups

For any finite reflection group G, let $\lambda \in E$ be a vector in the $\omega-$basis, such that

$$\lambda = \sum_{i=1}^{n} a_i \omega_i \equiv (a_1, a_2, \ldots, a_n), \quad a_i \in \mathbb{Z}^{\geq 0}. \tag{1.7.1}$$

Then, we have that $\lambda \in D^+$, and λ is a called a dominant weight. However, for $a_i \in \mathbb{Z}^{>0}$, $i \in \{1, \ldots, n\}$, the vector λ is strictly positive, and it does not lie on the boundary of D^+.

An orbit of points of a finite Coxeter group arises from the action of its elements on $\lambda \in E$ as

$$O_G(\lambda) = \{g\lambda \mid g \in G\}. \tag{1.7.2}$$

Therefore, λ is also called a dominant (seed) point, and it is used to characterize each orbit of a finite reflection group G. Note that in Chapter 3, the notation $O_\lambda(G)$ is also utilized to denote an orbit of G.

In the geometric interpretation, the points of an orbit are recognized as the vertices of a polytope in E. The number of orbit points can be determined by using a corresponding Coxeter/Dynkin diagram (Campagne *et al.* [**29**]). The coordinates of the dominant weight λ mark the nodes of a corresponding Coxeter/Dynkin diagram. The nodes that are marked by zeros indicate the reflections corresponding to a subgroup $G' \subset G$.

Therefore, the number of elements of an orbit with a dominant point λ is equal to

$$|O_G(\lambda)| = \frac{|G|}{|G'|} = \frac{|G|}{|\mathrm{Stab}_G(\lambda)|},$$

where the stabilizer of a point λ is determined by

$$\mathrm{Stab}_G(\lambda) = \{g\lambda = \lambda \mid g \in G\}. \tag{1.7.3}$$

If λ is strictly positive, then $|O_G(\lambda)| = |G|$. For every G, the size of a corresponding orbit with $\lambda = 0$ is given by $|O_G(0)| = 1$, since, in this case, $|G| = |G'|$. The orders of the crystallographic and non-crystallographic reflection groups are listed in Table 1.1.

1.8. Weyl orbit functions

There are three families of Weyl-orbit functions that have been defined for crystallographic root systems with one root length. The two families of (anti)symmetric multivariate exponential Weyl orbit functions, called $C-$ and $S-$functions, have been formulated and studied in detail in (Klimyk and Patera [**78, 79**]). Since this study focuses only on the $C-$and $S-$functions, the pertinent information about the third family, known as even orbit functions or $E-$functions, can be found in (Klimyk and Patera [**80**]). The discretized versions of such functions and their properties have been investigated in (Hrivnák and Patera [**63**]; Hrivnák *et al.* [**59**]). For crystallographic root systems that comprise the roots with two different lengths, the two families of orbit functions, called S^s-, S^l-functions, have been extensively studied [for instance, see (Hrivnák *et al.* [**59**])], where the notations l and s correspond to the long and short roots of a root system.

For any label $b \in E$ and any point $x \in E$, the complex-valued smooth $C-$ and $S-$functions are provided by the sum of exponential terms as

$$\Phi_b(x) = \sum_{w\in W} e^{2\pi \mathrm{i}\langle wb,x\rangle},$$
$$\varphi_b(x) = \sum_{w\in W} \det(w) e^{2\pi \mathrm{i}\langle wb,x\rangle},$$

where $\det(w)$ denotes the determinant of w. More precisely, $\det(w) = (-1)^k$ whenever w can be expressed as a product of k reflections, and $\det(w) = 1$, otherwise (Humphreys [**67**]).

For $C-$functions, all terms have positive sign, and such functions are called symmetric orbit functions. For $S-$functions, the sing of each contributing term depends on $\det(w) = \{\pm 1\}$, and such functions are called antisymmetric orbit functions. Let us recall the crucial properties of (anti)symmetric orbit functions:

- **Invariance**
  Since the scalar product $\langle\cdot,\cdot\rangle$ in E is invariant with respect to a crystallographic reflection group W, i.e., $\langle wx, wy\rangle = \langle x, y\rangle$, for $w \in W$ and $x, y \in E$, the corresponding $C-$ and $S-$functions are (anti)symmetric under the action of any element $w \in W$,

  $$\Phi_{wb}(x) = \Phi_b(wx) = \Phi_b(x),$$
  $$\varphi_{wb}(x) = \varphi_b(wx) = \det(w)\varphi_b(x).$$

  The discretized $C-$ and $S-$functions are invariant under the translation by any coroot-lattice vector $q^\vee \in Q^\vee$ as

  $$\Phi_b(x + q^\vee) = \Phi_b(x),$$
  $$\varphi_b(x + q^\vee) = \varphi_b(x).$$

- **Duality and scaling symmetry**
  The duality of $C-$ and $S-$functions is expressed as

$$\Phi_b(x) = \Phi_x(b), \quad \varphi_b(x) = \varphi_x(b).$$

  For any real-valued parameter $t \in \mathbb{R}$, the scaling symmetry is given by the relations,

$$\Phi_b(tx) = \Phi_{tb}(x), \quad \varphi_b(tx) = \varphi_{tb}(x).$$

- **Orthogonality**
  The continuous orthogonality of $C-$ and $S-$functions has been defined in (Klimyk and Patera [**78, 79**]; Moody and Patera [**105**]), and the discrete orthogonality has been studied in detail in (Hrivnák and Patera [**63**]) The discrete orthogonality of S^s- and S^l-functions has been investigated in (Hrivnák *et al.* [**59**]). In this study, the discrete orthogonality of $C-$ and $S-$functions is described in detail for the crystallographic refection group A_2 in Chapter 2.

1.9. Applications of finite reflection groups in the modelling of nanostructures

This section aims to discuss the applications of finite reflection groups in modelling various structures, such as fullerenes, viruses, biomolecules, and *de novo*-designed structures. As well, we briefly cover the real-world applications of the mentioned structures.

The discovery of the fullerene C_{60} (Kroto *et al.* [**84**]) has immediately attracted the great attention of research communities worldwide, stimulating numerous experimental and theoretical studies. The fullerene C_{60} is a hollow spherical molecule entirely composed of carbon. More precisely, it has a structure provided by the truncated icosahedron with the carbon atoms located at each vertex. Thus, the structure of C_{60} contains twenty hexagonal and twelve pentagonal faces. Each hexagonal face is adjacent to three hexagonal and three pentagonal faces. The molecule C_{60} has two types of bonds along the polygon-polygon edges: double bonds provided by an edge shared by two hexagonal faces and single bonds formed between pentagonal and hexagonal faces. This means that the fullerene molecules do not have free valencies, and hence, they act as insulators in their pure state (Degiorgi [**40**]).

During the past decades, more fullerene molecules were discovered to exist in nature (Diederich and Whetten [**42**]; Taylor and Walton [**137**]; Fowler and Manolopoulos [**52**]). The fullerenes can vary in size, and they are shaped as hollow spheroids, ellipsoids and tubes. The structures of the latter can be achieved by cutting a graphene layer (Geim and Novoselov [**53**]), rolling it into a cylindrical tube, and closing both ends with two hemispheres obtained by cutting the fullerene molecule in half. The resulting structures are called carbon nanotubes (Dresselhaus *et al.* [**46, 47**]). However, depending on the potential applications, it may not be necessary to close a nanotube's ends (Gupta *et al.* [**56**]; Rols *et al.* [**128**]). Moreover, multi-shell nanostructures, such as nested fullerenes (fullerene onions) and multi-wall nanotubes, have been also considered (Mar *et al.* [**96**]; Andrews *et al.* [**6**]).

The promising applications of the fullerene molecules, especially in electronics and medicine, have served as the stepping stone to the field of carbon-based nanotechnology. During the past decades, the biological applications of fullerene molecules, particularly those related to cancer and anti-viral treatment, have been thoroughly investigated. For example, due to the hollow-cage structure, the fullerenes can be used as traps or containers for other atoms or molecules, becoming suitable candidates for drug delivery (Bianco *et al.* [**12**]; Kazemzadeh and Mozafari [**73**]). On the other hand, the carbon nanotubes, which can vary in length and diameter, exhibit significant electrical and mechanical properties, making them appropriate for developing electrochemical biosensors (Yang *et al.* [**147**]), hard tissue engineering (Ravanbakhsh *et al.* [**129**]), and other pertinent applications (Popov [**121**]).

Due to the increasing interest in the mathematical modelling of carbon nanotubes, the group-theoretical approach to constructing such molecules has been developed in (Bodner *et al.* [**13, 14, 15**]). The main idea of such an approach is based on a symmetry-breaking mechanism. In this case, we utilize the symmetry reduction of the icosahedral group H_3 to the symmetries of its two-dimensional subgroups G'. This reduction permits us to consider the points of three-dimensional orbit corresponding to the vertices of the truncated icosahedron as a sum of two-dimensional orbits provided by the symmetries of the subgroups G'. The orbit decomposition provides the so-called 'pancake'-structure of a polytope. Then, the fullerene can be cut in half in such a way that the top and bottom caps contain the same number of two-dimensional faces. Adding more circular/polygonal orbits in the 'middle' of the decomposition results in the structures of larger fullerene molecules and closed carbon nanotubes of types armchair (Bodner *et al.* [**13**]), zig-zag (Bodner *et al.* [**14**]) and chiral (Bodner *et al.* [**15**]). For the first two types of nanotubes, an appropriate number of circular/polygonal orbits should be inserted between the fullerene's top and bottom caps to construct a larger fullerene molecule. However, many complete loops of a spiral of hexagons need to be inserted for the chiral case, making the structural extension of C_{60} quite challenging. Recently, symmetry breaking of the other two polytopes with icosahedral symmetry containing 60 vertices within their structures has been investigated in (Bourret and Grabowiecka [**18**]).

Symmetry breaking plays an essential role in the field of mathematical virology. Virus particles are molecular machines that constantly optimize their structures to infect a host faster and more efficiently. The virus structure contains a viral genome (nucleic acid, i.e., either single- or double-stranded RNA or DNA) and a viral capsid, which protects the viral genome. For the vast majority of viruses, the viral capsids possess helical or icosahedral symmetry. A viral capsid is assembled from building subunits called capsomers. In order

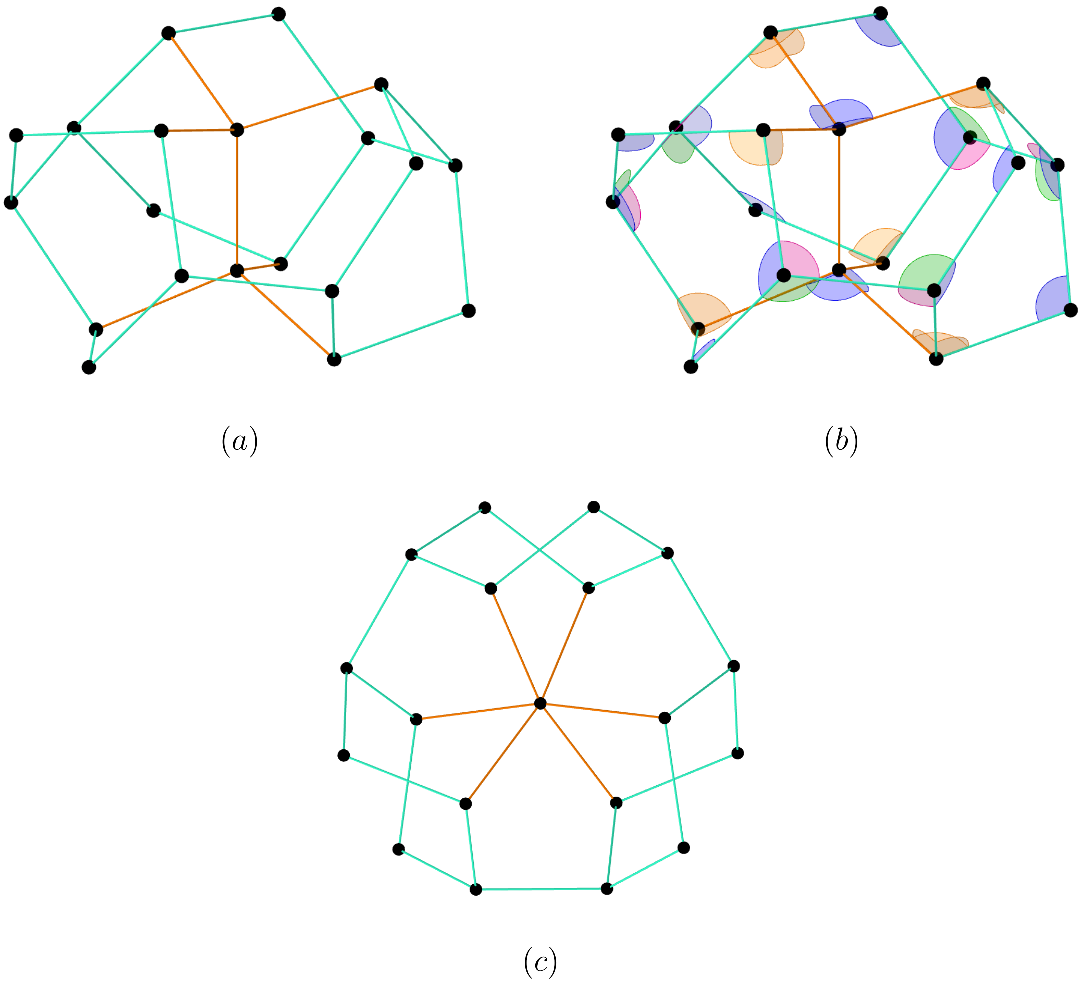
(*a*)

(*b*)

(*c*)

Fig. 1.6. The structure of the triplet is presented. (*a*) For simplicity, the bonds of tetrahedral atoms are depicted by orange edges; (*b*) The angles depicted by blue, orange, pink and green colors correspond to the values 109.47°, 101.02°, 100.67° and 117.58°, respectively. (*c*) The top-view of the triplet.

to describe non-quasi equivalent capsid architectures, the viral tiling theory has been developed in (Twarock [**140**]). The viral tiling theory allows constructing Penrose-like tilings on the surface of a sphere, which help to describe the assembly models of various viruses [for instance, see (Keef *et al.* [**75**])] In this case, each tile represents diverse types of interactions between the proteins forming a viral capsid. As the capsid architecture impacts the packaging of a viral genome, the multi-shell nanostructures, such as fullerene onions, have been employed to predict the organization of viral components (Dechant *et al.* [**38**]). Since all viruses are dynamic infectious agents that evolve, perform packaging of viral genome, as well as protecting and releasing it inside a host cell, a better understanding of symmetry breaking of the three-dimensional polytopes with icosahedral symmetry is crucial for the further developments in mathematical virology (Dechant and Twarock [**39**]).

In this thesis (see Chapters 4 and 5), a symmetry-breaking mechanism is applied to the family of the dual polytopes of the icosahedral group H_3 and crystallographic groups A_3, $B_3(C_3)$. Each family contains seven polytopes, which are provided by a particular type of seed point. The procedure developed for C_{60} (Bodner *et al.* [**13, 14, 15**]) is then applied to each considered polytope, allowing the construction of various types of nanotubes. Although some structures are purely abstract and cannot be 'fullerenes' as such, a symmetry-breaking technique still allows studying these objects in full mathematical generality so that potential future structures are included. If ever such structures would be found to exist in nature or manufactured, a promising area of research would be the investigation of their physical and chemical properties, as well as their potential applications. Moreover, the nanotubes presented in this thesis could be potentially useful for the description of the architecture of tube-shaped viruses (Twarock [**141**]).

Even though the approaches based on finite reflection groups are beneficial for modelling the (non)crystallographic structures, their applications become very limited when constructing hierarchical, modular and almost-symmetric structures. Indeed, it is a challenging task to model, for example, the crystalline modular structures described in (Bulienkov [**25**]). For example, in Figure 1.6, we present the triplet depicted in Figure 6(h) of (Bulienkov [**25**]) that has been modelled by hand using GeoGebra software. This triplet contains 20 vertices and 28 edges with the same lengths. In this structure, there are four different angles between the edges (see Figure 1.6(b)). As we can observe from Figure 1.6(c), the structure of the triplet viewed from the top exhibits 3-fold symmetry. However, this structure contains several non-planar hexagons, and it cannot be obtained using only finite reflection groups. Therefore, modelling such crystalline structures using group theoretical methods remains a very challenging problem. Understanding the assembly of such structures would significantly impact many scientific fields, including molecular biology, biomedicine, virology, and nanotechnology.

Chapter 2

Central splitting of A_2 discrete Fourier–Weyl transforms

by

Jiří Hrivnák[1], Mariia Myronova[2], and Jiří Patera[3]

(1) Department of Physics, Faculty of Nuclear Sciences and Physical Engineering, Czech Technical University in Prague, Břehová 7, 115 19 Prague 1, Czech Republic
jiri.hrivnak@fjfi.cvut.cz

(2) Département de Physique, Université de Montréal, Complexe des Sciences, 1375 Avenue Thérèse-Lavoie-Roux, Montréal, QC H2V 0B3, Canada
maria.myronova@umontreal.ca

(3) Centre de Recherches Mathématiques, Université de Montréal, C. P. 6128 Centre Ville, Montréal, QC H3C 3J7, Canada
patera@crm.umontreal.ca

This article was published in Symmetry.
Reference: Hrivnák, J.; Myronova, M.; Patera, J. (2020) Central splitting of A_2 discrete Fourier–Weyl transforms. *Symmetry*, **12**, 1828.

Author contributions: conceptualization, J.H., M.M. and J.P.; writing and editing, J.H., M.M. and J.P.; calculation, J.H. and M.M.; visualization, M.M.

Résumé. Deux types de transformées de Fourier-Weyl en treillis de poids discrets bivariés sont liés par la décomposition en division centrale. Les fonctions orbitales symétriques et antisymétriques de Weyl à deux variables du groupe de réflexion cristallographique A_2 constituent les noyaux des transformées considérées. La division centrale de toute fonction transportant des données en une somme de composantes, qui dépendent du nombre d'éléments du centre de A_2, est utilisée pour réduire la transformée de Fourier-Weyl du réseau de poids d'origine en différentes transformées de division de réseau de poids. Les éléments de réseau de poids se croisant avec un tiers de la région fondamentale du groupe affine de Weyl déterminent l'ensemble de points des transformées de division. Les décompositions matricielles unitaires des transformées de Fourier-Weyl du réseau de poids normalisé sont présentées. Le comportement d'interpolation et les matrices de transformées unitaires des transformées de Fourier-Weyl séparant le réseau de poids sont également illustrés.

Mots clés : fonction orbitale de Weyl, transformée de Fourier discrète, classe de congruence, treillis de poids, division central

Abstract. Two types of bivariate discrete weight lattice Fourier–Weyl transforms are related by the central splitting decomposition. The two-variable symmetric and antisymmetric Weyl orbit functions of the crystallographic reflection group A_2 constitute the kernels of the considered transforms. The central splitting of any function carrying the data into a sum of components governed by the number of elements of the center of A_2 is employed to reduce the original weight lattice Fourier–Weyl transform into the corresponding weight lattice splitting transforms. The weight lattice elements intersecting with one-third of the fundamental region of the affine Weyl group determine the point set of the splitting transforms. The unitary matrix decompositions of the normalized weight lattice Fourier–Weyl transforms are presented. The interpolating behavior and the unitary transform matrices of the weight lattice splitting Fourier–Weyl transforms are exemplified.

Keywords: Weyl orbit function, discrete Fourier transform, congruence class, weight lattice, central splitting

2.1. Introduction

The purpose of this article is to construct a decomposition of the discrete weight lattice Fourier–Weyl transforms (Hrivnák and Patera [**63**]; Patera and Zaratsyan [**118**]) associated with the crystallographic reflection group A_2 into the corresponding splitting transforms. The decomposition is achieved via the central splitting (Moody and Patera, [**105**]) of a given function that is sampled on points from the triangular fragment of the rescaled A_2 weight lattice. The unitary matrix decompositions of the normalized weight lattice Fourier–Weyl transforms serve as the first steps for development of fast recursive evaluation algorithms (Britanak *et al.* [**24**]).

The discrete Fourier transforms on lattices became possible after the uniform tori discretization of semisimple Lie groups was developed for cosine functions (Moody and Patera [**101, 102**]) and expanded to sine functions (Moody and Patera [**105**]). This approach provided the foundation for the Fourier calculus of (anti)symmetric orbit functions that have been developed on the points of the refined weight (Hrivnák and Walton [**65**]) dual weight (Hrivnák and Patera [**63**]; Hrivnák *et al.* [**59**]) and dual root lattices (Hrivnák and Motlochová [**62**]; Czyżycki *et al.* [**34**]). The three families of the Weyl orbit $C-$, $S-$ and $E-$functions (Klimyk and Patera [**78, 79, 80**]) together with their seven hybrid versions (Moody *et al.* [**99**]; Hrivnák *et al.* [**59**]; Hrivnák and Juránek [**60**]), which constitute the kernels of the discrete Fourier–Weyl transforms, have been formulated and described in full generality. The periodicity, (anti)symmetry and boundary properties of the (anti)symmetric Weyl orbit functions labeled by dominant weights from the weight lattices provide a framework for the generalized discrete cosine and sine transforms pertinent to digital data processing. For the crystallographic reflection group A_2, since the fundamental domain of the affine Weyl group has a shape of an equilateral triangle, the unique boundary behavior of the two-variable complex-valued Weyl orbit functions is imposed by the Dirichlet and Neumann boundary conditions (Klimyk and Patera [**78, 79**]). As finite sums of the multivariate exponential functions, the Weyl orbit functions are usually sampled on points of the rescaled (dual) weight lattice comprised within the fundamental region and labeled by weights from the magnified fundamental domain (Hrivnák and Patera [**63**]; Hrivnák *et al.* [**59**]). The decompositions of these weight lattice transforms to the related root-lattice-based transforms are founded on the idea of the central splitting.

The central splitting of any generic linear combination of the Weyl orbit functions (Moody and Patera [**105**], Section 7) is applied to discretized functions that are expressed as combinations of orbit functions via the weight lattice Fourier–Weyl transforms. Depending on the order of the center of the associated compact Lie group (Hrivnák and Patera [**63**], Moody and Patera [**105**]), a shortcut to a data-decomposition is provided by the central splitting of any function f, that is sampled on the weight lattice points contained in the A_2 fundamental region, into a sum of three decomposition functions f_0, f_1 and f_2. This consideration stems from the fact that the Fourier–Weyl transforms of each $f-$component depend only on one congruence class of the weight lattice labels which characterize the corresponding Weyl orbit functions (Moody and Patera [**105**]). Due to the interlaced additional argument symmetry of the decomposition functions f_0, f_1 and f_2 under the action of the extended affine Weyl group, their values are determined on the points of the refined weight lattice comprised within the corresponding kite-shaped fundamental domain. As a result, the reduction of the weight lattice transform is achieved, and the original decomposition of the function f splits into three smaller problems that are tackled faster and more efficiently. Since the root and dual root lattices as well as the weight and dual weight lattices of the root system A_2 coincide, the splitting Fourier–Weyl transforms that process the component functions are deduced from the dual-root lattice transforms. In particular, it appears that the crucial exact forms for the A_2 splitting transforms are obtained by reversing the roles of the points and labels inherent in the generalized dual root lattice transforms (Czyżycki *et al.* [**34**]; Hrivnák and Motlochová [**62**]).

The Fourier–Weyl transforms provide efficient tools for the corresponding Fourier methods (Li *et al.* [**90**]) and the associated multivariate Chebyshev polynomial methods (Moody *et al.* [**99**]). For two-variable Weyl orbit functions, the discrete and continuous cosine transforms, together with their continuous interpolations, are formulated in (Patera and Zaratsyan [**117, 118**]) and later extended to sine transforms in (Patera and Zaratsyan [**119**]). Furthermore, the interpolation applications of extended Weyl orbit functions have been recently tested for the discrete armchair honeycomb lattice transforms (Hrivnák and Motlochová [**61**]). In light of the relevance of such applications to digital data processing, in this paper, the developed A_2 splitting transforms are examined for their interpolation properties. In general, the discrete and continuous Fourier transforms are fundamental to numerous areas of science and technology involving data processing. Their pertinent applications span various domains, such as signal processing (Flamant *et al.* [**51**]; Püschel and Moura [**125**]), pattern recognition (Zheng *et al.* [**153**]), encryption (Liu *et al.* [**93**]), image and video compression/decompression (Rasheed *et al.* [**127**]), magnetic resonance imaging (Irarrazaval *et al.* [**69**]), ultrasound imaging (Lahav *et al.* [**86**]) and watermarking (Hernández *et al.* [**58**], Kahlessenane *et al.* [**71**]). Ever since the discovery of the fast Fourier transforms (Cooley and Tukey [**30**]), attempts to modify and improve the evaluation algorithms have been continuously undertaken (Plonka and Tasche [**120**]; Püschel and Moura [**124**]; Püschel [**123**]). Since the most ubiquitous recursive algorithms contain as their embedded steps the decompositions directly related to the central splitting idea (Britanak *et al.* [**24**]), the developed decomposition directly contributes to formulation of similar recursive evaluation algorithms on the equilateral triangle. Moreover, the decomposition techniques derived for the A_2 case represent a foundation for further generalizations of recursive formalisms to analogous 2D and 3D cases.

The paper is organized as follows. In Section 2.2, pertinent information concerning the A_2 root and weight lattices together with the induced crystallographic reflection group A_2 and its infinite extensions is recalled. The sets of points and weights of the weight lattice and splitting transforms are introduced. In Section 2.3, the definition of two families of (anti)symmetric orbit functions and their discrete orthogonality relations are provided, the weight lattice Fourier–Weyl transforms and their splitting versions are presented. In Section 2.4, the central splitting of the discrete weight lattice transforms is described in detail. The corresponding decomposition of the unitary matrices associated with the normalized discrete Fourier–Weyl transforms is deduced. Comments and follow-up questions are covered in the last section.

2.2. Splitting weight and point sets

2.2.1. Root and weight lattices

The fundamental concepts and pertinent properties of the simple Lie algebra A_2 and its root system are provided in (Bourbaki [**17**]; Humphreys [**66**]). The simple roots α_1 and α_2 of A_2 form a non-orthogonal $\alpha-$basis in the two-dimensional Euclidean space $\mathbb{R}^2$. The geometric properties of the simple roots of A_2, such as their lengths and the relative angle between them, are provided by the standard scalar product $\langle\, , \rangle$:

$$\langle \alpha_1, \alpha_1 \rangle = \langle \alpha_2, \alpha_2 \rangle = 2, \quad \langle \alpha_1, \alpha_2 \rangle = -1. \tag{2.2.1}$$

In addition, it is essential to introduce the basis of fundamental weights that is known as $\omega-$basis. The $\omega-$basis comprises the vectors ω_1 and ω_2, and the duality between $\alpha-$ and $\omega-$bases is provided by the relation

$$\langle \omega_i, \alpha_j \rangle = \delta_{ij}\, , \quad i, j \in \{1, 2\}. \tag{2.2.2}$$

The transformation between $\alpha-$ and $\omega-$basis is provided by the Cartan matrix as

$$\alpha = C\omega, \quad \omega = C^{-1}\alpha. \tag{2.2.3}$$

The Cartan matrix of A_2 and its inverse have the form

$$C = \begin{pmatrix} 2 & -1 \\ -1 & 2 \end{pmatrix}, \quad C^{-1} = \frac{1}{3}\begin{pmatrix} 2 & 1 \\ 1 & 2 \end{pmatrix}. \tag{2.2.4}$$

The vectors of the $\alpha-$basis can be explicitly written in terms of ω_1 and ω_2 as

$$\alpha_1 = 2\omega_1 - \omega_2, \quad \alpha_2 = -\omega_1 + 2\omega_2.$$

For the A_2 root system, the notions of the dual weights $\omega_k^\vee$ (Hrivnák and Patera [**63**]; Hrivnák and Motlochová[**62**]) together with the dual roots $\alpha_k^\vee$, $k \in \{1, 2\}$ coincide with the weights and roots, respectively,

$$\omega_k^\vee = \omega_k, \quad \alpha_k^\vee = \alpha_k. \tag{2.2.5}$$

Using the inverse transform, the vectors of the $\omega-$basis are provided in terms of α_1 and α_2 as

$$\omega_1 = \tfrac{2}{3}\alpha_1 + \tfrac{1}{3}\alpha_2, \quad \omega_2 = \tfrac{1}{3}\alpha_1 + \tfrac{2}{3}\alpha_2.$$

Similarly to the simple roots, the fundamental weights ω_1 and ω_2 are characterized by their lengths and the relative angle between them as

$$\langle \omega_1, \omega_1 \rangle = \langle \omega_2, \omega_2 \rangle = \tfrac{2}{3}, \quad \langle \omega_1, \omega_2 \rangle = \tfrac{1}{3}. \tag{2.2.6}$$

The scalar product of any two vectors $a = a_1\omega_1 + a_2\omega_2$ and $b = b_1\omega_1 + b_2\omega_2$ given in the $\omega-$basis has the form

$$\langle a, b\rangle = \frac{1}{3}(2a_1b_1 + a_1b_2 + a_2b_1 + 2a_2b_2). \tag{2.2.7}$$

All integer linear combinations of the simple roots α_1 and α_2 of A_2 form the root lattice $Q \subset \mathbb{R}^2$,

$$Q = \mathbb{Z}\alpha_1 + \mathbb{Z}\alpha_2.$$

Subsequently, the weight lattice P is provided by the set of all integer linear combinations of fundamental weights ω_1 and ω_2 as follows,

$$P = \mathbb{Z}\omega_1 + \mathbb{Z}\omega_2.$$

The weight lattice P decomposes into a union of the root lattice Q together with its shifted copies $(Q + \omega_i)$, $i \in \{1, 2\}$ as

$$P = Q \cup (Q + \omega_1) \cup (Q + \omega_2). \tag{2.2.8}$$

Hence, the points of the lattice P naturally split into three congruence classes P_k, $k \in$ {0,1,2} with respect to each component of the union (2.2.8) as

$$x = x_1\omega_1 + x_2\omega_2 \in P_k, \quad x_1 + 2x_2 = k \mod 3. \tag{2.2.9}$$

The reflections r_i, $i \in \{1, 2\}$ across the hyperplanes orthogonal to the simple root α_i and passing through the origin are linear maps that for any point $x \in \mathbb{R}^2$ are given as

$$r_i x = x - \langle x, \alpha_i\rangle\alpha_i. \tag{2.2.10}$$

The Weyl group W of A_2 is generated by the reflections r_i. The action of W on any point $x = x_1\omega_1 + x_2\omega_2 \in P$ produces the images of x that form the orbit of points equidistant from the origin,

$$Wx = \{(x_1, x_2), (-x_1, x_1 + x_2), (x_1 + x_2, -x_2), (x_2, -x_1 - x_2), (-x_1 - x_2, x_1), (-x_1, -x_2)\}. \tag{2.2.11}$$

The lattices Q and P are invariant under the action of the Weyl group,

$$WQ = Q, \quad WP = P. \tag{2.2.12}$$

The determinant c of the Cartan matrix C coincides with the order of the quotient group P/Q,

$$c = \det C = |P/Q| = 3. \tag{2.2.13}$$

The three representative elements z_k, $k \in \{0, 1, 2\}$ of the quotient group P/Q are according to the decomposition (2.2.8) chosen as

$$z_0 = 0, \quad z_1 = \omega_1, \quad z_2 = \omega_2. \tag{2.2.14}$$

2.2.2. Splitting weight sets

The affine Weyl group W_Q^{aff} is an infinite extension of the Weyl group W by shift vectors of the root lattice Q,

$$W_Q^{\text{aff}} = Q \rtimes W.$$

For $q \in Q$ and $w \in W$, the action of an element $T(q)w$ on any $x \in \mathbb{R}^2$ is denoted as

$$T(q)w \cdot x = wx + q.$$

The affine Weyl group is generated by the reflections r_i, $i \in \{1,2\}$ and the affine reflection r_0 provided by

$$r_0 x = r_\xi x + \xi, \quad r_\xi x = x - \langle x, \xi \rangle \xi, \tag{2.2.15}$$

where r_ξ represents the reflection across the hyperplane orthogonal to the highest root $\xi = \alpha_1 + \alpha_2$.

The affine reflections r_{α_i} across the hyperplanes orthogonal to the simple roots and passing through $\alpha_i/2$, $i \in \{1,2\}$ are given by the formula

$$r_{\alpha_i} x = r_i x + \alpha_i. \tag{2.2.16}$$

The fundamental region $F_Q \subset \mathbb{R}^2$ of W_Q^{aff} is represented by an equilateral triangle with the vertices $\{0, \omega_1, \omega_2\}$. Such a region contains precisely one point of each $W_Q^{\text{aff}}-$orbit,

$$F_Q = \{x_1\omega_1 + x_2\omega_2 \,|\, x_1, x_2 \geq 0, x_1 + x_2 \leq 1\}. \tag{2.2.17}$$

For any $M \in \mathbb{N}$, the weight sets Λ_M and $\widetilde{\Lambda}_M$ are determined by finite fragments of the weight lattice P contained within the magnified fundamental region MF_Q and its interior $\operatorname{int}(MF_Q)$, respectively,

$$\Lambda_M = P \cap MF_Q, \tag{2.2.18}$$

$$\widetilde{\Lambda}_M = P \cap \operatorname{int}(MF_Q). \tag{2.2.19}$$

The explicit forms of the weight sets Λ_M and $\widetilde{\Lambda}_M$ are as follows,

$$\Lambda_M = \left\{\lambda_1\omega_1 + \lambda_2\omega_2 \,|\, \lambda_0, \lambda_1, \lambda_2 \in \mathbb{Z}^{\geq 0}, \lambda_0 + \lambda_1 + \lambda_2 = M\right\}, \tag{2.2.20}$$

$$\widetilde{\Lambda}_M = \{\lambda_1\omega_1 + \lambda_2\omega_2 \,|\, \lambda_0, \lambda_1, \lambda_2 \in \mathbb{N}, \lambda_0 + \lambda_1 + \lambda_2 = M\}. \tag{2.2.21}$$

The weights in the weight sets (2.2.20) and (2.2.21) are determined by their Kac coordinates,

$$\lambda = [\lambda_0, \lambda_1, \lambda_2] \in \Lambda_M. \tag{2.2.22}$$

The splitting weight sets $\Lambda_M^{(k)}$, $k \in \{0,1,2\}$, that form a disjoint decomposition of the weight set Λ_M,

$$\Lambda_M = \Lambda_M^{(0)} \cup \Lambda_M^{(1)} \cup \Lambda_M^{(2)}, \tag{2.2.23}$$

are defined by finite fragments of the shifted copies (2.2.8) of the root lattice Q comprised within the region MF_Q,

$$\Lambda_M^{(k)} = P_k \cap MF_Q. \tag{2.2.24}$$

The interior splitting weight sets $\widetilde{\Lambda}_M^{(k)}$, $k \in \{0,1,2\}$, that form a disjoint decomposition of the weight set $\widetilde{\Lambda}_M$,

$$\widetilde{\Lambda}_M = \widetilde{\Lambda}_M^{(0)} \cup \widetilde{\Lambda}_M^{(1)} \cup \widetilde{\Lambda}_M^{(2)}, \tag{2.2.25}$$

are contained within the interior $\mathrm{int}(MF_Q)$,

$$\widetilde{\Lambda}_M^{(k)} = P_k \cap \mathrm{int}(MF_Q). \tag{2.2.26}$$

Taking into account the congruence decomposition relation (2.2.9) together with the forms of the weight sets (2.2.20) and (2.2.21), the weight sets $\Lambda_M^{(k)}$ and $\widetilde{\Lambda}_M^{(k)}$ are explicitly described as

$$\Lambda_M^{(k)} = \left\{\lambda_1\omega_1 + \lambda_2\omega_2 \,|\, \lambda_0, \lambda_1, \lambda_2 \in \mathbb{Z}^{\geq 0}, \lambda_0 + \lambda_1 + \lambda_2 = M, \lambda_1 + 2\lambda_2 = k \bmod 3\right\}, \tag{2.2.27}$$

$$\widetilde{\Lambda}_M^{(k)} = \{\lambda_1\omega_1 + \lambda_2\omega_2 \,|\, \lambda_0, \lambda_1, \lambda_2 \in \mathbb{N}, \lambda_0 + \lambda_1 + \lambda_2 = M, \lambda_1 + 2\lambda_2 = k \bmod 3\}. \tag{2.2.28}$$

The numbers of weights in the weight sets Λ_M and $\widetilde{\Lambda}_M$ are calculated in [**63**] as

$$|\Lambda_M| = \tfrac{1}{2}(M^2 + 3M + 2), \tag{2.2.29}$$

$$\left|\widetilde{\Lambda}_M\right| = \tfrac{1}{2}(M^2 - 3M + 2). \tag{2.2.30}$$

The numbers of weights in the splitting weight sets $\Lambda_M^{(k)}$, $k \in \{0,1,2\}$ together with their interior versions are determined in the following proposition.

Proposition 1. *The numbers of weights contained in the splitting sets $\Lambda_M^{(k)}$, $k \in \{0,1,2\}$ are determined as*

$$\left|\Lambda_M^{(0)}\right| = \begin{cases} \frac{1}{6}(M^2 + 3M + 6) & M = 0 \bmod 3, \\ \frac{1}{6}(M^2 + 3M + 2) & \textit{otherwise;} \end{cases} \tag{2.2.31}$$

$$\left|\Lambda_M^{(1)}\right| = \left|\Lambda_M^{(2)}\right| = \begin{cases} \frac{1}{6}(M^2 + 3M) & M = 0 \bmod 3, \\ \frac{1}{6}(M^2 + 3M + 2) & \textit{otherwise.} \end{cases} \tag{2.2.32}$$

The numbers of weights contained in the interior weight sets $\widetilde{\Lambda}_M^{(k)}$, $k \in \{0,1,2\}$ are given by

$$\left|\widetilde{\Lambda}_M^{(0)}\right| = \begin{cases} \frac{1}{6}(M^2 - 3M + 6) & M = 0 \bmod 3, \\ \frac{1}{6}(M^2 - 3M + 2) & \textit{otherwise;} \end{cases} \tag{2.2.33}$$

$$\left|\widetilde{\Lambda}_M^{(1)}\right| = \left|\widetilde{\Lambda}_M^{(2)}\right| = \begin{cases} \frac{1}{6}(M^2 - 3M) & M = 0 \bmod 3, \\ \frac{1}{6}(M^2 - 3M + 2) & \textit{otherwise.} \end{cases} \tag{2.2.34}$$

Proof. Preserving the notation for the point sets $F^{\mathbb{1}}_{Q^\vee,M}$ and $F^{\sigma^e}_{Q^\vee,M}$ of A_2 from (Hrivnák and Motlochová [**62**]), it holds that

$$\Lambda^{(0)}_M = MF^{\mathbb{1}}_{Q^\vee,M}, \tag{2.2.35}$$

$$\widetilde{\Lambda}^{(0)}_M = MF^{\sigma^e}_{Q^\vee,M}. \tag{2.2.36}$$

The point sets $F^{\mathbb{1}}_{Q^\vee,M}(0,\omega^\vee_k)$ and $F^{\sigma^e}_{Q^\vee,M}(0,\omega^\vee_k)$, $k \in \{1,2\}$ from (Czyżycki *et al.* [**34**]) are related to the current weight sets $\Lambda^{(k)}_M$ and $\widetilde{\Lambda}^{(k)}_M$ via the following relations,

$$\Lambda^{(k)}_M = MF^{\mathbb{1}}_{Q^\vee,M}(0,\omega^\vee_k), \tag{2.2.37}$$

$$\widetilde{\Lambda}^{(k)}_M = MF^{\sigma^e}_{Q^\vee,M}(0,\omega^\vee_k). \tag{2.2.38}$$

Thus, the current counting formulas are calculated from Theorems 5.4 and 5.5 in (Hrivnák and Motlochová [**62**]) and from Theorems 2 and 3 in (Czyżycki *et al.* [**34**]). ☐

A discrete function $h_M : \Lambda_M \to \mathbb{N}$ is defined for $\lambda \in \Lambda_M$ by its values on the Kac coordinates (2.2.22) with $\lambda_0, \lambda_1, \lambda_2 \neq 0$ as

$$h_M(\lambda) = \begin{cases} 1, & \lambda = [\lambda_0, \lambda_1, \lambda_2], \\ 2, & \lambda = [0, \lambda_1, \lambda_2], [\lambda_0, 0, \lambda_2], [\lambda_0, \lambda_1, 0], \\ 6, & \lambda = [0, 0, \lambda_2], [\lambda_0, 0, 0], [0, \lambda_1, 0]. \end{cases} \tag{2.2.39}$$

Since the $h-$function depends only on the number of zero-valued Kac coordinates of the weight $\lambda \in \Lambda_M$, it is invariant under the cyclic permutations of $[\lambda_0, \lambda_1, \lambda_2]$. The weight sets Λ_6, $\widetilde{\Lambda}_6$ and their decompositions $\Lambda^{(k)}_6$, $\widetilde{\Lambda}^{(k)}_6$, $k \in \{0,1,2\}$ are depicted in Figure 2.1.

2.2.3. Splitting point sets

The extension of the Weyl group W by shift vectors of the weight lattice P yields the extended affine Weyl group W^{aff}_P,

$$W^{\mathrm{aff}}_P = P \rtimes W.$$

For $p \in P$ and $w \in W$, the action of an element $T(p)w \in W^{\mathrm{aff}}_P$ on any $x \in \mathbb{R}^2$ is defined as

$$T(p)w \cdot x = wx + p.$$

The abelian group $\Gamma \subset W^{\mathrm{aff}}_P$ is the cyclic group of order 3,

$$\Gamma = \{\gamma_0, \gamma_1, \gamma_2\}, \tag{2.2.40}$$

and its elements are expressed by means of the generating reflections and weight lattice translations as follows,

$$\gamma_0 = T(0)1, \quad \gamma_1 = T(\omega_1)r_1r_2, \quad \gamma_2 = T(\omega_2)(r_1r_2)^2. \tag{2.2.41}$$

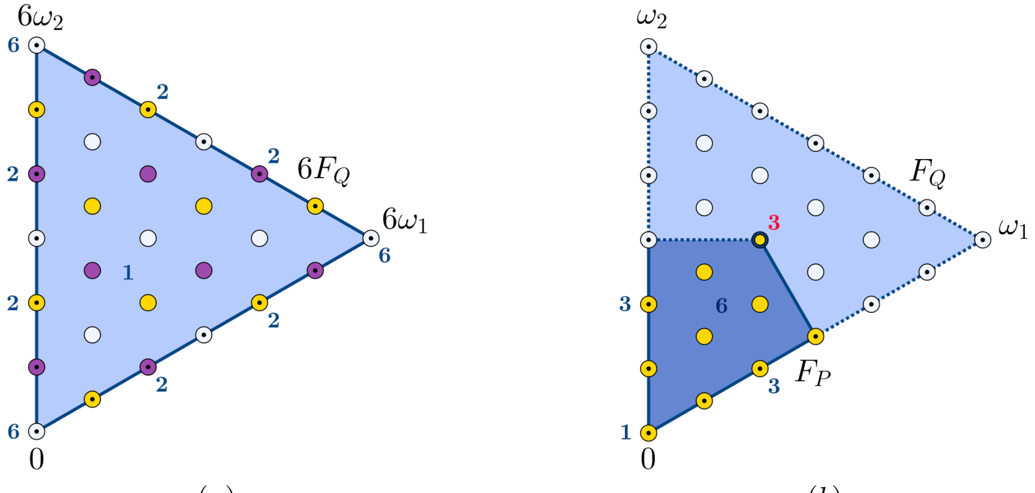

(a) (b)

Fig. 2.1. (a) The magnified fundamental region $6F_Q$ is depicted as the equilateral triangle which contains 28 points corresponding to the elements of the weight set Λ_6. The weight sets $\Lambda_6^{(0)}$, $\Lambda_6^{(1)}$ and $\Lambda_6^{(2)}$ are depicted by 10 light blue, 9 yellow and 9 magenta points, respectively. Omitting the dotted nodes on the boundary, the weight set $\widetilde{\Lambda}_6$ contains 10 points. The weight sets $\widetilde{\Lambda}_6^{(0)}$, $\widetilde{\Lambda}_6^{(1)}$ and $\widetilde{\Lambda}_6^{(2)}$ contain 4 light blue, 3 yellow and 3 magenta points. The blue numbers correspond to the values of the discrete $h-$function. (b) The fundamental domain F_Q of A_2, depicted by the equilateral triangle, contains 10 yellow nodes in the kite-shaped domain F_P that form the point set $F_6^{(0)}$. Excluding the point in center of F_Q, the sets $F_6^{(1)}$ and $F_6^{(2)}$ are depicted as 9 yellow nodes. The yellow nodes without the dotted ones on the boundary of F_Q correspond to the set $\widetilde{F}_6^{(0)}$. Omitting the central point of F_Q and the points on its boundary, 3 yellow nodes correspond to the point set $\widetilde{F}_6^{(1)}$, $\widetilde{F}_6^{(2)}$. The blue and red numbers correspond to the values of the discrete $\varepsilon-$ and $d-$functions, respectively.

The elements of the group Γ are equivalently expressed by application of the affine reflections r_{α_1}, r_{α_2} and r_0 on the shifted points $x+\omega_1$ and $x+\omega_2$,

$$\begin{aligned} r_0 r_{\alpha_1}(x+\omega_1) &= \gamma_1 x, \\ r_0 r_{\alpha_2}(x+\omega_2) &= \gamma_2 x. \end{aligned} \tag{2.2.42}$$

The points shifted by ω_1 and ω_2 are brought back to the fundamental region F_Q as shown in Figure 2.2.

The group Γ is isomorphic to the quotient group P/Q,

$$\Gamma \cong P/Q. \tag{2.2.43}$$

The fundamental domain F_P of the action of W_P^{aff} on $\mathbb{R}^2$ is the kite-shaped region comprised within the triangle F_Q that contains exactly one point of each $W_P^{\mathrm{aff}}-$orbit,

$$F_P = \{x_1\omega_1 + x_2\omega_2 \in F_Q \,|\, (2x_1+x_2<1, x_1+2x_2<1) \vee (2x_1+x_2=1, x_1 \geq x_2)\}\,. \tag{2.2.44}$$

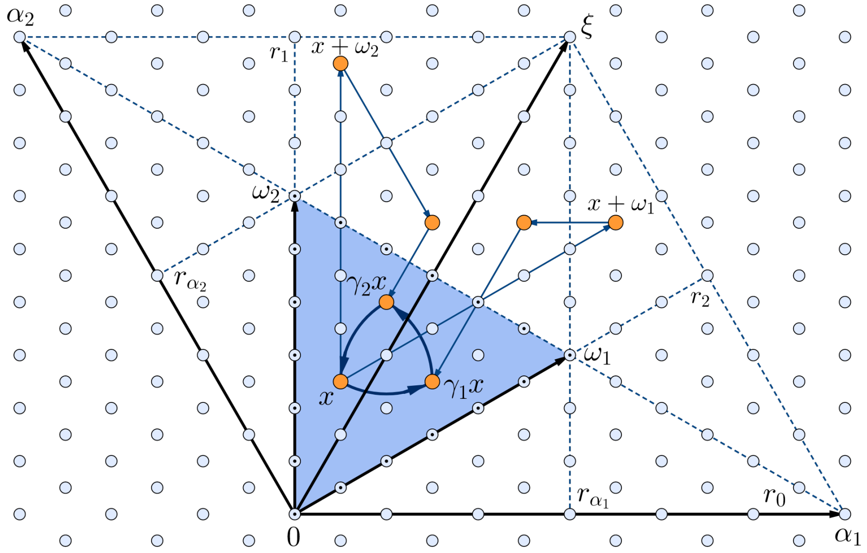

Fig. 2.2. The fundamental region F_Q is depicted by the blue triangle. The simple roots and fundamental weights are marked by α_i, ω_i, $i \in \{1,2\}$. The reflections r_i orthogonal to α_i pass through the origin. The points $x+\omega_1$ and $x+\omega_2$ are obtained by shifting of $x \in F_Q$ by the vectors ω_1 and ω_2. The affine reflections r_{α_i} are orthogonal to α_i, and they pass through $\frac{1}{2}\alpha_i$; the affine reflection r_0 passes through the middle of the highest root ξ. The points reflected back into F_Q coincide with the points obtained by the action of the elements γ_i of the cyclic group Γ.

The fundamental domain F_P, with the omitted central point of the triangle F_Q, forms the domain F'_P,

$$F'_P = \{x_1\omega_1 + x_2\omega_2 \in F_Q \,|\, (2x_1 + x_2 < 1, x_1 + 2x_2 < 1) \vee (2x_1 + x_2 = 1, x_1 > x_2)\}\,. \tag{2.2.45}$$

For any $M \in N$, the point sets F_M and $\widetilde{F}_M$ are described by the refined finite fragments of the weight lattice contained within the fundamental region F_Q and its interior, respectively,

$$F_M = \tfrac{1}{M} P \cap F_Q, \tag{2.2.46}$$

$$\widetilde{F}_M = \tfrac{1}{M} P \cap \mathrm{int}(F_Q). \tag{2.2.47}$$

The point sets F_M and $\widetilde{F}_M$ can be explicitly written as

$$F_M = \left\{ \frac{s_1}{M}\omega_1 + \frac{s_2}{M}\omega_2 \;\middle|\; s_0, s_1, s_2 \in \mathbb{Z}^{\geq 0}, s_0 + s_1 + s_2 = M \right\}, \tag{2.2.48}$$

$$\widetilde{F}_M = \left\{ \frac{s_1}{M}\omega_1 + \frac{s_2}{M}\omega_2 \;\middle|\; s_0, s_1, s_2 \in \mathbb{N}, s_0 + s_1 + s_2 = M \right\}. \tag{2.2.49}$$

The points of the point sets (2.2.48) and (2.2.49) are conveniently described by their Kac coordinates,

$$s = [s_0, s_1, s_2] \in F_M. \tag{2.2.50}$$

Direct comparison of the expressions for the point and weight sets (2.2.20), (2.2.21), (2.2.48) and (2.2.49) yield for the corresponding cardinalities that

$$|F_M| = |\Lambda_M|\,, \tag{2.2.51}$$

$$\left|\widetilde{F}_M\right| = \left|\widetilde{\Lambda}_M\right|. \tag{2.2.52}$$

Note that there is at most one point $s^{\mathrm{fix}} \in F_M$ whose coordinates satisfy the relation $s_0 = s_1 = s_2 = M/3$. Such a point is fixed by the action of Γ, and it is found in the center of the triangle F_Q, if an integer M is divisible by 3.

The splitting point set $F_M^{(0)}$ is determined by the points from F_M contained within the kite-shaped fundamental domain of the extended affine Weyl group F_P,

$$F_M^{(0)} = F_M \cap F_P \tag{2.2.53}$$

and the splitting point sets $F_M^{(1)}$ and $F_M^{(2)}$ are formed by the points from F_M included in the region F'_P,

$$F_M^{(1)} = F_M^{(2)} = F_M \cap F'_P. \tag{2.2.54}$$

The interior splitting point sets $\widetilde{F}_M^{(k)}$, $k \in \{0, 1, 2\}$ are defined similarly as

$$\widetilde{F}_M^{(0)} = \widetilde{F}_M \cap F_P, \tag{2.2.55}$$

$$\widetilde{F}_M^{(1)} = \widetilde{F}_M^{(2)} = \widetilde{F}_M \cap F'_P. \tag{2.2.56}$$

Using Formulas (2.2.44) and (2.2.45) together with the Kac coordinates (2.2.50), the point sets $F_M^{(k)}$ are expressed as

$$\begin{aligned} F_M^{(0)} &= \{[s_0, s_1, s_2] \in F_M \,|\, (s_0 > s_1, s_0 > s_2) \vee (s_0 = s_1 \geq s_2)\}\,, \\ F_M^{(1)} = F_M^{(2)} &= \{[s_0, s_1, s_2] \in F_M \,|\, (s_0 > s_1, s_0 > s_2) \vee (s_0 = s_1 > s_2)\}\,. \end{aligned} \tag{2.2.57}$$

Similarly, the interior point sets $\widetilde{F}_M^{(k)}$ are explicitly written as

$$\begin{aligned} \widetilde{F}_M^{(0)} &= \left\{[s_0, s_1, s_2] \in \widetilde{F}_M \,|\, (s_0 > s_1, s_0 > s_2) \vee (s_0 = s_1 \geq s_2)\right\}, \\ \widetilde{F}_M^{(1)} = \widetilde{F}_M^{(2)} &= \left\{[s_0, s_1, s_2] \in \widetilde{F}_M \,|\, (s_0 > s_1, s_0 > s_2) \vee (s_0 = s_1 > s_2)\right\}. \end{aligned} \tag{2.2.58}$$

The cardinalities of the splitting point sets are related to the numbers of elements of the corresponding weight sets in the following proposition.

Proposition 2. *The numbers of points contained in the splitting sets $F_M^{(k)}$ and $\widetilde{F}_M^{(k)}$, $k \in \{0, 1, 2\}$ coincide with the numbers of weights in the splitting sets $\Lambda_M^{(k)}$ and $\widetilde{\Lambda}_M^{(k)}$, respectively,*

$$\left|F_M^{(k)}\right| = \left|\Lambda_M^{(k)}\right|, \tag{2.2.59}$$

$$\left|\widetilde{F}_M^{(k)}\right| = \left|\widetilde{\Lambda}_M^{(k)}\right|. \tag{2.2.60}$$

PROOF. Preserving the notation for the weight sets from (Hrivnák and Motlochová [**62**]), it holds that

$$F_M^{(0)} = \tfrac{1}{M}\Lambda^{1}_{P,M}, \tag{2.2.61}$$

$$\widetilde{F}_M^{(0)} = \tfrac{1}{M}\Lambda^{\sigma^e}_{P,M}, \tag{2.2.62}$$

and the weight sets from (Czyżycki *et al.* [**34**]) are related to the current point sets $F_M^{(k)}$, $\widetilde{F}_M^{(k)}$, $k \in \{1,2\}$ via the relations

$$F_M^{(k)} = \tfrac{1}{M}\Lambda^{1}_{P,M}(0,\omega_k^\vee), \tag{2.2.63}$$

$$\widetilde{F}_M^{(k)} = \tfrac{1}{M}\Lambda^{\sigma^e}_{P,M}(0,\omega_k^\vee). \tag{2.2.64}$$

Thus, the current cardinality equalities are obtained from relations (2.2.61), (2.2.62) and Theorem 5.4 in (Hrivnák and Motlochová [**62**]) and from relations (2.2.63), (2.2.64) together with Theorem 2 in (Czyżycki *et al.* [**34**]). $\square$

The elements (2.2.40) of the abelian group Γ preserve the point set F_M and act on any point $s \in F_M$ as cyclic permutations of the Kac coordinates $[s_0, s_1, s_2]$,

$$\begin{aligned}
\gamma_0[s_0,s_1,s_2] &= [s_0,s_1,s_2],\\
\gamma_1[s_0,s_1,s_2] &= [s_2,s_0,s_1],\\
\gamma_2[s_0,s_1,s_2] &= [s_1,s_2,s_0].
\end{aligned}$$

A discrete function $\varepsilon : F_M \to \mathbb{N}$ is defined for $s \in F_M$ by its values on the Kac coordinates (2.2.50) with $s_0, s_1, s_2 \neq 0$ as

$$\varepsilon(s) = \begin{cases} 6, & s = [s_0,s_1,s_2],\\ 3, & s = [0,s_1,s_2],[s_0,0,s_2],[s_0,s_1,0],\\ 1, & s = [0,0,s_2],[s_0,0,0],[0,s_1,0]. \end{cases} \tag{2.2.65}$$

Similarly to the $h-$function (2.2.39), the $\varepsilon-$function is invariant under the permutation of the Kac coordinates $[s_0, s_1, s_2]$. Note also that the $h-$ and $\varepsilon-$functions are related for $\lambda \in \Lambda_M$ by the formula

$$h_M(\lambda) = 6\,\varepsilon^{-1}\left(\tfrac{\lambda}{M}\right). \tag{2.2.66}$$

A discrete function $d : F_M \to \mathbb{N}$ depends only on the equality of Kac coordinates $s_0 = s_1 = s_2$, and it takes one of the following two values,

$$d(s) = \begin{cases} 3, & s_0 = s_1 = s_2,\\ 1, & \text{otherwise}. \end{cases} \tag{2.2.67}$$

The point sets F_6, $\widetilde{F}_6$ together with their subsets $F_6^{(k)}$ and $\widetilde{F}_6^{(k)}$, $k \in \{0,1,2\}$ are depicted in Figure 2.1.

2.3. Weight lattice Fourier–Weyl transforms

2.3.1. $C-$ and $S-$functions

The Weyl orbit functions and their pertinent properties have been extensively studied in several papers, see for instance (Klimyk and Patera [**78, 79, 80**]). The orbit functions of A_2 can be written as sums of multivariate exponential functions $e^{2\pi\mathrm{i}\langle b,\,x\rangle}$, $b \in \mathbb{R}^2$ of the variable $x \in \mathbb{R}^2$. For any label $b \in \mathbb{R}^2$ and a point $x \in \mathbb{R}^2$, consider the two families of complex-valued smooth functions,

$$\Phi_b(x) = \sum_{w\in W} e^{2\pi\mathrm{i}\langle wb,\,x\rangle}, \tag{2.3.1}$$

$$\varphi_b(x) = \sum_{w\in W} \det(w)\, e^{2\pi\mathrm{i}\langle wb,\,x\rangle}. \tag{2.3.2}$$

The functions (2.3.1) and (2.3.2), known as the $C-$ and $S-$functions, correspond to the classical univariate cosine and sine functions. For the $C-$functions, all terms have positive sign; hence, they are referred to as symmetric orbit functions. The signs of terms composing $S-$functions depend on $\det(w)$, and they are called anti-symmetric orbit functions.

The duality of the Weyl orbit functions (Klimyk and Patera [**78, 79**]) is expressed as

$$\Phi_b(x) = \Phi_x(b), \qquad \varphi_b(x) = \varphi_x(b), \tag{2.3.3}$$

and, for any real-valued parameter $t \in \mathbb{R}$, the scaling symmetry is determined by

$$\Phi_b(tx) = \Phi_{tb}(x), \qquad \varphi_b(tx) = \varphi_{tb}(x). \tag{2.3.4}$$

Considering the scalar product (2.2.7) and expression for the Weyl orbit (2.2.11), the $C-$ and $S-$functions can be written for the label $b = b_1\omega_1 + b_2\omega_2$ and the point $x = x_1\omega_1 + x_2\omega_2$ in the $\omega-$basis explicitly as

$$\begin{aligned}\Phi_b(x) = {} & e^{\frac{2}{3}\pi\mathrm{i}((2b_1+b_2)x_1+(b_1+2b_2)x_2)} + e^{\frac{2}{3}\pi\mathrm{i}((-b_1+b_2)x_1+(b_1+2b_2)x_2)} + e^{\frac{2}{3}\pi\mathrm{i}((-b_1-2b_2)x_1+(b_1-b_2)x_2)} \\ & + e^{\frac{2}{3}\pi\mathrm{i}((-b_1-2b_2)x_1+(-2b_1-b_2)x_2)} + e^{\frac{2}{3}\pi\mathrm{i}((-b_1+b_2)x_1+(-2b_1-b_2)x_2)} + e^{\frac{2}{3}\pi\mathrm{i}((2b_1+b_2)x_1+(b_1-b_2)x_2)},\end{aligned} \tag{2.3.5}$$

$$\begin{aligned}\varphi_b(x) = {} & e^{\frac{2}{3}\pi\mathrm{i}((2b_1+b_2)x_1+(b_1+2b_2)x_2)} - e^{\frac{2}{3}\pi\mathrm{i}((-b_1+b_2)x_1+(b_1+2b_2)x_2)} + e^{\frac{2}{3}\pi\mathrm{i}((-b_1-2b_2)x_1+(b_1-b_2)x_2)} \\ & - e^{\frac{2}{3}\pi\mathrm{i}((-b_1-2b_2)x_1+(-2b_1-b_2)x_2)} + e^{\frac{2}{3}\pi\mathrm{i}((-b_1+b_2)x_1+(-2b_1-b_2)x_2)} - e^{\frac{2}{3}\pi\mathrm{i}((2b_1+b_2)x_1+(b_1-b_2)x_2)}.\end{aligned} \tag{2.3.6}$$

The $C-$ and $S-$functions are (anti)symmetric with respect to the action of any Weyl group element $w \in W$,

$$\Phi_b(wx) = \Phi_b(x), \qquad \varphi_b(wx) = \det(w)\,\varphi_b(x). \tag{2.3.7}$$

For the discretized labels from the weight lattice $\lambda \in P$, the $C-$ and $S-$functions are invariant under the translations by any root-lattice vector $q \in Q$,

$$\Phi_\lambda(x+q) = \Phi_\lambda(x), \qquad \varphi_\lambda(x+q) = \varphi_\lambda(x). \tag{2.3.8}$$

Therefore, both families of the orbit functions Φ_λ and φ_λ, $\lambda \in P$ are (anti)symmetric with respect to the affine Weyl group W_Q^{aff}. Hence, the $C-$ and $S-$functions are usually restricted to the corresponding fundamental domain (2.2.17). The normal derivative of the $C-$functions and values of the $S-$functions vanish on the boundary of F_Q. Symmetries of the orbit functions under the action of the $\Gamma-$group are formulated in the following proposition.

Proposition 3. *For any* $\lambda \in P_k$, $\gamma_j \in \Gamma$, $j,k \in \{0,1,2\}$ *and* $x \in \mathbb{R}^2$, *it holds that*

$$\Phi_\lambda(\gamma_j x) = e^{2\pi \mathrm{i} \langle z_k,\, z_j \rangle} \Phi_\lambda(x), \tag{2.3.9}$$

$$\varphi_\lambda(\gamma_j x) = e^{2\pi \mathrm{i} \langle z_k,\, z_j \rangle} \varphi_\lambda(x). \tag{2.3.10}$$

Proof. Taking into account identity (2.2.5), the representative elements z_j, $j \in \{0,1,2\}$ constitute according to (Czyżycki *et al.* [**34**]) admissible shifts of the root lattice of A_2. Thus, the invariance property (Czyżycki *et al.* [**34**], Equation 48) is specialized for any $\lambda \in P$ and $w \in W$ as

$$e^{2\pi \mathrm{i} \langle w\lambda,\, z_j \rangle} = e^{2\pi \mathrm{i} \langle \lambda,\, z_j \rangle}. \tag{2.3.11}$$

Moreover, for any weight $\lambda = z_k + q \in P_k$ with $q \in Q$, the $\mathbb{Z}-$duality relation (2.2.2) of the weight and root lattices guarantees that

$$e^{2\pi \mathrm{i} \langle \lambda,\, z_j \rangle} = e^{2\pi \mathrm{i} \langle z_k + q,\, z_j \rangle} = e^{2\pi \mathrm{i} \langle z_k,\, z_j \rangle}. \tag{2.3.12}$$

The action of the elements of the $\Gamma-$group of A_2 are for any $x \in \mathbb{R}^2$ from defining relation (2.2.41) given as

$$\gamma_j x = w_j x + z_j, \tag{2.3.13}$$

while it holds that

$$\det(w_j) = 1. \tag{2.3.14}$$

The symmetry properties of the $C-$functions under the action of the $\Gamma-$group are calculated for $\lambda \in P_k$ using (2.3.11), (2.3.12) and (2.3.13) as

$$\Phi_\lambda(\gamma_j x) = \sum_{w \in W} e^{2\pi \mathrm{i} \langle w\lambda,\, w_j x + z_j \rangle} = \sum_{w \in W} e^{2\pi \mathrm{i} \langle w\lambda,\, w_j x \rangle} e^{2\pi \mathrm{i} \langle w\lambda,\, z_j \rangle} = e^{2\pi \mathrm{i} \langle z_k,\, z_j \rangle} \Phi_\lambda(x).$$

In addition, utilizing relation (2.3.14), the resulting symmetry properties of the $S-$functions are obtained via the calculation

$$\begin{aligned}\varphi_\lambda(\gamma_j x) &= \sum_{w \in W} \det(w)\, e^{2\pi \mathrm{i} \langle w\lambda,\, w_j x + z_j \rangle} = \sum_{w \in W} \det(w)\, e^{2\pi \mathrm{i} \langle w\lambda,\, w_j x \rangle} e^{2\pi \mathrm{i} \langle w\lambda,\, z_j \rangle} \\ &= \det(w_j) e^{2\pi \mathrm{i} \langle z_k,\, z_j \rangle} \varphi_\lambda(x).\end{aligned}$$

□

2.3.2. Discrete orthogonality

The orthogonality relations of $C-$and $S-$functions whenever they are integrated over the fundamental region are described in (McKay and Patera [**97**]). Here we recall the discrete orthogonality relations of both families of functions, as well as define the discrete orthogonality of $C-$ and $S-$functions summed over finite point sets comprised within the kite-shaped region F_P. Employing the $\varepsilon-$function (2.2.65), the scalar product of two functions f,$g : F_M \to \mathbb{C}$ on a refined fragment of the weight lattice (2.2.46) contained within the fundamental domain F_Q is provided by the formula

$$\langle f, g\rangle_{F_M} = \sum_{s\in F_M} \varepsilon(s) f(s)\overline{g(s)}. \tag{2.3.15}$$

The Hilbert space $\mathcal{H}_M$ is the space of complex-valued functions $f : F_M \to \mathbb{C}$ equipped with the weighted scalar product (2.3.15).

Since the points of the interior point set $\widetilde{F}_M$ retain their Kac coordinates non-zero, the discrete $\varepsilon-$function takes according to (2.2.65) the constant value,

$$\varepsilon(s) = 6, \quad s \in \widetilde{F}_M. \tag{2.3.16}$$

Thus, the scalar product of two complex-valued functions f,$g : \widetilde{F}_M \to \mathbb{C}$ on the interior point set $\widetilde{F}_M$ is given as

$$\langle f, g\rangle_{\widetilde{F}_M} = 6 \sum_{s\in \widetilde{F}_M} f(s)\overline{g(s)}. \tag{2.3.17}$$

The Hilbert space $\widetilde{\mathcal{H}}_M$ is the space of complex-valued functions $f : \widetilde{F}_M \to \mathbb{C}$ equipped with the scalar product (2.3.17).

For any weights $\lambda, \lambda' \in \Lambda_M$, the discrete orthogonality relations of the $C-$functions (2.3.1) with respect to the scalar product (2.3.15) are of the form (Hrivnák and Patera [**63**]),

$$\langle \Phi_\lambda, \Phi_{\lambda'}\rangle_{F_M} = 18M^2 h_M(\lambda)\delta_{\lambda,\lambda'}, \tag{2.3.18}$$

and for any interior weights $\lambda, \lambda' \in \widetilde{\Lambda}_M$, the discrete orthogonality relations of the $S-$functions (2.3.2) are given as

$$\langle \varphi_\lambda, \varphi_{\lambda'}\rangle_{\widetilde{F}_M} = 18M^2 \delta_{\lambda,\lambda'}. \tag{2.3.19}$$

The scalar product of two functions f,$g : F_M^{(k)} \to \mathbb{C}$, $k \in \{0, 1, 2\}$ on the refined fragments of the weight lattice is defined as

$$\langle f, g\rangle_{F_M^{(k)}} = \sum_{s\in F_M^{(k)}} \varepsilon(s) d^{-1}(s) f(s)\overline{g(s)}. \tag{2.3.20}$$

The Hilbert spaces $\mathcal{H}_M^{(k)}$ are the spaces of complex-valued functions $f : F_M^{(k)} \to \mathbb{C}$ equipped with the weighted scalar product (2.3.20).

Taking into account the interior $\varepsilon-$function values (2.3.16), the interior scalar product of two functions $f, g : \widetilde{F}_M^{(k)} \to \mathbb{C}$, $k \in \{0,1,2\}$ is given by

$$\langle f, g\rangle_{\widetilde{F}_M^{(k)}} = 6 \sum_{s\in\widetilde{F}_M^{(k)}} d^{-1}(s) f(s)\overline{g(s)}. \tag{2.3.21}$$

Discrete orthogonality relations with respect to the scalar products (2.3.20) and (2.3.21) of the $C-$ and $S-$functions are formulated in the following proposition.

Proposition 4. *The discrete orthogonality relations of $C-$functions labeled by any weights $\lambda, \lambda' \in \Lambda_M^{(k)}$, $k \in \{0,1,2\}$ are of the form*

$$\langle \Phi_\lambda, \Phi_{\lambda'}\rangle_{F_M^{(k)}} = 6M^2 h_M(\lambda)\delta_{\lambda,\lambda'}. \tag{2.3.22}$$

The discrete orthogonality relations of $S-$functions labeled by any weights $\lambda, \lambda' \in \widetilde{\Lambda}_M^{(k)}$, $k \in \{0,1,2\}$ are determined as

$$\langle \varphi_\lambda, \varphi_{\lambda'}\rangle_{\widetilde{F}_M^{(k)}} = 6M^2 \delta_{\lambda,\lambda'}. \tag{2.3.23}$$

Proof. The discrete orthogonality relations of the A_2 orbit $C-$functions (Czyżycki *et al.* [**34**], Theorem 4) and the corresponding Plancherel formulas (Czyżycki *et al.* [**34**], Equation 172) lead for points $a, a' \in F^{\mathbb{1}}_{Q^\vee,M}(0,\omega_k^\vee)$, $k \in \{1,2\}$ to the following relations,

$$\sum_{\mu\in\Lambda^{\mathbb{1}}_{P,M}(0,\omega_k^\vee)} h_M^{-1}(\mu) d^{-1}\left(\tfrac{\mu}{M}\right)\, \Phi_\mu(a)\overline{\Phi_\mu(a')} = 6M^2\varepsilon^{-1}(a)\,\delta_{a,a'}. \tag{2.3.24}$$

Denoting $Ma = \lambda$, $Ma' = \lambda'$ and $\mu = Ms$, it follows from weight and point set relations (2.2.37) and (2.2.63) that $\lambda, \lambda' \in \Lambda_M^{(k)}$ and $s \in F_M^{(k)}$, $k \in \{1,2\}$. Thus, discrete orthogonality relation (2.3.24) is rewritten as

$$\sum_{s\in F_M^{(k)}} h_M^{-1}(Ms) d^{-1}(s)\, \Phi_{Ms}\left(\tfrac{\lambda}{M}\right)\overline{\Phi_{Ms}\left(\tfrac{\lambda'}{M}\right)} = 6M^2\varepsilon^{-1}\left(\tfrac{\lambda}{M}\right)\delta_{\lambda,\lambda'}. \tag{2.3.25}$$

Utilizing the duality and scaling symmetry of orbit functions (2.3.3) and (2.3.4) together with the relation between $h-$ and $\varepsilon-$functions (2.2.66), the discrete orthogonality (2.3.25) is reformulated as

$$\sum_{s\in F_M^{(k)}} \varepsilon(s) d^{-1}(s)\Phi_\lambda(s)\overline{\Phi_{\lambda'}(s)} = 6M^2 h_M(\lambda)\delta_{\lambda,\lambda'}. \tag{2.3.26}$$

The remaining case for $k = 0$ and the orthogonality relations of the $S-$functions over the interior sets are shown similarly via Theorem 6.4 in (Hrivnák and Motlochová [**62**]) together with relations (2.2.35), (2.2.61) and interior set expressions (2.2.36), (2.2.38), (2.2.62) and (2.2.64). ☐

2.3.3. Splitting transforms

Based on the discrete orthogonality relations of the two families of $C-$ and $S-$functions (2.3.18) and (2.3.19), the discrete Fourier analysis is applied in the context of the Weyl group symmetry. Taking into account cardinality formulas (2.2.51) and (2.2.52), the $C-$ and $S-$functions constitute orthogonal bases of the Hilbert spaces $\mathcal{H}_M$ and $\widetilde{\mathcal{H}}_M$, respectively. For a given complex-valued function $f : F_Q \to \mathbb{C}$, there exist two interpolating functions $\mathrm{I}[f]_M : \mathbb{R}^2 \to \mathbb{C}$ and $\widetilde{\mathrm{I}}[f]_M : \mathbb{R}^2 \to \mathbb{C}$. The interpolating functions $\mathrm{I}[f]_M$ and $\widetilde{\mathrm{I}}[f]_M$ are constructed as linear combinations of the Weyl orbit functions,

$$\mathrm{I}[f]_M(x) = \sum_{\lambda \in \Lambda_M} c_\lambda[f]_M \Phi_\lambda(x), \tag{2.3.27}$$

$$\widetilde{\mathrm{I}}[f]_M(x) = \sum_{\lambda \in \widetilde{\Lambda}_M} \widetilde{c}_\lambda[f]_M \varphi_\lambda(x), \tag{2.3.28}$$

which coincide with the function f on the interpolation nodes F_M and $\widetilde{F}_M$, respectively,

$$\mathrm{I}[f]_M(s) = f(s), \quad s \in F_M, \tag{2.3.29}$$

$$\widetilde{\mathrm{I}}[f]_M(s) = f(s), \quad s \in \widetilde{F}_M. \tag{2.3.30}$$

Due to discrete orthogonality relations (2.3.18) and (2.3.19), the frequency spectrum coefficients $c_\lambda[f]_M$, $\lambda \in \Lambda_M$ and $\widetilde{c}_\lambda[f]_M$, $\lambda \in \widetilde{\Lambda}_M$ are uniquely determined via the weight lattice Fourier–Weyl $C-$ and $S-$transforms (Hrivnák and Patera [**63**]) of A_2,

$$c_\lambda[f]_M = \frac{\langle f, \Phi_\lambda \rangle_{F_M}}{\langle \Phi_\lambda, \Phi_\lambda \rangle_{F_M}} = \left(18M^2 h_M(\lambda)\right)^{-1} \sum_{s \in F_M} \varepsilon(s) f(s) \overline{\Phi_\lambda(s)}, \tag{2.3.31}$$

$$\widetilde{c}_\lambda[f]_M = \frac{\langle f, \varphi_\lambda \rangle_{\widetilde{F}_M}}{\langle \varphi_\lambda, \varphi_\lambda \rangle_{\widetilde{F}_M}} = \left(3M^2\right)^{-1} \sum_{s \in \widetilde{F}_M} f(s) \overline{\varphi_\lambda(s)}. \tag{2.3.32}$$

Formulation of the weight lattice splitting Fourier–Weyl $C-$ and $S-$transforms on the Hilbert spaces $\mathcal{H}_M^{(k)}$ and $\widetilde{\mathcal{H}}_M^{(k)}$ is founded on orbit function orthogonal bases constructed in the following proposition.

Proposition 5. *For each $k \in \{0,1,2\}$, the $C-$functions Φ_λ, $\lambda \in \Lambda_M^{(k)}$ form an orthogonal basis of the Hilbert space $\mathcal{H}_M^{(k)}$, and the $S-$functions φ_λ, $\lambda \in \widetilde{\Lambda}_M^{(k)}$ form an orthogonal basis of the Hilbert space $\widetilde{\mathcal{H}}_M^{(k)}$.*

Proof. Discrete orthogonality relations of the $C-$ and $S-$functions in Proposition 4 guarantee that the functions Φ_λ, $\lambda \in \Lambda_M^{(k)}$ and φ_λ, $\lambda \in \widetilde{\Lambda}_M^{(k)}$ are linearly independent in the spaces $\mathcal{H}_M^{(k)}$ and $\widetilde{\mathcal{H}}_M^{(k)}$, respectively. The dimensions of the functional Hilbert spaces $\mathcal{H}_M^{(k)}$ and $\widetilde{\mathcal{H}}_M^{(k)}$ coincide with the cardinalities of the underlying point sets $F_M^{(k)}$ and $\widetilde{F}_M^{(k)}$, and

Proposition 2 provides that

$$\dim \mathcal{H}_M^{(k)} = \left|F_M^{(k)}\right| = \left|\Lambda_M^{(k)}\right|,$$
$$\dim \widetilde{\mathcal{H}}_M^{(k)} = \left|\widetilde{F}_M^{(k)}\right| = \left|\widetilde{\Lambda}_M^{(k)}\right|.$$

□

For a given complex-valued function $f : F_P \to \mathbb{C}$, utilizing the orthogonal bases of the discretized Weyl orbit functions, there exist six interpolating functions $\mathrm{I}[f]_M^{(k)} : \mathbb{R}^2 \to \mathbb{C}$ and $\widetilde{\mathrm{I}}[f]_M^{(k)} : \mathbb{R}^2 \to \mathbb{C}$, $k \in \{0,1,2\}$. The interpolating functions $\mathrm{I}[f]_M^{(k)}$ and $\widetilde{\mathrm{I}}[f]_M^{(k)}$ are constructed as linear combinations of the Weyl orbit functions,

$$\mathrm{I}[f]_M^{(k)}(x) = \sum_{\lambda \in \Lambda_M^{(k)}} c_\lambda[f]_M^{(k)} \Phi_\lambda(x), \tag{2.3.33}$$

$$\widetilde{\mathrm{I}}[f]_M^{(k)}(x) = \sum_{\lambda \in \widetilde{\Lambda}_M^{(k)}} \widetilde{c}_\lambda[f]_M^{(k)} \varphi_\lambda(x), \tag{2.3.34}$$

that coincide with the function f on the interpolation nodes $F_M^{(k)}$ and $\widetilde{F}_M^{(k)}$, respectively,

$$\mathrm{I}[f]_M^{(k)}(s) = f(s), \quad s \in F_M^{(k)}, \tag{2.3.35}$$

$$\widetilde{\mathrm{I}}[f]_M^{(k)}(s) = f(s), \quad s \in \widetilde{F}_M^{(k)}. \tag{2.3.36}$$

Obtained as the standard Fourier coefficients from Propositions 4 and 5, the frequency spectrum coefficients $c_\lambda[f]_M^{(k)}$, $\lambda \in \Lambda_M^{(k)}$ and $\widetilde{c}_\lambda[f]_M^{(k)}$, $\lambda \in \widetilde{\Lambda}_M^{(k)}$ are uniquely determined as

$$c_\lambda[f]_M^{(k)} = \frac{\langle f, \Phi_\lambda \rangle_{F_M^{(k)}}}{\langle \Phi_\lambda, \Phi_\lambda \rangle_{F_M^{(k)}}} = \left(6M^2 h_M(\lambda)\right)^{-1} \sum_{s \in F_M^{(k)}} \varepsilon(s) d^{-1}(s) f(s) \overline{\Phi_\lambda(s)}, \tag{2.3.37}$$

$$\widetilde{c}_\lambda[f]_M^{(k)} = \frac{\langle f, \varphi_\lambda \rangle_{\widetilde{F}_M^{(k)}}}{\langle \varphi_\lambda, \varphi_\lambda \rangle_{\widetilde{F}_M^{(k)}}} = M^{-2} \sum_{s \in \widetilde{F}_M^{(k)}} d^{-1}(s) f(s) \overline{\varphi_\lambda(s)}. \tag{2.3.38}$$

Frequency spectrum coefficients Formulas (2.3.37) and (2.3.38) constitute the forward weight lattice splitting Fourier–Weyl $C-$ and $S-$transforms, respectively. Interpolation properties of the splitting types of the Fourier–Weyl transforms are tested in the following example.

Example 6 (Interpolation by splitting transforms)**.** *As a model function for the interpolation tests of the splitting transforms, the following real-valued function f on the kite-shaped fundamental domain of the extended affine Weyl group F_P is introduced for any point $x = x_1\omega_1 + x_2\omega_2$ in the $\omega-$basis,*

$$f(x) = 0.4 e^{-\frac{1}{\sigma^2}\left(\left(x_1 - \frac{1}{6}\right)^2 + \frac{1}{3}\left(x_1 + 2x_2 - \frac{1}{2}\right)^2\right)}. \tag{2.3.39}$$

The $3D$ *graph and contour plot of the model function* f*, with* $\sigma = 0.065$ *chosen as a fixed value, are shown in Figure 2.3.*

The function f *is interpolated by the anti(symmetric) interpolating functions* (2.3.33) *and* (2.3.34) *with the frequency spectrum coefficients computed from the weight lattice splitting Fourier–Weyl transforms* (2.3.37) *and* (2.3.38)*, respectively. The symmetric interpolating functions* $\mathrm{I}[f]_M^{(0)}$ *and* $\mathrm{I}[f]_M^{(1)}$ *are for* $M = 10, 14$ *and* 18 *plotted in Figures 2.4 and 2.5.*

The antisymmetric interpolating functions $\widetilde{\mathrm{I}}[f]_M^{(0)}$ *and* $\widetilde{\mathrm{I}}[f]_M^{(1)}$ *are for* $M = 10, 14$ *and* 18 *plotted in Figures 2.6 and 2.7.*

The integral error estimates of both types of interpolations are presented in Table 2.1.

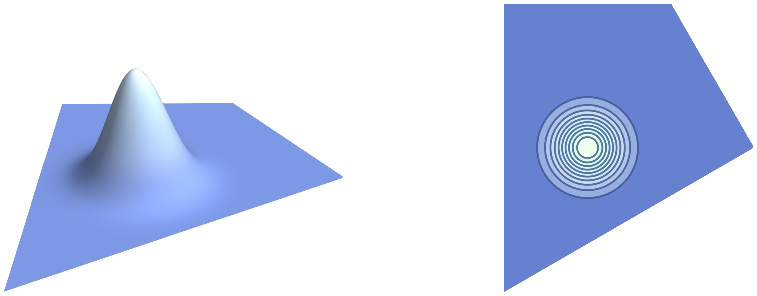

Fig. 2.3. The model function f plotted over the region F_P.

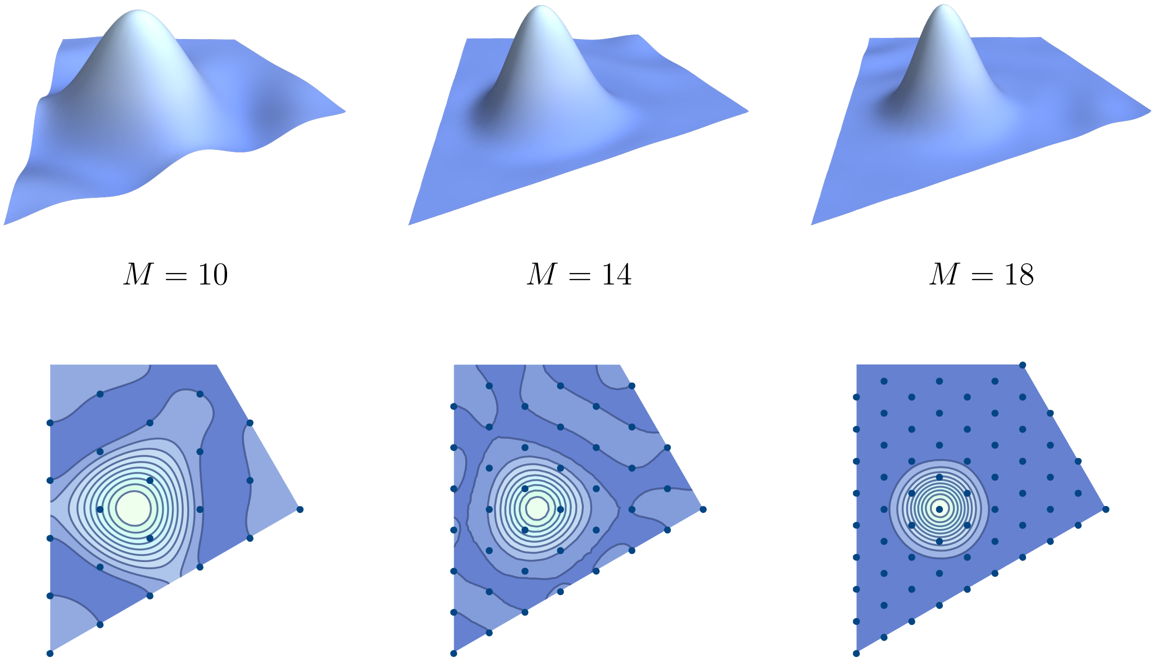

$M = 10$ $M = 14$ $M = 18$

Fig. 2.4. The interpolating functions $\mathrm{I}[f]_M^{(0)}$ are for $M = 10{,}14{,}18$ plotted over the region F_P. The sampling point sets $F_M^{(0)}$ of the interpolation are marked by the blue dots.

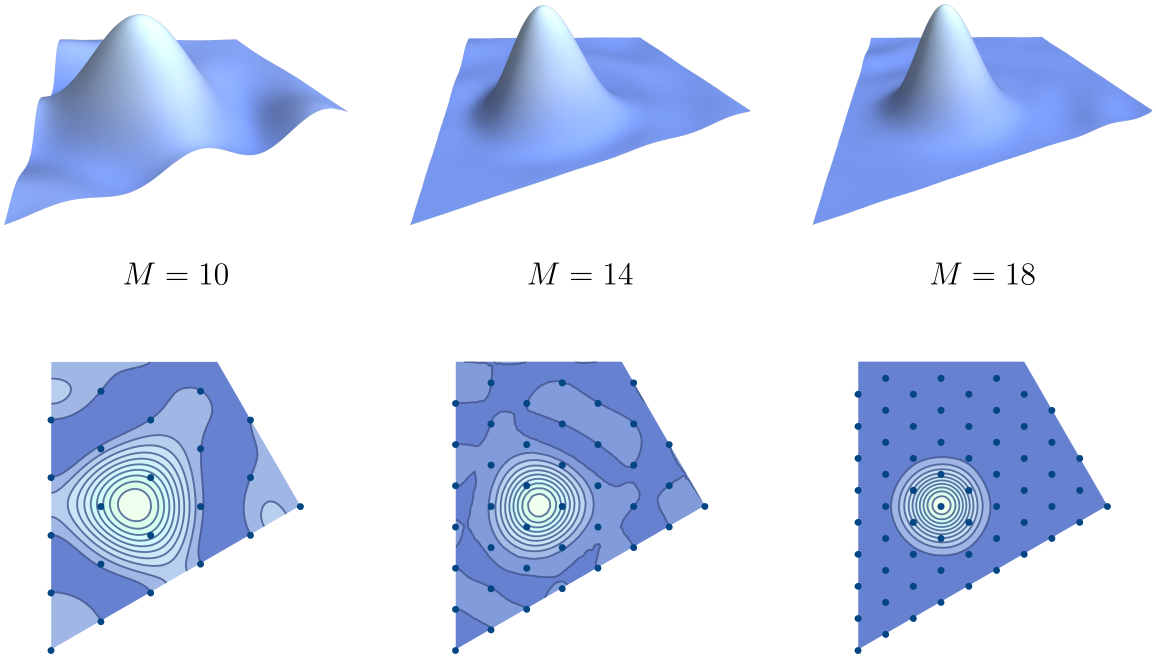
$M = 10$ $M = 14$ $M = 18$

Fig. 2.5. The interpolating functions $\mathrm{I}[f]_M^{(1)}$ are for $M = 10{,}14{,}18$ plotted over the region F_P. The sampling point sets $F_M^{(1)}$ of the interpolation are marked by the blue dots.

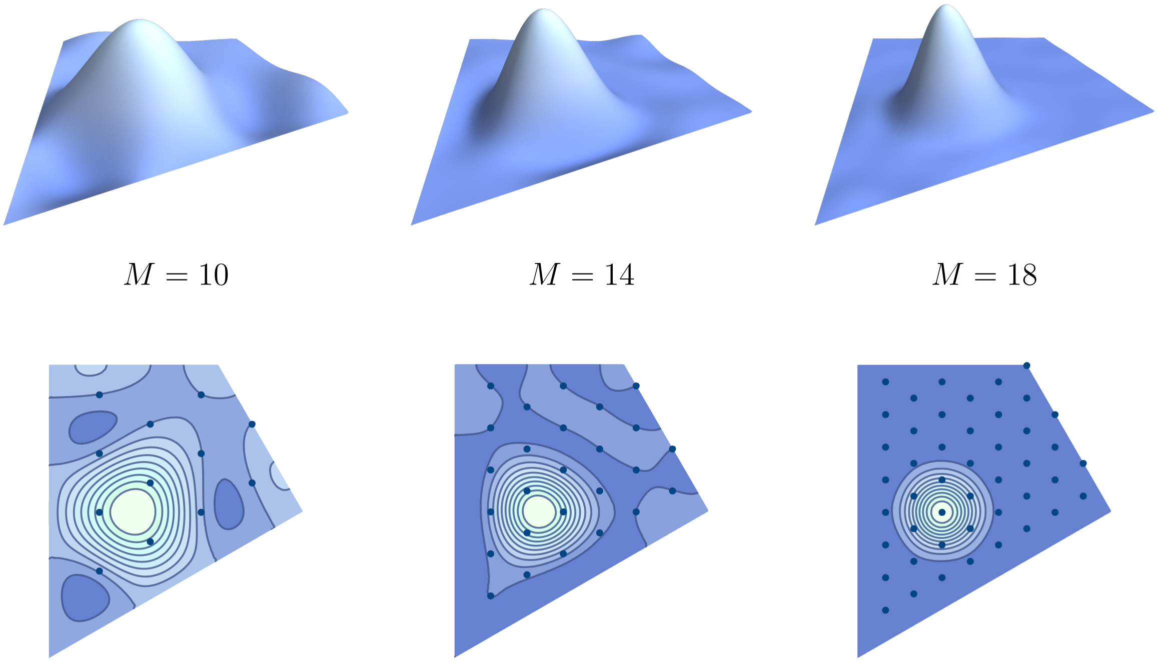
$M = 10$ $M = 14$ $M = 18$

Fig. 2.6. The interpolating functions $\widetilde{\mathrm{I}}[f]_M^{(0)}$ are for $M = 10{,}14{,}18$ plotted over the region F_P. The sampling point sets $\widetilde{F}_M^{(0)}$ of the interpolation are marked by the blue dots.

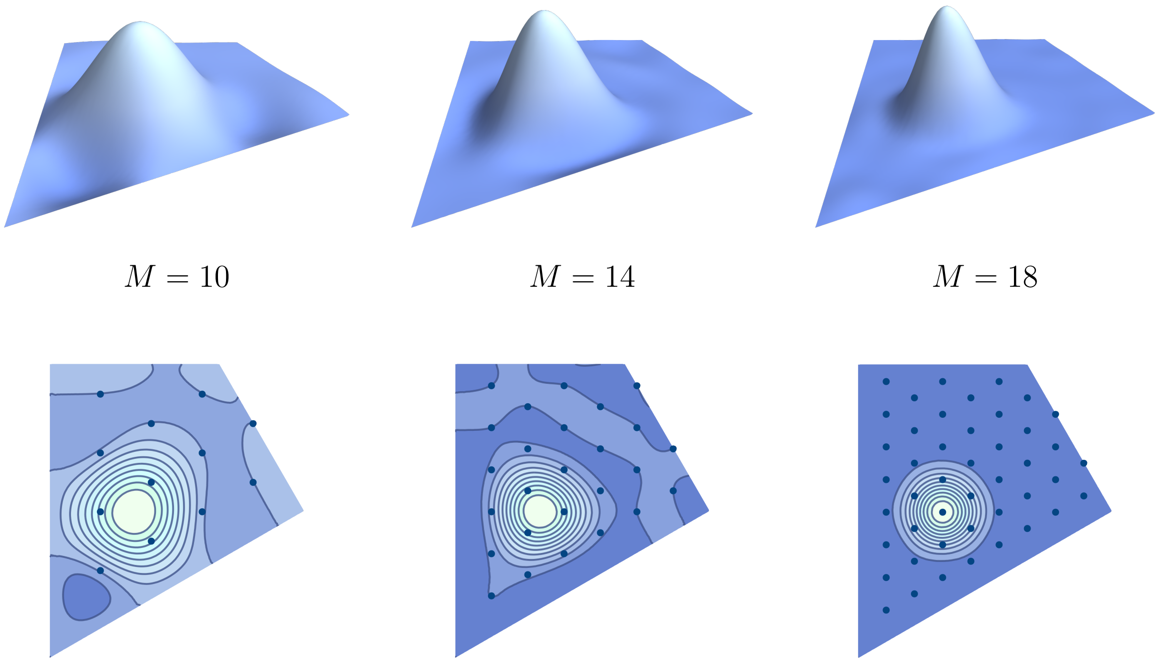

$M = 10$ $M = 14$ $M = 18$

Fig. 2.7. The interpolating functions $\widetilde{\mathrm{I}}[f]_M^{(1)}$ are for $M = 10{,}14{,}18$ plotted over the region F_P. The sampling point sets $\widetilde{F}_M^{(1)}$ of the interpolation are marked by the blue dots.

Table 2.1. The integral error estimates of the interpolations $\mathrm{I}[f]_M^{(0)}$, $\mathrm{I}[f]_M^{(1)}$, $\widetilde{\mathrm{I}}[f]_M^{(0)}$ and $\widetilde{\mathrm{I}}[f]_M^{(1)}$ are tabulated for $M = 10$, 12, 14, 16 and 18.

M	10	12	14	16	18
$\int_{F_P} \left\lvert f - \mathrm{I}[f]_M^{(0)} \right\rvert^2$	1377×10^{-7}	373×10^{-7}	123×10^{-7}	39×10^{-7}	4×10^{-7}
$\int_{F_P} \left\lvert f - \mathrm{I}[f]_M^{(1)} \right\rvert^2$	1530×10^{-7}	649×10^{-7}	117×10^{-7}	52×10^{-7}	9×10^{-7}
$\int_{F_P} \left\lvert f - \widetilde{\mathrm{I}}[f]_M^{(0)} \right\rvert^2$	1814×10^{-7}	763×10^{-7}	266×10^{-7}	69×10^{-7}	9×10^{-7}
$\int_{F_P} \left\lvert f - \widetilde{\mathrm{I}}[f]_M^{(1)} \right\rvert^2$	1520×10^{-7}	753×10^{-7}	255×10^{-7}	48×10^{-7}	9×10^{-7}

2.4. Central splitting

2.4.1. Central splitting of discrete transforms

The center of the compact simple Lie group $SU(3)$, associated with the root system A_2, is isomorphic to both groups Γ and P/Q. The central splitting of a function $f : F_Q \to \mathbb{C}$ represents the functional decomposition (Moody and Patera [**105**]) of the form

$$f = f_0 + f_1 + f_2, \tag{2.4.1}$$

where each component $f_k : F_Q \to \mathbb{C}$, $k \in \{0,1,2\}$ is determined by

$$f_k(x) = \frac{1}{3}\sum_{j=0}^{2} e^{-2\pi \mathrm{i}\langle z_k,\, z_j\rangle} f(\gamma_j x). \tag{2.4.2}$$

The current defining formula of the central splitting (2.4.2) is a specialization of relation (Moody and Patera [**105**], Equation 27) with incorporated action of the $\Gamma-$group elements from relations (2.2.41) and (2.2.42). The exponential coefficients $e^{-2\pi \mathrm{i}\langle z_k,\, z_j\rangle}$, $j,k \in \{0,1,2\}$ are calculated from relation (2.2.6) as elements of the group of the third roots of unity U_3,

$$U_3 = \{1, e^{\frac{2\pi \mathrm{i}}{3}}, e^{\frac{-2\pi \mathrm{i}}{3}}\}. \tag{2.4.3}$$

Direct calculations from defining relation (2.4.2) of the central splitting yields the following symmetry property of the component functions under the action of the $\Gamma-$group for $j \in \{0,1,2\}$ and $x \in \mathbb{R}^2$,

$$f_k(\gamma_j x) = e^{2\pi \mathrm{i}\langle z_k,\, z_j\rangle} f_k(x).$$

Based on the decomposition of the central components into the sum of orbit functions labeled by the weights from the corresponding congruence class from (Moody and Patera [**105**], Section 7), the central splitting is utilized to decompose the weight lattice Fourier–Weyl transform into the smaller splitting transforms.

Theorem 7 (Central Splitting of Weight Lattice Transforms)**.** *The spectral coefficients* $c_\lambda[f]_M$*,* $\lambda \in \Lambda_M^{(k)}$*,* $k \in \{0,1,2\}$ *of the weight lattice Fourier–Weyl* $C-$*transforms* (2.3.31)*, corresponding to the function* $f : F_M \to \mathbb{C}$*, coincide with the spectral coefficients of the splitting Fourier–Weyl* $C-$*transforms* (2.3.37) *of the central components* $f_k : F_M^{(k)} \to \mathbb{C}$*,*

$$c_\lambda[f]_M = c_\lambda[f_k]_M^{(k)}, \quad \lambda \in \Lambda_M^{(k)}. \tag{2.4.4}$$

The spectral coefficients $\widetilde{c}_\lambda[f]_M$*,* $\lambda \in \widetilde{\Lambda}_M^{(k)}$ *of the weight lattice Fourier–Weyl* $S-$*transforms* (2.3.32)*, corresponding to the function* $f : \widetilde{F}_M \to \mathbb{C}$*, coincide with the spectral coefficients of the splitting Fourier–Weyl* $S-$*transforms* (2.3.38) *of the central components* $f_k : \widetilde{F}_M^{(k)} \to \mathbb{C}$*,*

$$\widetilde{c}_\lambda[f]_M = \widetilde{c}_\lambda[f_k]_M^{(k)}, \quad \lambda \in \widetilde{\Lambda}_M^{(k)}. \tag{2.4.5}$$

Proof. The weight lattice Fourier–Weyl $C-$transform of the discretized function $f : F_M \to \mathbb{C}$ provides from relations (2.3.27) and (2.3.29) the following expansion,

$$f(s) = \sum_{\lambda \in \Lambda_M} c_\lambda[f]_M \Phi_\lambda(s), \quad s \in F_M. \tag{2.4.6}$$

The splitting Fourier–Weyl $C-$transform of the discretized central component $f_k : F_M^{(k)} \to \mathbb{C}$ provides from relations (2.3.33) and (2.3.35) the following expansion,

$$f_k(s) = \sum_{\lambda \in \Lambda_M^{(k)}} c_\lambda[f_k]_M^{(k)} \Phi_\lambda(s), \quad s \in F_M^{(k)}. \tag{2.4.7}$$

Substituting into the defining relation of the central splitting (2.4.2) the expansion (2.4.6) and taking into account the symmetry property (2.3.9) and the disjoint decomposition (2.2.23) yield for $s \in F_M^{(k)}$ that

$$\begin{aligned} f_k(s) &= \frac{1}{3}\sum_{j=0}^{2} e^{-2\pi \mathrm{i}\langle z_k,\, z_j\rangle} f(\gamma_j s) = \frac{1}{3}\sum_{j=0}^{2} e^{-2\pi \mathrm{i}\langle z_k,\, z_j\rangle} \sum_{\lambda\in\Lambda_M} c_\lambda[f]_M \Phi_\lambda(\gamma_j s) \\ &= \frac{1}{3}\sum_{j,l=0}^{2} e^{2\pi \mathrm{i}\langle z_l - z_k,\, z_j\rangle} \sum_{\lambda\in\Lambda_M^{(l)}} c_\lambda[f]_M \Phi_\lambda(s). \end{aligned} \tag{2.4.8}$$

Recall from (Hrivnák and Patera [**63**], Corollary 5.2) that for the classes of weights $\lambda = z_l + Q$, $\lambda' = z_k + Q$, $k, l \in \{0,1,2\}$ of the root system A_2, the orthogonality relations of the multivariate exponential functions are specialized to the form

$$\sum_{j=0}^{2} e^{2\pi \mathrm{i}\langle z_l - z_k,\, z_j\rangle} = 3\,\delta_{kl}. \tag{2.4.9}$$

Using the orthogonality relation of the multivariate exponential functions (2.4.9) in expression (2.4.8) provides the final form of the expansion of the discretized central component,

$$f_k(s) = \sum_{\lambda \in \Lambda_M^{(k)}} c_\lambda[f]_M \Phi_\lambda(s), \quad s \in F_M^{(k)}. \tag{2.4.10}$$

Comparing the resulting expression (2.4.10) to the original expansion of the central component (2.4.7) provides the statement (2.4.4). Since, for A_2, the crucial symmetry property of the $S-$functions (2.3.10) under the action of the $\Gamma-$group is of the same form as its $C-$functions counterpart, the version of the statement (2.4.5) is obtained similarly for $S-$functions via the comparison of the discrete transforms (2.3.28), (2.3.30) and (2.3.34), (2.3.36), together with the disjoint decomposition (2.2.25). $\square$

2.4.2. Decompositions of unitary transform matrices

The Fourier–Weyl transforms on a discrete set of points F_M are carried out by predetermined square matrices that multiply any given column-vector of data (Bodner *et al.* [**16**]). The currently constructed unitary transform matrices correspond to the normalized versions of the weight lattice Fourier–Weyl transforms. Any arbitrary fixed orderings of the weight sets $\Lambda_M^{(k)}$ and $\widetilde{\Lambda}_M^{(k)}$, $k \in \{0,1,2\}$ induce uniquely from the decompositions (2.2.23) and (2.2.25) the orderings of the weight sets Λ_M and $\widetilde{\Lambda}_M$. The fixed orderings of the splitting point sets $F_M^{(k)}$ and $\widetilde{F}_M^{(k)}$, $k \in \{0,1,2\}$ can be chosen independently on the ordering of the point sets F_M and $\widetilde{F}_M$.

Using formulas for the spectrum coefficients (2.3.31) and (2.3.32), the unitary matrices $\mathbb{I}_M$ and $\widetilde{\mathbb{I}}_M$ of the normalized weight lattice Fourier–Weyl $C-$ and $S-$transforms are given by their entries as follows,

$$(\mathbb{I}_M)_{\lambda s} = \sqrt{\frac{\varepsilon(s)}{18M^2 h_M(\lambda)}}\,\overline{\Phi_\lambda(s)}, \quad \lambda \in \Lambda_M, s \in F_M, \tag{2.4.11}$$

$$\left(\widetilde{\mathbb{I}}_M\right)_{\lambda s} = \frac{1}{\sqrt{3M^2}}\,\overline{\varphi_\lambda(s)}, \quad \lambda \in \widetilde{\Lambda}_M, s \in \widetilde{F}_M. \tag{2.4.12}$$

The unitary matrices $\mathbb{I}_M^{(k)}$ and $\widetilde{\mathbb{I}}_M^{(k)}$, $k \in \{0,1,2\}$ of the normalized splitting Fourier–Weyl $C-$ and $S-$transforms are constructed using the Formulas (2.3.37) and (2.3.38),

$$\left(\mathbb{I}_M^{(k)}\right)_{\lambda s} = \sqrt{\frac{\varepsilon(s)}{6M^2 d(s) h_M(\lambda)}}\,\overline{\Phi_\lambda(s)}, \quad \lambda \in \Lambda_M^{(k)}, s \in F_M^{(k)}, \tag{2.4.13}$$

$$\left(\widetilde{\mathbb{I}}_M^{(k)}\right)_{\lambda s} = \frac{1}{\sqrt{M^2 d(s)}}\,\overline{\varphi_\lambda(s)}, \quad \lambda \in \widetilde{\Lambda}_M^{(k)}, s \in \widetilde{F}_M^{(k)}. \tag{2.4.14}$$

The unitary transform matrices $\mathbb{T}_M$ and $\widetilde{\mathbb{T}}_M$, that realize the normalized central splitting (2.4.1), are represented by the following block matrices

$$\mathbb{T}_M = \begin{pmatrix} \mathbb{T}_M^{(0)} \\ \mathbb{T}_M^{(1)} \\ \mathbb{T}_M^{(2)} \end{pmatrix}, \quad \widetilde{\mathbb{T}}_M = \begin{pmatrix} \widetilde{\mathbb{T}}_M^{(0)} \\ \widetilde{\mathbb{T}}_M^{(1)} \\ \widetilde{\mathbb{T}}_M^{(2)} \end{pmatrix}, \tag{2.4.15}$$

where the block components $\mathbb{T}_M^{(k)}$ and $\widetilde{\mathbb{T}}_M^{(k)}$, $k \in \{0,1,2\}$ are determined by their entries as

$$\left(\mathbb{T}_M^{(k)}\right)_{ss'} = \frac{1}{3}\sqrt{\frac{3}{d(s)}} \sum_{j=0}^{2} e^{-2\pi \mathrm{i} \langle z_j, z_k \rangle} \delta_{\gamma_j s, s'}, \quad s \in F_M^{(k)}, s' \in F_M, \tag{2.4.16}$$

$$\left(\widetilde{\mathbb{T}}_M^{(k)}\right)_{ss'} = \frac{1}{3}\sqrt{\frac{3}{d(s)}} \sum_{j=0}^{2} e^{-2\pi \mathrm{i} \langle z_j, z_k \rangle} \delta_{\gamma_j s, s'}, \quad s \in \widetilde{F}_M^{(k)}, s' \in \widetilde{F}_M. \tag{2.4.17}$$

The unitary transform matrices of the normalized weight lattice Fourier–Weyl transforms are decomposed into the normalized central splitting matrices and splitting transform matrices in the following theorem.

Theorem 8 (Decompositions of Transform Matrices)**.** *The following matrix equalities hold for any $M \in \mathbb{N}$,*

$$\mathbb{I}_M = \left(\mathbb{I}_M^{(0)} \oplus \mathbb{I}_M^{(1)} \oplus \mathbb{I}_M^{(2)}\right) \mathbb{T}_M, \tag{2.4.18}$$

$$\widetilde{\mathbb{I}}_M = \left(\widetilde{\mathbb{I}}_M^{(0)} \oplus \widetilde{\mathbb{I}}_M^{(1)} \oplus \widetilde{\mathbb{I}}_M^{(2)}\right) \widetilde{\mathbb{T}}_M. \tag{2.4.19}$$

Proof. Performing the multiplication of the block matrices in statement (2.4.18) provides the matrix block form

$$\mathbb{I}_M = \begin{pmatrix} \mathbb{I}_M^{(0)} \mathbb{T}_M^{(0)} \\ \mathbb{I}_M^{(1)} \mathbb{T}_M^{(1)} \\ \mathbb{I}_M^{(2)} \mathbb{T}_M^{(2)} \end{pmatrix}. \tag{2.4.20}$$

Since the ordering of the weights labeling the rows of $\mathbb{I}_M$ is induced by the decomposition (2.2.23), the matrix equality (2.4.20) is reformulated via the corresponding entries for $k \in \{0,1,2\}$ as

$$(\mathbb{I}_M)_{\lambda s'} = \sum_{s \in F_M^{(k)}} \left(\mathbb{I}_M^{(k)}\right)_{\lambda s} \left(\mathbb{T}_M^{(k)}\right)_{ss'}, \quad \lambda \in \Lambda_M^{(k)}, s' \in F_M. \tag{2.4.21}$$

Direct calculations from defining relation (2.4.16), symmetry property (2.3.9) and $\varepsilon-$function $\Gamma-$invariance lead to the invariance of the following products for $\gamma_l \in \Gamma$, $l \in \{0,1,2\}$,

$$\sqrt{\varepsilon(\gamma_l s)}\,\overline{\Phi_\lambda(\gamma_l s)} \sum_{j=0}^{2} e^{-2\pi \mathrm{i} \langle z_j, z_k \rangle} \delta_{\gamma_j \gamma_l s, s'} = \sqrt{\varepsilon(s)}\,\overline{\Phi_\lambda(s)} \sum_{j=0}^{2} e^{-2\pi \mathrm{i} \langle z_j, z_k \rangle} \delta_{\gamma_j s, s'}. \tag{2.4.22}$$

Taking into account the $\Gamma-$invariance from expression (2.4.22) provides the following simplification of the matrix multiplication (2.4.21) for $\lambda \in \Lambda_M^{(k)}$ and $s' \in F_M$,

$$\begin{aligned} \sum_{s \in F_M^{(k)}} \left(\mathbb{I}_M^{(k)}\right)_{\lambda s} \left(\mathbb{T}_M^{(k)}\right)_{ss'} &= \sum_{s \in F_M^{(k)}} 3d^{-1}(s) \sqrt{\frac{\varepsilon(s)}{162 M^2 h_M(\lambda)}}\,\overline{\Phi_\lambda(s)} \sum_{j=0}^{2} e^{-2\pi \mathrm{i} \langle z_j, z_k \rangle} \delta_{\gamma_j s, s'} \\ &= \sum_{s \in F_M} \sqrt{\frac{\varepsilon(s)}{162 M^2 h_M(\lambda)}}\,\overline{\Phi_\lambda(s)} \sum_{j=0}^{2} e^{-2\pi \mathrm{i} \langle z_j, z_k \rangle} \delta_{\gamma_j s, s'}. \end{aligned} \tag{2.4.23}$$

Employing again the symmetry property (2.3.9) together with $\Gamma-$invariance of both $\varepsilon-$function and point set F_M yields from relation (2.4.23) the desired result,

$$\begin{aligned} \sum_{s \in F_M^{(k)}} \left(\mathbb{I}_M^{(k)}\right)_{\lambda s} \left(\mathbb{T}_M^{(k)}\right)_{ss'} &= \left(162 M^2 h_M(\lambda)\right)^{-\frac{1}{2}} \sum_{j=0}^{2} \sqrt{\varepsilon\left(\gamma_j^{-1} s'\right)}\,\overline{\Phi_\lambda\left(\gamma_j^{-1} s'\right)} e^{-2\pi \mathrm{i} \langle z_j, z_k \rangle} \\ &= \sqrt{\frac{\varepsilon(s')}{18 M^2 h_M(\lambda)}}\,\overline{\Phi_\lambda(s')} = (\mathbb{I}_M)_{\lambda s'}. \end{aligned}$$

The symmetry property of the $S-$functions (2.3.10) allows to obtain the $S-$transform matrix relation (2.4.19) by performing analogous steps. □

2.4.3. Decompositions of transform matrices $\mathbb{I}_3$ and $\widetilde{\mathbb{I}}_6$

The weights of the splitting weight sets $\Lambda_3^{(k)}$, $k \in \{0,1,2\}$ are calculated from expression (2.2.27) and ordered as

$$\begin{aligned} \Lambda_3^{(0)} &= \{[3,0,0],[1,1,1],[0,3,0],[0,0,3]\}, \\ \Lambda_3^{(1)} &= \{[2,1,0],[1,0,2],[0,2,1]\}, \\ \Lambda_3^{(2)} &= \{[2,0,1],[1,2,0],[0,1,2]\}. \end{aligned} \tag{2.4.24}$$

The ordering of the entire weight set Λ_3 is induced by the decomposition (2.2.23),

$$\Lambda_3 = \Lambda_3^{(0)} \cup \Lambda_3^{(1)} \cup \Lambda_3^{(2)},$$

where the weights of each splitting weight set are ordered as in the lists of weights (2.4.24). The points of the point set F_3 are calculated in Kac coordinates from relation (2.2.48), and ordered as follows,

$$F_3 = \{[3,0,0],[2,1,0],[2,0,1],[1,2,0],[1,1,1],[1,0,2],[0,3,0],[0,2,1],[0,1,2],[0,0,3]\}\,.$$

The unitary transform matrix $\mathbb{I}_3$ comprises rows indexed by the ordered weight set Λ_3 and columns indexed by the point set F_3. Utilizing the $C-$function formula (2.3.5), $h-$ and $\varepsilon-$function expressions (2.2.39) and (2.2.65), the transform matrix $\mathbb{I}_3$ is calculated from definition (2.4.11) as

$$\mathbb{I}_3 = \begin{pmatrix}
\frac{1}{3\sqrt{3}} & \frac{1}{3} & \frac{1}{3} & \frac{1}{3} & \frac{\sqrt{2}}{3} & \frac{1}{3} & \frac{1}{3\sqrt{3}} & \frac{1}{3} & \frac{1}{3} & \frac{1}{3\sqrt{3}} \\
\frac{\sqrt{2}}{3} & 0 & 0 & 0 & -\frac{1}{\sqrt{3}} & 0 & \frac{\sqrt{2}}{3} & 0 & 0 & \frac{\sqrt{2}}{3} \\
\frac{1}{3\sqrt{3}} & \frac{1}{3}e^{\frac{2\pi \mathrm{i}}{3}} & \frac{1}{3}e^{-\frac{2\pi \mathrm{i}}{3}} & \frac{1}{3}e^{-\frac{2\mathrm{i}\pi}{3}} & \frac{\sqrt{2}}{3} & \frac{1}{3}e^{\frac{2\pi \mathrm{i}}{3}} & \frac{1}{3\sqrt{3}} & \frac{1}{3}e^{\frac{2\pi \mathrm{i}}{3}} & \frac{1}{3}e^{-\frac{2\pi \mathrm{i}}{3}} & \frac{1}{3\sqrt{3}} \\
\frac{1}{3\sqrt{3}} & \frac{1}{3}e^{-\frac{2\pi \mathrm{i}}{3}} & \frac{1}{3}e^{\frac{2\pi \mathrm{i}}{3}} & \frac{1}{3}e^{\frac{2\mathrm{i}\pi}{3}} & \frac{\sqrt{2}}{3} & \frac{1}{3}e^{-\frac{2\pi \mathrm{i}}{3}} & \frac{1}{3\sqrt{3}} & \frac{1}{3}e^{-\frac{2\mathrm{i}\pi}{3}} & \frac{1}{3}e^{\frac{2\pi \mathrm{i}}{3}} & \frac{1}{3\sqrt{3}} \\
\frac{1}{3} & \frac{e^{\frac{2\pi \mathrm{i}}{9}}b}{6\sqrt{3}} & \frac{e^{-\frac{2\pi \mathrm{i}}{9}}a}{6\sqrt{3}} & \frac{e^{\frac{4\mathrm{i}\pi}{9}}a}{6\sqrt{3}} & 0 & \frac{e^{-\frac{4\pi \mathrm{i}}{9}}b}{6\sqrt{3}} & \frac{1}{3}e^{\frac{2\pi \mathrm{i}}{3}} & \frac{1}{3}\mathrm{i}e^{\frac{2\pi \mathrm{i}}{9}} & -\frac{1}{3}\mathrm{i}e^{-\frac{2\pi \mathrm{i}}{9}} & \frac{1}{3}e^{-\frac{2\pi \mathrm{i}}{3}} \\
\frac{1}{3} & \frac{e^{-\frac{4\pi \mathrm{i}}{9}}b}{6\sqrt{3}} & \frac{e^{\frac{4\pi \mathrm{i}}{9}}a}{6\sqrt{3}} & -\frac{1}{3}\mathrm{i}e^{-\frac{2\pi \mathrm{i}}{9}} & 0 & \frac{1}{3}\mathrm{i}e^{\frac{2\pi \mathrm{i}}{9}} & \frac{1}{3}e^{\frac{2\pi \mathrm{i}}{3}} & \frac{e^{\frac{2\mathrm{i}\pi}{9}}b}{6\sqrt{3}} & \frac{e^{-\frac{2\pi \mathrm{i}}{9}}a}{6\sqrt{3}} & \frac{1}{3}e^{-\frac{2\pi \mathrm{i}}{3}} \\
\frac{1}{3} & \frac{1}{3}\mathrm{i}e^{\frac{2\pi \mathrm{i}}{9}} & -\frac{1}{3}\mathrm{i}e^{-\frac{2\pi \mathrm{i}}{9}} & \frac{e^{-\frac{2\pi \mathrm{i}}{9}}a}{6\sqrt{3}} & 0 & \frac{e^{\frac{2\pi \mathrm{i}}{9}}b}{6\sqrt{3}} & \frac{1}{3}e^{\frac{2\pi \mathrm{i}}{3}} & \frac{e^{-\frac{4\mathrm{i}\pi}{9}}b}{6\sqrt{3}} & \frac{e^{\frac{4\pi \mathrm{i}}{9}}a}{6\sqrt{3}} & \frac{1}{3}e^{-\frac{2\pi \mathrm{i}}{3}} \\
\frac{1}{3} & \frac{e^{-\frac{2\pi \mathrm{i}}{9}}a}{6\sqrt{3}} & \frac{e^{\frac{2\pi \mathrm{i}}{9}}b}{6\sqrt{3}} & \frac{e^{-\frac{4\mathrm{i}\pi}{9}}b}{6\sqrt{3}} & 0 & \frac{e^{\frac{4\pi \mathrm{i}}{9}}a}{6\sqrt{3}} & \frac{1}{3}e^{-\frac{2\pi \mathrm{i}}{3}} & -\frac{1}{3}\mathrm{i}e^{-\frac{2\pi \mathrm{i}}{9}} & \frac{1}{3}\mathrm{i}e^{\frac{2\pi \mathrm{i}}{9}} & \frac{1}{3}e^{\frac{2\pi \mathrm{i}}{3}} \\
\frac{1}{3} & \frac{e^{\frac{4\pi \mathrm{i}}{9}}a}{6\sqrt{3}} & \frac{e^{-\frac{4\pi \mathrm{i}}{9}}b}{6\sqrt{3}} & \frac{1}{3}\mathrm{i}e^{\frac{2\pi \mathrm{i}}{9}} & 0 & -\frac{1}{3}\mathrm{i}e^{-\frac{2\pi \mathrm{i}}{9}} & \frac{1}{3}e^{-\frac{2\pi \mathrm{i}}{3}} & \frac{e^{-\frac{2\pi \mathrm{i}}{9}}a}{6\sqrt{3}} & \frac{e^{\frac{2\pi \mathrm{i}}{9}}b}{6\sqrt{3}} & \frac{1}{3}e^{\frac{2\pi \mathrm{i}}{3}} \\
\frac{1}{3} & -\frac{1}{3}\mathrm{i}e^{-\frac{2\pi \mathrm{i}}{9}} & \frac{1}{3}\mathrm{i}e^{\frac{2\pi \mathrm{i}}{9}} & \frac{e^{\frac{2\pi \mathrm{i}}{9}}b}{6\sqrt{3}} & 0 & \frac{e^{-\frac{2\pi \mathrm{i}}{9}}a}{6\sqrt{3}} & \frac{1}{3}e^{-\frac{2\pi \mathrm{i}}{3}} & \frac{e^{\frac{4\mathrm{i}\pi}{9}}a}{6\sqrt{3}} & \frac{e^{-\frac{4\pi \mathrm{i}}{9}}b}{6\sqrt{3}} & \frac{1}{3}e^{\frac{2\pi \mathrm{i}}{3}}
\end{pmatrix},$$

where $a = 3 + \sqrt{3}\mathrm{i}$ and $b = 3 - \sqrt{3}\mathrm{i}$.

Each unitary splitting matrix $\mathbb{I}_3^{(k)}$, $k \in \{0,1,2\}$ contains rows indexed by the corresponding weight set in (2.4.24) and columns indexed by the point sets $F_3^{(k)}$ obtained from expression (2.2.57) as

$$\begin{aligned} F_3^{(0)} &= \{[3,0,0],[2,1,0],[2,0,1],[1,1,1]\},\\ F_3^{(1)} = F_3^{(2)} &= \{[3,0,0],[2,1,0],[2,0,1]\}. \end{aligned}$$

Utilizing the $d-$function values from (2.2.67), the splitting transform matrices $\mathbb{I}_3^{(0)}$, $\mathbb{I}_3^{(1)}$ and $\mathbb{I}_3^{(2)}$ are calculated from definition (2.4.13) as

$$\mathbb{I}_3^{(0)} = \begin{pmatrix} \frac{1}{3} & \frac{1}{\sqrt{3}} & \frac{1}{\sqrt{3}} & \frac{\sqrt{2}}{3} \\ \sqrt{\frac{2}{3}} & 0 & 0 & -\frac{1}{\sqrt{3}} \\ \frac{1}{3} & \frac{e^{\frac{2\pi \mathrm{i}}{3}}}{\sqrt{3}} & \frac{e^{-\frac{2\pi \mathrm{i}}{3}}}{\sqrt{3}} & \frac{\sqrt{2}}{3} \\ \frac{1}{3} & \frac{e^{-\frac{2\pi \mathrm{i}}{3}}}{\sqrt{3}} & \frac{e^{\frac{2\pi \mathrm{i}}{3}}}{\sqrt{3}} & \frac{\sqrt{2}}{3} \end{pmatrix},$$

$$\mathbb{I}_3^{(1)} = \begin{pmatrix} \frac{1}{\sqrt{3}} & \frac{\mathrm{i}e^{\frac{2\pi \mathrm{i}}{9}}}{\sqrt{3}} & -\frac{\mathrm{i}e^{-\frac{2\pi \mathrm{i}}{9}}}{\sqrt{3}} \\ \frac{1}{\sqrt{3}} & \frac{1}{6}be^{-\frac{4\pi \mathrm{i}}{9}} & \frac{1}{6}ae^{\frac{4\pi \mathrm{i}}{9}} \\ \frac{1}{\sqrt{3}} & \frac{\mathrm{i}e^{\frac{2\pi \mathrm{i}}{9}}}{\sqrt{3}} & -\frac{\mathrm{i}e^{-\frac{2\pi \mathrm{i}}{9}}}{\sqrt{3}} \end{pmatrix},$$

$$\mathbb{I}_3^{(2)} = \begin{pmatrix} \frac{1}{\sqrt{3}} & \frac{1}{6}ae^{-\frac{2\pi \mathrm{i}}{9}} & \frac{1}{6}be^{\frac{2\pi \mathrm{i}}{9}} \\ \frac{1}{\sqrt{3}} & \frac{1}{6}ae^{\frac{4\pi \mathrm{i}}{9}} & \frac{1}{6}be^{-\frac{4\pi \mathrm{i}}{9}} \\ \frac{1}{\sqrt{3}} & -\frac{\mathrm{i}e^{-\frac{2\pi \mathrm{i}}{9}}}{\sqrt{3}} & \frac{\mathrm{i}e^{\frac{2\pi \mathrm{i}}{9}}}{\sqrt{3}} \end{pmatrix}.$$

The rows of the unitary central splitting matrix $\mathbb{T}_3$ are labeled by the union of the splitting point sets $F_3^{(0)} \cup F_3^{(1)} \cup F_3^{(2)}$, and the columns are labeled by the elements of the point set F_3. Thus, the transform matrix $\mathbb{T}_3$ is calculated from definitions (2.4.15) and (2.4.16) as

$$\mathbb{T}_3 = \begin{pmatrix} \frac{\sqrt{3}}{3} & 0 & 0 & 0 & 0 & 0 & \frac{\sqrt{3}}{3} & 0 & 0 & \frac{\sqrt{3}}{3} \\ 0 & \frac{\sqrt{3}}{3} & 0 & 0 & 0 & \frac{\sqrt{3}}{3} & 0 & \frac{\sqrt{3}}{3} & 0 & 0 \\ 0 & 0 & \frac{\sqrt{3}}{3} & \frac{\sqrt{3}}{3} & 0 & 0 & 0 & 0 & \frac{\sqrt{3}}{3} & 0 \\ 0 & 0 & 0 & 0 & 1 & 0 & 0 & 0 & 0 & 0 \\ \frac{\sqrt{3}}{3} & 0 & 0 & 0 & 0 & 0 & \frac{\sqrt{3}}{3}e^{\frac{2\pi \mathrm{i}}{3}} & 0 & 0 & \frac{\sqrt{3}}{3}e^{-\frac{2\pi \mathrm{i}}{3}} \\ 0 & \frac{\sqrt{3}}{3} & 0 & 0 & 0 & \frac{\sqrt{3}}{3}e^{-\frac{2\pi \mathrm{i}}{3}} & 0 & \frac{\sqrt{3}}{3}e^{\frac{2\pi \mathrm{i}}{3}} & 0 & 0 \\ 0 & 0 & \frac{\sqrt{3}}{3} & \frac{\sqrt{3}}{3}e^{\frac{2\pi \mathrm{i}}{3}} & 0 & 0 & 0 & 0 & \frac{\sqrt{3}}{3}e^{-\frac{2\pi \mathrm{i}}{3}} & 0 \\ \frac{\sqrt{3}}{3} & 0 & 0 & 0 & 0 & 0 & \frac{\sqrt{3}}{3}e^{-\frac{2\pi \mathrm{i}}{3}} & 0 & 0 & \frac{\sqrt{3}}{3}e^{\frac{2\pi \mathrm{i}}{3}} \\ 0 & \frac{\sqrt{3}}{3} & 0 & 0 & 0 & \frac{\sqrt{3}}{3}e^{\frac{2\pi \mathrm{i}}{3}} & 0 & \frac{\sqrt{3}}{3}e^{-\frac{2\pi \mathrm{i}}{3}} & 0 & 0 \\ 0 & 0 & \frac{\sqrt{3}}{3} & \frac{\sqrt{3}}{3}e^{-\frac{2\pi \mathrm{i}}{3}} & 0 & 0 & 0 & 0 & \frac{\sqrt{3}}{3}e^{\frac{2\pi \mathrm{i}}{3}} & 0 \end{pmatrix}. \tag{2.4.25}$$

The weights of the splitting weight sets $\widetilde{\Lambda}_6^{(k)}$, $k \in \{0,1,2\}$ are calculated from expression (2.2.28) and ordered as

$$\begin{aligned} \widetilde{\Lambda}_6^{(0)} &= \{[4,1,1],[2,2,2],[1,4,1],[1,1,4]\},\\ \widetilde{\Lambda}_6^{(1)} &= \{[3,2,1],[2,1,3],[1,3,2]\},\\ \widetilde{\Lambda}_6^{(2)} &= \{[3,1,2],[2,3,1],[1,2,3]\}. \end{aligned} \tag{2.4.26}$$

The ordering of the entire weight set $\widetilde{\Lambda}_6$ is induced by the decomposition (2.2.25),

$$\widetilde{\Lambda}_6 = \widetilde{\Lambda}_6^{(0)} \cup \widetilde{\Lambda}_6^{(1)} \cup \widetilde{\Lambda}_6^{(2)},$$

where the weights of each splitting weight set are ordered as in the sets of weights (2.4.26).

The points of the point set $\widetilde{F}_6$ are calculated in Kac coordinates from relation (2.2.49) and ordered as follows,

$$\widetilde{F}_6 = \{[4,1,1],[3,2,1],[3,1,2],[2,3,1],[2,2,2],[2,1,3],[1,4,1],[1,3,2],[1,2,3],[1,1,4]\}.$$

Utilizing the $S-$function formula (2.3.6), the transform matrix $\widetilde{\mathbb{I}}_6$ is calculated from definition (2.4.12) as

$$\widetilde{\mathbb{I}}_6 = \begin{pmatrix}
\frac{\mathrm{i}}{6} & \frac{\mathrm{i}}{3} & \frac{\mathrm{i}}{3} & \frac{\mathrm{i}}{3} & \frac{\mathrm{i}}{2} & \frac{\mathrm{i}}{3} & \frac{\mathrm{i}}{6} & \frac{\mathrm{i}}{3} & \frac{\mathrm{i}}{3} & \frac{\mathrm{i}}{6} \\
\frac{\mathrm{i}}{2} & 0 & 0 & 0 & -\frac{\mathrm{i}}{2} & 0 & \frac{\mathrm{i}}{2} & 0 & 0 & \frac{\mathrm{i}}{2} \\
\frac{\mathrm{i}}{6} & -\frac{b}{6\sqrt{3}} & \frac{b}{6\sqrt{3}} & \frac{b}{6\sqrt{3}} & \frac{\mathrm{i}}{2} & -\frac{b}{6\sqrt{3}} & \frac{\mathrm{i}}{6} & -\frac{b}{6\sqrt{3}} & \frac{b}{6\sqrt{3}} & \frac{\mathrm{i}}{6} \\
\frac{\mathrm{i}}{6} & \frac{b}{6\sqrt{3}} & -\frac{b}{6\sqrt{3}} & -\frac{b}{6\sqrt{3}} & \frac{\mathrm{i}}{2} & \frac{b}{6\sqrt{3}} & \frac{\mathrm{i}}{6} & \frac{b}{6\sqrt{3}} & -\frac{b}{6\sqrt{3}} & \frac{\mathrm{i}}{6} \\
\frac{\mathrm{i}}{3} & -\frac{e^{-\frac{2\pi\mathrm{i}}{9}}b}{6\sqrt{3}} & \frac{e^{\frac{2\pi\mathrm{i}}{9}}a}{6\sqrt{3}} & -\frac{e^{-\frac{\pi\mathrm{i}}{9}}a}{6\sqrt{3}} & 0 & \frac{e^{\frac{\pi\mathrm{i}}{9}}b}{6\sqrt{3}} & -\frac{b}{6\sqrt{3}} & -\frac{e^{\frac{\pi\mathrm{i}}{9}}a}{6\sqrt{3}} & \frac{e^{-\frac{\pi\mathrm{i}}{9}}b}{6\sqrt{3}} & \frac{b}{6\sqrt{3}} \\
\frac{\mathrm{i}}{3} & \frac{e^{\frac{\pi\mathrm{i}}{9}}b}{6\sqrt{3}} & -\frac{e^{-\frac{\pi\mathrm{i}}{9}}a}{6\sqrt{3}} & \frac{e^{-\frac{\pi\mathrm{i}}{9}}b}{6\sqrt{3}} & 0 & -\frac{e^{\frac{\pi\mathrm{i}}{9}}a}{6\sqrt{3}} & -\frac{b}{6\sqrt{3}} & -\frac{e^{-\frac{2\pi\mathrm{i}}{9}}b}{6\sqrt{3}} & \frac{e^{\frac{2\pi\mathrm{i}}{9}}a}{6\sqrt{3}} & \frac{b}{6\sqrt{3}} \\
\frac{\mathrm{i}}{3} & -\frac{e^{\frac{\pi\mathrm{i}}{9}}a}{6\sqrt{3}} & \frac{e^{-\frac{\pi\mathrm{i}}{9}}b}{6\sqrt{3}} & \frac{e^{\frac{2\pi\mathrm{i}}{9}}a}{6\sqrt{3}} & 0 & -\frac{e^{-\frac{2\pi\mathrm{i}}{9}}b}{6\sqrt{3}} & -\frac{b}{6\sqrt{3}} & \frac{e^{\frac{\pi\mathrm{i}}{9}}b}{6\sqrt{3}} & -\frac{e^{-\frac{\pi\mathrm{i}}{9}}a}{6\sqrt{3}} & \frac{b}{6\sqrt{3}} \\
\frac{\mathrm{i}}{3} & \frac{e^{\frac{2\pi\mathrm{i}}{9}}a}{6\sqrt{3}} & -\frac{e^{-\frac{2\pi\mathrm{i}}{9}}b}{6\sqrt{3}} & \frac{e^{\frac{\pi\mathrm{i}}{9}}b}{6\sqrt{3}} & 0 & -\frac{e^{-\frac{\pi\mathrm{i}}{9}}a}{6\sqrt{3}} & \frac{b}{6\sqrt{3}} & \frac{e^{-\frac{\pi\mathrm{i}}{9}}b}{6\sqrt{3}} & -\frac{e^{\frac{\pi\mathrm{i}}{9}}a}{6\sqrt{3}} & -\frac{b}{6\sqrt{3}} \\
\frac{\mathrm{i}}{3} & -\frac{e^{-\frac{\pi\mathrm{i}}{9}}a}{6\sqrt{3}} & \frac{e^{\frac{\pi\mathrm{i}}{9}}b}{6\sqrt{3}} & -\frac{e^{\frac{\pi\mathrm{i}}{9}}a}{6\sqrt{3}} & 0 & \frac{e^{-\frac{\pi\mathrm{i}}{9}}b}{6\sqrt{3}} & \frac{b}{6\sqrt{3}} & \frac{e^{\frac{2\pi\mathrm{i}}{9}}a}{6\sqrt{3}} & -\frac{e^{-\frac{2\pi\mathrm{i}}{9}}b}{6\sqrt{3}} & -\frac{b}{6\sqrt{3}} \\
\frac{\mathrm{i}}{3} & \frac{e^{-\frac{\pi\mathrm{i}}{9}}b}{6\sqrt{3}} & -\frac{e^{\frac{\pi\mathrm{i}}{9}}a}{6\sqrt{3}} & -\frac{e^{-\frac{2\pi\mathrm{i}}{9}}b}{6\sqrt{3}} & 0 & \frac{e^{\frac{2\pi\mathrm{i}}{9}}a}{6\sqrt{3}} & \frac{b}{6\sqrt{3}} & -\frac{e^{-\frac{\pi\mathrm{i}}{9}}a}{6\sqrt{3}} & \frac{e^{\frac{\pi\mathrm{i}}{9}}b}{6\sqrt{3}} & -\frac{b}{6\sqrt{3}}
\end{pmatrix},$$

where $a = 3 + \sqrt{3}\mathrm{i}$ and $b = 3 - \sqrt{3}\mathrm{i}$.

Each unitary splitting matrix $\widetilde{\mathbb{I}}_6^{(k)}$, $k \in \{0,1,2\}$ contains rows indexed by the corresponding interior weight set in (2.4.26) and columns indexed by the interior point sets $\widetilde{F}_6^{(k)}$ obtained from expression (2.2.58) as

$$\begin{aligned}
\widetilde{F}_6^{(0)} &= \{[4,1,1],[3,2,1],[3,1,2],[2,2,2]\}, \\
\widetilde{F}_6^{(1)} = F_6^{(2)} &= \{[4,1,1],[3,2,1],[3,1,2]\}.
\end{aligned}$$

The splitting transform matrices $\widetilde{\mathbb{I}}_6^{(0)}$, $\widetilde{\mathbb{I}}_6^{(1)}$ and $\widetilde{\mathbb{I}}_6^{(2)}$ are calculated from definition (2.4.14) as

$$\widetilde{\mathbb{I}}_6^{(0)} = \begin{pmatrix}
\frac{\mathrm{i}}{2\sqrt{3}} & \frac{\mathrm{i}}{\sqrt{3}} & \frac{\mathrm{i}}{\sqrt{3}} & \frac{\mathrm{i}}{2} \\
\frac{i\sqrt{3}}{2} & 0 & 0 & -\frac{\mathrm{i}}{2} \\
\frac{\mathrm{i}}{2\sqrt{3}} & -\frac{1}{6}b & \frac{1}{6}b & \frac{\mathrm{i}}{2} \\
\frac{\mathrm{i}}{2\sqrt{3}} & \frac{1}{6}b & -\frac{1}{6}b & \frac{\mathrm{i}}{2}
\end{pmatrix},$$

$$\widetilde{\mathbb{I}}_6^{(1)} = \begin{pmatrix}
\frac{\mathrm{i}}{\sqrt{3}} & -\frac{1}{6}be^{-\frac{2\mathrm{i}\pi}{9}} & \frac{1}{6}ae^{\frac{2\mathrm{i}\pi}{9}} \\
\frac{\mathrm{i}}{\sqrt{3}} & \frac{1}{6}be^{\frac{\mathrm{i}\pi}{9}} & -\frac{1}{6}ae^{-\frac{\mathrm{i}\pi}{9}} \\
\frac{\mathrm{i}}{\sqrt{3}} & -\frac{1}{6}ae^{\frac{\mathrm{i}\pi}{9}} & \frac{1}{6}be^{-\frac{\mathrm{i}\pi}{9}}
\end{pmatrix},$$

$$\widetilde{\mathbb{I}}_6^{(2)} = \begin{pmatrix}
\frac{\mathrm{i}}{\sqrt{3}} & \frac{1}{6}ae^{\frac{2\mathrm{i}\pi}{9}} & -\frac{1}{6}be^{-\frac{2\mathrm{i}\pi}{9}} \\
\frac{\mathrm{i}}{\sqrt{3}} & -\frac{1}{6}ae^{-\frac{\mathrm{i}\pi}{9}} & \frac{1}{6}be^{\frac{\mathrm{i}\pi}{9}} \\
\frac{\mathrm{i}}{\sqrt{3}} & \frac{1}{6}be^{-\frac{\mathrm{i}\pi}{9}} & -\frac{1}{6}ae^{\frac{\mathrm{i}\pi}{9}}
\end{pmatrix}.$$

Using the Formulas (2.4.15) and (2.4.17) to construct the unitary central splitting matrix $\widetilde{\mathbb{T}}_6$, the rows are labeled by the union of the point sets $\widetilde{F}_6^{(0)} \cup \widetilde{F}_6^{(1)} \cup \widetilde{F}_6^{(2)}$, and the columns are labeled by the elements of the interior point set $\widetilde{F}_6$. Since the ordering of the interior point sets for $M = 6$ is chosen to be compatible with the ordering of the $C-$transform point sets for $M = 3$, the transform matrix $\widetilde{\mathbb{T}}_6$ coincides with the splitting matrix $\mathbb{T}_3$,

$$\widetilde{\mathbb{T}}_6 = \mathbb{T}_3.$$

2.5. Concluding remarks

- The decompositions of the weight lattice Fourier–Weyl transforms into the splitting transforms are considered as a point of departure in exploring the fast bivariate discrete Fourier transforms involving the (anti)symmetric orbit functions of the Weyl group A_2. The central splitting method offers an advantageous approach to computational efficiency, using the reduction of the initial weight lattice Fourier–Weyl transform into three smaller-weight lattice splitting transforms. Even though the recursive method to determine the further splitting of currently developed two-variable cosine and sine transforms has not been determined yet, the demonstrated reduced weight transform is considered as a stepping stone towards the fast discrete transforms. Moreover, analogously to the interpolation tests conducted for cosine and sine discrete transforms (Patera and Zaratsyan [**117, 118, 119**]), the developed discrete splitting transforms also manifest excellent interpolation properties.
- For the crystallographic reflection group A_1, repeatedly using the central splitting of one-variable discrete cosine and sine transforms produces the standard versions of the fast split-radix transforms (Britanak [**24**]). In this case, the possibility of rearranging the splitting point sets into the original format governed by the affine Weyl group ensures the central splitting method's recursive behavior. The decompositions of the transform matrices, similar to the formulated unitary matrix decompositions in Theorem 8, have been rigorously proven for the one-dimensional sine and cosine transforms in (Plonka and Tasche [**120**]). However, in the case of the A_2 group, since a further splitting of the points in the kite-shaped domain has not been formulated yet, the recursive central splitting method remains an unsolved problem.
- Given the importance of multi-dimensional digital data processing (Atoyan and Patera [**8**]; Klimyk and Patera [**81**]; Nesterenko and Patera [**107**]; Li and Xu [**91**]; Li *et al.* [**90**]), a central-splitting mechanism could be potentially developed for other compact simple Lie groups with non-trivial elements of the center, such as A_n with its center provided by a cyclic group of $n+1$ elements, B_n, C_n and E_7 with the center given by a cyclic group of order 2, D_n whose center contains 4 elements, E_6 that equivalently to A_2 has 3 elements of the center. Such an approach would be considered as a first

step to a general multidimensional fast transform. Since a similar behavior of the central splitting in the case of the finite reflection group A_n is expected, the extension of the developed Fourier–Weyl transforms to higher-dimensional cases should be treated independently.

- Another family of orbit functions, known as $E-$functions, is obtained by symmetrizing multivariate exponential terms over even subgroups of a considered Weyl group. Such functions are developed in (Klimyk and Patera [**80**]), and their corresponding Fourier–Weyl transforms together with continuous interpolations are examined in detail (Hrivnák and Patera [**64**]). There is one type of the $E-$functions for the root systems with the roots of one length (Moody and Patera [**105**]). For the root systems with two lengths of simple roots, the six types of $E-$functions, together with their even complex-valued dual weight lattice Fourier–Weyl transforms, are formulated in (Hrivnák and Juránek [**60**]). Hence, instead of the discrete transforms based on the $C-$ and $S-$functions, the central splitting of the transforms developed by means of the $E-$functions represents an open problem. Furthermore, the Fourier–Weyl transforms with their kernel represented by the combinations of different types of Weyl orbit functions have not been previously explored.

Acknowledgments

The authors are grateful to Alexandra Patera for editorial assistance. J.H. gratefully acknowledges support from the Czech Science Foundation (GAČR), Grant No. 19-19535S. M.M. and J.P. are grateful for partial support of this work by the Natural Sciences and Engineering Research Council of Canada (NSERC), Grant No. RGPIN-2016-04199.

Chapter 3

Nested polyhedra and indices of orbits of Coxeter groups of non-crystallographic type

by

Mariia Myronova[1], Jiří Patera[2], and Marzena Szajewska[3]

([1]) Département de Physique, Université de Montréal, Complexe des Sciences,
1375 Avenue Thérèse-Lavoie-Roux, Montréal, QC H2V 0B3, Canada
maria.myronova@umontreal.ca

([2]) Centre de Recherches Mathématiques, Université de Montréal,
C. P. 6128 Centre Ville, Montréal, QC H3C 3J7, Canada
patera@crm.umontreal.ca

([3]) Department of Mathematics, University of Białystok,
1M Ciołkowskiego, PL-15-245, Białystok, Poland
m.szajewska@math.uwb.edu.pl

This article was published in Symmetry.
Reference: Myronova, M.; Patera, J.; Szajewska, M. (2020) Nested polyhedra and indices of orbits of Coxeter groups of non-crystallographic type. *Symmetry*, **12**, 1737.

Author contributions: conceptualization, M.M., J.P. and M.S.; writing and editing, M.M., J.P. and M.S.; calculation, M.M. and M.S.; visualization, M.M.

Résumé. Les invariants des représentations de dimension finie des algèbres de Lie simples, comme les indices de degré pair et les nombres d'anomalies, sont considérés dans le contexte des groupes non cristallographiques de réflexion finie H_2, H_3 et H_4. En utilisant une représentation-orbite comme remplacement, les définitions et les propriétés des indices sont formulées pour des orbites individuelles des groupes examinés. Les indices des ordres deux et quatre du produit tensoriel des orbites k sont déterminés. En utilisant les règles de branchement pour les groupes de Coxeter non cristallographiques, l'indice d'incorporation est défini de la même manière que l'indice de Dynkin d'une représentation. De plus, puisque la définition des indices peut être appliquée à toute orbite de type non cristallographique, l'algorithme permettant de rechercher les orbites de rayons plus petits contenus dans tout rayon considéré est présenté pour les groupes de Coxeter H_2 et H_3. Les structures géométriques des polytopes imbriqués sont illustrées.

Mots clés : groupe de Coxeter, polytope imbriqué, indice d'orbite, indice d'ordre supérieur, numéro d'anomalie, multiplicité de poids, algorithme de recherche, diagramme arborescent

Abstract. The invariants of finite-dimensional representations of simple Lie algebras, such as even-degree indices and anomaly numbers, are considered in the context of the non-crystallographic finite reflection groups H_2, H_3 and H_4. Using a representation-orbit replacement, the definitions and properties of the indices are formulated for individual orbits of the examined groups. The indices of orders two and four of the tensor product of k orbits are determined. Using the branching rules for the non-crystallographic Coxeter groups, the embedding index is defined similarly to the Dynkin index of a representation. Moreover, since the definition of the indices can be applied to any orbit of non-crystallographic type, the algorithm allowing to search for the orbits of smaller radii contained within any considered one is presented for the Coxeter groups H_2 and H_3. The geometrical structures of nested polytopes are exemplified.

Keywords: Coxeter group, nested polytope, orbit index, higher-order index, anomaly number, weight multiplicity, search algorithm, tree-diagram

3.1. Introduction

The purpose of this paper is to formulate the definitions of the even- and odd-degree indices for orbits of the non-crystallographic Coxeter groups H_2, H_3 and H_4 (the symmetry group of a regular pentagon, a regular icosahedron and the 600-cell, respectively). In this case, the definition of the indices of irreducible representations of simple Lie algebras provides a foundation for the indices of orbits. The generalization of properties of the formulated indices is achieved by examining the individual orbits of the investigated groups.

A significant number of applications of non-crystallographic Coxeter groups in solid-state physics (Talis *et al.* [**135**]), chemistry (Nespolo *et al.* [**106**]) and structural genomics (Terwilliger [**138**]) motivates the current study. The symmetries of the H_2 and H_4 groups play an essential role in the construction and description of quasicrystals (Levitov and Rhyner [**89**]). The icosahedral symmetry of the Coxeter group H_3 reveals the structure of the extensive diversity of spherical molecules (Fowler and Manolopoulos [**52**]). Moreover, during the past few years, the H_3 group has gained considerable interest in mathematical virology, since it serves as a blueprint for examining and describing the architecture and assembly of spherical viruses (Dechant *et al.* [**38**]; Indelicato *et al.* [**68**]; Salthouse *et al.* [**130**]; Twarock [**142**]).

The pertinent information about the non-crystallographic reflection groups H_n, $n \in \{2, 3, 4\}$ can be found in (Chen *et al.* [**28**]; Shcherbak [**131**]). Even though any Weyl orbit is linked to a finite-dimensional representation of a Lie algebra, this relation does not exist for the non-crystallographic cases. In general, any orbit $O_\lambda(G)$ of a finite Coxeter group G arises from the action of the corresponding reflections on the dominant (seed) point $\lambda \in \mathbb{R}^n$. The coordinates of λ are commonly provided in the $\omega-$basis, and they take values of any non-negative real numbers. Since any orbit of H_3 can be represented geometrically by a Euclidean (spherical) polytope, the variation of the coordinates of $\lambda \in \mathbb{R}^3$ impacts the lower-dimensional faces represented by edges (arcs) and polygons (tiles on a sphere). As a result, a deeper understanding of a chosen seed point is achieved. The numbers and types of faces of a polytope are determined using the decoration procedure applied to a Coxeter–Dynkin diagram (Champagne *et al.* [**29**]).

During the past decades, it has been convenient to characterize representations of simple Lie algebras by their dimensions (Kirillov [**77**]; Ramond [**126**]). Even though the formula for the dimension is well-known, its difficulty in practical exploitation rapidly increases together with the rank of a corresponding Lie algebra. To overcome this problem, E.B. Dynkin introduced the index that can be calculated for any irreducible representation (Braden [**19**]; Panyushev [**114**]). Since then, the "Dynkin index" is considered as a powerful tool for the classification of semisimple subalgebras of simple Lie algebras (Dynkin [**48**]). The further development of research led to the discovery of the higher-degree indices of finite irreducible representations that have been formulated in (Patera *et al.* [**116**]). Since the decomposition of the tensor product of representations of a simple Lie algebra into the direct sum of irreducible components is important and relevant to many branches of physics, the general formulas for indices of such decompositions are determined in (Okubo and Patera [**110, 111**]).

In this paper, we define the analogs of the higher-degree indices replacing irreducible representations of simple Lie algebras by orbits of the non-crystallographic finite reflection groups. This approach yields several advantages, since the orbit size is finite, and the product of orbits is always decomposable. Hence, the even- and odd-degree indices of orbits of non-crystallographic type are formulated in Sections 3.2 and 3.3. The former include the lower-order indices of the tensor product of orbits. The latter are recognized in physics as the anomaly numbers, since they determine the symmetry-breaking parameters defined for particle systems (Okubo [**108**]; Okubo and Patera [**112**]; Patera and Sharp [**115**]). For the odd-degree index, it is only necessary to determine whether it is zero or not. In our framework, such indices are considered as a generalization of the anomaly numbers of irreducible representations (Zhang *et al.* [**151**]).

The Dynkin index remains a valid invariant only if a single orbit of non-crystallographic type is involved in its definition. Therefore, in Section 3.4, we explore the analog of such an invariant called the embedding index. The calculations of the index proceed whenever the branching rule for a finite reflection group and its subgroup is known ($G' \subset G$). For crystallographic reflection groups, the branching rules are determined for the rank up to $n = 8$ (for instance, see (Larouche *et al.* [**88**]; Larouche and Patera [**87**]) and references therein). Recently, the branching rules have been formulated for the non-crystallographic reflection groups as well (Grabowiecka *et al.* [**54**]).

Furthermore, since we are restricted to the non-crystallographic groups, we introduce a search algorithm to find the orbits of smaller radii that may appear inside an initial one (Section 3.5). Here, such orbits are referred to as 'lower orbits.' The subtraction of the simple roots of H_n, $n \in \{2, 3, 4\}$ from a seed point λ with its coordinates in the $\omega-$basis provides the dominant points of lower orbits. We demonstrate that this method coincides with the root-subtraction for orbits of crystallographic type. Such a procedure forms a weight system similar to the one of a representation. In the geometrical interpretation, any obtained set of lower orbits together with a starting one results in the structure of nested polyhedra (Janner [**70**]; Thomas *et al.* [**139**]; Zelevinsky [**150**]). Such a set of polytopes is quite unusual, as it differs from the sets obtained for crystallographic cases. For the latter, whenever any two polytopes with dominant points consecutively obtained by the subtraction method are considered, one can notice that each vertex of a larger polytope is found in the middle of each edge of a polytope of smaller radius. In contrast, the nested polyhedra of non-crystallographic types do not have this property.

3.2. Even-degree indices for orbits

The important information about the even-degree indices of representations of simple Lie algebras can be found in several papers (Okubo and Patera [**110**]; Ramond [**126**]; Patera *et al.* [**116**]). In this section, considered analogs possess the same properties as the decomposition of products does. However, this property is limited to the indices of degrees two, four and, for some groups, six. Replacing an irreducible representation of a simple Lie algebra with an orbit of a finite reflection group has several advantages:

- the size of an orbit of any Coxeter group is always limited;
- the points of an orbit have only real numbers as their coordinates;
- the product of several orbits can always be decomposed into the sum of orbits of smaller sizes.

Definition 1. *Let G be a finite reflection group, and $O_\lambda(G)$ be an orbit of elements with a dominant point λ. The number defined by*

$$I_\lambda^{2p}(G) = \sum_{\mu \in O_\lambda(G)} \langle \mu, \mu \rangle^p, \quad p \in \mathbb{N},$$

is called the $2p$-order index of an orbit $O_\lambda(G)$. The summation extends over all the elements of $O_\lambda(G)$, and $\langle \cdot, \cdot \rangle$ denotes the scalar product in the weight space of G.

Remark 2. *For $p = 0$, the zero-order index of an orbit $O_\lambda(G)$ is equal to its size:*

$$I_\lambda^0(G) = |O_\lambda(G)|,$$

where $|O_\lambda(G)|$ denotes the size of an orbit generated by the action of G on a seed point λ. The sizes of orbits of the examined non-crystallographic groups are presented in Table 3.1.

Since the elements of any orbit $O_\lambda(G)$ are equidistant from the origin, we have the following remark.

Remark 3. *The formula for even-degree indices has the form:*

$$I_\lambda^{2p}(G) = |O_\lambda(G)| \langle \lambda, \lambda \rangle^p, \quad p \in \mathbb{N}. \tag{3.2.1}$$

Proposition 4. *For the non-crystallographic reflection groups, the general formulas for $2p$-order indices are the following ones:*

$$\begin{aligned}
(3-\tau)^p I_{(a_1,a_2)}^{2p}(H_2) &= |O_{(a_1,a_2)}(H_2)| \cdot [2(a_1^2 + \tau a_1 a_2 + a_2^2)]^p, \\
(4-2\tau)^p I_{(a_1,a_2,a_3)}^{2p}(H_3) &= |O_{(a_1,a_2,a_3)}(H_3)| \cdot [(3-\tau)a_1^2 + 4a_2^2 + 3a_3^2 + 4a_1a_2 + 2\tau a_1 a_3 + 4\tau a_2 a_3]^p, \\
(5-3\tau)^p I_{(a_1,a_2,a_3,a_4)}^{2p}(H_4) &= |O_{(a_1,a_2,a_3,a_4)}(H_4)| \cdot [2((2-\tau)a_1^2 + (3-\tau)a_2^2 + 3a_3^2 + 2a_4^2 + (3-\tau)a_1a_2 \\
&\qquad + 2a_1a_3 + \tau a_1 a_4 + 4a_2a_3 + 2\tau a_2 a_4 + 3\tau a_3 a_4)]^p,
\end{aligned}$$

where $\tau = \frac{1+\sqrt{5}}{2} = 1.618\ldots$ is the positive solution of the quadratic equation $x^2 = x + 1$ known as the golden ratio.

Proof. The inner product $\langle \cdot, \cdot \rangle$ of the elements of orbits of the non-crystallographic groups H_n has the following form:

$$\langle (a_1, \ldots, a_n), (b_1, \ldots, b_n) \rangle = \begin{pmatrix} a_1 \ldots \; a_n \end{pmatrix} C_{H_n}^{-1} \begin{pmatrix} b_1 \\ \vdots \\ b_n \end{pmatrix}, \quad n \in \{2, 3, 4\}. \tag{3.2.2}$$

where $C_{H_n}^{-1}$ is the inverse Cartan matrix (Table 3.2). Applying (3.2.2) to (3.2.1), the desired formulas can be immediately obtained. □

λ	$\lvert O_\lambda(H_2)\rvert$
$(a,0)$	5
$(0,b)$	5
(a,b)	10

λ	$\lvert O_\lambda(H_3)\rvert$
$(a,0,0)$	12
$(0,b,0)$	30
$(0,0,c)$	20
$(a,b,0)$	60
$(a,0,c)$	60
$(0,b,c)$	60
(a,b,c)	120

λ	$\lvert O_\lambda(H_4)\rvert$
$(a,0,0,0)$	120
$(0,b,0,0)$	720
$(0,0,c,0)$	1200
$(0,0,0,d)$	600
$(a,b,0,0)$	1440
$(a,0,c,0)$	3600
$(a,0,0,d)$	2400
$(0,b,c,0)$	3600
$(0,b,0,d)$	3600
$(0,0,c,d)$	2400
$(a,b,c,0)$	7200
$(a,b,0,d)$	7200
$(a,0,c,d)$	7200
$(0,b,c,d)$	7200
(a,b,c,d)	14400

Table 3.1. The sizes of orbits $O_\lambda(H_n)$ of the non-crystallographic groups H_n, $n \in \{2,3,4\}$ provided for each type of dominant point λ with the coefficients $a,b,c,d \in \mathbb{R}^{>0}$.

$$C_{H_2} = \begin{pmatrix} 2 & -\tau \\ -\tau & 2 \end{pmatrix} \qquad C_{H_2}^{-1} = \tfrac{1}{3-\tau}\begin{pmatrix} 2 & \tau \\ \tau & 2 \end{pmatrix}$$

$$C_{H_3} = \begin{pmatrix} 2 & -1 & 0 \\ -1 & 2 & -\tau \\ 0 & -\tau & 2 \end{pmatrix} \qquad C_{H_3}^{-1} = \tfrac{1}{2}\begin{pmatrix} 2+\tau & 2+2\tau & 1+2\tau \\ 2+2\tau & 4+4\tau & 2+4\tau \\ 1+2\tau & 2+4\tau & 3+3\tau \end{pmatrix}$$

$$C_{H_4} = \begin{pmatrix} 2 & -1 & 0 & 0 \\ -1 & 2 & -1 & 0 \\ 0 & -1 & 2 & -\tau \\ 0 & 0 & -\tau & 2 \end{pmatrix} \qquad C_{H_4}^{-1} = \begin{pmatrix} 2+2\tau & 3+4\tau & 4+6\tau & 3+5\tau \\ 3+4\tau & 6+8\tau & 8+12\tau & 6+10\tau \\ 4+6\tau & 8+12\tau & 12+18\tau & 9+15\tau \\ 3+5\tau & 6+10\tau & 9+15\tau & 8+12\tau \end{pmatrix}$$

Table 3.2. The Cartan matrices and their inverses for the non-crystallographic groups H_2, H_3 and H_4.

Definition 5. *Let G be a finite reflection group. The direct sum of orbits with dominant points $\lambda_1, \ldots, \lambda_k$, $k \geq 2$, is provided by the formula:*

$$O_{\lambda_1 \oplus \ldots \oplus \lambda_k}(G) = \bigcup_{\substack{\mu_i \in O_{\lambda_i(G)} \\ i \in \{1,2,\ldots,k\}}} \mu_i = O_{\lambda_1}(G) \cup \ldots \cup O_{\lambda_k}(G). \tag{3.2.3}$$

The size of the direct sum is equal to

$$|O_{\lambda_1 \oplus \ldots \oplus \lambda_k}(G)| = |O_{\lambda_1}(G)| + \ldots + |O_{\lambda_k}(G)|. \tag{3.2.4}$$

Definition 6. *Let G be a finite reflection group. The tensor product of orbits of G with dominant points $\lambda_1, \dots, \lambda_k$, $k \geq 2$, is provided by the summation of elements of each orbit with all elements of other orbits as*

$$O_{\lambda_1 \otimes \dots \otimes \lambda_k}(G) = \bigcup_{\substack{\mu_i \in O_{\lambda_i(G)} \\ i \in \{1,2,\dots,k\}}} (\mu_1 + \dots + \mu_k). \tag{3.2.5}$$

The size of the tensor product is equal to

$$|O_{\lambda_1 \otimes \dots \otimes \lambda_k}(G)| = |O_{\lambda_1}(G)| \cdot \ldots \cdot |O_{\lambda_k}(G)|. \tag{3.2.6}$$

Remark 7. *The tensor product of k orbits of G decomposes into a union of several orbits (Háková et al. [**57**]). In this case, the highest weight is $\lambda_1 + \dots + \lambda_k$, and the product of orbits decomposes as follows:*

$$\lambda_1 \otimes \dots \otimes \lambda_k = (\lambda_1 + \dots + \lambda_k) \cup \dots \cup \text{ other lower-order orbits.}$$

Example 8. *Let us consider two orbits, $O_{(1,0)}(H_2)$ and $O_{(0,\tau)}(H_2)$. The direct sum (3.2.3) and tensor product (3.2.5) of orbits are written explicitly as*

$$\begin{aligned} O_{(1,0)\oplus(0,\tau)}(H_2) = &\{(1,0), (-1,\tau), (\tau,-\tau), (-\tau,1), (0,-1), \\ &(0,\tau), (\tau+1,-\tau), (-\tau-1,\tau+1), (\tau,-\tau-1), (-\tau,0)\}; \\ O_{(1,0)\otimes(0,\tau)}(H_2) = &\{(1,\tau), (\tau+2,-\tau), (-\tau,\tau+1), (\tau+1,-\tau-1), (1-\tau,0), (-1,2\tau), \\ &(\tau,0), (-\tau-2,2\tau+1), (\tau-1,-1), (-\tau-1,\tau), (\tau,0), (2\tau+1,-2\tau), \\ &(-1,1), (2\tau,-2\tau-1), (0,-\tau), (-\tau,\tau+1), (1,1-\tau), (-2\tau-1,\tau+2), \\ &(0,-\tau), (-2\tau,1), (0,\tau-1), (\tau+1,-\tau-1), (-\tau-1,\tau), (\tau,-\tau-2), (-\tau,-1)\}. \end{aligned}$$

The tensor product of two orbits decomposes into the union of orbits as

$$\underset{5}{(1,0)} \underset{\cdot}{\otimes} \underset{5}{(0,\tau)} \underset{=}{=} \underset{10}{(1,\tau)} \underset{+}{\cup} \underset{2\cdot5}{2(\tau,0)} \underset{+}{\cup} \underset{5}{(0,\tau-1)}\,.$$

The numbers attached to the dominant points correspond to the sizes of the orbits of H_2 provided by (3.2.4) and (3.2.6) (see Table 3.1). The number of elements of the orbit product is equal to the number of elements after the decomposition.

Proposition 9. *Let G be a finite reflection group. The formulas for lower-order indices of the tensor product of k orbits of G are given by:*

$$(i) \qquad I^2_{\lambda_1 \otimes \dots \otimes \lambda_k}(G) = \prod_{i=1}^{k} I^0_{\lambda_i}(G) \sum_{j=1}^{k} \frac{I^2_{\lambda_j}(G)}{|O_{\lambda_j}(G)|} = \sum_{j=1}^{k} \left(I^2_{\lambda_j}(G) \prod_{\substack{i \neq j \\ i=1}}^{k} I^0_{\lambda_i}(G) \right),$$

$$(ii) \quad I^4_{\lambda_1 \otimes \dots \otimes \lambda_k}(G) = \sum_{j=1}^{k} \left(I^4_{\lambda_j}(G) \prod_{\substack{i \neq j \\ i=1}}^{k} I^0_{\lambda_i}(G) \right) + \frac{2(r+2)}{r} \sum_{\substack{j,l=1 \\ j \neq l}}^{k} \left(I^2_{\lambda_j}(G) I^2_{\lambda_l}(G) \prod_{\substack{i \neq j,l \\ i=1}}^{k} I^0_{\lambda_i}(G) \right),$$

where $k \in \mathbb{N}^{\geq 2}$, and r denotes the rank of G.

Proof. (i) Using the Equation (3.2.1), we immediately have

$$\begin{aligned}
I^2_{\lambda_1\otimes\cdots\otimes\lambda_k}(G) &= |O_{\lambda_1\otimes\cdots\otimes\lambda_k}(G)|\cdot\langle\lambda_1\otimes\cdots\otimes\lambda_k,\lambda_1\otimes\cdots\otimes\lambda_k\rangle\\
&= |O_{\lambda_1}(G)|\cdot|O_{\lambda_2}(G)|\ldots|O_{\lambda_k}(G)|\cdot(\langle\lambda_1,\lambda_1\rangle+\langle\lambda_2,\lambda_2\rangle+\ldots+\langle\lambda_k,\lambda_k\rangle)\\
&= \prod_{i=1}^{k} I^0_{\lambda_i}(G)\cdot\sum_{j=1}^{k}\langle\lambda_j,\lambda_j\rangle = \sum_{j=1}^{k}\left(I^2_{\lambda_j}(G)\prod_{\substack{i\neq j\\ i=1}}^{k} I^0_{\lambda_i}(G)\right).
\end{aligned}$$

(ii) Let us recall the pertinent properties of orbits of finite reflection groups. Considering any point $\mu=(\mu_1,\ldots,\mu_r)$, where $r = rank\ G$, we obtain

$$\sum_{\mu\in O_\lambda(G)}\mu_i=0,\qquad \sum_{\mu\in O_\lambda(G)}\mu_i\mu_j=\frac{\delta_{ij}}{r}\sum_{\mu\in O_\lambda(G)}\mu^2.$$

Hence, the index for $p=2$ can be written as

$$\begin{aligned}
I^4_{\lambda_1\otimes\cdots\otimes\lambda_k}(G) &= |O_{\lambda_1\otimes\cdots\otimes\lambda_k}(G)|\cdot\langle\lambda_1\otimes\cdots\otimes\lambda_k,\lambda_1\otimes\cdots\otimes\lambda_k\rangle^2\\
&= |O_{\lambda_1}(G)|\cdot|O_{\lambda_2}(G)|\ldots|O_{\lambda_k}(G)|\cdot\left(\sum_{i,j=1}^{k}\langle\lambda_i,\lambda_i\rangle\langle\lambda_j,\lambda_j\rangle+4\sum_{i,j=1}^{k}\langle\lambda_i,\lambda_j\rangle^2\right).
\end{aligned}$$

Using the properties of orbits, we obtain the following expressions:

$$\begin{aligned}
&|O_{\lambda_1}(G)|\cdot|O_{\lambda_2}(G)|\ldots|O_{\lambda_k}(G)|\cdot\left(\sum_{i=1}^{k}\langle\lambda_i,\lambda_i\rangle^2+2\sum_{\substack{i,j=1\\ i\neq j}}^{k}\langle\lambda_i,\lambda_i\rangle\langle\lambda_j,\lambda_j\rangle+\frac{4\delta_{ij}}{r}\sum_{i,j=1}^{k}\langle\lambda_i,\lambda_j\rangle^2\right)\\
&= |O_{\lambda_1}(G)|\cdot|O_{\lambda_2}(G)|\ldots|O_{\lambda_k}(G)|\cdot\left(\sum_{i=1}^{k}\langle\lambda_i,\lambda_i\rangle^2+\frac{2(r+2)}{r}\sum_{\substack{i,j=1\\ i\neq j}}^{k}\langle\lambda_i,\lambda_i\rangle\langle\lambda_j,\lambda_j\rangle\right)\\
&= \sum_{j=1}^{k}\left(I^4_{\lambda_j}(G)\prod_{\substack{i\neq j\\ i=1}}^{k} I^0_{\lambda_i}(G)\right)+\frac{2(r+2)}{r}\sum_{\substack{j,l=1\\ j\neq l}}^{k}\left(I^2_{\lambda_j}(G)I^2_{\lambda_l}(G)\prod_{\substack{i\neq j,l\\ i=1}}^{k} I^0_{\lambda_i}(G)\right).
\end{aligned}$$

□

Remark 10. *In general, the indices of the k-th tensor product of orbits of a group G are defined recursively as*

$$I^{2p}_{\lambda_1\otimes\cdots\otimes\lambda_k}(G)=I^{2p}_{\lambda_1\otimes(\lambda_2\otimes\cdots\otimes\lambda_k)}(G),\quad k\in\mathbb{N}^{\geq 2}.$$

The obvious observation is

$$I^{2p}_{\lambda_1\oplus\ldots\oplus\lambda_k}(G)=\sum_{i=1}^{k} I^{2p}_{\lambda_i}(G).$$

Example 11. *Let us calculate the second-order index of the tensor product of the orbits $O_{(1,0)}(H_2)$ and $O_{(0,1)}(H_2)$. Such a product decomposes as*

$$(1,0)\otimes(0,1)=(1,1)\cup(\tau-1,\tau-1)\cup 5(0,0).$$

Therefore, using the decomposition given above, we can calculate the second-degree index as follows:

$$I^2_{(1,0)\otimes(0,1)}(H_2) = I^2_{(1,1)}(H_2) + I^2_{(\tau-1,\tau-1)}(H_2) + 5I^2_{(0,0)}(H_2) = \frac{20(\tau+2)}{3-\tau} + 20 + 0 = \frac{100}{3-\tau}.$$

Taking into consideration Proposition 9, the same result is obtained:

$$I^2_{(1,0)\otimes(0,1)}(H_2) = I^2_{(1,0)}(H_2)I^0_{(0,1)}(H_2) + I^0_{(1,0)}(H_2)I^2_{(0,1)}(H_2) = 5\cdot\frac{10}{3-\tau} + 5\cdot\frac{10}{3-\tau} = \frac{100}{3-\tau}.$$

Proposition 12. *Let $G = G_1 \times \ldots \times G_k$ be a finite reflection group. The formula for $2p$-order indices of the product of k orbits $\lambda_i \in O(G_i)$, $i \in \{1,2,\ldots,k\}$ is provided by:*

$$I^{2p}_{\lambda_1\otimes\cdots\otimes\lambda_k}(G) = \sum_{j=1}^{k}\left(I^{2p}_{\lambda_j}(G_j) \prod_{\substack{i\neq j\\ i=1}}^{k} I^0_{\lambda_i}(G_i)\right) = \prod_{i=1}^{k} |O_{\lambda_i}(G_i)| \cdot \sum_{j=1}^{k} \langle \lambda_j, \lambda_j\rangle^p. \tag{3.2.7}$$

Proof. For any group $G = G_1 \times \ldots \times G_k$, the inner product has the following form:

$$\langle \lambda_1 \otimes \cdots \otimes \lambda_k, \mu_1 \otimes \cdots \otimes \mu_k \rangle_G = \langle \lambda_1, \mu_1\rangle_{G_1} + \ldots + \langle \lambda_k, \mu_k\rangle_{G_k}.$$

It is easy to verify that Formula (3.2.7) holds. ☐

3.3. Odd-degree indices for orbits

The odd-order index of an irreducible representation serves as a parameter limiting the symmetry of the mathematical model of particle physics and its diverse extensions (Okubo [**108**]). The triangular anomaly numbers have been defined for the Lie group $SU(n)$ by the sum of cubes of the components of the weights corresponding to the $U(1)$ subgroup in the reduction $SU(n) \supset U(1)\times SU(n-1)$ (Patera and Sharp [**115**]).

In general, the crucial part of obtaining the anomaly number lies in determining the vector v passing through the origin of the weight space. For any Coxeter group H_n, $n \in \{2,3,4\}$, the orbits of its lower subgroup span $\mathbb{R}^{n-1}$ orthogonal to v. Projecting the orbit points onto v and calculating the sum of the distances between the obtained projections, we can determine whether this sum yields zero or not. Generally, the highest weight of the unitary group $U(1)$ sets the direction of v. However, other suitable vectors are not excluded, and they are utilized as long as the resulting sum is not equal to zero.

The non-zero anomaly numbers exist only for those groups that have a corresponding symmetric Coxeter–Dynkin diagram. From such diagrams for the non-crystallographic groups (Figure 3.1), it follows that the anomaly number of the Coxeter group H_2 is not equal to zero. The non-crystallographic groups H_3 and H_4 are anomaly-free groups, as their Coxeter–Dynkin diagrams are non-symmetric.

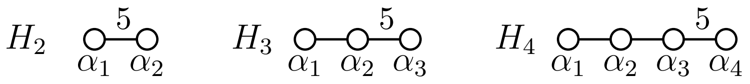
H_2
5
α_1 α_2
H_3
5
α_1 α_2 α_3
H_4
5
α_1 α_2 α_3 α_4

Fig. 3.1. The Coxeter–Dynkin diagrams of the non-crystallographic groups H_n, $n \in \{2,3,4\}$. The nodes correspond to the simple roots α_k, $k \in \{1,\dots,n\}$.

The nodes of the Coxeter–Dynkin diagrams of H_n, $n \in \{2,3,4\}$ can be also labeled by the reflections r_k across the hyperplanes orthogonal to α_k, $k \in \{1,\dots,n\}$. For a non-crystallographic group H_n and any point $x \in \mathbb{R}^n$, the reflection formula is provided by the scalar product (3.2.2) as

$$r_k x = x - \langle x, \alpha_k\rangle \alpha_k, \quad k \in \{1,\dots,n\}. \tag{3.3.1}$$

Definition 13. *Let G be a Coxeter group H_n, $n \in \{2,3,4\}$ of non-crystallographic type. The number defined by*

$$A_\lambda^{2p-1}(G) = \sum_{\mu \in O_\lambda(G)} \langle \mu, v\rangle^{2p-1}, \quad p \in \mathbb{N}, \tag{3.3.2}$$

where v is a vector orthogonal to the simple roots $\alpha_1,\dots,\alpha_{n-1}$, is called the anomaly number or $(2p-1)$-th-order index of an orbit $O_\lambda(H_n)$.

Example 14. *Consider an orbit of the non-crystallographic group H_2 with a dominant point $\lambda = (a,b)$ shown in Figure 3.2. In this case, the weight ω_2 can be chosen as the vector v, since it is orthogonal to the simple root α_1. Hence, using Formula (3.3.2), the calculations of the anomaly numbers yield:*

$$A_{(a,b)}^{2p-1}(H_2) = \sum_{\mu \in O_{(a,b)}(H_2)} \langle \mu, (0,1)\rangle^{2p-1} = 2\left(\frac{1}{\tau-3}\right)^{2p-1} \Big\{(a(\tau-1)-b(\tau-1))^{2p-1}$$
$$-(a\tau+2b)^{2p-1} - (a\tau+b(\tau-1))^{2p-1} + (2a+b\tau)^{2p-1} + (a(\tau-1)+b\tau)^{2p-1}\Big\}.$$

Remark 15. *We can generalize Definition 13 by taking into consideration the following statements:*

- *The anomaly numbers $A_{(a,b)}^1(H_2) = A_{(a,b)}^3(H_2) = 0$, for any $a, b \in \mathbb{R}$.*
- *The odd-order indices $A_{(a,b)}^{2p-1}(H_2) \neq 0$, for $a \neq b$ and $p > 2$.*
- *For the Coxeter groups H_3 and H_4, as any orbit contains the elements with positive and negative signs, the anomaly numbers obtained for any orbit are equal to zero:*

$$A_\lambda^{2p-1}(H_n) = \sum_{\mu \in O_\lambda(H_n)} \langle \mu, v\rangle^{2p-1} = 0, \quad n = 3,4.$$

Definition 16. *Let G be the non-crystallographic finite reflection group H_2. The number defined by*

$$A_\lambda^p(H_2) = \sum_{\mu \in O_\lambda(H_2)} \langle \mu, \omega_2\rangle^p, \quad p \in \mathbb{N} \cup \{0\}$$

is called the p-th-order anomaly number of an orbit $O_\lambda(H_2)$.

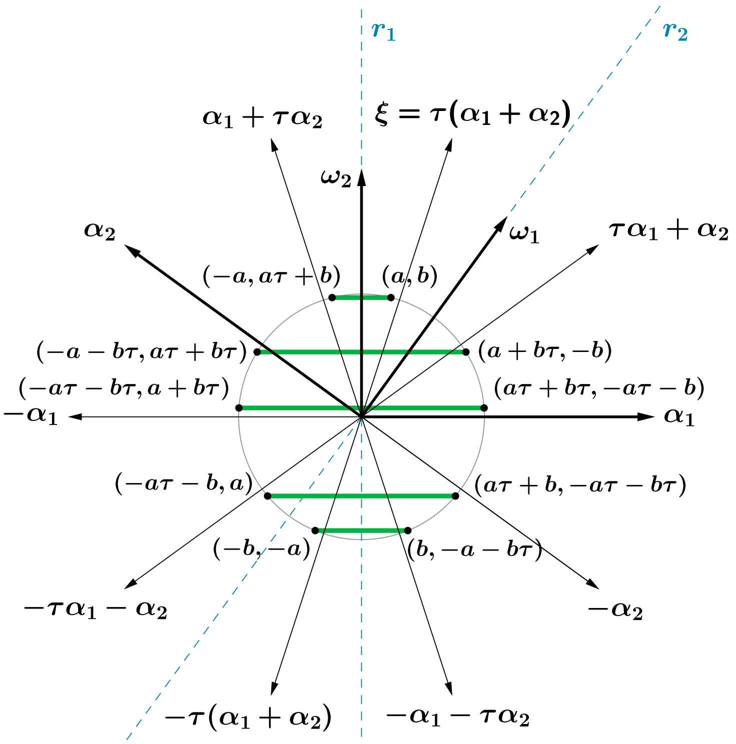
r_1
r_2
$\alpha_1+\tau\alpha_2$
$\xi=\tau(\alpha_1+\alpha_2)$
ω_2
α_2
ω_1
$\tau\alpha_1+\alpha_2$
$(-a,a\tau+b)$
(a,b)
$(-a-b\tau,a\tau+b\tau)$
$(a+b\tau,-b)$
$(-a\tau-b\tau,a+b\tau)$
$(a\tau+b\tau,-a\tau-b)$
$-\alpha_1$
α_1
$(-a\tau-b,a)$
$(a\tau+b,-a\tau-b\tau)$
$(-b,-a)$
$(b,-a-b\tau)$
$-\tau\alpha_1-\alpha_2$
$-\alpha_2$
$-\tau(\alpha_1+\alpha_2)$
$-\alpha_1-\tau\alpha_2$

Fig. 3.2. The root system of the Coxeter group H_2. The dashed lines r_1 and r_2 correspond to the reflecting hyperplanes orthogonal to the simple roots α_1 and α_2, respectively. The root ξ denotes the highest root of H_2. The coordinates of the points of an orbit with a dominant point $\lambda=(a,b)$ of H_2 are listed. The orbits of the reflection group A_1 are depicted by green segments.

From Definition 16, one can immediately notice the following relation:

$$A^0_\lambda(H_2)=|O_\lambda(H_2)|.$$

The general formulas for the p-th-order anomaly number of any orbit of the H_2 group are given by:

$$\begin{aligned}(3-\tau)^pA^p_{(a,b)}(H_2)&=2[((a{-}b)(1{-}\tau))^p{+}(a\tau{+}2b)^p{+}(-2a{-}b\tau)^p\\&\quad+(a(1{-}\tau){-}b\tau)^p{+}(a\tau{+}b(\tau{-}1))^p],\quad a,b\neq 0,\\(3-\tau)^pA^p_{(a,0)}(H_2)&=2[(a(1{-}\tau))^p{+}(a\tau)^p]{+}(-2a)^p,\quad a\neq 0,\\(3-\tau)^pA^p_{(0,b)}(H_2)&=2[(b(\tau{-}1))^p{+}(-b\tau)^p]{+}(2b)^p,\quad b\neq 0.\end{aligned}\tag{3.3.3}$$

Comparing the formulas for the lower even-order indices (Proposition 4) and for p-th-order anomaly numbers (3.3.3), one can observe the following equalities:

$$
\begin{aligned}
A^0_\lambda(H_2) &= I^0_\lambda(H_2),\\
A^2_\lambda(H_2) &= \frac{1}{3-\tau} I^2_\lambda(H_2),\\
A^4_\lambda(H_2) &= \frac{3}{2(3-\tau)^2} I^4_\lambda(H_2),\\
A^6_\lambda(H_2) &= \frac{5}{2(3-\tau)^3} I^6_\lambda(H_2),\\
A^8_\lambda(H_2) &= \frac{35}{8(3-\tau)^4} I^8_\lambda(H_2).
\end{aligned}
$$

Similarly to the even-order indices, the formulas for the direct sum and tensor product can be derived for the anomaly numbers of orbits for the Coxeter group H_2.

Proposition 17. *The formula for the p-th-order anomaly number of the direct sum of k orbits* $\lambda_i \in O_{\lambda_i}(H_2)$, $i \in \{1, 2, \ldots, k\}$ *is given by:*

$$A^p_{\lambda_1 \oplus \ldots \oplus \lambda_k}(H_2) = \sum_{i=1}^{k} A^p_{\lambda_i}(H_2).$$

The formulas for the p-th-order anomaly numbers of the tensor product of two and three orbits $\lambda_i \in O_{\lambda_i}(H_2)$, $i \in \{1, 2, 3\}$ *are given by:*

$$
\begin{aligned}
A^p_{\lambda_1 \otimes \lambda_2}(H_2) &= \sum_{i=0}^{2} \binom{p}{i} A^i_{\lambda_1}(H_2) A^{p-i}_{\lambda_2}(H_2),\\
A^p_{\lambda_1 \otimes \lambda_2 \otimes \lambda_3}(H_2) &= \sum_{i=0}^{3} \binom{p}{i} A^i_{\lambda_1}(H_2) \sum_{j=0}^{3-i} \binom{p-i}{j} A^j_{\lambda_2}(H_2) A^{p-i-j}_{\lambda_3}(H_2).
\end{aligned}
$$

Remark 18. *In general, the p-th-order anomaly numbers of k-th tensor product of orbits of the* H_2 *group are defined recursively as follows:*

$$A^p_{\lambda_1 \otimes \cdots \otimes \lambda_k}(H_2) = A^p_{\lambda_1 \otimes (\lambda_2 \otimes \cdots \otimes \lambda_k)}(H_2), \quad k \in \mathbb{N}^{\geq 2}.$$

3.4. Embedding index

In order to determine the embedding index of an irreducible representation, the branching rule should be defined for a given Lie algebra and its subalgebra (Okubo [**109**]). Such rules have been calculated for numerous irreducible representations of simple Lie algebras (McKay and Patera [**97**]). Applying the branching rule to any orbit of a non-crystallographic reflection group, we can reduce any chosen orbit to a sum of several orbits. Such a decomposition corresponds to the subgroups of a chosen Coxeter group. Dividing the size of an orbit of any Coxeter group by the size of its reduced orbit provides a specific ratio called the embedding index.

G	G'	γ
H_2	A_1	2
H_3	$A_1{\times}A_1{\times}A_1$	1
H_3	A_2	3/2
H_3	H_2	3/2
H_4	$A_2{\times}A_2$	1
H_4	$H_2{\times}H_2$	1
H_4	$A_1{\times}A_1{\times}A_1{\times}A_1$	1
H_4	$H_3{\times}A_1$	1
H_4	A_4	1
H_4	D_4	1

Table 3.3. The embedding index γ provided for the non-crystallographic groups H_n, $n \in \{2, 3, 4\}$ and their maximal subgroups G'.

The index considered in this section depends only on the rank r of a finite reflection group. Whenever any branching rule is established, it takes the same value for all orbits. Given that the embedding index can be obtained for any orbit of a crystallographic reflection group, we demonstrate that this property holds for the non-crystallographic groups H_n, $n \in \{2, 3, 4\}$ as well.

Definition 19. *Let G be a reflection group of order n, and $G_1{\times}\dots{\times}G_k$, $k \leq n$, be a maximal subgroup of G. The second-order index of the embedding $G \hookleftarrow G_1{\times}\dots{\times}G_k$ is given by the formula:*

$$\gamma = \frac{I^2(G)}{I^2(G_1{\times}\dots{\times}G_k)}. \tag{3.4.1}$$

Remark 20. *The formula for the embedding index is generalized for any parameter k. However, in this paper, we focus only on the non-crystallographic cases with $k \in \{2, 3, 4\}$.*

Using the Formula (3.4.1), we calculate the embedding indices γ for any Coxeter group of non-crystallographic type and its maximal subgroup (Table 3.3).

Theorem 21. *For any Coxeter group G of non-crystallographic type, the embedding index γ is a fraction of the ranks, i.e., those of a group G and its maximal subgroup G', namely:*

$$\gamma = \frac{\textit{rank } G}{\textit{rank } G'}.$$

Proof. Let us consider the two cases: (i) rank $G =$ rank G', and (ii) rank $G >$ rank G'.

(i) The elements of any orbit $O_\lambda(G)$ of a group G are found on the surface of a sphere with a finite radius. Applying the branching rule method to λ, we obtain several orbits of the subgroup G' of a group G. Since rank $G' =$ rank G, all elements of orbits of G' are found on the surface of a sphere of the same radius. Since the second-order index is given by the sum of squared distances between the orbit points and the origin, we have that $I^2(G) = I^2(G')$. In such a case, the index γ is equal to 1.

(ii) First, let us recall that for any orbit $O_\lambda(H_3)$, the orbit points have the coordinates (x, y, z) in the $\omega-$basis. In this case, some particular values occur an equal number of times for x, y and z. This property arises due to the impact of the tetrahedral symmetry of the non-crystallographic H_3 group on the orbit points.

For instance, the orbits of any maximal subgroup G' of the Coxeter group H_3 are selected in the following way:

- consider the points of an orbit $O_\lambda(H_3)$;
- remove the first coordinate of each point in the case of H_2, and the third one for the crystallographic group A_2;
- among all the points in $\mathbb{R}^2$ select those with non-negative coordinates; such points provide the orbits of G' in $\mathbb{R}^2$.

Considering the values appearing at each coordinate, the index I^2 of the subgroup G' of H_3 is equal to $\frac{2}{3}I^2(H_3)$. Therefore, the embedding index $\gamma = \frac{3}{2}$. A similar explanation can be provided for the H_2 group. ☐

3.5. Lower orbits of H_2 and H_3

For simple Lie algebras, using the highest weight of an irreducible representation, we can determine its dominant weight multiplicities by subtracting the simple roots (Bremner *et al.* [**21**]). Hence, the computational problem comprises the following components:

- determination of the highest weight;
- subtraction of simple roots from the highest weight;
- an algorithm that describes the subtraction path.

For crystallographic cases, the appearance of dominant weight multiplicities arrises from the non-commutativity of the certain elements of a Lie algebra (Moody and Patera [**100**]; Bremner [**20**]). A similar procedure can be developed and properly applied to individual orbits of the considered non-crystallographic groups. The multiple occurrences of equal dominant weights within one system necessarily involve the same number of dominant points of corresponding lower orbits.

In this section, we only examine the groups H_n, $n \in \{2, 3\}$; their simple roots α_i, $i \in \{1, \dots, n\}$ are provided by the Cartan matrices (Table 3.2). In order to identify all lower orbits of H_2 and H_3, the algorithm contains the following steps:

(i)**:** determine a dominant point $\lambda = (l_1, \dots, l_i)$, $l_i = a_i + b_i\tau \in \mathbb{Z}[\tau]^{>0}$, $i \in \{1, \dots, n\}$;

(ii)**:** establish a correspondence between the coordinates of a dominant point λ and the index $i \in \{1, \dots, n\}$ of a simple root α_i: $i \to l_i$;

(iii)**:** if at least one of $l_i > 0$, $i \in \{1, \dots, n\}$, then proceed the following subtraction:

- if $b_i = 0$, then $\mu_i = \lambda - j \cdot \alpha_i$, $j \in \{1, \dots, a_i\}$;
- if $b_i \geq 1$:
  - and $a_i = 0$, then $\mu_i = \lambda - k\tau \cdot \alpha_i$, $k \in \{1, \dots, b_i\}$;
  - and $a_i \geq 1$, then $\mu_i = \lambda - k\frac{l_i}{gcd(a_i,b_i)} \cdot \alpha_i$, $k \in \{1, 2, \dots, gcd(a_i,b_i)\}$;

(*iv*)**:** replace a point λ in (*i*) with μ_i;

(*v*)**:** repeat the steps (*ii*)–(*iv*) until at least one of the coordinates μ_i is greater than zero.

This recursive method provides a tree-diagram for any dominant point λ of the H_2 and H_3 groups (Figures 3.3–3.5). Such a method allows one to determine the coordinates of dominant points of lower orbits starting from any chosen λ. In order to generalize the formulas for the coordinates, it is convenient to consider the dominant points with their coordinates provided by integer coefficients. Furthermore, to obtain such expressions, we only consider the coordinates of dominant points λ with equal 'dynamic' coefficients. For example, in the case of H_3, if $\lambda = (a, b, 0)$, it is necessary to consider $a = b$. However, for $\lambda = (a, b, c)$ and $a, b, c > 0$, the number of vertices of a corresponding orbit is $|O_{(a,b,c)}(H_3)| = 120$, and the generalization of the coordinates of lower orbits becomes less apparent. Therefore, this case is omitted in this paper.

Let us consider a dominant point $\lambda = (a, 0)$ of H_2. Hence, we can generalize the coordinates of obtained seed points of lower orbits as follows:

$$
\begin{array}{lll}
(a,0) & & a\in\mathbb{N}; \quad (3.5.1)\\
(a-2k-2,(k+1)\tau), & k\in\left\{0,\dots,\left[\frac{a}{2}\right]-1\right\} & a\in\mathbb{N}^{\geq 2};\\
\left(\frac{a-2k}{2}\tau-\frac{a+2k}{2},2k\tau\right), & k\in\left\{0,\dots,\left[\frac{a}{10}\right]\right\} & a=2n,\, n\in\mathbb{N};\\
\left(\frac{a-2k-1}{2}\tau-\frac{a+2k+1}{2},(2k+1)\tau\right), & k\in\left\{0,\dots,\left[\frac{a-2}{10}\right]\right\} & a=2n+1,\, n\in\mathbb{N}^{\geq 2}.
\end{array}
$$

For a dominant point $\lambda = (a, a)$ of H_2, only half of the dominant points of lower orbits are provided as

$$
\begin{array}{lll}
(a,a),(0,0) & & a\in\mathbb{N};\\
 & & (3.5.2)\\
(a-2k,a+k\tau), & k\in\left\{1,\dots,\left[\frac{a}{2}\right]\right\} & a\in\mathbb{N}^{\geq 2};\\
\left((a-2k)\tau-\frac{a+2k}{2},2k(\tau+1)\right), & k\in\left\{0,\dots,\left[\frac{a-n}{2}\right]\right\} & a=2n,\, n\in\mathbb{N};\\
\left((a-2k-1)\tau-\frac{a+2k+1}{2},(2k+1)\tau\right), & k\in\left\{0,\dots,\left[\frac{a-n}{2}\right]-1\right\} & a=2n+1,\, n\in\mathbb{N}^{\geq 2}.
\end{array}
$$

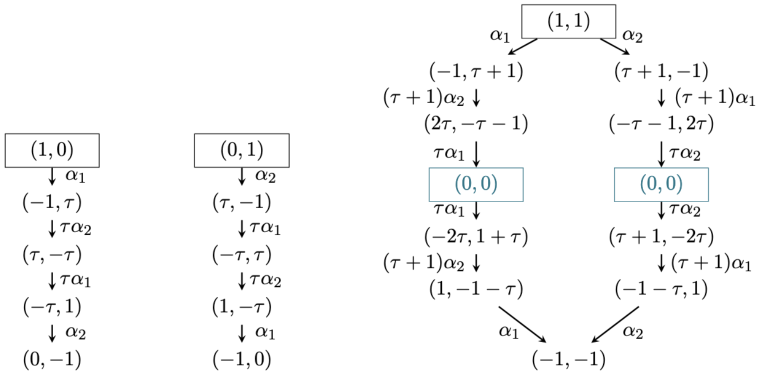

(a) (b) (c)

Fig. 3.3. The tree-diagram for the orbits of H_2. (a) $O_{(1,0)}(H_2)$; (b) $O_{(0,1)}(H_2)$; (c) $O_{(1,1)}(H_2)$. The dominant points are displayed in boxes. The points that do not belong to $O_{(1,1)}(H_2)$ are depicted by blue color.

The formulas for $\lambda = (0, a)$ and the formulas for the other half of the points obtained from $\lambda = (a, a)$ are derived by interchanging the coordinates as $(x, y) \to (y, x)$ of (3.5.1) and (3.5.2), respectively.

For the Coxeter group H_3, the formulas for the coordinates of dominant points of lower orbits are listed in Table 3.4. The notation $\left[\,\cdot\,\right]$ corresponds to the integer part of a number. In order to generalize each case depending on the type of a dominant point, we only consider $a, b, c \in \{1, 2, \ldots, 9\}$. However, such a generalization can be potentially obtained for any $a, b, c \in \mathbb{N}$.

In the case of the H_3 group, applying reflections given by the Formula (3.3.1) to dominant points of lower orbits, we obtain the structures of nested polytopes, with their vertices provided in the $\omega-$basis. In Examples 24 and 25, to demonstrate the geometric structure of nested polytopes in $\mathbb{R}^3$, the orthonormal $\alpha-$ and $\omega-$bases of H_3 defined in (Chen *et al.* [**28**]) are utilized.

The subtraction paths for the non-crystallographic group H_4 can be constructed in a similar way. However, for $a, b, c, d > 0$, an orbit of such a group contains the large number of elements: $|O_{(a,b,c,d)}(H_4)| = 120^2$. In this case, the computational routine becomes laborious. Even though for the non-crystallographic cases, the actual method for determining such multiplicities has not yet been developed, it will likely prove related to determining the multiplicities for crystallographic reflection groups.

In general, to obtain the dominant points of lower orbits, one can choose λ with any non-negative real numbers as its coordinates. As shown in Example 22, the values from the ring $\mathbb{Z}[\tau]$ can as well represent the coordinates of a dominant point λ. However, such a choice does not affect the subtraction path. Moreover, it is worth mentioning that the definitions of indices introduced in previous sections of this paper also apply to any lower orbits obtained using the introduced algorithm.

$(\boldsymbol{a},\mathbf{0},\mathbf{0})$:	
$(a-2k,k,0),\quad k\in\left\{0,\dots,\left[\frac{a}{2}\right]\right\}$	any a
$\left(0,\frac{a}{2}(\tau-1),0\right)$	even a
$\left(0,\left[\frac{a}{2}\right]\tau-\left[\frac{a+2}{2}\right],\tau\right)$	odd $a>3$
$(\mathbf{0},\boldsymbol{a},\mathbf{0})$:	
$(k,a-2k,k\tau),\quad k\in\left\{0,\dots,\left[\frac{a}{2}\right]\right\}$	any a
$(0,0,0),\ \left(\frac{a}{2}(\tau-1),0,\frac{a}{2}\right),\ \left(a,\frac{a}{2}(\tau-1),0\right)$	even a
$\left(\left[\frac{a}{2}\right]\tau-\left[\frac{a+2}{2}\right],\tau+1,\left[\frac{a}{2}\right]-\tau\right),\ \left(a,\left[\frac{a}{2}\right]\tau-\left[\frac{a+2}{2}\right],\tau\right)$	odd $a>3$
$(\mathbf{0},\mathbf{0},\boldsymbol{a})$:	
$(0,k\tau,a-2k),\quad k\in\left\{0,\dots,\left[\frac{a}{2}\right]\right\}$	any a,
$\left(0,\frac{a}{2}(\tau-1),0\right),\ \left(\frac{a}{2}\tau,0,\frac{a}{2}(\tau-1)\right)$	even a
$\left(\left[\frac{a}{2}\right]\tau,\tau,\left[\frac{a}{2}\right]\tau-\left[\frac{a+2}{2}\right]\right),\ \left(\tau+1,\left[\frac{a}{2}\right]\tau-\left[\frac{a+2}{2}\right],0\right)$	odd $a>3$
$(\boldsymbol{a},\boldsymbol{a},\mathbf{0})$:	
$(a,a,0),(0,0,a\tau),(a,a(\tau-1),0)$	any a
$(a-2k,a+k,0),(a+k,a-2k,k\tau),\quad k\in\left\{1,\dots,\left[\frac{a}{2}\right]\right\}$	$a>1$
$\frac{a}{2}(2\tau-1,0,2-\tau),\frac{a}{2}(0,\tau-1,0),\frac{a}{2}(4,\tau-1,0),\frac{a}{2}(0,2-\tau,a)$	even a
$(a,(a-1)\tau-(a+1),2\tau)$	$a>4$
$\left(2a,\left[\frac{a}{2}\right]\tau-\left[\frac{a}{2}+1\right],\tau\right),\ \left(0,\left[\frac{a}{2}\right]\tau-\left[\frac{a}{2}+1\right],\tau\right)$	odd $a>3$
$(a,(a-2)\tau-(a+2),4\tau)$	$a>8$
$(\boldsymbol{a},\mathbf{0},\boldsymbol{a})$:	
$(a,0,a),\ (a\tau,0,0)$	any a
$(a-2k,k,a),\ (a,k\tau,a-2k),\quad k\in\left\{1,\dots,\left[\frac{a}{2}\right]\right\}$	$a>1$,
$\left(0,(a-2k-1)\tau-\left[\frac{a}{2}+k+1\right],(2k+1)(\tau+1)\right),\quad k\in\left\{0,\dots,\left[\frac{a-2}{4}\right]\right\}$	$a>1$
$\frac{a}{2}(0,1,0),\frac{a}{2}(\tau+2,0,\tau-1),\frac{a}{2}(1,0,2-\tau),\frac{a}{2}(\tau-1,0,2\tau-1)$	even a
$\left(0,(a-2k)\tau-\frac{a}{2}-k,2k(\tau+1)\right),\quad k\in\left\{0,\dots,\left[\frac{a}{4}\right]\right\}$	
$\left(\tau+2,\left[\frac{a}{2}\right]\tau-1,0\right)$	odd $a>1$
$\left(\left[\frac{a}{2}\right]\tau+a,\tau,\left[\frac{a}{2}\right]\tau-\left[\frac{a}{2}+1\right]\right),\ \left(\left[\frac{a}{2}\right]\tau-\left[\frac{a}{2}+1\right],\tau+1,(a-1)\tau-\left[\frac{a}{2}+1\right]\right)$	odd $a>3$
$\left(2\tau+4,\left(\frac{a}{2}-1\right)\tau-2,0\right)$	even $a>4$
$\left(3\tau+6,\left[\frac{a}{2}-1\right]\tau-3,0\right)$	odd $a>5$
$(\mathbf{0},\boldsymbol{a},\boldsymbol{a})$:	
$(0,a,a),(a(\tau+1),0,0)$	any a
$(k,a-2k,k\tau+a),\ (0,k\tau+a,a-2k),\quad k\in\left\{1,\dots,\left[\frac{a}{2}\right]\right\}$	$a>1$
$(0,0,a),\frac{a}{2}(2\tau-1,0,\tau),\ \left(0,\frac{a}{2}(\tau-1),0\right)$	even a
$\left(\left(\frac{a}{2}-k\right)(\tau+1),2k(\tau+1),(a-2k)\tau-\left[\frac{a}{2}+k\right]\right)$	even a
$\left(a,(a-2k)\tau-\frac{a}{2}-k,2k(\tau+1)\right),\quad k\in\left\{0,\dots,\left[\frac{a}{4}\right]\right\}$	
$\left(\left[\frac{a}{2}-k\right](\tau+1),(2k+1)(\tau+1),(a-2k-1)\tau-\left[\frac{a}{2}+k+1\right]\right)$	odd $a>1$
$\left(a,(a-2k-1)\tau-\left[\frac{a}{2}+k+1\right],(2k+1)(\tau+1)\right),\quad k\in\left\{0,\dots,\left[\frac{a-3}{4}\right]\right\}$	
$\left((a-1)\tau-\left[\frac{a}{2}+1\right],2\tau+1,\left[\frac{a}{2}-1\right]\tau-1\right)$	odd $a>3$

Table 3.4. Dominant points for lower orbits obtained by subtraction of the simple roots $\alpha_1,\alpha_2,\alpha_3$ of H_3 are listed for any type of a dominant point of the initial orbit: $(a,0,0)$, $(0,a,0)$, $(0,0,a)$, $(a,a,0)$, $(0,a,a)$, $(a,0,a)$. The coefficients are provided by the values $a\in\{1,2,\dots,9\}$.

Example 22. *Let us consider the orbit of the non-crystallographic group H_2 arising from the dominant point with at least one irrational coordinate, namely $(\tau, 1)$. The subtraction of the simple roots α_1 and α_2 of H_2 yields the tree-diagram shown in Figure 3.4.*

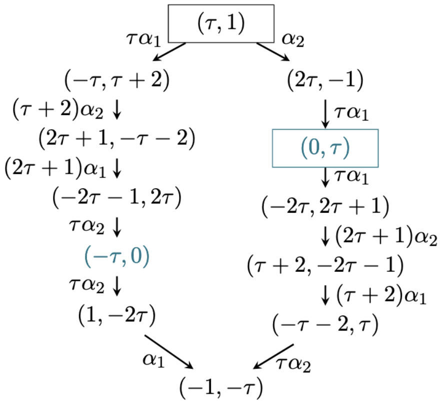
(τ, 1)
τα1
α2
(−τ, τ + 2)
(2τ, −1)
(τ + 2)α2
τα1
(2τ + 1, −τ − 2)
(0, τ)
(2τ + 1)α1
τα1
(−2τ − 1, 2τ)
(−2τ, 2τ + 1)
τα2
(2τ + 1)α2
(−τ, 0)
(τ + 2, −2τ − 1)
τα2
(τ + 2)α1
(1, −2τ)
(−τ − 2, τ)
α1
τα2
(−1, −τ)

Fig. 3.4. The tree-diagram for the orbit $O_{(\tau,1)}(H_2)$. The dominant points are displayed in boxes. The points that do not belong to $O_{(\tau,1)}(H_2)$ are depicted by blue color.

Example 23. *Consider the orbits of H_3 with the dominant points $(1, 0, 0)$ and $(0, 0, 1)$. The coordinates of the orbit-points are obtained from the tree-diagrams provided in Figure 3.5.*

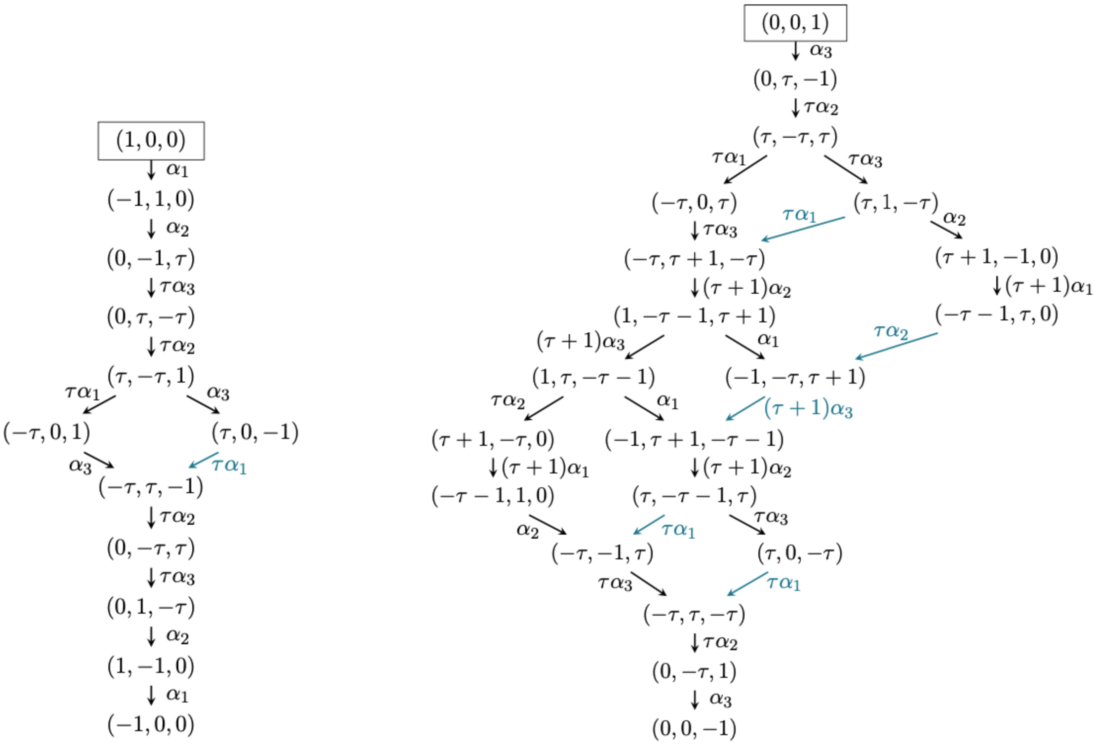
(1, 0, 0)
α1
(−1, 1, 0)
α2
(0, −1, τ)
τα3
(0, τ, −τ)
τα2
(τ, −τ, 1)
τα1
α3
(−τ, 0, 1)
(τ, 0, −1)
α3
τα1
(−τ, τ, −1)
τα2
(0, −τ, τ)
τα3
(0, 1, −τ)
α2
(1, −1, 0)
α1
(−1, 0, 0)
(0, 0, 1)
α3
(0, τ, −1)
τα2
(τ, −τ, τ)
τα1
τα3
(−τ, 0, τ)
(τ, 1, −τ)
τα1
α2
τα3
(−τ, τ + 1, −τ)
(τ + 1, −1, 0)
(τ + 1)α2
(τ + 1)α1
(1, −τ − 1, τ + 1)
(−τ − 1, τ, 0)
(τ + 1)α3
α1
τα2
(1, τ, −τ − 1)
(−1, −τ, τ + 1)
τα2
α1
(τ + 1)α3
(τ + 1, −τ, 0)
(−1, τ + 1, −τ − 1)
(τ + 1)α1
(τ + 1)α2
(−τ − 1, 1, 0)
(τ, −τ − 1, τ)
α2
τα1
τα3
(−τ, −1, τ)
(τ, 0, −τ)
τα3
τα1
(−τ, τ, −τ)
τα2
(0, −τ, 1)
α3
(0, 0, −1)

(*a*) (*b*)

Fig. 3.5. The tree-diagrams constructed for the orbits of H_3. (*a*) $O_{(1,0,0)}(H_3)$; (*b*) $O_{(0,0,1)}(H_3)$. The subtraction paths that yield already existing points are marked by blue color.

Example 24. *Consider the orbit of H_3 with the seed point $(2, 0, 0)$. As shown in the tree-diagram below, such an orbit has two lower orbits with the dominant points $(0, 1, 0)$ and $(0, -\tau', 0)$, where $\tau' = 1 - \tau$. The nested polytopes are generated as presented in Figure 3.6.*

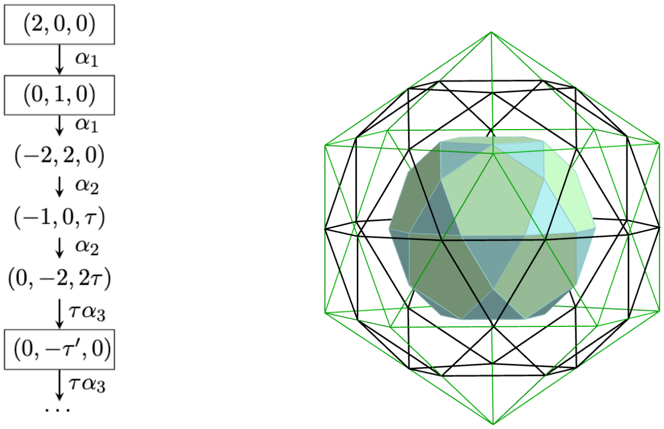

(a) (b)

Fig. 3.6. (a) The tree-diagram for the orbit $O_{(2,0,0)}(H_3)$; (b) the corresponding nested polytopes. The orbits $O_{(2,0,0)}(H_3)$, $O_{(0,1,0)}(H_3)$ and $O_{(0,-\tau',0)}(H_3)$ are presented in green, black and bold colors, respectively.

Example 25. *Consider the orbits $O_{(3,1,0)}(H_3)$ and $O_{(0,1,3)}(H_3)$. Applying the subtraction of the simple roots, we find the following dominant points of lower orbits:*

$$(3, 1, 0): \quad (3, 1, 0), (1, 2, 0), (2, 0, \tau), (0, 1, \tau);$$

$$(0, 1, 3): \quad (0, 1, 3), (0, \tau + 1, 1), (\tau + 1, 0, 2), (\tau + 1, \tau - 1, 2\tau - 2).$$

Both of the nested polytopes consist of four orbits of different radii, as shown in Figure 3.7. Depending on the radius of each orbit that is descending from left to right, they are distinguished by cyan, blue, green and black colors.

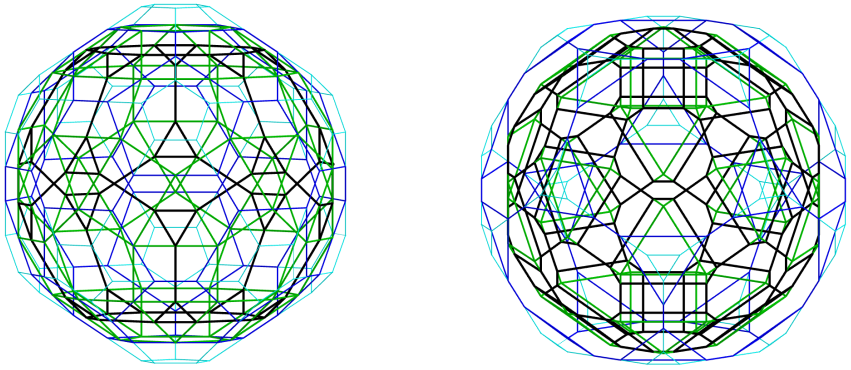

(a) (b)

Fig. 3.7. The nested polytopes provided by the algorithm of root-subtraction. (a) $O_{(3,1,0)}(H_3)$; (b) $O_{(0,1,3)}(H_3)$.

3.6. Concluding remarks

- The decomposition of a tensor product of representations of a simple Lie algebra into a direct sum of irreducible components given by Young tableaux symmetries plays an essential role in physics. As the indices of the representations help to determine such a decomposition (Háková *et al.* [**57**]), we demonstrate that their definitions can be extended to orbits of the non-crystallographic Coxeter groups. As a result, the notation of the even- and odd-order indices of representations are reformulated for the orbits of H_n, $n \in \{2,3,4\}$.
- It would be useful to generalize the properties of higher-order indices and anomaly numbers of orbits, similarly to (Patera *et al.* [**115**]; Patera and Sharp [**115**]). Along with these properties, one could potentially obtain the formulas for the explicit forms of higher even-order indices of a tensor product of orbits. Moreover, the expressions for the even-order indices, anomaly numbers and embedding indices could be reformulated and adapted to orbits of any finite reflection group of crystallographic type.
- Even though the Coxeter groups of non-crystallographic types do not have underlying Lie algebras, the recursive algorithm introduced in Section 3.5 is shown to be similar to the algorithm developed for the weight multiplicities of simple Lie groups (Bremner *et al.* [**21**]). It is important to mention that our algorithm also provides the seed points of orbits that are smaller in radius than an initial orbit (referred to as 'lower orbits'). The geometrical construction of sets of lower orbits results in the structures of nested polytopes. Since the recursive rules are only applied to a dominant point λ of the non-crystallographic groups H_2 and H_3, one could consider applying them to any seed point of the H_4 group as well. As the size of an orbit $|O_{(a,b,c,d)}(H_4)| = 120^2$, for $a,b,c,d > 0$, the generalization of the formulas for the coordinates of the seed points of lower orbits is considered as future research. Moreover, it would be an interesting task to generalize the formulas given in Table 3.4 for any $a \in \mathbb{N}$, as it was done for the H_2 case.

Acknowledgments

The authors are grateful to Dr. A. Patera for helpful comments and editorial assistance. The authors gratefully acknowledge support from the Natural Sciences and Engineering Research Council of Canada (NSERC), Grant No. RGPIN-2016-04199.

Chapter 4

On symmetry breaking of dual polyhedra of the non-crystallographic group H_3

by

Mariia Myronova[1]

(1) Département de Physique, Université de Montréal, Complexe des Sciences,
1375 Avenue Thérèse-Lavoie-Roux, Montréal, H2V 0B3, Québec, Canada
maria.myronova@umontreal.ca

This article has been accepted for publication in Acta Crystallographica Section A: Foundations and Advances.

Author contributions: conceptualization, M.M., J.P.; writing and editing, M.M.; calculation, M.M.; visualization, M.M.

RÉSUMÉ. L'étude des polyèdres décrits dans cet article est pertinente pour la symétrie icosaédrique dans l'assemblage de diverses molécules sphériques, biomolécules et virus. Un mécanisme de brisure de symétrie est appliqué à la famille des $\mathcal{V}_{H_3}(\lambda)-$polytopes construits pour chaque type de point dominant λ. Dans cette étude, un polytope $\mathcal{V}_{H_3}(\lambda)$ est considéré comme un dual d'un $\mathcal{D}_{H_3}(\lambda)-$polytope obtenu à partir de l'action du groupe de Coxeter H_3 sur un seul point $\lambda \in \mathbb{R}^3$. La symétrie de H_3 est réduite à la symétrie de ses sous-groupes bidimensionnels H_2, $A_1 \times A_1$ et A_2 qui servent à examiner la structure géométrique de $\mathcal{V}_{H_3}(\lambda)-$polytopes. Ce dernier est présenté comme un empilement d'orbites paralléles circulaires/polygonales connues sous le nom de 'pancake'-structure d'un polytope. L'insertion de plus d'orbites dans une décomposition orbitale aboutit à l'extension de la $\mathcal{V}_{H_3}(\lambda)-$structure dans divers nanotubes. De plus, puisqu'un $\mathcal{V}_{H_3}(\lambda)-$polytope peut contenir les orbites obtenues par l'action de H_3 sur les points de départ $(a,0,0)$, $(0,b,0)$ et $(0,0,c)$ dans sa structure, les stellations des $\mathcal{V}_{H_3}(\lambda)-$polytopes à face plane sont construites chaque fois que les rayons de ces orbites sont correctement mis à l'échelle. Enfin, puisque le fullerène C_{20} a la structure dodécaédrique de $\mathcal{V}_{H_3}(a,0,0)$, la construction des plus petits fullerènes C_{24}, C_{26}, C_{28}, C_{30} avec les nanotubes C_{20+6N}, C_{20+10N} sont présentés.
Mots clés : groupe de Coxeter, double polytope, décomposition en orbite, fullerène, nanotube, polytope étoilé

ABSTRACT. The study of the polyhedra described in this paper is relevant to the icosahedral symmetry in the assembly of various spherical molecules, biomolecules and viruses. A symmetry-breaking mechanism is applied to the family of polytopes $\mathcal{V}_{H_3}(\lambda)$ constructed for each type of dominant point λ. Here a polytope $\mathcal{V}_{H_3}(\lambda)$ is considered as a dual of a $\mathcal{D}_{H_3}(\lambda)-$polytope obtained from the action of the Coxeter group H_3 on a single point $\lambda \in \mathbb{R}^3$. The H_3-symmetry is reduced to the symmetry of its two-dimensional subgroups H_2, $A_1 \times A_1$ and A_2 that are used to examine the geometric structure of $\mathcal{V}_{H_3}(\lambda)-$polytopes. The latter is presented as a stack of parallel circular/polygonal orbits known as the 'pancake'-structure of a polytope. Inserting more orbits into an orbit decomposition results in the extension of the $\mathcal{V}_{H_3}(\lambda)-$structure into various nanotubes. Moreover, since a $\mathcal{V}_{H_3}(\lambda)-$polytope may contain the orbits obtained by the action of H_3 on the seed points $(a,0,0)$, $(0,b,0)$ and $(0,0,c)$ within its structure, the stellations of flat-faced $\mathcal{V}_{H_3}(\lambda)-$polytopes are constructed whenever the radii of such orbits are appropriately scaled. Finally, since the fullerene C_{20} has the dodecahedral structure of $\mathcal{V}_{H_3}(a,0,0)$, the construction of the smallest fullerenes C_{24}, C_{26}, C_{28}, C_{30} together with the nanotubes C_{20+6N}, C_{20+10N} is presented.
Keywords: Coxeter group, dual polytope, orbit decomposition, fullerene, nanotube, stellated polytope

4.1. Introduction

Finite reflection groups (known as Coxeter groups) underlie many structural phenomena found in nature. There are two types of finite reflection groups: crystallographic groups (or Weyl groups) and non-crystallographic ones. Unlike the Weyl groups, the non-crystallographic ones are not related to a corresponding Lie algebra. There are three non-crystallographic Coxeter groups with 5-fold symmetry: H_2 (dihedral group), H_3 (icosahedral group) and H_4 of order 10, 120 and 14400, correspondingly (Chen *et al.* [**28**]). The Coxeter group H_4 does not have an official name in physics, even though it contains all the other non-crystallographic groups within it ($H_2 \subset H_3 \subset H_4$). In general, such groups are used to describe aperiodic sets of points (or quasi-crystals) and various spherical molecules (Moody and Patera [**104**]; Moody *et al.* [**98**]; Dechant *et al.* [**36**]; Dechant *et al.* [**37**]; Baake and Grimm [**10**]; Zappa [**149**]; Salthouse *et al.* [**130**]).

The icosahedral symmetry of the non-crystallographic group H_3 is versatile in its applications in physics and chemistry; it provides the description of molecular structures and density maps of macromolecules, such as proteins and nucleic acids [for instance, see (Atiyah and Sutcliffe [**7**]; Terwilliger [**138**])]. As well, the H_3-symmetry is relevant in the description of various spherical molecules and viruses. The theory established in (Caspar and Klug [**27**]) proposed an elegant conceptualization of the structural organization of simple viruses in terms of triangulations. It had a significant impact on further research in biophysics and mathematical virology (Twarock and Luque [**143**]). In the work of (Twarock [**142**]; Keef and Twarock [**74**]), the icosahedral group H_3 is considered as an indispensable tool for representation of the architecture and structural assembly of spherical viruses. The dynamic virus structure (a nucleocapsid that further adapts to a specific host) has the form of a viral genome enclosed inside of a viral capsid (Aznar *et al.* [**9**]). The latter most commonly possess helical or icosahedral symmetry (Kerner [**76**]). Moreover, cone- and rod-shaped capsid structures have also been observed, and the latter has been recognized to have helical symmetry. (Carter & Saunders, 2007; Prasad & Schmid, 2012).

There are interesting connections between icosahedral viruses and fullerene molecules, which are presented in (Dechant *et al.* [**38**]). In general, the Coxeter group H_3 plays an important role in describing the structures of icosahedral fullerenes (Dresselhaus *et al.* [**46**]). Ever since the discovery of the fullerene C_{60} (Kroto *et al.* [**84**]) (also referred to as *Buckminsterfullerene*, or *"buckyball"*), it remains the most famous representative of its large family. Another important category of fullerenes are carbon nanotubes. The latter are particularly interesting due to their astonishing physical and mechanical properties (Eletskii and Smirnov [**49**]; Balandin [**11**]) and wide range of specialized applications (Pandolfo and Hollenkamp [**113**]; Zhang *et al.* [**152**]). For example, single- and multi-wall carbon nanotubes are used for more efficient drug delivery, i.e., for transporting and translocating therapeutic molecules (Bianco *et al.* [**12**]).

Recognizing the importance of the H_3 group in the assembly of icosahedral molecules, such as viruses and fullerenes, in this paper, we examine in detail the dual polyhedra of non-crystallographic type $V_{H_3}(\lambda)$. The main goal is to extend the structures of $V_{H_3}(\lambda)$ to tube-like structures, such as carbon nanotubes, considering a well-known mechanism described in (Bodner *et al.* [**13**], [**14**], [**15**]). A connection between the family of $V_{H_3}(\lambda)-$polyhedra and the structures of spherical viruses, biomolecules and fullerenes warrants the study of chosen polytopes in mathematical generality. However, it is important to note that fullerene structures are subject to several physical constraints, such as valency, bond length, and the angles between the bonds (e.g., the molecule C_{20} might be less stable because of the extreme conditions (Wang *et al.* [**145**]), which might also give a physical criterion for inserting orbits at certain distances from the mathematical point of view). Therefore, some of the resulting tube-like structures coming out of the approach later in this paper might violate these physical constraints at face value. Nonetheless, for simplicity, we will refer to all such structures as “fullerenes”, but this should be understood in a broader sense. We defer discussion of the concrete physical constraints and focus on the extensive interest that the description of such structures provides in the context of understanding virus structures, nanocages, fulleroids and multi-shell nanostructures.

Adapting the notations of (Champagne *et al.* [**29**]), the polytopes generated by the action of the Coxeter group H_3 on a single point $\lambda \in \mathbb{R}^3$ are denoted as $\mathcal{D}_{H_3}(\lambda)-$polytopes, and those that are generated from the face of highest dimension (in this case, polygons) are referred to as $\mathcal{V}_{H_3}(\lambda)-$polytopes. The polytopes considered in this study are uniform convex polytopes. The notations $\mathcal{D}$ and $\mathcal{V}$ stand for Delaunay and Voronoi domains. The duality between $\mathcal{D}(\lambda)-$ and $\mathcal{V}(\lambda)-$polytopes is well-established, as the proximity cells of the vertices of one form a dual tiling of the sphere of another one (Moody and Patera [**103**]). Both of them are invariant under the action of H_3. Such structures are commonly known in solid-state physics as Brillouin zones and Wigner-Seitz cells.

As the vertices of any $\mathcal{D}_{H_3}(\lambda)-$polytope belong to one orbit $O_{H_3}(\lambda)$, it is convenient to characterize both by a dominant point (or a seed point) $\lambda = (a, b, c)$, i.e., the point that has non-negative coordinates in the $\omega-$basis (Section 4.2). Such a point is unique for each orbit, and it lies within the fundamental region F (Section 4.3). The size of an orbit depends only on a choice of λ, and it is always finite. Depending on the coordinates of λ (whether some of them are zero or not), eight types of dominant points are possible to consider (up to topology). Since the orbit with the coordinates $a,b,c = 0$ contains only one point (the origin), this case is omitted. For the other seven types of seed points, the coordinates of λ with equal values of a, b and/or c are usually examined, as such cases yield regular $\mathcal{D}(\lambda)-$polytopes.

Employing the Wythoff construction (Chen *et al.* [**28**]), we can build a Euclidean (a polytope with the flat faces) or a spherical polytope. The latter is usually obtained from a central projection of a flat-faced polytope onto the surface of a sphere (Figure 4.4). In the case of a flat-faced polytope, although several types of regular polygons can represent the two-dimensional faces of $\mathcal{D}(\lambda)$, those of $\mathcal{V}(\lambda)$ are only of one type, and they are not necessarily regular. Depending on the type of seed point λ, the dual pairs of flat-faced polytopes, $\mathcal{D}_{H_3}(\lambda)$ and $\mathcal{V}_{H_3}(\lambda)$, are shown in Figure 4.1.

Owing to the fact that any finite reflection group has a corresponding Coxeter–Dynkin diagram, the recursive decoration technique applied to the nodes of a diagram was developed in (Moody and Patera [**103**]) and later adapted in (Champagne *et al.* [**29**]). The recursive decoration rules are recalled in Section 4. It follows from the decoration of a Coxeter–Dynkin diagram that $\mathcal{V}_{H_3}(\lambda)-$polytopes (except the self-dual pair dodecahedron-icosahedron) may contain three types of appropriately scaled orbits arising from the action of H_3 on the dominant points $(a, 0, 0)$, $(0, b, 0)$ and $(0, 0, c)$ (Table 4.3). Here these orbits are called *generic.* Even though the decoration method is not extensively used, it thoroughly provides all the pertinent information about the types and multiplicities of faces of any n-dimensional polytope and its dual (Section 5). Scaling the radii of such orbits (Section 4.6), we obtain the stellations of $\mathcal{V}_{H_3}(\lambda)-$polytopes (Coxeter [**33**]; Shephard [**132**]) presented in Section 4.7.

During the past decades, there were several attempts to generate a complete list of fullerene isomers: the spiral algorithm (Manolopoulos *et al.* [**95**]), the algorithm using folding nets (Yoshida and Osawa [**148**]), the algorithm based on the stitching of patches bounded by a zigzag (Brinkmann and Dress [**22**]; Brinkmann *et al.* [**23**]). However, as here only the polytopes with H_3-symmetry are considered, a remarkable approach to a structural extension of the fullerene C_{60} (the truncated icosahedron) explicitly described in (Bodner *et al.* [**13**], [**14**], [**15**]) serves as a powerful tool to our research. In these papers, the vertices of C_{60} are split between the parallel circular/polygonal orbits depending on the symmetry of a two-dimensional subgroup $G' \subset H_3$. The reduction of the icosahedral symmetry $H_3 \to H_2 \times A_1$, $H_3 \to A_2 \times A_1$, $H_3 \to A_1 \times A_1 \times A_1$ determines the ‘pancake’-decomposition of C_{60} (Bodner *et al.* [**13**]). Depending on the order of G', there is a specific number of points that belong to each two-dimensional orbit. Knowing the ‘pancake’-structure of a polytope, its symmetry can be broken, and more circular/polygonal orbits can be inserted in the middle of a decomposition. Therefore, the extension of the structure of C_{60} results in the larger fullerene molecules and closed nanotubes. In this case, preserving a distance between inserted orbits allows to retain the edge lengths and the angles essential for fullerene structures. Recently this approach have been applied to the rhombicosidodecahedron and the truncated dodecahedron, since both contain 60 vertices within their structures (Bourret and Grabowiecka [**18**]).

Inspired by the work done for the molecule C_{60}, here a symmetry-breaking mechanism is applied to the family of dual polyhedra $\mathcal{V}_{H_3}(\lambda)$. Even though these polytopes are well-known, the possible ways to extend their structures were not previously explored. The pertinent information about the 'pancake'-structure of an icosahedral polytope is recalled in Section 4.8. The results of the orbit decompositions for $\mathcal{V}_{H_3}(\lambda)$ are presented for every type of dominant point λ in Appendix A. The points determining each 'pancake' of $\mathcal{V}_{H_3}(\lambda)-$polytopes, the numbers of points of two-dimensional orbits and the corresponding numerical values of the squared radii are presented in Appendix B.

In this study, there are two ways to consider in order to extend the structure of a polytope $\mathcal{V}_{H_3}(\lambda)$ by using its 'pancake'-structure: (i) duplicating the middle 'pancakes' and inserting them back into a polytope while preserving the spacing between them; (ii) constructing a two-dimensional tiling, rolling it onto a cylinder and seamlessly closing both ends with half-polytopes. In Section 4.9, taking into account both approaches, we construct the closed tubes. Naturally, there are many possibilities to tile a two-dimensional plane with regular, non-regular and star polygons (Grünbaum and Shephard [**55**]). However, as we are restricted by the symmetries of the H_3 group and its two-dimensional subgroups, the scope significantly decreases to a few choices. To preserve the number of points of each 'pancake,' only the certain types of tilings in $\mathbb{R}^2$ are considered, for instance, see Figure 4.24.

Finally, since the fullerene C_{20} has the dodecahedral structure of $\mathcal{V}_{H_3}(a, 0, 0)$, its symmetry breaking is considered independently in Section 4.10. The molecule C_{20} is the only fullerene smaller than C_{60} that has the icosahedral symmetry. Although breaking the symmetry of a fullerene can be achieved by breaking the symmetry of its dual polytope, here the structure of C_{20} is broken directly by considering the two-dimensional subgroups of the Coxeter group H_3. Including more orbits in the 'pancake'-structure, the fullerene C_{20} is extended into the hollow cage nanotubes C_{20+6N} and C_{20+10N}, where N indicates the number of inserted circular/polygonal orbits. Moreover, unfolding C_{20} in $\mathbb{R}^2$ yields the net of pentagons that is further modified by inserting up to five hexagons (Figure 4.32). In this case, folding the constructed nets to achieve a spheroidal molecular structure, the fullerenes C_{24}, C_{26}, C_{28} and C_{30} are obtained.

4.2. Bases of the icosahedral group H_3

4.2.1. The $\alpha-$ and $\omega-$bases

Any finite reflection group G of rank n has a corresponding root system (Deodhar [**41**]). The pertinent information about a root system can be extracted from a corresponding Coxeter–Dynkin diagram. The nodes of a diagram are usually labeled by the generators

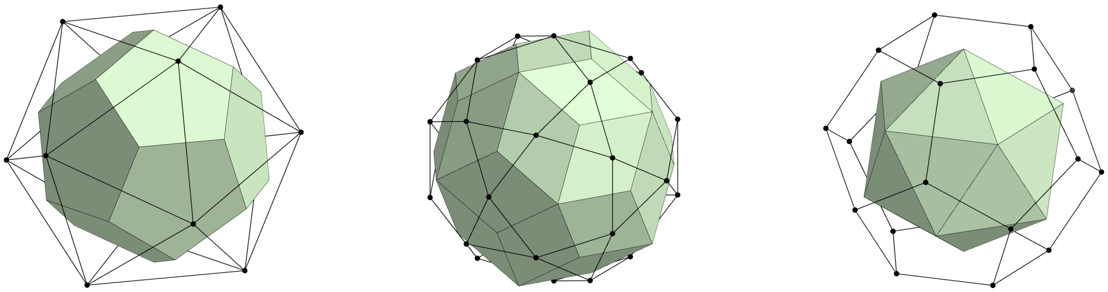

$\lambda = (a, 0, 0)$

Icosahedron –
Dodecahedron

$\lambda = (0, b, 0)$

Icosidodecahedron –
Rhombic triacontahedron

$\lambda = (0, 0, c)$

Dodecahedron –
Icosahedron

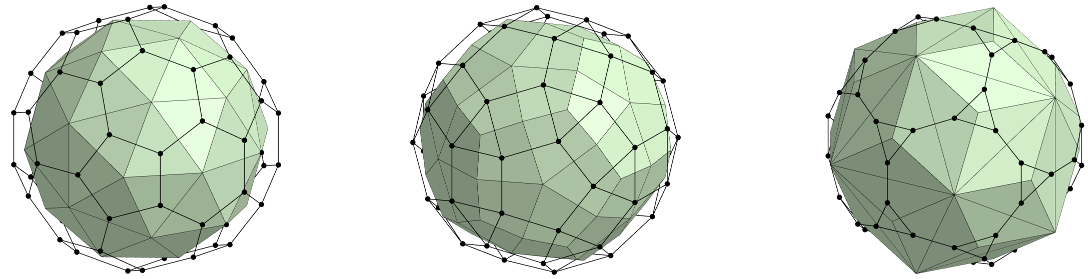

$\lambda = (a, b, 0)$

Truncated icosahedron –
Pentakis dodecahedron

$\lambda = (a, 0, c)$

Rhombicosidodecahedron –
Deltoidal hexecontahedron

$\lambda = (0, b, c)$

Truncated dodecahedron –
Triakis icosahedron

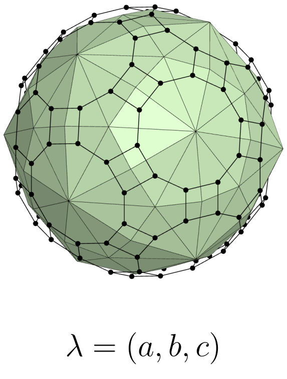

$\lambda = (a, b, c)$

Truncated icosidodecahedron –
Disdyakis triacontahedron

Fig. 4.1. The dual pairs of polytopes of the Coxeter group H_3 are constructed for each type of dominant point λ.

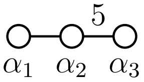

Fig. 4.2. The Coxeter–Dynkin diagram of the non-crystallographic group H_3. The nodes of the diagram are labeled by the simple roots α_k, $k \in \{1,2,3\}$. The links between the nodes provide the relative angles between the simple roots: $\angle(\alpha_1,\alpha_2) = \frac{2\pi}{3}$, $\angle(\alpha_2,\alpha_3) = \frac{4\pi}{5}$, $\angle(\alpha_1,\alpha_3) = \frac{\pi}{2}$.

of the finite reflection group, i.e., the reflections r_k passing across the corresponding reflecting hyperplanes (mirrors) m_k, $k \in \{1,2,\dots,n\}$. The simple roots α_k are the normal vectors to m_k, and we use them to label the nodes of a Coxeter–Dynkin diagram. The links of a diagram correspond to the relative angles between the vectors α_k. The Coxeter–Dynkin diagram of the non-crystallographic group H_3 is presented in Figure 4.2.

For the Coxeter group H_3, the lengths of the simple roots α_k, $k \in \{1,2,3\}$ and the relative angles between them are provided by the Cartan matrix:

$$C_{H_3} = (\langle \alpha_j, \alpha_k \rangle) = \begin{pmatrix} 2 & -1 & 0 \\ -1 & 2 & -\tau \\ 0 & -\tau & 2 \end{pmatrix}, \tag{4.2.1}$$

where $\langle \cdot, \cdot \rangle$ is the standard scalar product, and τ denotes the positive solution of the quadratic equation $x^2 - x - 1 = 0$ known as the golden ratio,

$$\tau = \frac{1}{2}(1+\sqrt{5}) \approx 1.618, \quad \tau' = \frac{1}{2}(1-\sqrt{5}) = -\frac{1}{\tau} \approx -0.618. \tag{4.2.2}$$

The basis of the fundamental weights is known as the $\omega-$basis. The lengths of ω_k-vectors, as well as the relative angles between them, are provided by the inverse of the Cartan matrix (4.2.1):

$$C_{H_3}^{-1} = (\langle \omega_j, \omega_k \rangle) = \frac{1}{2} \begin{pmatrix} 2+\tau & 2+2\tau & 1+2\tau \\ 2+2\tau & 4+4\tau & 2+4\tau \\ 1+2\tau & 2+4\tau & 3+3\tau \end{pmatrix}. \tag{4.2.3}$$

The duality relation between the $\alpha-$ and $\omega-$bases is given by the scalar product $\langle \cdot, \cdot \rangle$ as

$$\langle \alpha_j, \omega_k \rangle = \delta_{jk}, \quad j,k \in \{1,2,3\}, \tag{4.2.4}$$

where δ_{jk} is the Kronecker delta.

Hence, using the Cartan matrix and its inverse, we can relate the two bases as follows:

$$\alpha_j = \sum_{k=1}^{3} C_{H_3}\omega_k, \quad \omega_k = \sum_{j=1}^{3} C_{H_3}^{-1}\alpha_j.$$

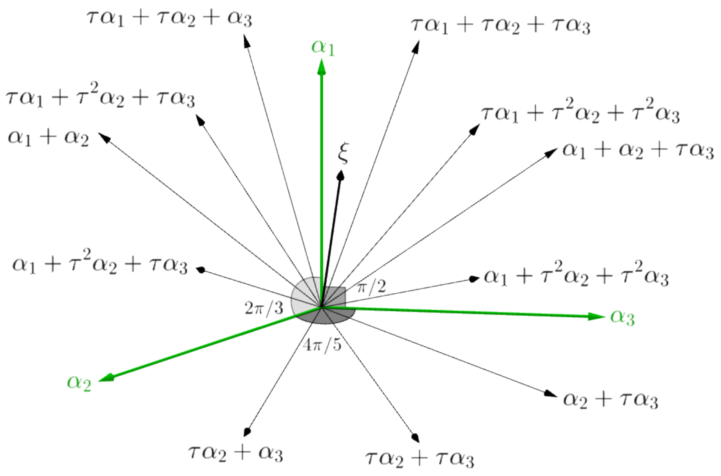
$\tau\alpha_1+\tau\alpha_2+\alpha_3$
α_1
$\tau\alpha_1+\tau\alpha_2+\tau\alpha_3$
$\tau\alpha_1+\tau^2\alpha_2+\tau\alpha_3$
$\tau\alpha_1+\tau^2\alpha_2+\tau^2\alpha_3$
$\alpha_1+\alpha_2$
ξ
$\alpha_1+\alpha_2+\tau\alpha_3$
$\alpha_1+\tau^2\alpha_2+\tau\alpha_3$
$\pi/2$
$\alpha_1+\tau^2\alpha_2+\tau^2\alpha_3$
$2\pi/3$
α_3
$4\pi/5$
α_2
$\alpha_2+\tau\alpha_3$
$\tau\alpha_2+\alpha_3$
$\tau\alpha_2+\tau\alpha_3$

Fig. 4.3. The 15 positive roots of the non-crystallographic group H_3 are presented. The simple roots α_k, $k \in \{1,2,3\}$ are depicted by green color. The root $\xi = \tau\alpha_1 + 2\tau\alpha_2 + \tau^2\alpha_3$ stands for the highest root. The values of the angles between the simple roots α_k are provided.

Using the matrices (4.2.1) and (4.2.3), the simple roots α_k and the fundamental weights ω_k can be written explicitly as

$$\begin{aligned}
\alpha_1 &= 2\omega_1 - \omega_2, & \omega_1 &= \left(1+\tfrac{1}{2}\tau\right)\alpha_1 + (1+\tau)\alpha_2 + \left(\tfrac{1}{2}+\tau\right)\alpha_3,\\
\alpha_2 &= -\omega_1 + 2\omega_2 - \tau\omega_3, & \omega_2 &= (1+\tau)\alpha_1 + (2+2\tau)\alpha_2 + (1+2\tau)\alpha_3,\\
\alpha_3 &= -\tau\omega_2 + 2\omega_3; & \omega_3 &= \left(\tfrac{1}{2}+\tau\right)\alpha_1 + (1+2\tau)\alpha_2 + \tfrac{3}{2}\left(1+\tau\right)\alpha_3.
\end{aligned}$$

4.2.2. The orthonormal bases

The root system of the icosahedral group H_3 contains 30 roots. The 15 positive roots are listed in (Eq. 6.13) of (Champagne *et al.* [**29**]). In Figure 4.3, the positive roots of H_3 are illustrated using the orthonormal bases relative to the $\alpha-$ and $\omega-$bases of H_3 (Chen *et al.* [**28**]):

$$\begin{aligned}
\alpha_1 &= (0,0,1), & \omega_1 &= \tfrac{1}{2}(\tau,0,1),\\
\alpha_2 &= \tfrac{1}{2}(\tau-1,-\tau,-1), & \omega_2 &= (\tau,0,0),\\
\alpha_3 &= (0,1,0); & \omega_3 &= \tfrac{1}{2}(\tau^2,1,0).
\end{aligned} \tag{4.2.5}$$

4.2.3. The mixed bases

The icosahedral group H_3 contains the following two-dimensional subgroups G':

(*i*) H_2, a dihedral group of order 10;
(*ii*) A_2, a dihedral group of order 6;
(*iii*) $A_1 \times A_1$, a dihedral group of order 4;

It is worth mentioning that the crystallographic groups (*ii*) and (*iii*) are the Weyl groups of the Lie algebras A_2 and $A_1 \times A_1$, respectively.

G'	*Diagram*	*Reflections*	*Mixed basis*
H_2	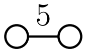	r_2, r_3	$\{\alpha_1, \omega_2, \omega_3\}$
A_2	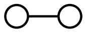	r_1, r_2	$\{\omega_1, \omega_2, \alpha_3\}$
$A_1 \times A_1$	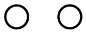	r_1, r_3	$\{\omega_1, \alpha_2, \omega_3\}$

Table 4.1. The two-dimensional subgroups of the Coxeter group H_3.

The reflections generating a subgroup $G' \subset H_3$ can be extracted from the Coxeter–Dynkin diagram (Figure 4.2). We label the nodes of the diagram corresponding to the generators of G' by the vectors ω_k, $k \in \{1, 2, 3\}$. From the duality relation (4.2.4), we have that the vectors ω_i and ω_j, $i, j \in \{1, 2, 3\}$, $i \neq j$ span the plane orthogonal to the vector α_k, $k \in \{1, 2, 3\}$, $k \neq i \neq j$. Hence, for each subgroup G', the mixed basis is formed as presented in Table 4.1.

4.2.4. The ω'−basis

Since it is essential to consider the $\omega-$basis for the construction of flat-faced or spherical $\mathcal{D}(\lambda)-$polytopes, the corresponding $\omega'-$basis that comprises appropriately scaled vectors of the $\omega-$basis can be conveniently utilized in the case of $\mathcal{V}(\lambda)-$polytopes (Champagne *et al.* [**29**]). For the Coxeter group H_3, any dominant (seed) point λ in the $\omega-$basis is provided by the linear combination of the fundamental weights as

$$\lambda = (a, b, c) \equiv a\omega_1 + b\omega_2 + c\omega_3, \quad a, b, c \in \mathbb{Z}^{\geq 0}. \tag{4.2.6}$$

For simplicity, we consider the values of coefficients a, b, c to be equal to zero or one, as they yield the regular $\mathcal{D}_{H_3}(\lambda)-$polytopes.

Using formula (4.2.6), the scaling coefficients a_k are determined by the scalar product $\langle \cdot, \cdot \rangle$ as

$$a_k = \frac{\langle \lambda, \lambda \rangle}{\langle \omega_k, \lambda \rangle}, \tag{4.2.7}$$

where a_k have the form $a + b\tau$, for $a, b \in \mathbb{Q}^{\geq 0}$. Therefore, there is a one-to-one correspondence between the vectors of the $\omega-$ and $\omega'-$bases:

$$\omega'_k = c_k \omega_k, \quad c_k = a_k / a_1,$$

where c_k, $k \in \{1, 2, 3\}$ are the normalized scaling coefficients. Depending on the type of dominant point λ, the values of the coefficients c_k are listed in Table 4.2. Therefore, the dominant points of orbits that are found within the structures of $\mathcal{V}_{H_3}(\lambda)-$polytopes are

λ	c_1	c_2	c_3
$(1,0,0)$	1	$\frac{1}{2}(3-\tau)$	$3\tau-4$
$(0,1,0)$	1	$\frac{1}{2}$	$\tau-1$
$(0,0,1)$	1	$\frac{1}{2}$	$\frac{1}{3}\tau$
$(1,1,0)$	1	$\frac{1}{6}(5-\tau)$	$\frac{1}{3}(5\tau-6)$
$(1,0,1)$	1	$-\frac{3}{2}(\tau-2)$	$-\frac{3}{11}(\tau-4)$
$(0,1,1)$	1	$\frac{1}{2}$	$\frac{1}{11}(8-\tau)$
$(1,1,1)$	1	$\frac{5}{22}(\tau-4)$	$-\frac{5}{3}(\tau-2)$

Table 4.2. Scaling coefficients c_k, $k \in \{1,2,3\}$ for the vectors of the $\omega-$basis.

denoted as $\lambda' \equiv \omega'_k$, $k \in \{1,2,3\}$, and they are provided in terms of the $\omega'-$basis as

$$\begin{aligned}(a',0,0) &\equiv \omega'_1 = c_1\omega_1,\\ (0,b',0) &\equiv \omega'_2 = c_2\omega_2,\\ (0,0,c') &\equiv \omega'_3 = c_3\omega_3.\end{aligned} \tag{4.2.8}$$

4.3. Reflections and reflection graphs

4.3.1. Reflections of the Coxeter group H_3

The action of the reflections r_k on any point $x \in \mathbb{R}^3$ is given by the formula (Humphreys [**67**]; Chen *et al.* [**28**]):

$$r_k x = x - 2\frac{\langle x, \alpha_k\rangle}{\langle \alpha_k, \alpha_k\rangle}\alpha_k, \quad k \in \{1,2,3\}. \tag{4.3.1}$$

However, since the simple roots α_k have the same lengths, we have that $\langle \alpha_k, \alpha_k\rangle = 2$, and formula (4.3.1) takes the simplified form

$$r_k x = x - \langle x, \alpha_k\rangle\alpha_k, \quad k \in \{1,2,3\}. \tag{4.3.2}$$

Taking into account the duality between the $\alpha-$ and $\omega-$bases provided by (4.2.4), formula (4.3.2) can be written as

$$r_k\omega_j = \omega_j - \delta_{jk}\alpha_k, \quad k, j \in \{1,2,3\}. \tag{4.3.3}$$

The three reflections, r_1, r_2 and r_3, satisfy the following identities:

$$r_1^2 = r_2^2 = r_3^2 = 1, \quad (r_1r_2)^3 = 1, \quad (r_2r_3)^5 = 1, \quad (r_1r_3)^2 = 1.$$

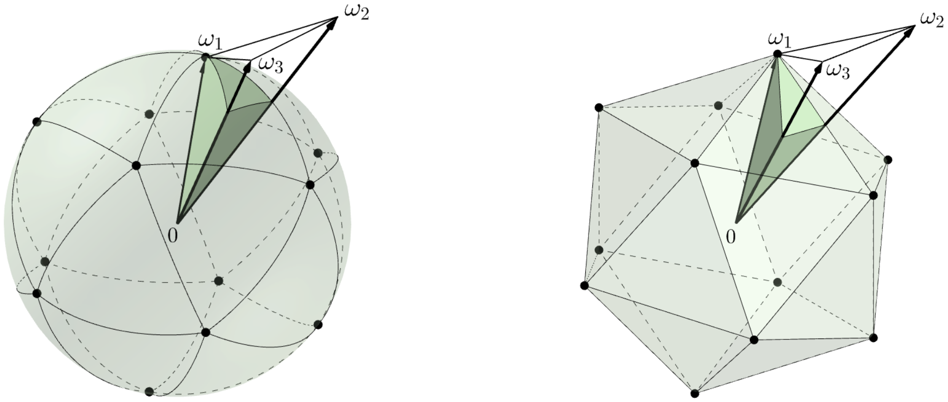

Fig. 4.4. The spherical and Euclidean polytopes are provided by the structure of the icosahedron $\mathcal{D}_{H_3}(1,0,0)$. The vectors ω_k, $k = \{1,2,3\}$ label the fundamental weights. The fundamental region F is provided by the vertices $\{0, \omega_1, \omega_2, \omega_3\}$.

Acting on any point $\lambda \in \mathbb{R}^3$ with the reflections (4.3.3), the points of an orbit $O_{H_3}(\lambda)$ of the icosahedral group H_3 are obtained. The coordinates of λ are commonly chosen in such a way that it does not lie at the intersection of the hyperplanes, i.e., it does not lie at the origin.

4.3.2. The fundamental region of H_3

In the three-dimensional real Euclidean space $\mathbb{R}^3$, the fundamental region F is a tetrahedron that is bounded by the mirrors m_k, $k = \{1,2,3\}$ of H_3, and it is restricted by the tile with the vertices provided by the vectors ω_k, $k \in \{1,2,3\}$ (see Figure 4.4). Any point λ is found within the region bounded by the mirrors or on the boundaries created by them; therefore, it has only non-negative coefficients as its coordinates. In general, scaling the coordinates of λ continuously through the space affects the sizes of one- and two-dimensional faces of a dual pair of polytopes, $\mathcal{D}(\lambda)$ and $\mathcal{V}(\lambda)$; however, it will not change the number of dual faces, their multiplicities and their intersections (Champagne *et al.* [**29**]).

4.3.3. Reflection graphs

The reflection graph is an amazing feature naturally arising from the actions of the reflections of any finite reflection group G on a single point in space. Such a graph is embedded in the construction of a polytope of any dimension. The reflection graph starts at the dominant point λ and ends at $-\lambda$. It has the form of a directed acyclic graph formed by the vertices of a polytope and the edges that are oriented from one vertex to another. For such a graph, the edges do not necessarily coincide with the one-dimensional faces of a considered polytope (for instance, see Figure 4.5(a)). The number of directed edges arising from any vertex of the reflection graph depends only on the number of positive entries in each vertex's coordinates. Therefore, since we are restricted by three dimensions, we may

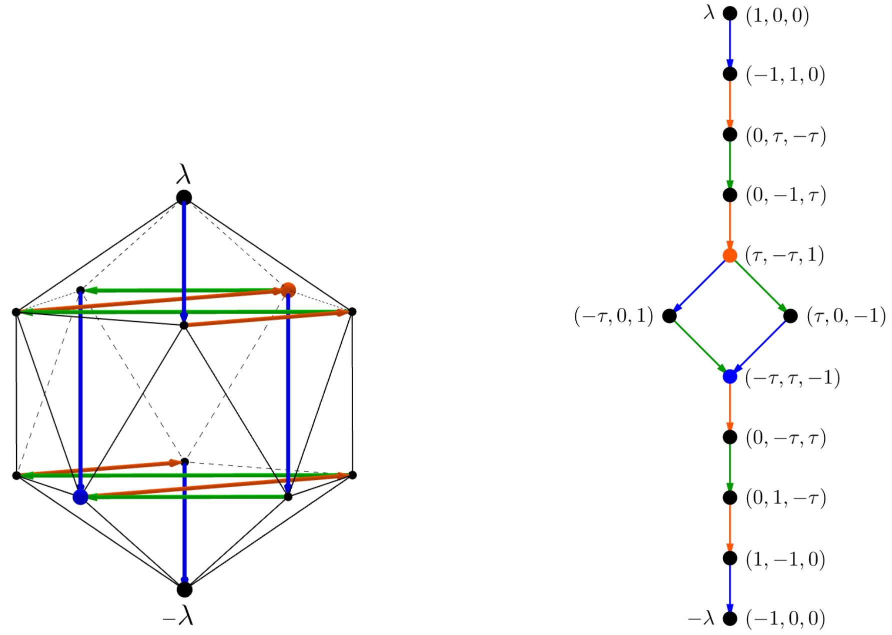

(a) (b)

Fig. 4.5. (a) The icosahedron $\mathcal{D}_{H_3}(1,0,0)$ is presented. The directed edges corresponding to the reflections r_1, r_2 and r_3 are depicted by blue, orange and green colors, respectively. The orange and blue points indicate the vertices providing branching and rejoining of the reflection graph. (b) The planar reflection graph.

have up to three directed edges pointed from one vertex, which, in this context, we will call branches. For example, the reflection graph constructed using a dominant point $(a, 0, 0)$, where $a > 0$, has only one starting branch (see Figure 4.5(b)), and the one obtained using the point (a, b, c), where a, b, $c > 0$, has three branches at the very beginning (Figure 4.6(b)). Note that, for any reflection graph, new branches will develop as soon as a vertex with two or three positive entries in its coordinates appears within an orbit of a polytope. Since the reflections determine the considered graphs, the branches arising from one vertex may rejoin at another one. Let us consider the following example.

Example 1. *Consider the icosahedron obtained by the action of the Coxeter group* H_3 *on the dominant point* $\lambda = (1, 0, 0)$*. The reflection graph obtained for the icosahedron* $\mathcal{D}_{H_3}(1,0,0)$ *is shown in Figure 4.5*(a)*. For simplicity, we present in Figure 4.5*(b) *the corresponding planar graph, together with the coordinates of each point of the icosahedron. The reflection graph begins at the point* $(1, 0, 0)$*. However, at the point* $(\tau, -\tau, 1)$ *(depicted by orange color) two branches develop, as this point can be reflected using* r_1 *and* r_3*. After, the branches rejoin at the point* $(-\tau, \tau, -1)$ *(depicted by blue color), and the graph ends at the point* $(-1, 0, 0)$*.*

In Example 2, the initial reflection graph has three starting branches (see Figure 4.6(b)). In this case, we demonstrate the action of the reflections r_1, r_2 and r_3 on the dominant point $\lambda = (1, 1, 1)$, providing three two-dimensional faces of the polytope meeting at one vertex. Constructing the reflection graph beyond the illustrated vertex, we determine all the vertices of the $\mathcal{D}_{H_3}(1,1,1)-$polytope (Figure 4.6($a$)). Similarly to Example 2, for each $\mathcal{D}_{H_3}(\lambda)-$polytope, the two-dimensional faces meeting at the vertex provided by λ, as well as the corresponding facets of $\mathcal{V}_{H_3}(\lambda)$, are presented in Figure 4.7.

Example 2. *Consider the truncated icosidodecahedron $\mathcal{D}_{H_3}(1,1,1)$ shown in Fig. 6(a). There are three types of facets meeting at each vertex of this polytope: hexagon, square and decagon. They are generated by the reflections r_1 and r_2 of A_2, r_1 and r_3 of $A_1 \times A_1$, r_2 and r_3 of H_2, respectively. Applying the reflections r_k, $k \in \{1,2,3\}$ to the point $\lambda = (1,1,1)$, the coordinates of the vertices of the faces are calculated explicitly in the $\omega-$basis as*

Hexagon:

$$\begin{aligned}
& & (1,1,1) \\
r_1(1,1,1) &= & (-1,2,1) \\
r_2(1,1,1) &= & (2,-1,1+\tau) \\
r_1r_2(1,1,1) &= & (-2,1,1+\tau) \\
r_2r_1(1,1,1) &= & (1,-2,1+2\tau) \\
r_1r_2r_1(1,1,1) = r_2r_1r_2(1,1,1) &= & (-1,-1,1+2\tau)
\end{aligned}$$

Square:

$$\begin{aligned}
& & (1,1,1) \\
r_1(1,1,1) &= & (-1,2,1) \\
r_3(1,1,1) &= & (1,1+\tau,-1) \\
r_1r_3(1,1,1) = r_3r_1(1,1,1) &= & (-1,2+\tau,-1)
\end{aligned}$$

Decagon:

$$\begin{aligned}
& & (1,1,1) \\
r_2(1,1,1) &= & (2,-1,1+\tau) \\
r_3(1,1,1) &= & (1,1+\tau,-1) \\
r_2r_3(1,1,1) &= & (\tau+2,-\tau-1,2\tau) \\
r_3r_2(1,1,1) &= & (2,2\tau,-\tau-1) \\
r_3r_2r_3(1,1,1) &= & (\tau+2,\tau+1,-2\tau) \\
r_2r_3r_2(1,1,1) &= & (2\tau+2,-2\tau,\tau+1) \\
r_2r_3r_2r_3(1,1,1) &= & (2\tau+3,-\tau-1,1) \\
r_3r_2r_3r_2(1,1,1) &= & (2\tau+2,1,-\tau-1) \\
r_3r_2r_3r_2r_3(1,1,1) = r_2r_3r_2r_3r_2(1,1,1) &= & (2\tau+3,-1,-1)
\end{aligned}$$

The beginning of the reflection graph is demonstrated in Figure 4.6(b).

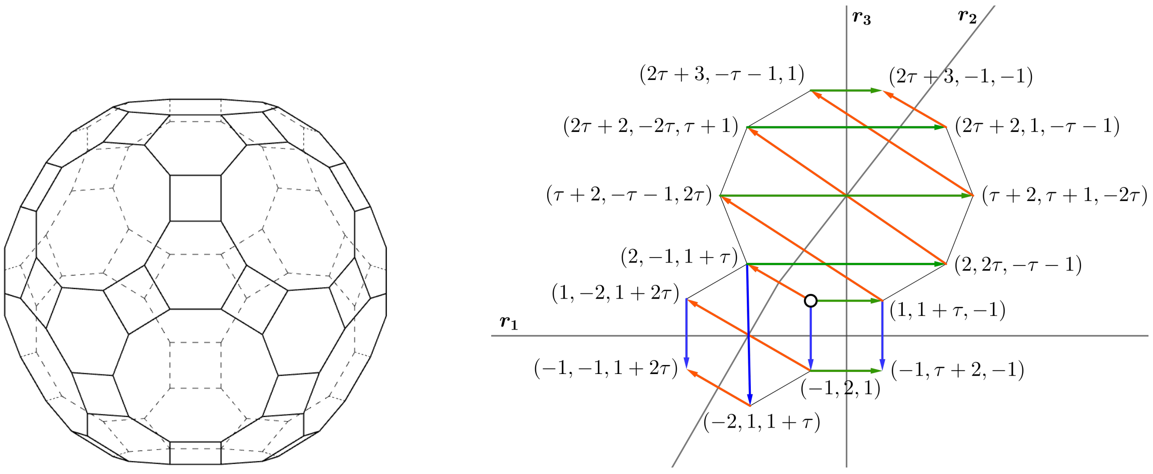

(a) (b)

Fig. 4.6. (a) The polytope $\mathcal{D}_{H_3}(1,1,1)$. (b) The vertex of $\mathcal{D}_{H_3}(1,1,1)$. The dominant point $\lambda = (1,1,1)$ is depicted by an empty node. The actions of reflections r_1, r_2 and r_3 are illustrated by blue, orange and green arrows, respectively.

4.4. Decoration of the Coxeter–Dynkin diagram

Any finite reflection group G is conveniently characterized by its Coxeter–Dynkin diagram. The decoration method developed in (Moody and Patera [**103**]; Champagne *et al.* [**29**]) plays a significant role in the description of faces of $\mathcal{D}(\lambda)-$ and $\mathcal{V}(\lambda)-$polytopes, generated by the action of G on any point $\lambda \in \mathbb{R}^n$.

In general, the recursive decoration rules can be applied to a Coxeter–Dynkin diagram regardless of the geometry of space (whether it is Euclidean or not), its metric (whether it is defined or not) and G (whether it is finite or infinite) acting in this space. The uniformity of the decoration technique equips us with the geometry of faces of $\mathcal{D}(\lambda)-$ and $\mathcal{V}(\lambda)-$polytopes arising from each step of the decoration procedure. Such rules depend neither on the angle between the simple roots of G nor on their lengths (as the links of a diagram do not change during the decoration, and the nodes correspond to the generators of G).

The decoration of a Coxeter–Dynkin diagram of G starts from choosing a seed point $\lambda \in \mathbb{R}^n$. There are three types of nodes that we use for the decoration of a diagram: □, ♦, ♢. The first node indicates the active mirrors (i.e., the reflections r_k, $k \in \{1,2,\dots,n\}$ that act non-trivially on λ), the second and third nodes represent the reflections that generate the stabilizers of the faces of $\mathcal{D}(\lambda)$ and $\mathcal{V}(\lambda)$, correspondingly. Note that during past years, the symbols for the decoration procedure have been changed several times. The decoration symbols that are used in this study are inherited from (Szajewska [**133**]), and they are in one-to-one correspondence with the notations: □, ⊙, ⊠ (Moody and Patera [**103**]); □, ○, ⊠ (Champagne *et al.* [**29**]); ◇, ●, ○ (Szajewska [**134**]).

Let us recall the recursive decoration rules:

(*i*) replace the original nodes of a diagram corresponding to the non-zero coordinates of λ by $\Box$, and the nodes corresponding to zeros (if there are any) by $\Diamond$;

(*ii*) replace only one $\Box$ of a diagram by ⧫ at a time;

(*iii*) replace every $\Diamond$ adjacent to ⧫ by $\Box$;

(*iv*) repeat the steps (*ii*) and (*iii*) as long as possible, until only one $\Box$ remains in the final diagram(s).

Hence, at the step (*i*), replacing the nodes of the initial diagram by $\Box$ equips us with the set of active mirrors. After that, the replacement in (*ii*) and (*iii*) activates the corresponding mirrors to generate the edges, as well as to further obtain the two-dimensional faces of $\mathcal{D}(\lambda)-$polytopes. In the case of $\mathcal{V}(\lambda)-$polytopes, the decorated diagrams of each step are interpreted in the reversed order. The decoration rules are applied to a Coxeter–Dynkin digram with n nodes that contains no ⧫ among them. Afterwards, a diagram is decorated to have k of ⧫ nodes and $n-k$ of $\Box$ or $\Diamond$ nodes, where n is the rank of G and $1 \leq k \leq n-1$.

Let us consider the diagrams obtained at the last step of the decoration procedure. Depending on the type of a dominant point $\lambda \in \mathbb{R}^3$, a $\mathcal{V}(\lambda)-$polytope generated by the action of G may contain up to three orbits $O(\lambda')$ within its structure, where λ' are provided by expression (4.2.8). In this paper, these three types of orbits are called *generic* orbits. The presence of generic orbits within the structure of a polytope $\mathcal{V}(\lambda)$ is provided in Table 4.3. Moreover, unlike for spherical polyhedra, the points of the orbits of flat-faced $\mathcal{V}_{H_3}(\lambda)-$polytopes may not be found on the surface of the same sphere.

In Example 3, the decoration rules are applied to the Coxeter–Dynkin diagram of the H_3 group corresponding to the seed point $\lambda = (0, 1, 0)$. The steps of the decoration are shown in Figure 4.8. For any type of a dominant point λ, the decoration of the Coxeter–Dynkin diagram of H_3 is considered in Tables 4.6, 4.7.

4.5. Faces of dual polytopes

The information about the faces of dual polytopes $\mathcal{D}(\lambda)$ and $\mathcal{V}(\lambda)$ can be conveniently extracted from the corresponding decorated Coxeter–Dynkin diagram (Champagne *et al.* [**29**]). There is a one-to-one correspondence between the faces d_k of $\mathcal{D}(\lambda)$ and the faces v_{n-k-1} of $\mathcal{V}(\lambda)$, where $0 \leq k \leq n-1$. In the three-dimensional real Euclidean space $\mathbb{R}^3$, there are three different types of faces: $d_0(v_0)$, $d_1(v_1)$ and $d_2(v_2)$. The faces are represented by the vertices, edges and two-dimensional faces or facets (regular polygons) of $\mathcal{D}(\lambda)$ and $\mathcal{V}(\lambda)$, respectively. Even though $\mathcal{D}(\lambda)-$polytopes have up to three different types of facets, $\mathcal{V}(\lambda)-$polytopes have only one type of v_2. If there are several decorated diagrams appearing at the steps (*ii*) and (*iii*) of the decoration procedure, it is convenient to distinguish the faces of the same dimension labeling them by $j \in \{1, 2, \ldots, n\}$. In this case, we can use

	Orbits of $\mathcal{V}(\lambda)$*−polytope*		
λ	$\square - \blacklozenge \overset{5}{-} \blacklozenge$	$\blacklozenge - \square \overset{5}{-} \blacklozenge$	$\blacklozenge - \blacklozenge \overset{5}{-} \square$
$(a,0,0)$			✓
$(0,b,0)$	✓		✓
$(0,0,c)$	✓		
$(a,b,0)$	✓		✓
$(a,0,c)$	✓	✓	✓
$(0,b,c)$	✓		✓
(a,b,c)	✓	✓	✓

Table 4.3. The orbits of a polytope $\mathcal{V}_{H_3}(\lambda)$ are presented for each type of dominant point λ. The scaled orbits $(a',0,0),(0,b',0)$ and $(0,0,c')$ are presented by means of the corresponding decorated Coxeter–Dynkin diagrams. The generic orbits within the structure of a $\mathcal{V}_{H_3}(\lambda)-$polytope are marked by ✓.

the notation $d_k^j(v_{n-k-1}^j)$. For example, following the rules of the decoration procedure, the polytope $\mathcal{D}_{H_3}(0,b,0)$ has 30 vertices (type d_0), 60 edges (type d_1), 12 pentagonal (type d_2^1) and 20 triangular (type d_2^2) faces (Table 4.7).

Example 3. *To obtain the orbits* $O_{H_3}(\lambda')$ *of* $\mathcal{V}_{H_3}(0,1,0)$ *(rhombic triacontahedron), let us consider the decoration of the Coxeter–Dynkin diagram (Figure 4.8).*

Considering the two diagrams obtained at the last step of the decoration procedure, we can extract the seed points of each generic orbit of the polytope $\mathcal{V}_{H_3}(0,1,0)$ *(see Table 4.4). The orbits of the icosahedron and the dodecahedron should be suitably scaled. Using the scaling factors listed in Table 4.2, the dominant points of two orbits of* $\mathcal{V}_{H_3}(0,1,0)$ *are*

$$\square - \blacklozenge \overset{5}{-} \blacklozenge \quad : \quad \omega_1' = c_1\omega_1 \equiv (1,0,0) = A;$$

$$\blacklozenge - \blacklozenge \overset{5}{-} \square \quad : \quad \omega_3' = c_3\omega_3 \equiv (0,0,\tau-1) = B.$$

The non-active reflections of the initial diagram, r_1 *and* r_3*, become active for the decorated diagrams obtained in the last step of the decoration procedure. Therefore, we have to apply these reflections to both points* A *and* B *in the* $\omega'-$*basis:*

$$r_1A = r_3r_1A = (-1,1,0) = C,$$

$$r_3B = r_1r_3B = (0,-1,1-\tau) = D.$$

Hence, the vertices of the two-dimensional face v_2 *of* $\mathcal{V}_{H_3}(0,1,0)$*, are obtained. The points* A*,* B*,* C *and* D *are in one-to-one correspondence with the points in Table 4.5. Further application of the reflections of* H_3 *to the seed points* A *and* B *yields the vertices* v_0^1 *and* v_0^2 *of* $\mathcal{V}_{H_3}(0,1,0)$*.*

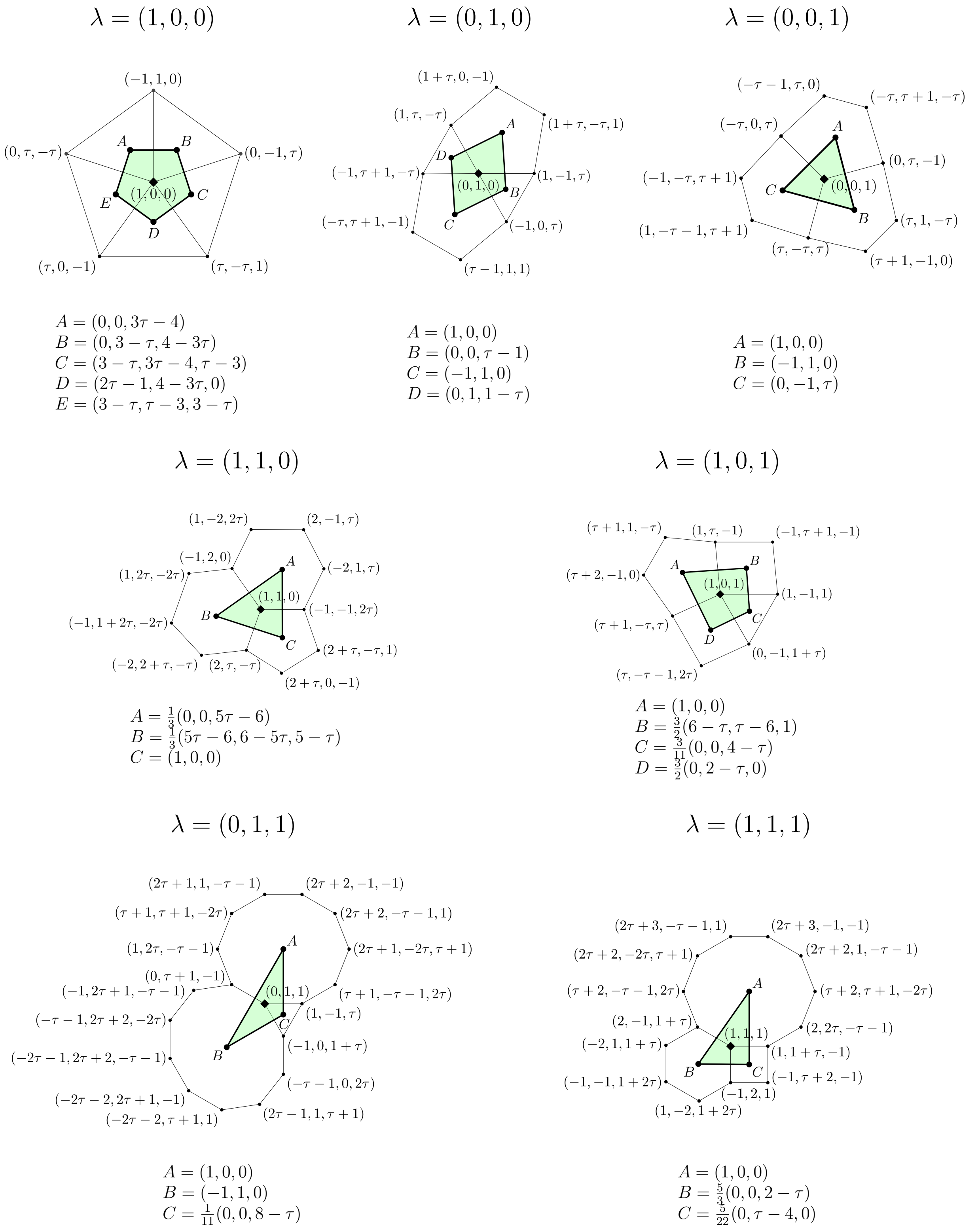
(−1, 1, 0)
(0, τ, −τ)
(0, −1, τ)
A
B
C
D
E
(1, 0, 0)
(τ, 0, −1)
(τ, −τ, 1)
(1 + τ, 0, −1)
(1, τ, −τ)
(1 + τ, −τ, 1)
A
D
(−1, τ + 1, −τ)
(0, 1, 0)
(1, −1, τ)
B
(−τ, τ + 1, −1)
C
(−1, 0, τ)
(τ − 1, 1, 1)
(−τ − 1, τ, 0)
(−τ, τ + 1, −τ)
(−τ, 0, τ)
A
(0, τ, −1)
(−1, −τ, τ + 1)
C
(0, 0, 1)
B
(τ, 1, −τ)
(1, −τ − 1, τ + 1)
(τ, −τ, τ)
(τ + 1, −1, 0)
(1, −2, 2τ)
(2, −1, τ)
(−1, 2, 0)
A
(1, 2τ, −2τ)
(−2, 1, τ)
(1, 1, 0)
B
(−1, −1, 2τ)
(−1, 1 + 2τ, −2τ)
C
(2 + τ, −τ, 1)
(−2, 2 + τ, −τ)
(2, τ, −τ)
(2 + τ, 0, −1)
(τ + 1, 1, −τ)
(1, τ, −1)
(−1, τ + 1, −1)
B
A
(τ + 2, −1, 0)
(1, 0, 1)
(1, −1, 1)
C
(τ + 1, −τ, τ)
D
(0, −1, 1 + τ)
(τ, −τ − 1, 2τ)
(2τ + 1, 1, −τ − 1)
(2τ + 2, −1, −1)
(τ + 1, τ + 1, −2τ)
(2τ + 2, −τ − 1, 1)
A
(1, 2τ, −τ − 1)
(2τ + 1, −2τ, τ + 1)
(0, τ + 1, −1)
(−1, 2τ + 1, −τ − 1)
(τ + 1, −τ − 1, 2τ)
(0, 1, 1)
(1, −1, τ)
(−τ − 1, 2τ + 2, −2τ)
C
(−1, 0, 1 + τ)
(−2τ − 1, 2τ + 2, −τ − 1)
B
(−τ − 1, 0, 2τ)
(−2τ − 2, 2τ + 1, −1)
(−2τ − 2, τ + 1, 1)
(2τ − 1, 1, τ + 1)
(2τ + 3, −τ − 1, 1)
(2τ + 3, −1, −1)
(2τ + 2, −2τ, τ + 1)
(2τ + 2, 1, −τ − 1)
A
(τ + 2, −τ − 1, 2τ)
(τ + 2, τ + 1, −2τ)
(2, −1, 1 + τ)
(2, 2τ, −τ − 1)
(1, 1, 1)
(−2, 1, 1 + τ)
(1, 1 + τ, −1)
B
C
(−1, τ + 2, −1)
(−1, −1, 1 + 2τ)
(−1, 2, 1)
(1, −2, 1 + 2τ)

$\lambda = (1,0,0)$

$A = (0,0,3\tau-4)$
$B = (0,3-\tau,4-3\tau)$
$C = (3-\tau,3\tau-4,\tau-3)$
$D = (2\tau-1,4-3\tau,0)$
$E = (3-\tau,\tau-3,3-\tau)$

$\lambda = (0,1,0)$

$A = (1,0,0)$
$B = (0,0,\tau-1)$
$C = (-1,1,0)$
$D = (0,1,1-\tau)$

$\lambda = (0,0,1)$

$A = (1,0,0)$
$B = (-1,1,0)$
$C = (0,-1,\tau)$

$\lambda = (1,1,0)$

$A = \frac{1}{3}(0,0,5\tau-6)$
$B = \frac{1}{3}(5\tau-6,6-5\tau,5-\tau)$
$C = (1,0,0)$

$\lambda = (1,0,1)$

$A = (1,0,0)$
$B = \frac{3}{2}(6-\tau,\tau-6,1)$
$C = \frac{3}{11}(0,0,4-\tau)$
$D = \frac{3}{2}(0,2-\tau,0)$

$\lambda = (0,1,1)$

$A = (1,0,0)$
$B = (-1,1,0)$
$C = \frac{1}{11}(0,0,8-\tau)$

$\lambda = (1,1,1)$

$A = (1,0,0)$
$B = \frac{5}{3}(0,0,2-\tau)$
$C = \frac{5}{22}(0,\tau-4,0)$

Fig. 4.7. The vertices of polytopes $\mathcal{D}_{H_3}(\lambda)$ and the corresponding two-dimensional faces of $\mathcal{V}_{H_3}(\lambda)$ (indicated by green color) are presented for each type of λ (marked by black rhombus node). The coordinates are provided in the $\omega-$ and $\omega'-$basis for $\mathcal{D}_{H_3}(\lambda)$ and $\mathcal{V}_{H_3}(\lambda)$, respectively.

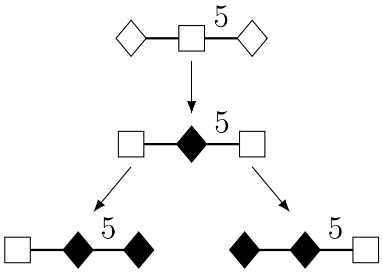

Fig. 4.8. The decoration method applied to the diagram of $\mathcal{D}_{H_3}(0,1,0)$. The orbits of $\mathcal{V}_{H_3}(0,1,0)$ are presented at the last step of the decoration procedure.

It is well-known that the number of faces of a polytope is determined by Euler's formula,

$$V + F - E = 2, \tag{4.5.1}$$

where V, F and E stand for the number of vertices, facets and edges of a considered polytope.

In order to count the number of faces of a polytope, firstly, one has to know their stabilizers in G. For any given face of a polytope or its dual, the stabilizer has the form:

$$\mathrm{Stab}_G d_k = \mathrm{Stab}_G v_{n-k-1} = G(\mathcal{D}) \times G(\mathcal{V}),$$

where $G(\mathcal{D})$ and $G(\mathcal{V})$ are mutually commuting subgroups of G; more precisely, $G(\mathcal{D})$ and $G(\mathcal{V})$ are the groups of reflections indicated by ⧫ and ◊ node(s) accordingly in the corresponding decorated diagram.

The number of faces of a dual pair of polytopes can be obtained from the formula:

$$N(d_k) = N(v_{n-k-1}) = \frac{|G|}{|G(\mathcal{D})||G(\mathcal{V})|}. \tag{4.5.2}$$

In the case of a $\mathcal{D}(\lambda)-$polytope, while $G(\mathcal{D})$ transforms the face d_k into itself (as it is a symmetry group of the face), $G(\mathcal{V})$ fixes that face point-wise. However, if we consider a dual polytope $\mathcal{V}(\lambda)$, the roles of the subgroups $G(\mathcal{D})$ and $G(\mathcal{V})$ interchange for the face v_{n-k-1}.

The polytopes considered in this paper are vertex-transitive, hence, each vertex is surrounded by the same types of polygons. The decoration technique allows us to determine the number of faces of maximal dimension meeting at each vertex. To find out how many faces of dimension p are meeting at the face of lower dimension $q\,(p > q)$, one has to consider the reflections generating the stabilizers of these faces. The stabilizer of f_q in the stabilizer of f_p is provided by the formula:

$$\mathrm{Stab}_{\mathrm{Stab}_G f_q} f_p = \mathrm{Stab}_G f_p \cap \mathrm{Stab}_G f_q.$$

Hence, the number of faces f_p having in common the face f_q is

$$N(f_p) = \frac{|\mathrm{Stab}_G f_q|}{|\mathrm{Stab}_G f_p \cap \mathrm{Stab}_G f_q|}. \tag{4.5.3}$$

λ	Seed point of $\mathcal{D}_{H_3}(\lambda)$	Seed point of $\mathcal{V}_{H_3}(\lambda)$
$(1,0,0)$	ω_1	ω'_3
$(0,1,0)$	ω_2	ω'_1, ω'_3
$(0,0,1)$	ω_3	ω'_1
$(1,1,0)$	$\omega_1+\omega_2$	ω'_1, ω'_3
$(1,0,1)$	$\omega_1+\omega_3$	ω'_1, ω'_3
$(0,1,1)$	$\omega_2+\omega_3$	ω'_1, ω'_3
$(1,1,1)$	$\omega_1+\omega_2+\omega_3$	ω'_1, ω'_2, ω'_3

Table 4.4. The seed points λ of $\mathcal{D}_{H_3}(\lambda)$ and λ' of its dual $\mathcal{V}_{H_3}(\lambda)$. The first column indicates a dominant point λ in the coordinate form, the second column provides λ as a linear combination of the fundamental weights ω_k, and the third column provides λ' as the vectors ω'_k, $k\in\{1,2,3\}$.

To construct the faces of a $\mathcal{V}_{H_3}(\lambda)-$polytope, one has to switch to $\omega'-$basis. For $\mathcal{V}_{H_3}(\lambda)-$polytopes, the seed points λ' of the orbits comprised within their structures are listed in Table 4.4.

Considering each type of seed point λ' in the $\omega'-$basis, the lengths of the edges of $\mathcal{V}_{H_3}(\lambda)$ are determined as a Euclidean distance by using formula (4.3.3):

$$\begin{aligned}
|\omega'_1-r_1\omega'_1| &= |2\omega'_1+\omega'_2| = |2c_1\omega_1+c_2\omega_2|,\\
|\omega'_2-r_2\omega'_2| &= |-\omega'_1+2\omega'_2-\tau\omega'_3| = |-c_1\omega_1+2c_2\omega_2-\tau c_3\omega_3|,\\
|\omega'_3-r_3\omega'_3| &= |-\tau\omega'_2+2\omega'_3| = |-\tau c_2\omega_2+2c_3\omega_3|,
\end{aligned}$$

where the vectors ω_k, $k\in\{1,2,3\}$ are considered in the orthonormal basis (4.2.5), and the scaling factors are provided in Table 4.2. Thus, the approximate lengths of the edges of $\mathcal{V}_{H_3}(\lambda)$ together with the relative angles are presented in Table 4.5.

Example 4. *Consider the dual pair of polytopes generated by the action of the Coxeter group H_3 on a single point $\lambda=(a,0,0)$. To demonstrate the geometric transformations hidden behind the decoration technique, the vertices of the polytopes $\mathcal{D}_{H_3}(a,0,0)$ and $\mathcal{V}_{H_3}(a,0,0)$ are projected onto a sphere centered at the origin of $\mathbb{R}^3$ (see Figure 4.9).*

Let us consider each step of the decoration of the Coxeter–Dynkin diagram of H_3. In case of the $\mathcal{D}_{H_3}(a,0,0)-$polytope, the $G(\mathcal{D})$ group stands for the symmetry group of the face d_2 and $G(\mathcal{V})$ fixes that face point-by-point. Thus, acting on the point $(a,0,0)$ (depicted by orange color) with the reflection r_1 of (ii) yields the edge a. Furthermore, acting on such a point with the reflections r_1 and r_2 of (iii) provides the triangular face of the icosahedron.

The faces of $\mathcal{V}_{H_3}(a,0,0)$ are constructed in a similar way, however, the roles of $G(\mathcal{D})$ and $G(\mathcal{V})$ are interchanged. Starting from the diagram of (iii) corresponding to the seed point

λ	v_2	v_0	$\lvert v_1\rvert$	*Angles*
$(1,0,0)$	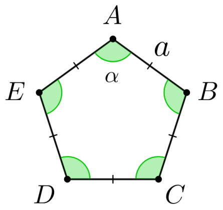	$A=\omega_3'$ $B=r_3\omega_3'$ $C=r_3r_2r_3\omega_3'$ $D=r_2r_3r_2r_3\omega_3'$ $E=r_2r_3\omega_3'$	$a=0.854$	$\alpha=108°$
$(0,1,0)$	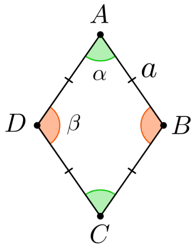	$A=\omega_1'$ $B=\omega_3'$ $C=r_1\omega_1'$ $D=r_3\omega_3'$	$a=0.588$	$\alpha=63.43°$ $\beta=116.57°$
$(0,0,1)$	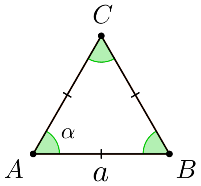	$A=\omega_1'$ $B=r_1\omega_1'$ $C=r_2r_1\omega_1'$	$a=1$	$\alpha=60°$
$(1,1,0)$	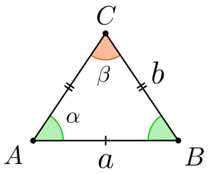	$A=\omega_3'$ $B=r_3\omega_3'$ $C=\omega_1'$	$a=0.697$ $b=0.593$	$\alpha=55.69°$ $\beta=68.62°$
$(1,0,1)$	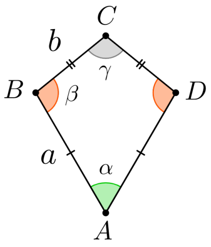	$A=\omega_1'$ $B=\omega_2'$ $C=\omega_3'$ $D=r_2\omega_2'$	$a=0.514$ $b=0.334$	$\alpha=67.79°$ $\beta=86.97°$ $\gamma=118.27°$
$(0,1,1)$	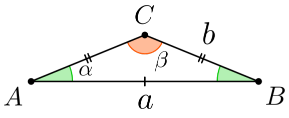	$A=\omega_1'$ $B=r_1\omega_1'$ $C=\omega_3'$	$a=1$ $b=0.580$	$\alpha=30.48°$ $\beta=119.04°$
$(1,1,1)$	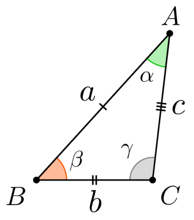	$A=\omega_1'$ $B=\omega_3'$ $C=\omega_2'$	$a=0.593$ $b=0.321$ $c=0.504$	$\alpha=32.77°$ $\beta=58.24°$ $\gamma=88.99°$

Table 4.5. The faces v_2 of $\mathcal{V}_{H_3}(\lambda)$ are presented for each type of dominant point λ (see Figure 4.7). The faces v_0 are generated by the corresponding reflections applied to λ' indicated in Table 4.4. The approximate lengths of the edges v_1 are denoted by a, b, c, and the relative angles are denoted by α, β, γ.

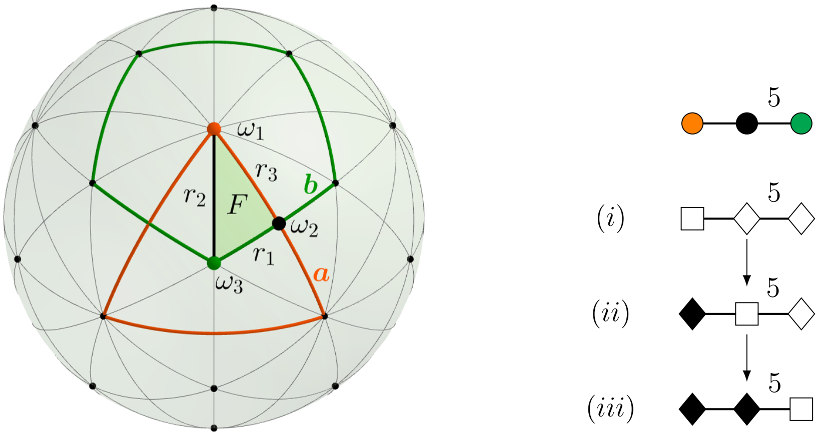

Fig. 4.9. On the left, the vertices of $\mathcal{D}_{H_3}(a,0,0)$ and $\mathcal{V}_{H_3}(a,0,0)$ are found on the surface of a sphere $\mathcal{S}$. The green tile corresponds to the fundamental region F of H_3. The points provided by the vectors ω_1, ω_2 and ω_3 are depicted by orange, green and black colors, respectively. On the right, the recursive decoration rules are applied to the Coxeter–Dynkin diagram of H_3.

Decoration	d_k	v_{2-k}	N	*Type of* d_k	*Type of* v_{2-k}
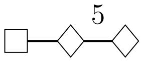	d_0	v_2	12	vertices	pentagon
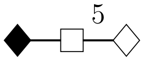	d_1	v_1	30	triangle-triangle	pentagon-pentagon
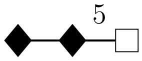	d_2	v_0	20	triangle	vertices

Table 4.6. The types and the numbers of faces d_k and v_{2-k} of $\mathcal{D}_{H_3}(a,0,0)$ and $\mathcal{V}_{H_3}(a,0,0)$, respectively, are provided for each decorated Coxeter–Dynkin diagram of H_3. The polygon-polygon notation corresponds to the types of edges shared by the two-dimensional faces of a polytope. The number of faces $N(d_k)$ and $N(v_{2-k})$ is denoted by N.

$(0,0,c')$ *(marked by green color), and acting on such a point with the reflection* r_3 *of* (ii) *yields the edge* b*. Finally, acting on the point* $(0,0,c')$ *with the reflections* r_1 *and* r_3 *yields the pentagonal face of the dodecahedron.*

It is obvious that $\mathcal{D}_{H_3}(a,0,0)$ *and* $\mathcal{V}_{H_3}(a,0,0)$ *are self-dual polytopes. The numbers and the types of faces of both polytopes are listed in Table 4.6.*

4.6. Orbits of $\mathcal{V}_{H_3}(\lambda)$−polytopes

Applying the recursive decoration rules to the Coxeter–Dynkin diagram of H_3 yields up to three different decorated diagrams appearing at the last step of the procedure. Such diagrams provide the symmetry of two-dimensional faces of a $\mathcal{D}_{H_3}(\lambda)-$ polytope, as well as the vertices of its dual $\mathcal{V}_{H_3}(\lambda)$. The orbits of the latter can be extracted from Table 4.3, and they are determined by the dominant points λ' of expression (4.2.8).

λ	*Decoration*	d_k	v_{2-k}	N	*Type of* d_k	*Type of* v_{2-k}
$(0,b,0)$	◇—□$\overset{5}{—}$◇	d_0	v_2	30	vertices	rhombus
	□—◆$\overset{5}{—}$□	d_1	v_1	60	triangle-pentagon	rhombus-rhombus
	◆—◆$\overset{5}{—}$□	d_2^1	v_0^2	20	triangle	vertices
	□—◆$\overset{5}{—}$◆	d_2^2	v_0^1	12	pentagon	vertices
$(a,b,0)$	□—□$\overset{5}{—}$◇	d_0	v_2	60	vertices	triangle
	◆—□$\overset{5}{—}$◇	d_1^1	v_1^2	30	hexagon-hexagon	triangle-triangle
	□—◆$\overset{5}{—}$□	d_1^2	v_1^1	60	hexagon-pentagon	triangle-triangle
	◆—◆$\overset{5}{—}$□	d_2^1	v_0^2	20	hexagon	vertices
	□—◆$\overset{5}{—}$◆	d_2^2	v_0^1	12	pentagon	vertices
$(a,0,c)$	□—◇$\overset{5}{—}$□	d_0	v_2	60	vertices	kite
	◆—□$\overset{5}{—}$□	d_1^1	v_1^2	60	triangle-rectangle	kite-kite
	□—□$\overset{5}{—}$◆	d_1^2	v_1^1	60	rectangle-pentagon	kite-kite
	◆—◆$\overset{5}{—}$□	d_2^1	v_0^3	20	triangle	vertices
	◆—□$\overset{5}{—}$◆	d_2^2	v_0^2	30	rectangle	vertices
	□—◆$\overset{5}{—}$◆	d_2^3	v_0^1	12	pentagon	vertices
$(0,b,c)$	◇—□$\overset{5}{—}$□	d_0	v_2	60	vertices	triangle
	□—◆$\overset{5}{—}$□	d_1^1	v_1	60	triangle-decagon	triangle-triangle
	◇—□$\overset{5}{—}$◆	d_1^2	v_1	30	decagon-decagon	triangle-triangle
	◆—◆$\overset{5}{—}$□	d_2^1	v_0^2	20	triangle	vertices
	□—◆$\overset{5}{—}$◆	d_2^2	v_0^1	12	decagon	vertices
(a,b,c)	□—□$\overset{5}{—}$□	d_0	v_2	120	vertices	triangle
	◆—□$\overset{5}{—}$□	d_1^1	v_1^3	60	hexagon-rectangle	triangle-triangle
	□—◆$\overset{5}{—}$□	d_1^2	v_1^2	60	hexagon-decagon	triangle-triangle
	□—□$\overset{5}{—}$◆	d_1^3	v_1^1	60	rectangle-decagon	triangle-triangle
	◆—◆$\overset{5}{—}$□	d_2^1	v_0^3	20	hexagon	vertices
	◆—□$\overset{5}{—}$◆	d_2^2	v_0^2	30	rectangle	vertices
	□—◆$\overset{5}{—}$◆	d_2^3	v_0^1	12	decagon	vertices

Table 4.7. Decorations of the Coxeter–Dynkin diagram of H_3 are presented for dominant points λ, namely $(0,b,0)$, $(a,b,0)$, $(a,0,c)$, $(0,b,c)$ and (a,b,c). The faces d_k and v_{2-k}, $k \in \{0,1,2\}$ correspond to the faces of $\mathcal{D}(\lambda)$ and $\mathcal{V}(\lambda)$. The polygon-polygon notation corresponds to the types of edges shared by the two-dimensional faces of a polytope. The number of faces $N(d_k)$ and $N(v_{2-k})$ is denoted by N.

The orbits of the non-crystallographic group H_3 with the dominant points $(a,0,0)$, $(0,b,0)$, $(0,0,c)$ are explicitly provided by the sets of points as

$$\begin{aligned}
O_{H_3}(a,0,0) &= \{\pm(a,0,0), \pm(-a,a,0), \pm(0,-a,a\tau), \pm(0,a\tau,-a\tau), \pm(a\tau,-a\tau,a),\\
&\pm(-a\tau,0,a)\};\\
O_{H_3}(0,b,0) &= \{\pm(0,b,0), \pm(b,-b,b\tau), \pm(-b,0,b\tau), \pm(b,b\tau,-b\tau), \pm(-b,b(1+\tau),-b\tau),\\
&\pm(b(1+\tau),-b\tau,b), \pm(b\tau,-b(1+\tau),b(1+\tau)), \pm(-b(1+\tau),b,b),\\
&\pm(b(1+\tau),0,-b), \pm(-b\tau,-b,b(1+\tau)), \pm(b\tau,b\tau,-b(1+\tau)),\\
&\pm(-b(1+\tau),b(1+\tau),-b), \pm(-b\tau,2b\tau,-b(1+\tau)), \pm(2b\tau,-b\tau,0),\\
&\pm(0,-b(1+\tau),2b\tau)\};\\
O_{H_3}(0,0,c) &= \{\pm(0,0,c), \pm(0,c\tau,-c), \pm(c\tau,-c\tau,c\tau), \pm(-c\tau,0,c\tau), \pm(c\tau,c,-c\tau),\\
&\pm(-c\tau,c(1+\tau),-c\tau), \pm(c(1+\tau),-c,0), \pm(c,-c(1+\tau),c(1+\tau)),\\
&\pm(-c(1+\tau),c\tau,0), \pm(-c,-c\tau,c(1+\tau))\}.
\end{aligned}$$

Hence, the polytopes $\mathcal{V}_{H_3}(\lambda)$ are composed from the unions of orbits $O_{H_3}(\lambda')$ as

$$\begin{aligned}
\mathcal{V}_{H_3}(a,0,0) &: O_{H_3}(0,0,c'),\\
\mathcal{V}_{H_3}(0,0,c) &: O_{H_3}(a',0,0),\\
\mathcal{V}_{H_3}(0,b,0) &: O_{H_3}(a',0,0) \cup O_{H_3}(0,0,c'),\\
\mathcal{V}_{H_3}(a,b,0) &: O_{H_3}(a',0,0) \cup O_{H_3}(0,0,c'),\\
\mathcal{V}_{H_3}(0,b,c) &: O_{H_3}(a',0,0) \cup O_{H_3}(0,0,c'),\\
\mathcal{V}_{H_3}(a,0,c) &: O_{H_3}(a',0,0) \cup O_{H_3}(0,b',0) \cup O_{H_3}(0,0,c'),\\
\mathcal{V}_{H_3}(a,b,c) &: O_{H_3}(a',0,0) \cup O_{H_3}(0,b',0) \cup O_{H_3}(0,0,c').
\end{aligned}$$

The squared radius of an orbit $O_{H_3}(\lambda)$ with a dominant point $\lambda = (a,b,c)$ is calculated via the formula,

$$R^2_{H_3}(\lambda) = \begin{pmatrix} a & b & c \end{pmatrix} C^{-1}_{H_3} \begin{pmatrix} a \\ b \\ c \end{pmatrix} = \tfrac{1}{(2-\tau)} \left[\tfrac{1}{2}(a\tau+c)^2 + (b\tau+c)^2 + (a+b)^2 - \tau(a^2+b^2)\right]. \tag{4.6.1}$$

	$\mathcal{V}_{H_3}(\lambda)$						
$R^2_{H_3}(\lambda')$	$(1,0,0)$	$(0,1,0)$	$(0,0,1)$	$(1,1,0)$	$(1,0,1)$	$(0,1,1)$	$(1,1,1)$
$(a',0,0)$		1.809	1.809	1.809	1.809	1.809	1.809
$(0,b',0)$					1.719		1.535
$(0,0,c')$	2.865	1.5		1.906	1.657	1.322	1.592

Table 4.8. The numerical values of the squared radii $R^2_{H_3}(\lambda')$ of the orbits $O_{H_3}(\lambda')$ of $\mathcal{V}_{H_3}(\lambda)-$polytopes.

Using formula (4.6.1), the squared radius for each orbit $O_{H_3}(\lambda')$ of a polytope $\mathcal{V}_{H_3}(\lambda)$ has the following form

$$R^2_{H_3}(a',0,0) = \begin{pmatrix} a' & 0 & 0 \end{pmatrix} C^{-1}_{H_3} \begin{pmatrix} a' \\ 0 \\ 0 \end{pmatrix} = (a')^2 R^2_{H_3}(1,0,0), \tag{4.6.2}$$

$$R^2_{H_3}(0,b',0) = \begin{pmatrix} 0 & b' & 0 \end{pmatrix} C^{-1}_{H_3} \begin{pmatrix} 0 \\ b' \\ 0 \end{pmatrix} = (b')^2 R^2_{H_3}(0,1,0), \tag{4.6.3}$$

$$R^2_{H_3}(0,0,c') = \begin{pmatrix} 0 & 0 & c' \end{pmatrix} C^{-1}_{H_3} \begin{pmatrix} 0 \\ 0 \\ c' \end{pmatrix} = (c')^2 R^2_{H_3}(0,0,1). \tag{4.6.4}$$

The numerical values of the squared radii (4.6.2)–(4.6.4) are calculated in Table 4.8 for each orbit $O_{H_3}(\lambda')$ of $\mathcal{V}_{H_3}(\lambda)-$polytopes.

4.7. Stellations of dual polyhedra of H_3

As demonstrated in Section 4.6, the family of dual polytopes $\mathcal{V}_{H_3}(\lambda)$, except the dual pair icosahedron-dodecahedron, have two or three orbits $O_{H_3}(\lambda')$ contained within their structure. Therefore, each of the polytopes $\mathcal{V}_{H_3}(0,a,0)$, $\mathcal{V}_{H_3}(a,b,0)$ and $\mathcal{V}_{H_3}(0,b,c)$ has two orbits of the dominant points $(a',0,0)$ and $(0,0,c')$; the polytopes $\mathcal{V}_{H_3}(a,0,c)$ and $\mathcal{V}_{H_3}(a,b,c)$ contain the orbits generated by the reflections r_k, $k \in \{1,2,3\}$ applied to the seed points $(a',0,0)$, $(0,b',0)$, $(0,0,c')$. The $\mathcal{V}_{H_3}(\lambda)-$polytopes are shown together with the fundamental region F represented by one of the faces of the simplex (triangular tile with its edges highlighted by orange color) relative to the $\omega'-$basis in Figures 4.10, 4.11, 4.12.

In order to construct the stellations of the $\mathcal{V}_{H_3}(\lambda)-$polytopes, it is convenient to introduce the scaling factors x, y, z for each generic orbit as

$$\begin{aligned} x \cdot O_{H_3}(a',0,0) &= O_{H_3}(xa',0,0);\\ y \cdot O_{H_3}(0,b',0) &= O_{H_3}(0,yb',0);\\ z \cdot O_{H_3}(0,0,c') &= O_{H_3}(0,0,zc'). \end{aligned}$$

Multiplying the coordinates a', b' and/or c' by any coefficients $x, y, z \in \mathbb{R}^{\geq 0}$ provides the scaling of the corresponding radii of orbits $O_{H_3}(\lambda')$ given by formulas (4.6.2)–(4.6.4). As a result, we obtain different types of stellations of $\mathcal{V}_{H_3}(\lambda)$.

Example 5. *The polytope $\mathcal{V}_{H_3}(0,b,0)$ is considered (see Figure 4.10). The structure of such a polytope is given by the union of two orbits $O_{H_3}(a',0,0) \cup O_{H_3}(0,0,c')$. Hence, the vertices of $O_{H_3}(a',0,0)$ and $O_{H_3}(0,0,c')$ are found on the surfaces of spheres of the radii R_1 and R_2, respectively.*

Let one consider the two cases: (i) $x > z$, (ii) $x < z$. Thus, fixing the radius of one orbit, and scaling up or down the radius of the second one, provides the following two types of stellations of $\mathcal{V}_{H_3}(0,b,0)$:

- (i) *the small stellated dodecahedron (or first stellation of the dodecahedron) (Figure 4.10(c)),*
- (ii) *the excavated dodecahedron (or third stellation of the icosahedron) (Figure 4.10(d)).*

In a similar way, the same types of stellations are obtained for $\mathcal{V}_{H_3}(a,b,0)$.

Application of the stellation procedure to the orbits of the polytope $\mathcal{V}_{H_3}(0,b,c)$ results in the structure of the great dodecahedron and the great stellated dodecahedron shown in Figure 4.11. The polytopes $\mathcal{V}_{H_3}(a,0,c)$ and $\mathcal{V}_{H_3}(a,b,c)$ are shown in Figure 4.12, and their stellations have a similar structure. Thus, the stellations of the $\mathcal{V}_{H_3}(a,b,c)-$polytope are illustrated in Figure 4.13.

4.8. Orbit decompositions of $\mathcal{V}_{H_3}(\lambda)-$polytopes

The non-crystallographic group H_3 can be decomposed into a product of the subgroups $H_2 \times A_1$, $A_2 \times A_1$, and $A_1 \times A_1 \times A_1$. As was shown in (Bodner *et al.* [**13**], [**14**], [**15**]), the decomposition of vertices of $\mathcal{D}(\lambda)-$polytopes into orbits of the two-dimensional subgroups of H_3 can be presented geometrically.

To extract the symmetry of a two-dimensional subgroup $G' \subset H_3$, one should consider its Coxeter–Dynkin diagram (Table 4.1). Examining the geometric structure of the G' orbits in $\mathbb{R}^3$, we observe the set of circular/polygonal orbits of crystallographic or non-crystallographic type. The set of orbits obtained by isolating a two-dimensional subgroup G', that is orthogonal to an element of the $\alpha-$basis, represents the 'pancake'-structure of a polytope. The spacing between the 'pancakes' is provided by the one-dimensional subgroup A_1 of H_3. In

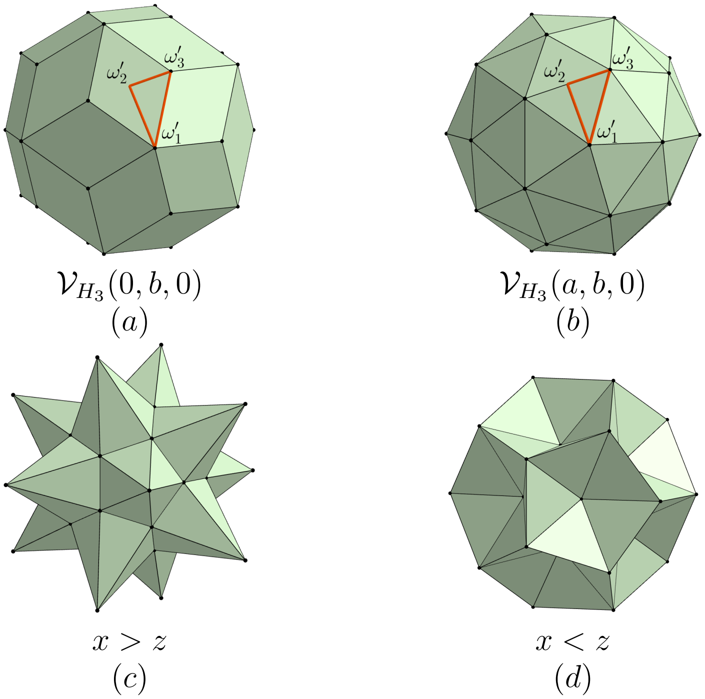

$\mathcal{V}_{H_3}(0, b, 0)$
(a)

$\mathcal{V}_{H_3}(a, b, 0)$
(b)

$x > z$
(c)

$x < z$
(d)

Fig. 4.10. The polytopes $\mathcal{V}_{H_3}(0, b, 0)$ and $\mathcal{V}_{H_3}(a, b, 0)$ are shown in (a) and (b). The fundamental region F is depicted by the orange triangle. The stellations of $\mathcal{V}_{H_3}(0, b, 0)$ and $\mathcal{V}_{H_3}(a, b, 0)$ are provided with respect to the scaling factors x and z by (c) the small stellated dodecahedron and (d) the excavated dodecahedron.

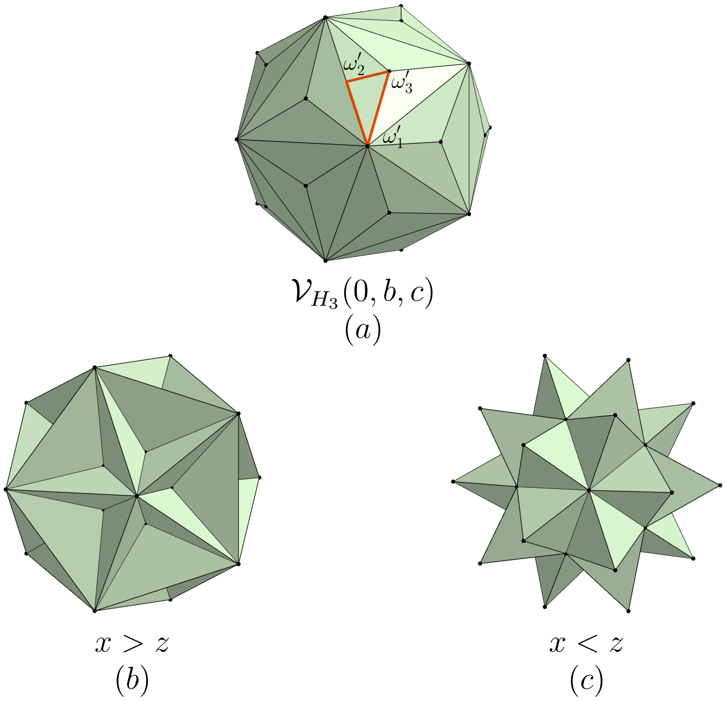

$\mathcal{V}_{H_3}(0, b, c)$
(a)

$x > z$
(b)

$x < z$
(c)

Fig. 4.11. (a) The polytope $\mathcal{V}_{H_3}(0, b, c)$ is shown. The fundamental region F is depicted by the orange triangle. The stellations of $\mathcal{V}_{H_3}(0, b, c)$ are provided with respect to the scaling factors x and z by (b) the great dodecahedron, (c) the great stellated dodecahedron.

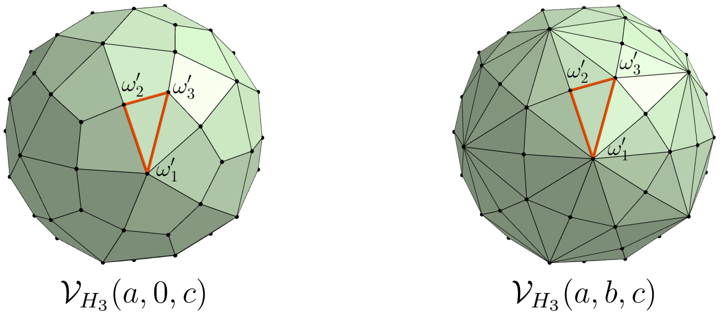

Fig. 4.12. The polytopes $\mathcal{V}_{H_3}(a,0,c)$ and $\mathcal{V}_{H_3}(a,b,c)$ are shown. The fundamental region F is depicted by the orange triangle.

this case, the simple root of A_1 sets the direction, say l, that is orthogonal to the 'pancakes' provided by G'. Projecting any point of each 'pancake' onto l yields a set of points with their coordinates corresponding to the $\alpha-$component of the related mixed basis (Table 4.1). In this case, the distances between the projected points can be calculated as a one-dimensional Euclidean distance.

To obtain an orbit-decomposition of $\mathcal{V}_{H_3}(\lambda)$, we should consider only one two-dimensional subgroup at a time. Using a mix of the $\alpha-$ and $\omega-$bases together with the inverse of the Cartan matrix (4.2.3), we can construct the transformation matrices depending on the reduction of the H_3-symmetry. The matrices take the form of the identity matrices, for which one column is replaced by a column of $C_{H_3}^{-1}$ corresponding to a chosen α_k-direction, $k \in \{1,2,3\}$. Hence, multiplying the points of $O_{H_3}(\lambda)$ by such matrices yields an orbit provided in terms of the mixed basis. More precisely,

$$H_2: \qquad (a,b,c)\begin{pmatrix} 1+\frac{1}{2}\tau & 0 & 0 \\ 1+\tau & 1 & 0 \\ \frac{1}{2}+\tau & 0 & 1 \end{pmatrix} = \left(\left(1+\tfrac{1}{2}\tau\right)a+(1+\tau)\,b+\left(\tfrac{1}{2}+\tau\right)c, b, c\right);$$

$$A_1\times A_1: \qquad (a,b,c)\begin{pmatrix} 1 & 1+\tau & 0 \\ 0 & 2+2\tau & 0 \\ 0 & 1+2\tau & 1 \end{pmatrix} = (a, (1+\tau)a+(2+2\tau)b+(1+2\tau)c, c);$$

$$A_2: \qquad (a,b,c)\begin{pmatrix} 1 & 0 & \frac{1}{2}+\tau \\ 0 & 1 & 1+2\tau \\ 0 & 0 & \frac{3}{2}(1+\tau) \end{pmatrix} = \left(a, b, \left(\tfrac{1}{2}+\tau\right)a+(1+2\tau)\,b+\tfrac{3}{2}\,(1+\tau)\,c\right).$$

Once the transformation is completed, the points are sorted depending on a chosen two-dimensional subgroup of H_3:

(i) for H_2, the second and third coordinates should be of the same sign;
(ii) for $A_1 \times A_1$, the first and third coordinates should be the same sign;
(iii) for A_2, the first and second coordinates should be of the same sign.

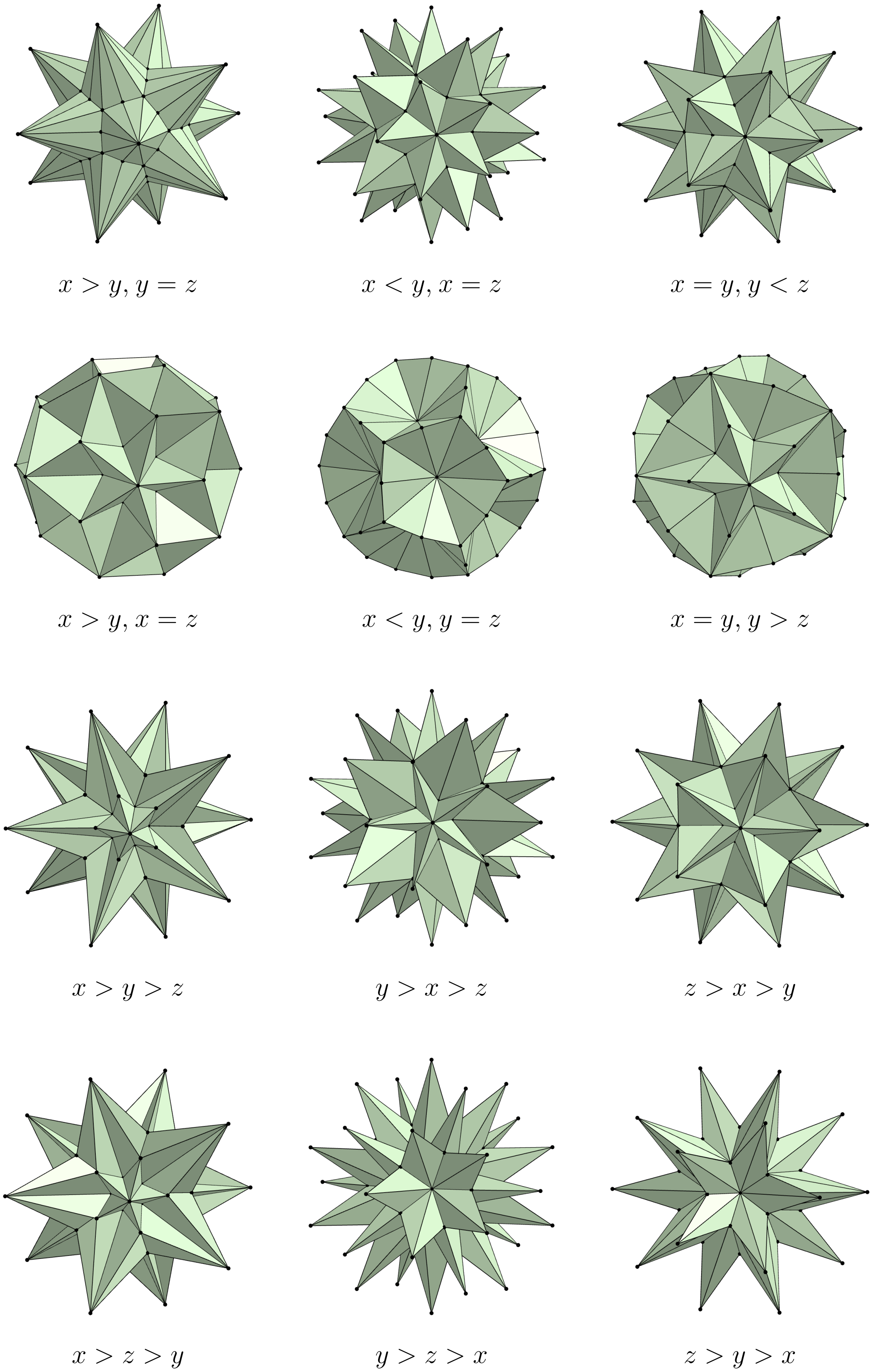

$x > y, y = z$ $x < y, x = z$ $x = y, y < z$

$x > y, x = z$ $x < y, y = z$ $x = y, y > z$

$x > y > z$ $y > x > z$ $z > x > y$

$x > z > y$ $y > z > x$ $z > y > x$

Fig. 4.13. Depending on the scaling factors x, y, z, the twelve different types of stellations of $\mathcal{V}_{H_3}(a, b, c)$ are presented.

Among the sorted points, those with non-negative indicated coordinates stand for the points $\mu \in \mathbb{R}^3$ that determine each 'pancake' in terms of a mixed basis. The coordinates of μ relative to the subgroups $G' \subset H_3$ form the dominant points $\mu' \in \mathbb{R}^2$ of G'. The number of points of $O_{G'}(\mu')$ is provided by formula (4.5.2). Whenever the group $A_1 \times A_1$ is considered in the reduction of the H_3-symmetry, several orbits can be determined by the same α_k-coordinate, $k \in \{1,2,3\}$. Therefore, such orbits belong to one 'pancake'. For that reason, the number of two-dimensional orbits does not necessarily coincide with the number of 'pancakes' of a considered polytope (for example, see Figures A.3−A.7 for the polytopes viewed from the direction perpendicular to the simple root α_2). The numbers of circular orbits and 'pancakes' obtained for $\mathcal{V}_{H_3}(\lambda)-$polytopes are listed in Table 4.9. The 'pancake'-structures of $\mathcal{V}_{H_3}(\lambda)$ for each type of dominant point λ are presented in Figures A.1−A.7 of Appendix A.

The Cartan matrices $C_{G'}$ and the inverse Cartan matrices $C_{G'}^{-1}$ are

$$C_{H_2} = \begin{pmatrix} 2 & -\tau \\ -\tau & 2 \end{pmatrix}, \quad C_{A_1\times A_1} = \frac{1}{3}\begin{pmatrix} 2 & 0 \\ 0 & 2 \end{pmatrix}, \quad C_{A_2} = \begin{pmatrix} 2 & -1 \\ -1 & 2 \end{pmatrix};$$

$$C_{H_2}^{-1} = \frac{1}{3-\tau}\begin{pmatrix} 2 & \tau \\ \tau & 2 \end{pmatrix}, \quad C_{A_1\times A_1}^{-1} = \frac{1}{2}\begin{pmatrix} 1 & 0 \\ 0 & 1 \end{pmatrix}, \quad C_{A_2}^{-1} = \frac{1}{3}\begin{pmatrix} 2 & 1 \\ 1 & 2 \end{pmatrix}.$$

For each subgroup G' of H_3, the squared radii of orbits with a dominant point $\mu' = (a,b)$ can be written explicitly as

$$R^2_{H_2}(\mu') = \begin{pmatrix} a & b \end{pmatrix} C_{H_2}^{-1}\begin{pmatrix} a \\ b \end{pmatrix} = \tfrac{2}{3-\tau}(a^2 + ab\tau + b^2), \tag{4.8.1}$$

$$R^2_{A_2}(\mu') = \begin{pmatrix} a & b \end{pmatrix} C_{A_2}^{-1}\begin{pmatrix} a \\ b \end{pmatrix} = \tfrac{2}{3}(a^2 + ab + b^2), \tag{4.8.2}$$

$$R^2_{A_1\times A_1}(\mu') = \begin{pmatrix} a & b \end{pmatrix} C_{A_1\times A_1}^{-1}\begin{pmatrix} a \\ b \end{pmatrix} = \tfrac{1}{2}(a^2 + b^2). \tag{4.8.3}$$

The points μ that determine each circular/polygonal orbit in the mixed basis, the squared radii of $O_{G'}(\mu')$ calculated via the formulas (4.8.1)–(4.8.3), and the numbers of points that belong to each $O_{G'}(\mu')$ are listed in Tables B.1−B.7 of Appendix B.

4.9. Symmetry breaking of $\mathcal{V}_{H_3}(\lambda)$ and related tubes

Since we would like to preserve the two-dimensional faces v_2 of $\mathcal{V}_{H_3}(\lambda)-$polytopes, the symmetry breaking of a polytope proceeds in the following way:

(i) choose a two-dimensional subgroup $G' \subset H_3$, and consider the coordinates of vertices of $\mathcal{V}_{H_3}(\lambda)$ in the corresponding mixed basis;

	H_2		$A_1 \times A_1$		A_2	
λ	*Orbits*	*'Pancakes'*	*Orbits*	*'Pancakes'*	*Orbits*	*'Pancakes'*
$(a, 0, 0)$	4	4	7	7	6	6
$(0, b, 0)$	8	8	12	7	10	10
$(0, 0, c)$	4	4	5	5	4	4
$(a, b, 0)$	8	8	12	11	10	10
$(a, 0, c)$	13	13	21	19	17	17
$(0, b, c)$	8	8	12	11	10	10
(a, b, c)	13	13	21	19	17	17

Table 4.9. The numbers of orbits and 'pancakes' are provided for each two-dimensional subgroup $G' \subset H_3$ by the orbit decompositions of $\mathcal{V}_{H_3}(\lambda)-$polytopes. The dominant points λ with $a = b = c$ are considered.

(*ii*) after the orbit decomposition is completed, choose only those 'pancakes' that are involved in the structure of the two-dimensional faces located at the 'equator' of a considered polytope, i.e., the faces that intersect a plane passing through the center of an isogonal polyhedron;

(*iii*) construct the symmetry-breaking path that proceeds along the edges of the facets determined by the 'pancakes' from (*ii*); note that the edges are selected in such a way that the same number of the two-dimensional faces belongs to each half of a polytope.

(*iv*) break the structure of a considered polytope in half to obtain the top and bottom caps.

For clarity, the edges of a polytope that belong to the symmetry-breaking path are depicted by bold segments (for instance, see Figure 4.14). After a polytope $\mathcal{V}_{H_3}(\lambda)$ is broken in half, the two-dimensional faces determined by (*ii*), that belong to the top and bottom caps of a polytope, are presented in gray and green colors, respectively. Therefore, unfolding the colored ring of polygons results in the two-dimensional nets shown in Figures 4.14, 4.18, 4.21. The rings of polygons can be extended by duplicating the 'pancakes' and stacking them on top of each other while preserving the distances between them. Extending the structures of such nets, rolling them onto a cylinder and seamlessly closing the ends with the corresponding caps result in the structures of closed tubes. Here the difference from the approach in (Bodner *et al.* [**13**], [**14**], [**15**]) lies in the additional rotation of 'pancakes' (rings of polygons) determined in (*ii*) to satisfy the two-dimensional tilings shown in Figures 4.16(b), 4.20(b).

In this section, we construct the closed tubes arising from the broken-in-half polytopes $\mathcal{V}_{H_3}(a, 0, 0)$, $\mathcal{V}_{H_3}(0, b, 0)$ and $\mathcal{V}_{H_3}(0, 0, c)$. The $\mathcal{V}_{H_3}(\lambda)-$polytopes, that are constructed for the other four types of λ, contain two or three generic orbits within their structures. Hence, the closed tubes obtained from broken-in-half polytopes $\mathcal{V}_{H_3}(a,b,0)$, $\mathcal{V}_{H_3}(a,0,c)$, $\mathcal{V}_{H_3}(0,b,c)$ and $\mathcal{V}_{H_3}(a,b,c)$ will contain more points, because more pancakes are involved in (*ii*). The possible inserts for such cases are presented in Figure 4.24, and they resemble the inserts for the polytopes in Subsections 4.9.1–4.9.3. For each insert, the small black arrows indicate the joining of the symmetry-breaking path once the net is folded onto a cylinder.

Note that some of the obtained tubes might violate the physical constraints pertinent to the fullerene structure. Due to the valency (for instance, see Figure 4.15(*a*)) or extreme angles (Figure 4.15(*b*)), the exemplified structures are not likely to represent models of fullerenes. However, such nanotubes could potentially model yet to be discovered, or de novo designed structures that can be of potential use in nanoscience. Nevertheless, we would like to demonstrate the construction of the closed tubes in mathematical generality. Therefore, the tube-like structures illustrated in Figures 4.16, 4.17(*b*), 4.20(*b*), 4.21, 4.22, 4.23 are possible to consider, as the orbit decompositions of the corresponding polytopes permit their existence. In Figures 4.16, 4.17(*b*), the pentagonal faces are planar, as they are preserved while breaking the symmetry of the corresponding polytopes.

4.9.1. The $\mathcal{V}_{H_3}(1,0,0)$−polytope

In Fig 4.14, a symmetry-breaking mechanism applied to the dodecahedron $\mathcal{V}_{H_3}(1,0,0)$.

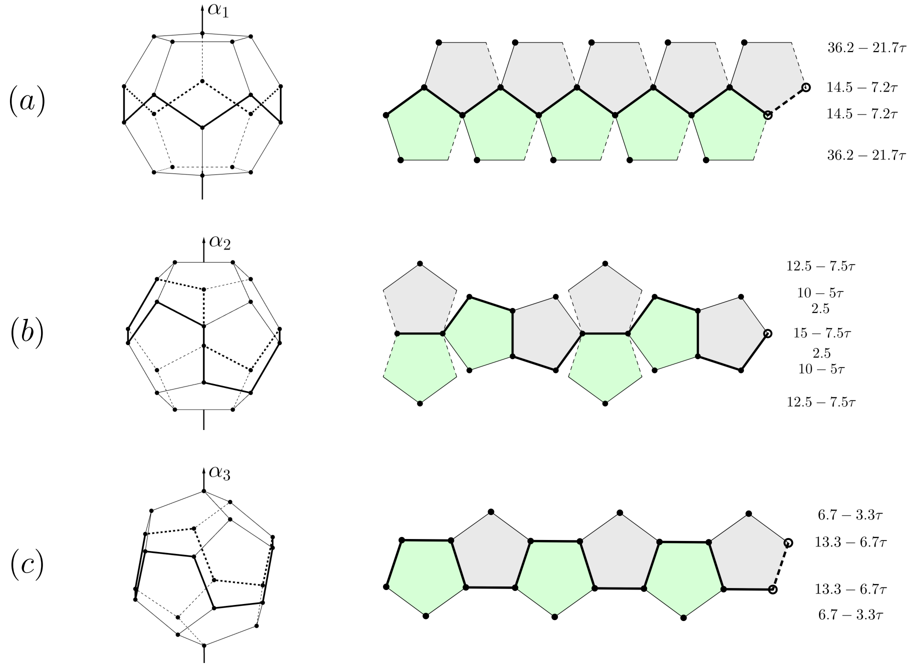

Fig. 4.14. On the left, the polytope $\mathcal{V}_{H_3}(1,0,0)$ is viewed from the direction orthogonal to the simple root (*a*) α_1, (*b*) α_2, (*c*) α_3. The values of the squared radii are listed on the right for each 'pancake'.

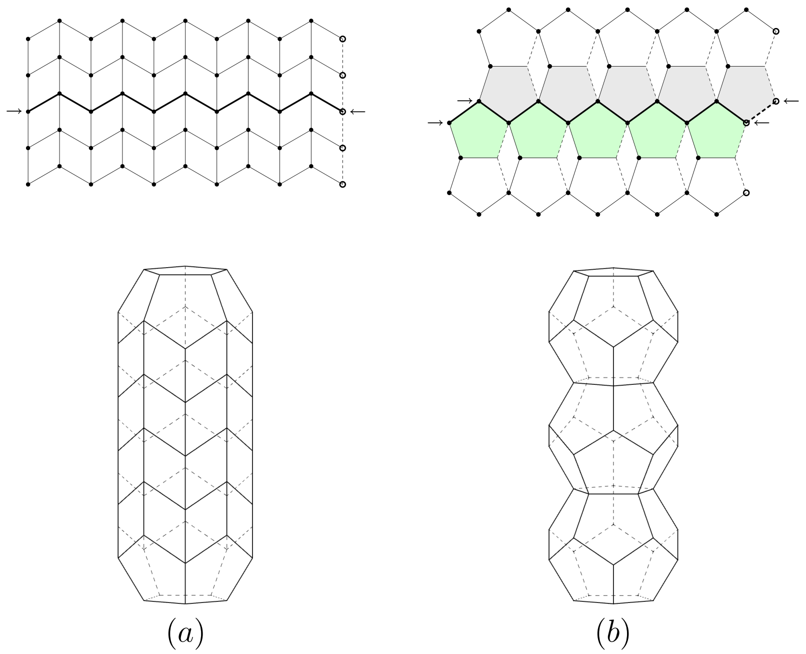
(a) (b)

Fig. 4.15. For $\mathcal{V}_{H_3}(a,0,0)$ viewed from the direction orthogonal to the simple root α_1, the inserts and the corresponding tubes are presented in the columns (a) and (b).

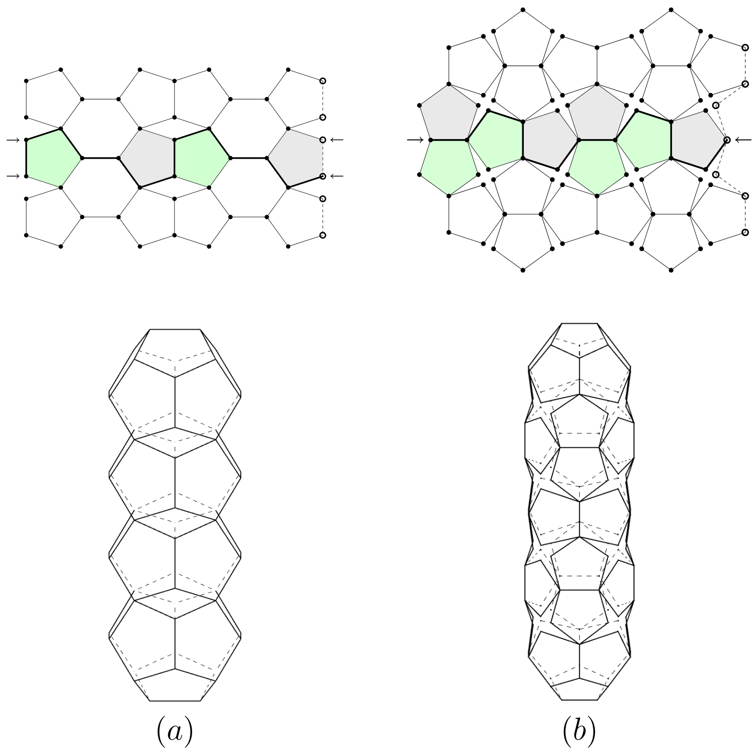
(a) (b)

Fig. 4.16. For $\mathcal{V}_{H_3}(a,0,0)$ viewed from the direction orthogonal to the simple root α_2, the inserts and the corresponding tubes are presented in the columns (a) and (b).

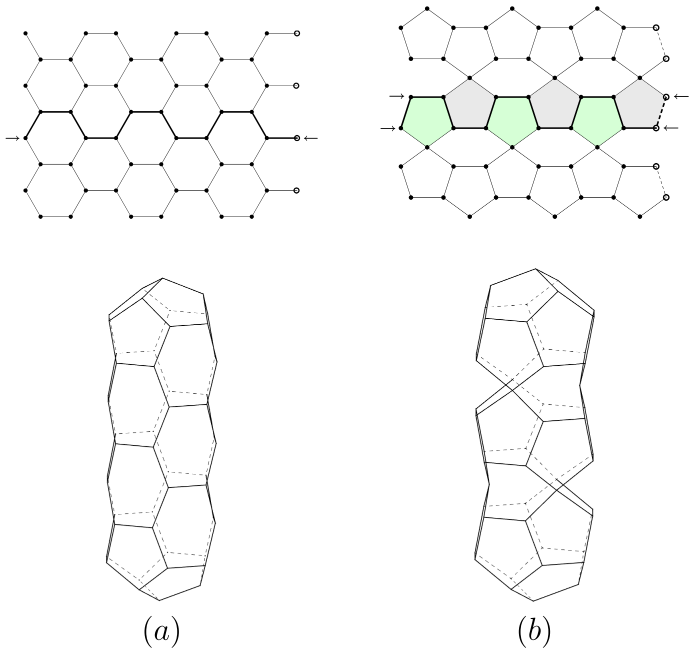

Fig. 4.17. For $\mathcal{V}_{H_3}(a,0,0)$ viewed from the direction orthogonal to the simple root α_3, the inserts and the corresponding tubes are presented in the columns (a) and (b).

4.9.2. The $\mathcal{V}_{H_3}(0,0,1)-$polytope

In Figure 4.18, a symmetry-breaking mechanism is applied to the icosahedron $\mathcal{V}_{H_3}(0,0,1)$.

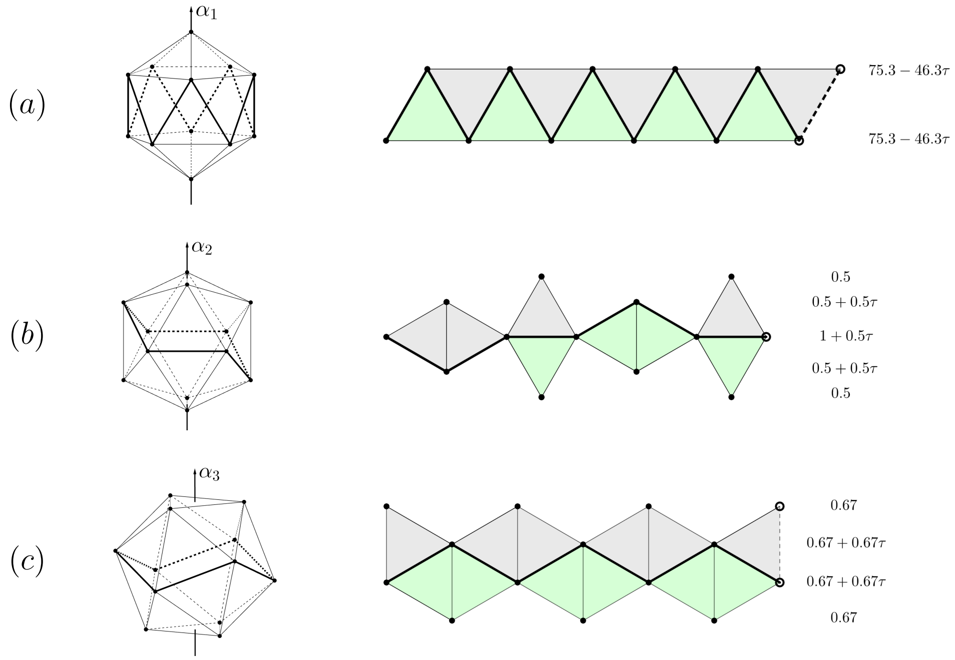
(a)
α_1
$75.3-46.3\tau$
$75.3-46.3\tau$
(b)
α_2
0.5
$0.5+0.5\tau$
$1+0.5\tau$
$0.5+0.5\tau$
0.5
(c)
α_3
0.67
$0.67+0.67\tau$
$0.67+0.67\tau$
0.67

Fig. 4.18. On the left, the polytope $\mathcal{V}_{H_3}(0,0,1)$ is viewed from the direction orthogonal to the simple root (a) α_1, (b) α_2, (c) α_3. The values of the squared radii are listed on the right for each 'pancake'.

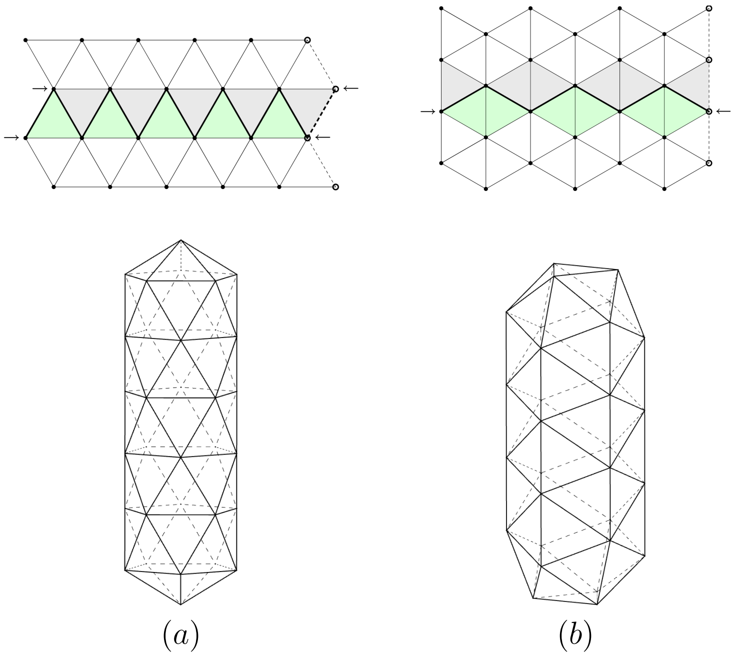

(*a*) (*b*)

Fig. 4.19. For $\mathcal{V}_{H_3}(0,0,c)$ viewed from the direction orthogonal to the simple roots α_1 and α_3, the inserts and the corresponding tubes are presented in the columns (*a*) and (*b*), respectively.

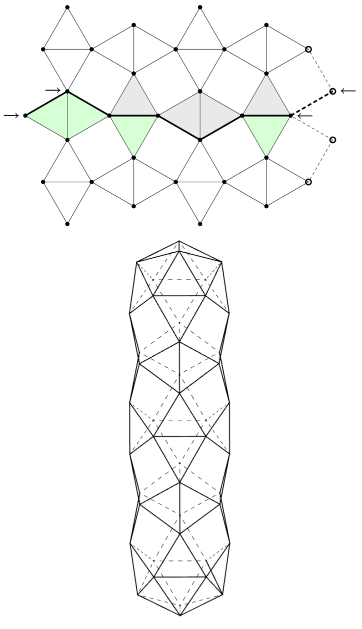

(*a*) (*b*)

Fig. 4.20. For $\mathcal{V}_{H_3}(0,0,c)$ viewed from the directions orthogonal to the simple root α_2, the inserts and the corresponding tubes are presented in the columns (*a*) and (*b*).

4.9.3. The $\mathcal{V}_{H_3}(0,1,0)$−polytope

In Figure 4.21, a symmetry-breaking mechanism is applied to the rhombic triacontahedron $\mathcal{V}_{H_3}(0,1,0)$.

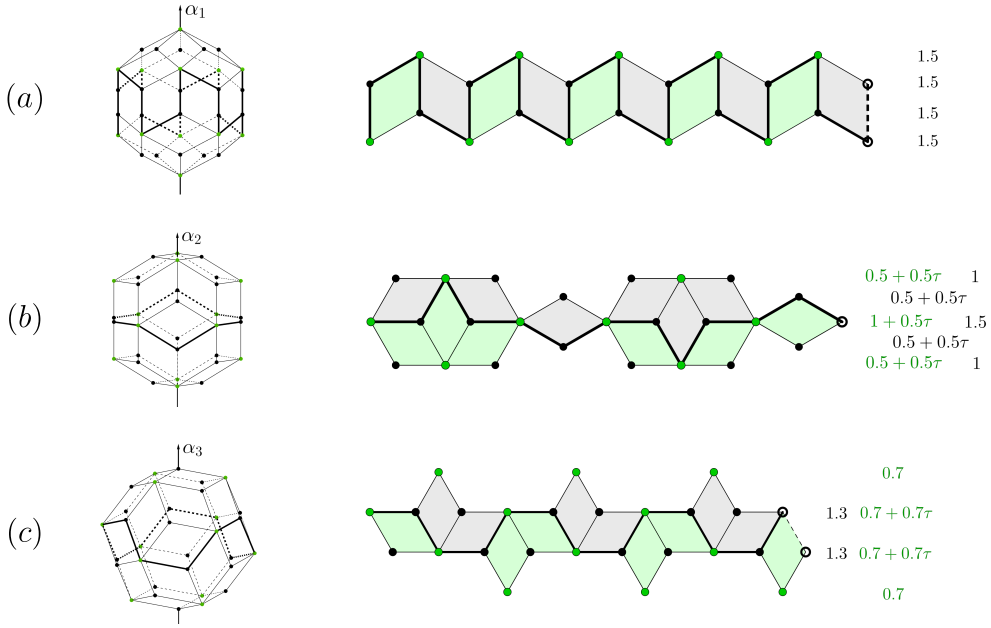
(a)
α1
1.5
1.5
1.5
1.5
(b)
α2
0.5 + 0.5τ 1
0.5 + 0.5τ
1 + 0.5τ 1.5
0.5 + 0.5τ
0.5 + 0.5τ 1
(c)
α3
0.7
1.3 0.7 + 0.7τ
1.3 0.7 + 0.7τ
0.7

Fig. 4.21. On the left, the polytope $\mathcal{V}_{H_3}(0,1,0)$ is viewed from the direction orthogonal to the simple root (a) α_1, (b) α_2, (c) α_3. The values of squared radii are listed on the right for each 'pancake'.

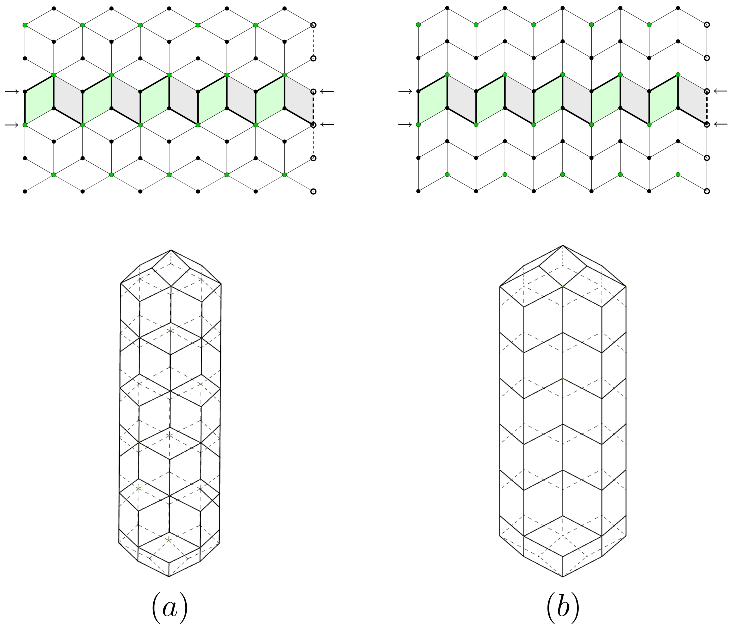

Fig. 4.22. For $\mathcal{V}_{H_3}(0,b,0)$ viewed from the direction orthogonal to the simple root α_1, the inserts and the corresponding tubes are presented in the columns (a) and (b).

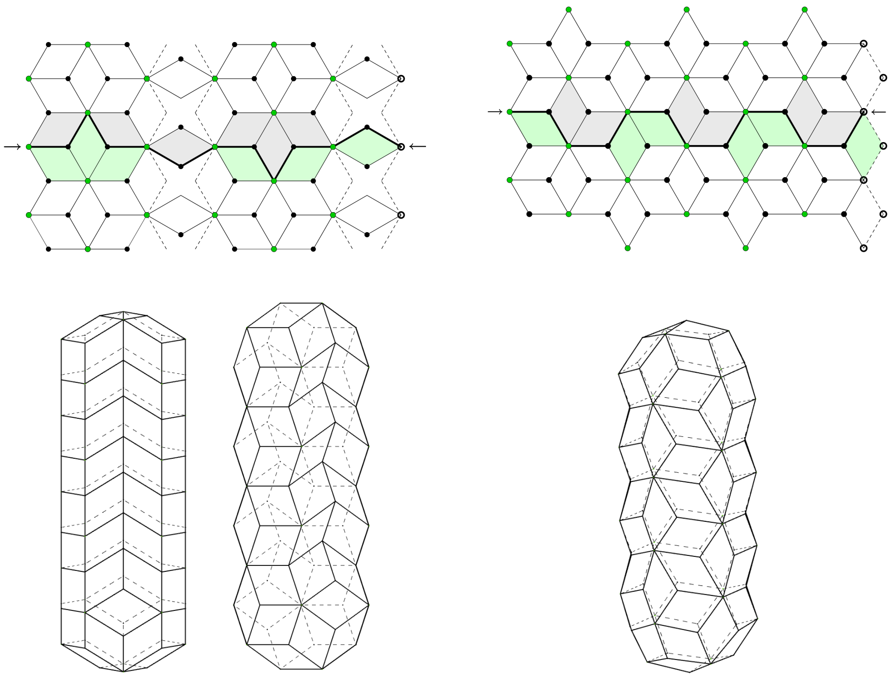

(*a*) (*b*)

Fig. 4.23. For $\mathcal{V}_{H_3}(0, b, 0)$ viewed from the directions orthogonal to the simple root α_2 and α_3, the inserts and the corresponding tubes are presented in the columns (*a*) and (*b*), respectively. In (*a*) the same tube is viewed from a different angle.

4.10. Symmetry breaking of the fullerene C_{20}

The fullerene C_{20} is the smallest member of the fullerene family. It has the structure of the dodecahedron with carbon atoms placed at its vertices (Figure 4.25). Breaking the symmetry of C_{20} plays a significant role in the construction of larger fullerene molecules and nanotubes.

It is convenient to define the notations for the faces of the considered fullerenes. Hence, the vertices are denoted by f_0, the edges by f_1, and the two types of two-dimensional faces by f_2^1 (pentagons) and f_2^2 (hexagons). The numbers of faces of a fullerene are restricted by the Euler's formula (4.5.1), and they are provided by the expressions (Fowler and Manolopoulos [**52**]):

$$N(f_0) = n, \quad N(f_1) = \frac{3n}{2}, \quad N(f_2) = \frac{n}{2} + 2, \quad N(f_2^1) = 12, \quad N(f_2^2) = \frac{n}{2} - 10.$$

where n indicates the number of carbon atoms of a fullerene.

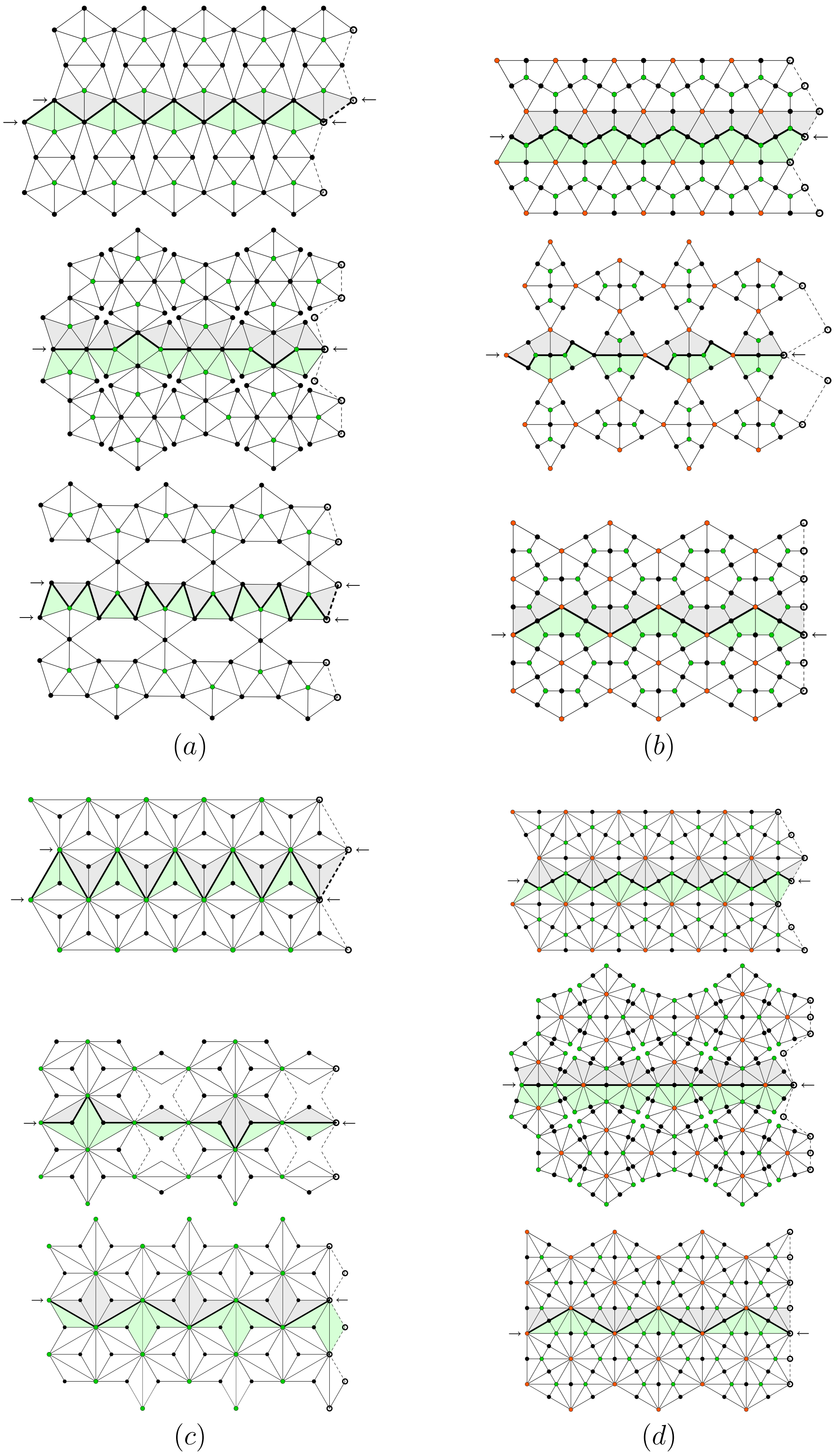

(a) (b)

(c) (d)

Fig. 4.24. The possible inserts are presented in columns for the polytopes (a) $\mathcal{V}_{H_3}(a,b,0)$, (b) $\mathcal{V}_{H_3}(a,0,c)$, (c) $\mathcal{V}_{H_3}(0,b,c)$, (d) $\mathcal{V}_{H_3}(a,b,c)$, and they are ordered for the directions of the simple roots α_1, α_2, α_3 from top to bottom.

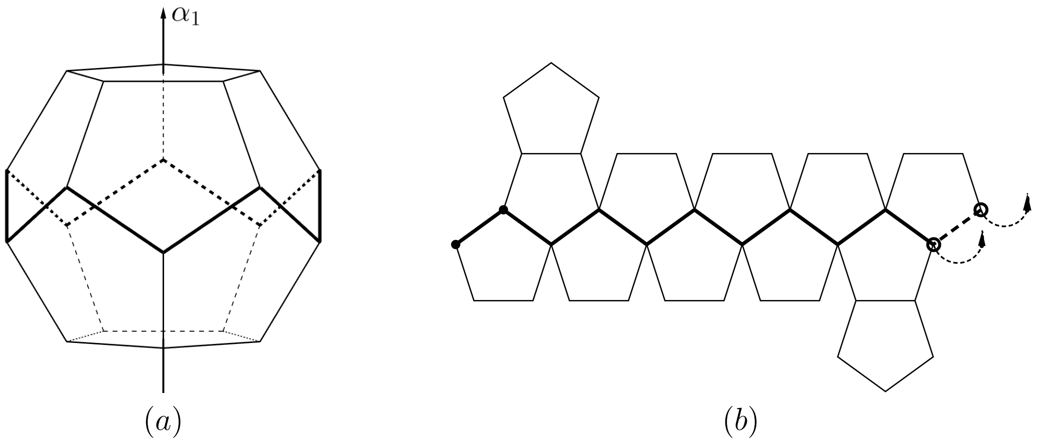

(*a*) (*b*)

Fig. 4.25. (*a*) The fullerene C_{20} is oriented in the direction of the simple root α_1. The edges depicted by bold segments correspond to the symmetry-breaking path. (*b*) The net of C_{20}.

The dual to the structure of the fullerene C_{20} is the icosahedron. The faces of an icosahedral fullerene can be reconstructed from its dual polytope, using the method described in (Caspar & Klug, 1962) or the Coxeter construction (Coxeter, 1971; Fowler & Manolopoulos, 2006). Both methods are based on subtriangulations of the two-dimensional faces of the icosahedron into $20T$ smaller triangles. The number $T = h^2 + hk + k^2$ is the triangulation number, where $h > 0$, $k \geq 0$. Hence, depending on the value of T, we can construct the structures of icosadeltahedra. The two-dimensional net of the latter has a dual hexagon-pentagon tilling, which is trivalent by construction, and, therefore, relevant to model fullerene structures. Interchanging the integers h and k yields two icosadeltahedron-fullerene pairs that are enantiomers of each other.

To directly extend the structure of C_{20} without referring to its dual, one can utilize the technique described in Section 4.9. In this section, we focus on the construction of four smallest fullerenes (C_{24}, C_{26}, C_{28} and C_{30}) and two types of carbon nanotubes (C_{20+10N} and C_{20+6N}). The considered fullerenes are obtained by adding up to five hexagonal faces into the structure of C_{20}. n this case, the different symmetries are observed for each constructed fullerene (Figure 4.32). The nanotubes are obtained by duplicating and inserting more 'pancakes' into the orbit decomposition of the fullerene C_{20}.

Similarly to the construction of tubes for the dodecahedron $\mathcal{V}_{H_3}(a, 0, 0)$ presented in Subsection 4.9.1, the vertices of C_{20} are considered in the mixed bases: $\{\alpha_1, \omega_2, \omega_3\}$, $\{\omega_1, \alpha_2, \omega_3\}$, $\{\omega_1, \omega_2, \alpha_3\}$. The net of C_{20}, shown in Figure 4.25(*b*), is deformed by adding more hexagons (Figure 4.32). The numbers of faces together with the symmetries of the examined fullerenes are listed in Table 4.10. The notation is partially adapted from (Fowler & Manolopoulos, 2006), where n is the number of carbon atoms, and m labels each differently assembled fullerene with the same number of vertices, i.e., each fullerene isomer.

Table 4.10. The symmetries and number of faces of the fullerenes C_{20}, C_{24}, C_{26}, $C_{28:m}$, $C_{30:m}$ are presented.

Fullerene	*Point group*	$N(f_0)$	$N(f_1)$	$N(f_2^1)$	$N(f_2^2)$
C_{20}	I_h	20	30	12	0
C_{24}	D_{6d}	24	36	12	2
C_{26}	D_{3h}	26	39	12	3
$C_{28:1}$	D_2	28	42	12	4
$C_{28:2}$	T_d	28	42	12	4
$C_{30:1}$	D_{5h}	30	45	12	5
$C_{30:2}$	C_{2v}	30	45	12	5
$C_{30:3}$	C_{2v}	30	45	12	5

Let us consider the dodecahedron, whose 'pancakes' provided by the subgroup $H_2 \subset H_3$ are oriented in the direction of the simple root α_1. As the two-dimensional faces should be preserved, the symmetry breaking proceeds along the bold edges shown in Figure 4.26(a). After breaking C_{20} in half, we keep the faces of the top cap depicted by gray color. To obtain the bottom cap, we reflect the top one across the plane spanned by the vectors ω_2 and ω_3. Adding a ring of hexagons into the broken structure, yields the fullerene $C_{30:1}$ (Figure 4.26(c)). Furthermore, inserting more rings of hexagons into $C_{30:1}$ yields the structure of the carbon nanotube C_{20+10N}, where N denotes the number of inserted 'pancakes'. For example, for $N = 3$, the nanotube C_{50} is shown in Figure 4.26(d). For the fullerene C_{24} shown in Figure 4.26(b), the initial net of C_{20} (Figure 4.25) is extended by adding two pentagons. Such a procedure results in the replacement of the top and bottom pentagons by hexagons, see Figure 4.32. As a result, each two-dimensional orbit of C_{20}, that has the H_2-symmetry, gains one extra point. In a similar way, the structure of the fullerene $C_{30:2}$ is obtained (Figure 4.27).

Breaking the symmetry of C_{20}, whose 'pancake'-structure is provided by the symmetry group $A_1 \times A_1 \subset H_3$, yields the fullerenes $C_{28:2}$ (Figure 4.28(b)) and $C_{30:3}$ (Figure 4.29(b)). In the case of $C_{28:2}$, the top cap with its faces depicted by gray color is reflected across the plane spanned by the vectors ω_1 and ω_3 to obtain the bottom cap. The latter is rotated by $\pi/2$ to form the fullerene. For the fullerene $C_{30:3}$, only the top cap of C_{20} contributes to the structure of $C_{30:3}$.

Finally, let us consider the molecule C_{20}, whose 'pancakes' provided by the subgroup $A_2 \subset H_3$ are oriented in the α_3-direction. In this case, applying the symmetry breaking yields two fullerenes, namely C_{26} and $C_{28:1}$, shown in Figure 4.31(b) and Figure 4.30(b), respectively. The structure of the molecule C_{26} can be extended into the carbon nanotube

C_{20+6N}. For example, for $N = 5$, the carbon nanotube C_{50} is presented in Figure 4.31(c). In this case, to close the nanotube on both ends, the bottom cap is obtained by reflecting the top one across the plane spanned by the vectors ω_1 and ω_2.

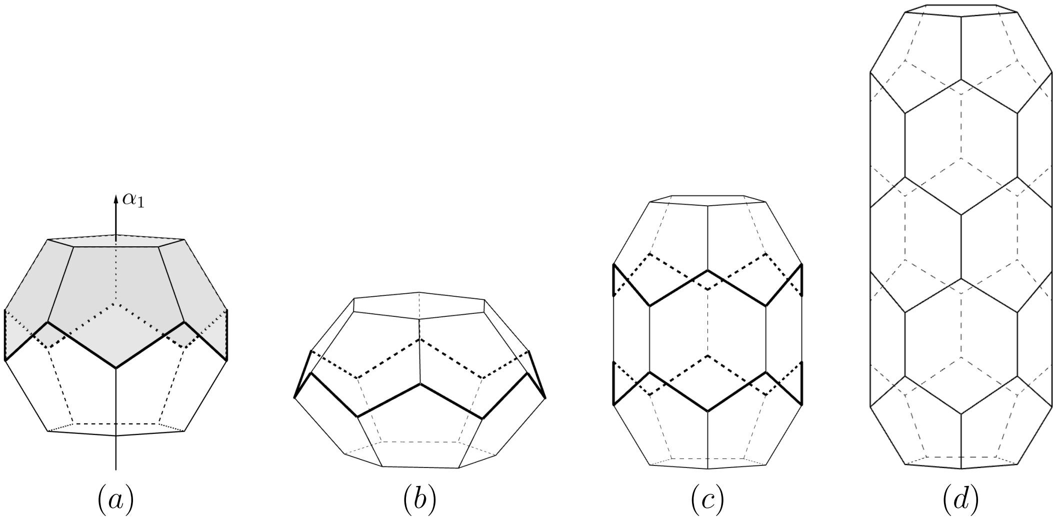

Fig. 4.26. (a) The fullerene C_{20} is viewed from the direction orthogonal to the simple root α_1. The faces depicted by gray color are kept after the symmetry of C_{20} is broken. (b) The fullerene C_{24}. (c) The fullerene $C_{30:1}$. (d) The structure of $C_{30:1}$ is extended into the nanotube C_{50}.

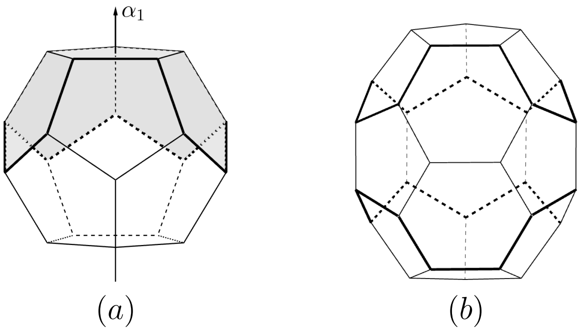

Fig. 4.27. (a) The fullerene C_{20} is viewed from the direction orthogonal to the simple root α_1. The faces depicted by gray color are kept after the symmetry of C_{20} is broken. (b) The fullerene $C_{30:2}$.

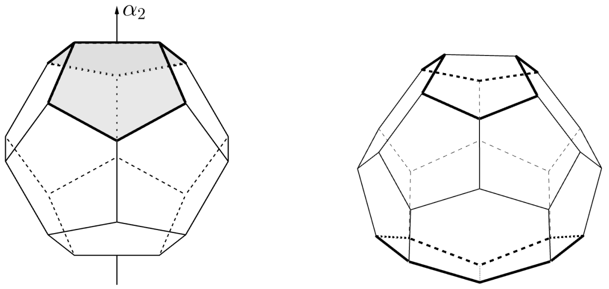

(a) (b)

Fig. 4.28. (a) The fullerene C_{20} is viewed from the direction orthogonal to the simple root α_2. The faces depicted by gray color are kept after the symmetry of C_{20} is broken. (b) The fullerene $C_{28:2}$.

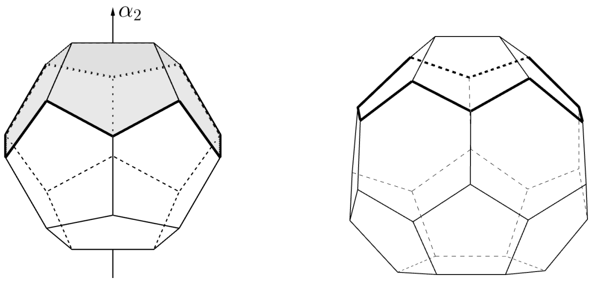

(a) (b)

Fig. 4.29. (a) The fullerene C_{20} is viewed from the direction orthogonal to the simple root α_2. The faces depicted by gray color are kept after the symmetry of C_{20} is broken. (b) The fullerene $C_{30:3}$.

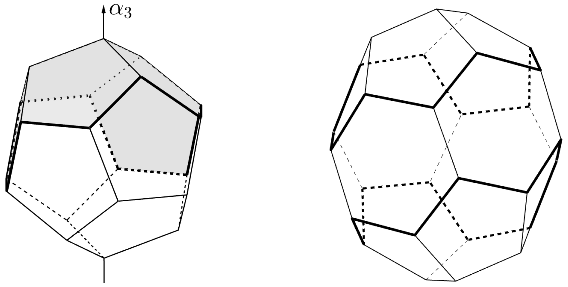

(a) (b)

Fig. 4.30. (a) The fullerene C_{20} is viewed from the direction orthogonal to the simple root α_3. The faces depicted by gray color are kept after the symmetry of C_{20} is broken. (b) The fullerene $C_{28:1}$.

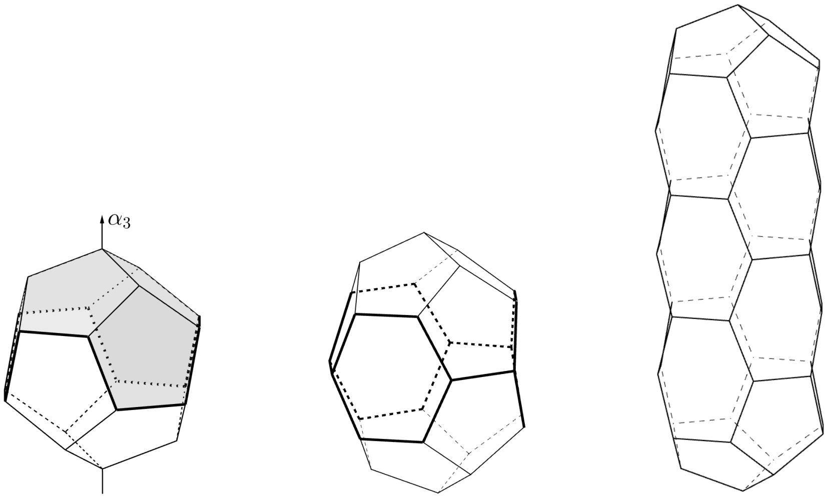

(a) (b) (c)

Fig. 4.31. (a) The fullerene C_{20} is viewed from the direction orthogonal to the simple root α_3. The faces depicted by gray color are kept after the symmetry of C_{20} is broken. (b) The fullerene C_{26}. (c) The structure of C_{26} is extended into the nanotube C_{50}.

4.11. Concluding remarks

- In this paper, we consider the family of polytopes $\mathcal{V}_{H_3}(\lambda)$ constructed for seven types of dominant point λ. The decoration rules, that are applied to a Coxeter–Dynkin diagram, play a significant role in the description of faces of polytopes and their duals (Champagne *et al.* [**29**]). Applying these rules to the Coxeter–Dinkin diagram of H_3, we determine the types and the numbers of faces of considered $\mathcal{V}_{H_3}(\lambda)-$polytopes. The reflection graph arises from the action of the reflections of H_3 on a dominant point λ. Using the reflection graph, we illustrate the facets that belong to the vertex of a $\mathcal{D}_{H_3}(\lambda)-$polytope provided by λ and, therefore, determine a two-dimensional face of its dual $\mathcal{V}_{H_3}(\lambda)$. Moreover, since we can obtain several decorated Coxeter–Dynkin diagrams at the last step of the decoration procedure, it might be useful to develop the rules that unite such diagrams into one. Thus, a $\mathcal{V}(\lambda)-$polytope will have only one corresponding decorated Coxeter–Dynkin diagram.
- The reductions of the H_3-symmetry, namely $H_3 \to H_2 \times A_1$, $H_3 \to A_2 \times A_1$ and $H_3 \to A_1 \times A_1 \times A_1$, are employed in order to obtain the orbit decompositions of $\mathcal{V}_{H_3}(\lambda)-$polytopes. The corresponding mixed bases $\{\alpha_1, \omega_2, \omega_3\}$, $\{\omega_1, \alpha_2, \omega_3\}$, $\{\omega_1, \omega_2, \alpha_3\}$ are utilized to determine the orbit decomposition for each considered polytope. Applying a symmetry-breaking mechanism (Bodner *et al.* [**13**]) to the family of $\mathcal{V}_{H_3}(\lambda)-$polyhedra results in the structure of broken-in-half polytopes. Duplicating the 'pancakes' and inserting them into the structures of $\mathcal{V}_{H_3}(\lambda)$ yield the exemplified tube-like structures. The structures of obtained tubes may serve as a

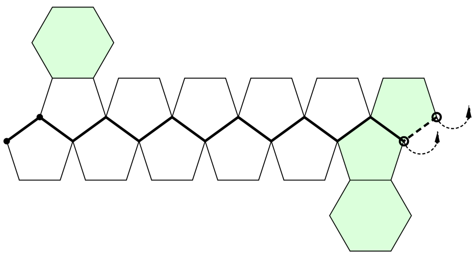

$C_{24}\,(\alpha_1)$

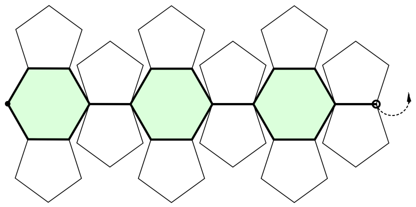

$C_{28}\,(\alpha_3)$

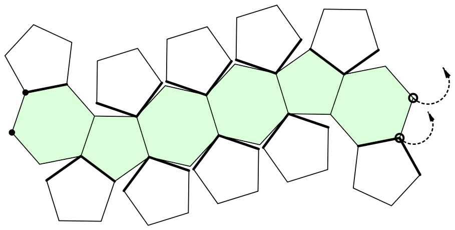

$C_{28:1}\,(\alpha_3)$

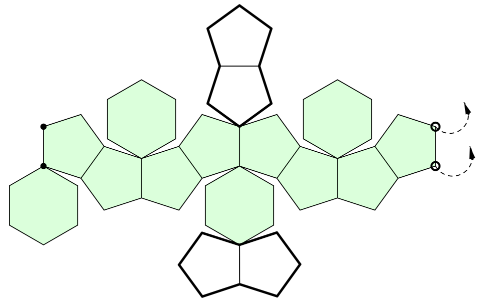

$C_{28:2}\,(\alpha_2)$

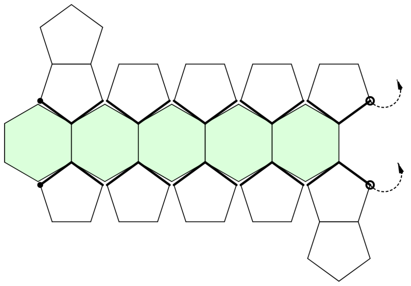

$C_{30:1}\,(\alpha_1)$

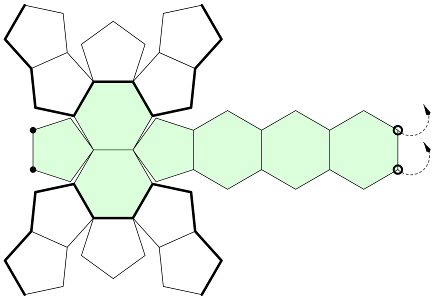

$C_{30:2}\,(\alpha_1)$

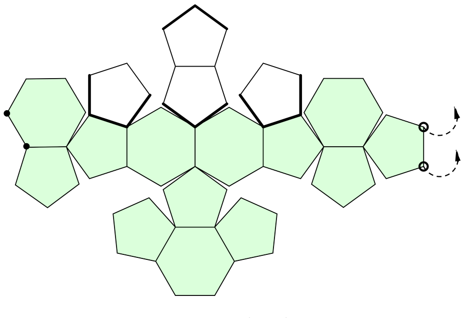

$C_{30:3}\,(\alpha_2)$

Fig. 4.32. The two-dimensional nets of the fullerenes C_{24}, C_{26}, $C_{28:m}$, $C_{30:m}$ are presented. The bold edges are in one-to-one correspondence with the edges chosen at the start of the symmetry breaking procedure. The faces depicted by green color are inserted whenever the symmetry of C_{20} is broken. The empty and filled nodes indicate an overlap as the net is folded onto a cylinder.

starting point in describing their physical and chemical properties. Breaking the symmetry of $\mathcal{V}(\lambda)-$polytopes of the crystallographic reflection groups A_3, B_3 and C_3 is considered as a continuation of this paper.

- Since the structures of $\mathcal{V}_{H_3}(\lambda)-$polytopes may contain up to three generic orbits, we demonstrate the construction of stellations for considered polytopes. In this study, the stellations are obtained by scaling the radii of generic orbits. As a result, the lengths of one-dimensional faces of a polytope change depending on a chosen scaling factor. Using the same approach, the construction of stellated dual polyhedra of the crystallographic type should be treated independently.
- For the fullerene molecule C_{20}, that has the structure of $\mathcal{V}_{H_3}(a,0,0)$, using the reduction of the H_3-symmetry to the two-dimensional subgroups H_2 and A_2 yields the two families of nanotubes, C_{20+10N} and C_{20+6N}, respectively. The symmetry reduction $H_3 \to A_1 \times A_1 \times A_1$ is the most complicated among the three considered cases, as it yields a chiral nanotube (Bodner *et al.* [**15**]). In this case, the way to extend the structure of C_{20} with its 'pancakes' oriented in the α_2-direction merits further investigation. The relevance of the icosahedral group to the modelling of chiral polyhedra can be found, for example, in (Koca and Koca [**83**]).
- For any finite reflection group G, the branching rules providing the symmetry reduction were determined in several papers [for instance, see (Grabowiecka *et al.* [**54**]) and the references therein]. Applying a symmetry-breaking mechanism to $\mathcal{D}(\lambda)-$ and $\mathcal{V}(\lambda)-$polytopes, their structures can be extended into tube-like structures. In particular, an extension of the structures of $\mathcal{D}(\lambda)-$polyhedra of crystallographic type remains an open problem. The crystallographic and non-crystallographic tube-like structures may potentially be employed as the building blocks in the construction of multi-shell nanostructures (Kuo and Deng [**85**]; Diudea *et al.* [**45**]) and zeolite-like structures [for example, see (Taylor *et al.* [**136**]) and the references therein]. Moreover, such tube structures can be interesting to the field of mathematical virology (Keef and Twarock [**74**]).

Acknowledgments

The author would like to express her gratitude to Dr. M. Szajewska and Dr. A. Patera for their helpful comments and editorial assistance in preparing this paper. She would also like to thank Prof. J. Patera for his valuable remarks and stimulating discussions. The author is grateful to the co-editor Prof. U. Grimm and the anonymous referees for their constructive and helpful suggestions to improve the manuscript. This work was supported in part by the Natural Sciences and Engineering Research Council of Canada, No. RGPIN-2016-04199.

Chapter 5

Symmetry breaking of dual polyhedra of crystallographic type

In this chapter, we extend the research presented in Chapter 4 to the families of dual polytopes obtained using the crystallographic reflection groups A_3, B_3 and C_3. Using the notations introduced in Chapter 4, the pairs of dual polytopes are referred to as $\mathcal{D}_W(\lambda)-$ and $\mathcal{V}_W(\lambda)-$polytopes, where W corresponds to the crystallographic groups A_3, B_3 and C_3 (see Figures 5.1 and 5.2). The family of $\mathcal{D}_W(\lambda)-$polytopes is obtained applying the reflections of W to each type of dominant point $\lambda \in \mathbb{R}^3$. The structures of $\mathcal{V}_W(\lambda)-$polytopes may contain up to three orbits obtained by the action of W on the seed points $(a', 0, 0)$, $(0, b', 0)$ and $(0, 0, c')$. Since we are interested in breaking the symmetry of $\mathcal{V}_W(\lambda)-$polytopes, as well as their structural extension into nanotubes, we present the orbit decompositions for three families of dual polytopes of the crystallographic type.

5.1. Bases associated with the crystallographic reflection groups in $\mathbb{R}^3$

5.1.1. The $\alpha-$ and $\omega-$bases

In the three-dimensional real Euclidean space $\mathbb{R}^3$, it is useful to introduce a pair of dual bases, i.e. $\alpha-$ and $\omega-$bases, that are associated with the symmetry of a finite crystallographic reflection group W. The $\alpha-$ and $\omega-$bases are related via a Cartan matrix and its inverse,

$$\alpha_j = \sum_{k=1}^{3} C_W \omega_k, \qquad \omega_k = \sum_{j=1}^{3} C_W^{-1} \alpha_j, \tag{5.1.1}$$

where a Cartan matrix is provided by

$$C_W = \left(\frac{2\langle \alpha_j, \alpha_k \rangle}{\langle \alpha_k, \alpha_k \rangle} \right), \quad j, k \in \{1, 2, 3\}. \tag{5.1.2}$$

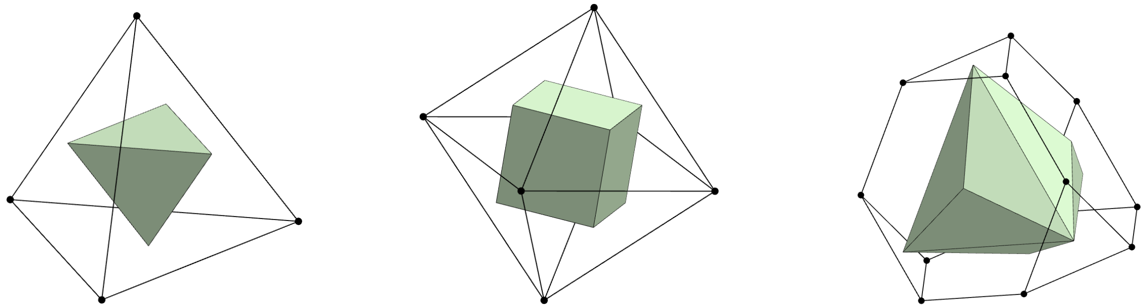

$\lambda = (a,0,0)$
$\lambda = (0,0,c)$

Tetrahedron – Tetrahedron

$\lambda = (0,b,0)$

Octahedron – Cube

$\lambda = (a,b,0)$
$\lambda = (0,b,c)$

Truncated tetrahedron – Triakis tetrahedron

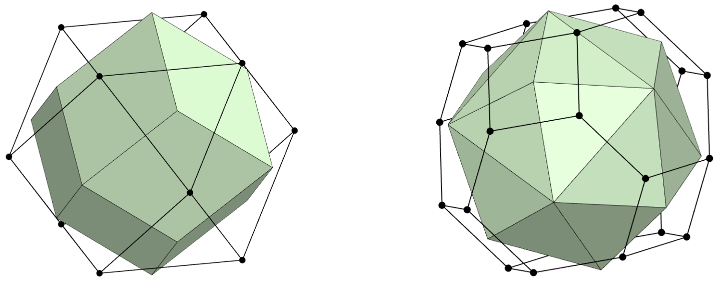

$\lambda = (a,0,c)$

Cuboctahedron – Rhombic dodecahedron

$\lambda = (a,b,c)$

Truncated octahedron – Tetrakis hexahedron

Fig. 5.1. The dual pairs of polytopes of the crystallographic group A_3 are constructed for each type of dominant point λ.

For the considered groups, the Cartan matrices and their inverses are listed in Table 5.1. Since the simple roots of the crystallographic groups B_3 and C_3 have two different lengths, the length of the long simple root is determined as $\langle \alpha_{\mathrm{long}}, \alpha_{\mathrm{long}} \rangle = 2$.

The dual bases $\alpha^\vee$ and $\omega^\vee$ are determined by the relations:

$$\alpha^\vee = \frac{2\alpha_i}{\langle \alpha_i, \alpha_i \rangle}, \quad \omega^\vee = \frac{2\omega_i}{\langle \alpha_i, \alpha_i \rangle}. \tag{5.1.3}$$

The duality relations between $\alpha-$, $\omega-$, $\alpha^\vee-$ and $\omega^\vee-$bases are

$$\langle \alpha_i, \omega_j^\vee \rangle = \langle \alpha_i^\vee, \omega_j \rangle = \delta_{ij}, \tag{5.1.4}$$

where δ_{ij} is the Kronecker delta.

Since the simple roots α_k are orthogonal to the reflecting hyperplanes m_k, $k \in \{1,2,3\}$, we use them to label the nodes of the corresponding Coxeter–Dynkin diagrams (Figure 5.3).

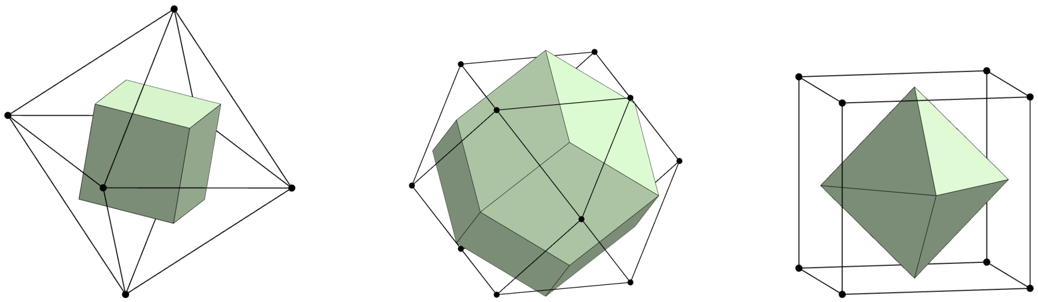

$\lambda = (a, 0, 0)$

Octahedron –
Cube

$\lambda = (0, b, 0)$

Cuboctahedron –
Rhombic dodecahedron

$\lambda = (0, 0, c)$

Cube –
Octahedron

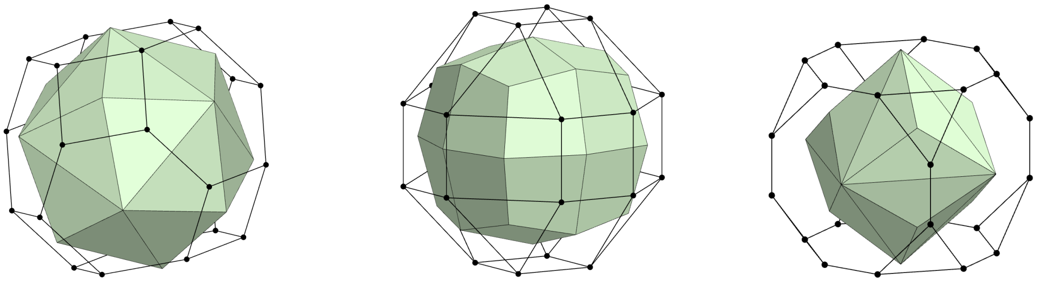

$\lambda = (a, b, 0)$

Truncated octahedron –
Tetrakis hexahedron

$\lambda = (a, 0, c)$

Rhombicuboctahedron –
Deltoidal icositetrahedron

$\lambda = (0, b, c)$

Truncated cube –
Triakis octahedron

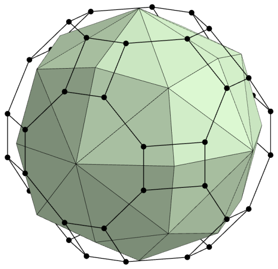

$\lambda = (a, b, c)$

Truncated cuboctahedron –
Disdyakis dodecahedron

Fig. 5.2. The dual pairs of polytopes of the crystallographic group B_3 and C_3 are constructed for each type of dominant point λ.

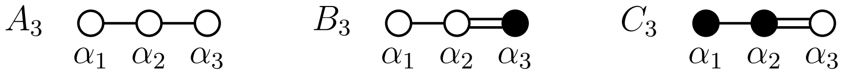
A_3
α_1 α_2 α_3
B_3
α_1 α_2 α_3
C_3
α_1 α_2 α_3

Fig. 5.3. The Dynkin diagrams associated with the crystallographic groups A_3, B_3 and C_3. The nodes of the diagrams correspond either to the vectors of the $\alpha-$basis, or to the basis vectors of the $\omega-$basis, or to the reflections r_k in the reflecting hyperplanes m_k, $k \in \{1,2,3\}$.

$$C_{A_3} = \begin{pmatrix} 2 & -1 & 0 \\ -1 & 2 & -1 \\ 0 & -1 & 2 \end{pmatrix} \qquad C_{A_3}^{-1} = \tfrac{1}{4}\begin{pmatrix} 3 & 2 & 1 \\ 2 & 4 & 2 \\ 1 & 2 & 3 \end{pmatrix}$$

$$C_{B_3} = \begin{pmatrix} 2 & -1 & 0 \\ -1 & 2 & -2 \\ 0 & -1 & 2 \end{pmatrix} \qquad C_{B_3}^{-1} = \tfrac{1}{2}\begin{pmatrix} 2 & 2 & 2 \\ 2 & 4 & 4 \\ 1 & 2 & 3 \end{pmatrix}$$

$$C_{C_3} = \begin{pmatrix} 2 & -1 & 0 \\ -1 & 2 & -1 \\ 0 & -2 & 2 \end{pmatrix} \qquad C_{C_3}^{-1} = \tfrac{1}{2}\begin{pmatrix} 2 & 2 & 1 \\ 2 & 4 & 2 \\ 2 & 4 & 3 \end{pmatrix}$$

Table 5.1. The Cartan matrices and their inverses are listed for the crystallographic reflection groups A_3, B_3 and C_3.

For the crystallographic reflection group A_3, all the simple roots have the same length, $\langle \alpha_i, \alpha_i \rangle = 2$, $i \in \{1,2,3\}$. Therefore, the vectors of the $\alpha-$ and $\omega-$bases, together with their duals, are explicitly written as

$$\begin{aligned} \alpha_1 &= 2\omega_1 - \omega_2, & \omega_1 &= \tfrac{3}{4}\alpha_1 + \tfrac{1}{2}\alpha_2 + \tfrac{1}{4}\alpha_3, \\ \alpha_2 &= -\omega_1 + 2\omega_2 - \omega_3, & \omega_2 &= \tfrac{1}{2}\alpha_1 + \alpha_2 + \tfrac{1}{2}\alpha_3, \\ \alpha_3 &= -\omega_2 + 2\omega_3; & \omega_3 &= \tfrac{1}{4}\alpha_1 + \tfrac{1}{2}\alpha_2 + \tfrac{3}{4}\alpha_3. \end{aligned} \tag{5.1.5}$$

$$\alpha_i^\vee = \alpha_i, \qquad \omega_i^\vee = \omega_i, \quad i \in \{1,2,3\}.$$

For the crystallographic reflection group B_3, there are two long and one short simple roots, $\langle \alpha_1, \alpha_1 \rangle = \langle \alpha_2, \alpha_2 \rangle = 2$, $\langle \alpha_3, \alpha_3 \rangle = 1$. Therefore, the vectors of the $\alpha-$ and $\omega-$bases, together with their duals, are explicitly written as

$$\begin{aligned} \alpha_1 &= 2\omega_1 - \omega_2, & \omega_1 &= \alpha_1 + \alpha_2 + \alpha_3, \\ \alpha_2 &= -\omega_1 + 2\omega_2 - 2\omega_3, & \omega_2 &= \alpha_1 + 2\alpha_2 + 2\alpha_3, \\ \alpha_3 &= -\omega_2 + 2\omega_3; & \omega_3 &= \tfrac{1}{2}\alpha_1 + \alpha_2 + \tfrac{3}{2}\alpha_3. \\ \alpha_1^\vee &= \alpha_1, & \omega_1^\vee &= \omega_1, \\ \alpha_2^\vee &= \alpha_2, & \omega_2^\vee &= \omega_2, \\ \alpha_3^\vee &= 2\alpha_3, & \omega_3^\vee &= 2\omega_3, \end{aligned} \tag{5.1.6}$$

For the crystallographic reflection group C_3, there are two short and one long simple roots $\langle\alpha_1,\alpha_1\rangle = \langle\alpha_2,\alpha_2\rangle = 1$, $\langle\alpha_3,\alpha_3\rangle = 2$. Therefore, the vectors of the $\alpha-$ and $\omega-$bases, together with their duals, are explicitly written as

$$\begin{aligned}
&\alpha_1 = 2\omega_1 - \omega_2, && \omega_1 = \alpha_1 + \alpha_2 + \tfrac{1}{2}\alpha_3,\\
&\alpha_2 = -\omega_1 + 2\omega_2 - \omega_3, && \omega_2 = \alpha_1 + 2\alpha_2 + 2\alpha_3,\\
&\alpha_3 = -2\omega_2 + 2\omega_3; && \omega_3 = \tfrac{1}{2}\alpha_1 + 2\alpha_2 + \tfrac{3}{2}\alpha_3.\\
&\alpha_1^\vee = 2\alpha_1, && \omega_1^\vee = 2\omega_1,\\
&\alpha_2^\vee = 2\alpha_2, && \omega_2^\vee = 2\omega_2,\\
&\alpha_3^\vee = \alpha_3, && \omega_3^\vee = \omega_3,
\end{aligned} \tag{5.1.7}$$

5.1.2. The orthonormal bases

For each $\alpha-$ and $\omega-$basis, there is an associated orthonormal basis that allows visualizing the geometry of considered polytopes. The orthonormal bases for the crystallographic groups A_3, B_3 and C_3, that are recalled in this subsection, have been determined in (Moody *et al.* [**98**]). However, the choice of such bases is not unique. Other orthonormal bases are possible to consider, as long as the basis vectors satisfy the lengths and relative angles between them.

For the crystallographic reflection group A_3, the orthonormal bases are

$$\begin{aligned}
&\alpha_1 = (1,-1,0), && \omega_1 = \left(\tfrac{5}{6},-\tfrac{1}{6},-\tfrac{1}{6}\right),\\
&\alpha_2 = (0,1,-1), && \omega_2 = \left(\tfrac{2}{3},\tfrac{2}{3},-\tfrac{1}{3}\right),\\
&\alpha_3 = \left(\tfrac{1}{3},\tfrac{1}{3},\tfrac{4}{3}\right); && \omega_3 = \left(\tfrac{1}{2},\tfrac{1}{2},\tfrac{1}{2}\right).
\end{aligned} \tag{5.1.8}$$

For the crystallographic reflection group B_3, the orthonormal bases are

$$\begin{aligned}
&\alpha_1 = (1,-1,0), && \omega_1 = (1,0,0),\\
&\alpha_2 = (0,1,-1), && \omega_2 = (1,1,0),\\
&\alpha_3 = (0,0,1); && \omega_3 = \left(\tfrac{1}{2},\tfrac{1}{2},\tfrac{1}{2}\right).
\end{aligned} \tag{5.1.9}$$

For the crystallographic reflection group C_3, the orthonormal bases are

$$\begin{aligned}
&\alpha_1 = \left(\tfrac{1}{\sqrt{2}},-\tfrac{1}{\sqrt{2}},0\right), && \omega_1 = (\tfrac{1}{\sqrt{2}},0,0),\\
&\alpha_2 = \left(0,\tfrac{1}{\sqrt{2}},-\tfrac{1}{\sqrt{2}}\right), && \omega_2 = (\tfrac{1}{\sqrt{2}},\tfrac{1}{\sqrt{2}},0),\\
&\alpha_3 = (0,0,\sqrt{2}); && \omega_3 = \left(\tfrac{1}{\sqrt{2}},\tfrac{1}{\sqrt{2}},\tfrac{1}{\sqrt{2}}\right).
\end{aligned} \tag{5.1.10}$$

5.1.3. The mixed bases

Let us denote by W' a two-dimensional subgroup of a crystallographic group W. The reflections generating a subgroup W' are provided by the nodes of a corresponding Dynkin diagram (Figure 5.3). The mixed basis, that has been introduced is (Bodner *et al.* [**13**]), is determined by using the duality relation of the $\alpha-$ and $\omega-$bases (5.1.4). In this case,

W	*W′*	*Diagram*	*Reflections*	*Mixed basis*
A_3	A_2	○—○	r_2, r_3	$\{\alpha_1, \omega_2, \omega_3\}$
	$A_1 \times A_1$	○ ○	r_1, r_3	$\{\omega_1, \alpha_2, \omega_3\}$
	A_2	○—○	r_1, r_2	$\{\omega_1, \omega_2, \alpha_3\}$
B_3	B_2	○═●	r_2, r_3	$\{\alpha_1, \omega_2, \omega_3\}$
	$A_1 \times A_1$	○ ●	r_1, r_3	$\{\omega_1, \alpha_2, \omega_3\}$
	A_2	○—○	r_1, r_2	$\{\omega_1, \omega_2, \alpha_3\}$
C_3	C_2	●═○	r_2, r_3	$\{\alpha_1, \omega_2, \omega_3\}$
	$A_1 \times A_1$	○ ○	r_1, r_3	$\{\omega_1, \alpha_2, \omega_3\}$
	A_2	●—●	r_1, r_2	$\{\omega_1, \omega_2, \alpha_3\}$

Table 5.2. The two-dimensional subgroups of the crystallographic groups A_3, B_3 and C_3 and the corresponding mixed bases.

any two vectors of the $\omega-$basis, ω_i and ω_j, span a plane orthogonal to one of the simple roots α_k, for $i, j, k \in \{1, 2, 3\}$ and $i \neq j \neq k$. Therefore, for each considered crystallographic group, A_3, B_3 and C_3, labeling the nodes of a Coxeter–Dynkin diagram corresponding to the generators of W' by the vectors of the $\omega-$basis, we obtain three mixed bases,

$$\{\alpha_1, \omega_2, \omega_3\}, \quad \{\omega_1, \alpha_2, \omega_3\}, \quad \{\omega_1, \omega_2, \alpha_3\}.$$

For the crystallographic groups A_3, B_3 and C_3, the two-dimensional subgroups W' together with the corresponding mixed bases are provided in Table 5.2.

5.1.4. The $\omega'-$basis

In order to construct a dual Euclidean or spherical polytope of the crystallographic type, we consider the $\omega'-$basis that comprises appropriately scaled vectors of the $\omega-$basis. For any crystallographic group W in $\mathbb{R}^3$, the dominant (seed) point λ is provided by the linear combination of the fundamental weights as

$$\lambda = (a, b, c) \equiv a\omega_1 + b\omega_2 + c\omega_3, \quad a, b, c \in \mathbb{Z}^{\geq 0}. \tag{5.1.11}$$

For the crystallographic groups A_3, B_3 and C_3, the fundamental region F is the simplex that has the shape of a pyramid with the vertices $\{0, \omega_1^\vee, \omega_2^\vee, \omega_3^\vee\}$, $\{0, \omega_1^\vee, \frac{1}{2}\omega_2^\vee, \frac{1}{2}\omega_3^\vee\}$ and $\{0, \frac{1}{2}\omega_1^\vee, \frac{1}{2}\omega_2^\vee, \omega_3^\vee\}$, respectively. Since the coordinates of a dominant point λ are non-negative, we have that λ lies within the interior of the finite region F or on its boundary. Depending on the non-zero coordinates of (5.1.11), there are eight types of dominant points that are

	A_3			B_3			C_3		
λ	c_1	c_2	c_3	c_1	c_2	c_3	c_1	c_2	c_3
$(1,0,0)$	1	$\frac{3}{2}$	3	1	1	2	1	1	1
$(0,1,0)$	1	$\frac{1}{2}$	1	1	$\frac{1}{2}$	1	1	$\frac{1}{2}$	$\frac{1}{2}$
$(0,0,1)$	1	$\frac{1}{2}$	$\frac{1}{3}$	1	$\frac{1}{2}$	$\frac{2}{3}$	1	$\frac{1}{2}$	$\frac{1}{3}$
$(1,1,0)$	1	$\frac{5}{6}$	$\frac{5}{3}$	1	$\frac{2}{3}$	$\frac{4}{3}$	1	$\frac{2}{3}$	$\frac{2}{3}$
$(1,0,1)$	1	1	1	1	$\frac{2}{3}$	1	1	$\frac{3}{4}$	$\frac{3}{5}$
$(0,1,1)$	1	$\frac{1}{2}$	$\frac{3}{5}$	1	$\frac{1}{2}$	$\frac{4}{5}$	1	$\frac{1}{2}$	$\frac{3}{7}$
$(1,1,1)$	1	$\frac{3}{4}$	1	1	$\frac{3}{5}$	1	1	$\frac{5}{8}$	$\frac{5}{9}$

Table 5.3. Scaling coefficients c_k, $k \in \{1,2,3\}$ for the vectors of the $\omega-$basis of the A_3, B_3 and C_3 groups.

possible to consider. Since the point $\lambda = (0,0,0)$ lies at the intersection of the reflecting hyperplanes m_k, $k = \{1,2,3\}$, this case is omitted here. Therefore, we focus on the following seed points:

$$(a,0,0),\ (0,b,0),\ (0,0,c),\ (a,b,0),\ (a,0,b),\ (0,b,c),\ (a,b,c). \tag{5.1.12}$$

For simplicity, we often choose the coordinates a, b and c of (5.1.11) to be equal to 0 or 1.

Using expression (5.1.11), we can determine the scaling coefficients for the vectors of the $\omega-$basis as

$$a_k = \frac{\langle \lambda, \lambda \rangle}{\langle \omega_k, \lambda \rangle}, \quad a_k \in \mathbb{Q}^{>0}, \quad k \in \{1,2,3\}.$$

There is one-to-one correspondence between the $\omega-$ and $\omega'-$bases,

$$\omega'_k = c_k \omega_k, \quad k \in \{1,2,3\},$$

where $c_k = a_k/a_1$ are the normalized scaling coefficients listed in Table 5.3.

The dominant points of the orbits found within the structure of $\mathcal{V}_W(\lambda)-$polytopes are denoted by λ'. The coordinates of such points can be determined as

$$\lambda' \equiv \omega'_k, \quad k \in \{1,2,3\}. \tag{5.1.13}$$

The seed points λ' can be written explicitly as

$$(a',0,0) \equiv \omega'_1 = c_1\omega_1,$$

$$(0,b',0) \equiv \omega'_2 = c_2\omega_2,$$

$$(0,0,c') \equiv \omega'_3 = c_3\omega_3.$$

5.2. The reflections of a crystallographic group W

A crystallographic finite reflection group W in $\mathbb{R}^3$ is generated by three reflection operations r_k, $k \in \{1,2,3\}$. For any point $x \in \mathbb{R}^3$, the reflection is defined by the formula:

$$r_k x = x - 2\frac{\langle x, \alpha_k \rangle}{\langle \alpha_k, \alpha_k \rangle}\alpha_k, \quad k \in \{1,2,3\}. \tag{5.2.1}$$

For the crystallographic groups A_3, B_3 and C_3, the reflection operations, r_1, r_2 and r_3, satisfy the following identities:

$$\begin{aligned}
A_3 &: \quad r_1^2 = r_2^2 = r_3^2 = 1,\ (r_1r_2)^3 = 1,\ (r_2r_3)^3 = 1,\ (r_1r_3)^2 = 1;\\
B_3 &: \quad r_1^2 = r_2^2 = r_3^2 = 1,\ (r_1r_2)^3 = 1,\ (r_2r_3)^4 = 1,\ (r_1r_3)^2 = 1;\\
C_3 &: \quad r_1^2 = r_2^2 = r_3^2 = 1,\ (r_1r_2)^3 = 1,\ (r_2r_3)^4 = 1,\ (r_1r_3)^2 = 1.
\end{aligned}$$

An orbit of points $O_W(\lambda)$ is generated by the action of W on a seed point λ given by formula (5.1.11). An orbit of points $O_W(\lambda')$ is obtained by the action of W on a point λ' given by expression (5.1.13).

5.3. Dual polytopes of the crystallographic groups A_3, B_3 and C_3.

Since the root system of any finite Coxeter group G has a uniquely associated Coxeter–Dynkin diagram, the faces of any polytope can be described using the decoration technique proposed in (Champagne *et al.* [**29**]). For any finite reflection group G, the decoration rules for a Coxeter–Dynkin diagram are recalled in Section 4.4. In order to describe the faces of $\mathcal{D}_W(\lambda)-$ and $\mathcal{V}_W(\lambda)-$polytopes of the crystallographic type, we apply the decoration rules to the Coxeter–Dynkin diagrams of the crystallographic groups A_3 (Table 5.4), B_3 and C_3 (Table 5.5). We denote the faces of $\mathcal{D}_W(\lambda)-$ and $\mathcal{V}_W(\lambda)-$polytopes as d_k and v_{n-k-1}, respectively, where n is the rank of W. The number of faces of a polytope generated by W, as well as the number of p-dimensional faces meeting at the q-dimensional face ($p < q$), are provided by the counting formulas (4.5.2) and (4.5.3) in Section 4.5.

For any crystallographic reflection group W, considering each type of dominant point λ' from formula (5.1.13), the lengths of the one-dimensional faces of $\mathcal{V}_W(\lambda)$ are determined in the $\omega-$basis as a Euclidean distance by using the reflection formula (5.2.1).

- the lengths of the edges of $\mathcal{V}_{A_3}(\lambda)-$polytope are determined as

$$\begin{aligned}
&|\omega_1' - r_1\omega_1'| = |2\omega_1' - \omega_2'| = |2c_1\omega_1 - c_2\omega_2|,\\
&|\omega_2' - r_2\omega_2'| = |-\omega_1' + 2\omega_2' - \omega_3'| = |-c_1\omega_1 + 2c_2\omega_2 - c_3\omega_3|,\\
&|\omega_2' - r_3\omega_3'| = |-\omega_2' + 2\omega_3'| = |-c_2\omega_2 - 2c_3\omega_3|;
\end{aligned}$$

λ	*Decoration*	d_k	v_{2-k}	N	*Type of* d_k	*Type of* v_{2-k}
$(a,0,0)$	□—◇—◇	d_2^1	v_0^3	4	vertices	triangle
	◆—□—◇	d_2^2	v_0^2	6	triangle-triangle	triangle-triangle
	◆—◆—□	d_2^3	v_0^1	4	triangle	vertices
$(0,b,0)$	◇—□—◇	d_0	v_2	6	vertices	rectangle
	□—◆—□	d_1	v_1	12	triangle-triangle	rectangle-rectangle
	◆—◆—□	d_2^1	v_0^2	4	triangle	vertices
	□—◆—◆	d_2^2	v_0^1	4	triangle	vertices
$(0,0,c)$	◇—◇—□	d_2^1	v_0^3	4	vertices	triangle
	◇—□—◆	d_2^2	v_0^2	6	triangle-triangle	triangle-triangle
	■—◆—◇	d_2^3	v_0^1	4	triangle	vertices
$(a,b,0)$	□—□—◇	d_0	v_2	12	vertices	triangle
	□—◆—□	d_1^2	v_1^1	12	triangle-hexagon	triangle-triangle
	◆—□—◇	d_1^1	v_1^2	6	hexagon-hexagon	triangle-triangle
	◆—◆—□	d_2^1	v_0^2	4	hexagon	vertices
	□—◆—◆	d_2^2	v_0^1	4	triangle	vertices
$(a,0,c)$	□—◇—□	d_0	v_2	12	vertices	rhombus
	◆—□—□	d_1^1	v_1^2	12	triangle-rectangle	rhombus-rhombus
	□—□—◆	d_1^2	v_1^1	12	triangle-rectangle	rhombus-rhombus
	◆—◆—□	d_2^1	v_0^3	4	triangle	vertices
	◆—□—◆	d_2^2	v_0^2	6	rectangle	vertices
	□—◆—◆	d_2^3	v_0^1	4	triangle	vertices
$(0,b,c)$	◇—□—□	d_0	v_2	12	vertices	triangle
	□—◆—□	d_1^1	v_1	12	triangle-hexagon	triangle-triangle
	◇—□—◆	d_1^2	v_1	6	hexagon-hexagon	triangle-triangle
	◆—◆—□	d_2^1	v_0^2	4	triangle	vertices
	□—◆—◆	d_2^2	v_0^1	4	hexagon	vertices
(a,b,c)	□—□—□	d_0	v_2	24	vertices	triangle
	◆—□—□	d_1^1	v_1^3	12	hexagon-rectangle	triangle-triangle
	□—◆—□	d_1^2	v_1^2	12	hexagon-hexagon	triangle-triangle
	□—□—◆	d_1^3	v_1^1	12	hexagon-rectangle	triangle-triangle
	◆—◆—□	d_2^1	v_0^3	4	hexagon	vertices
	◆—□—◆	d_2^2	v_0^2	6	rectangle	vertices
	□—◆—◆	d_2^3	v_0^1	4	hexagon	vertices

Table 5.4. Decorations of the Coxeter–Dynkin diagram of A_3 are presented for dominant points λ, namely $(0,b,0)$, $(a,b,0)$, $(a,0,c)$, $(0,b,c)$ and (a,b,c). The faces d_k and v_{2-k}, $k \in \{0,1,2\}$ correspond to the faces of $\mathcal{D}(\lambda)$ and $\mathcal{V}(\lambda)$. The polygon-polygon notation corresponds to the types of edges shared by the two-dimensional faces of a polytope. The number of faces $N(d_k)$ and $N(v_{2-k})$ is denoted by N.

λ	*Decoration*	d_k	v_{2-k}	N	*Type of* d_k	*Type of* v_{2-k}
$(a,0,0)$	□—◇$\overset{4}{—}$◇	d_2^1	v_0^3	6	vertices	rectangle
	◆—□$\overset{4}{—}$◇	d_2^2	v_0^2	12	triangle-triangle	rectangle-rectangle
	◆—◆$\overset{4}{—}$□	d_2^3	v_0^1	8	triangle	vertices
$(0,b,0)$	◇—□$\overset{4}{—}$◇	d_0	v_2	12	vertices	rhombus
	□—◆$\overset{4}{—}$□	d_1	v_1	24	triangle-rectangle	rhombus-rhombus
	◆—◆$\overset{4}{—}$□	d_2^1	v_0^2	8	triangle	vertices
	□—◆$\overset{4}{—}$◆	d_2^2	v_0^1	6	rectangle	vertices
$(0,0,c)$	◇—◇$\overset{4}{—}$□	d_2^1	v_0^3	8	vertices	triangle
	◇—□$\overset{4}{—}$◆	d_2^2	v_0^2	12	rectangle-rectangle	triangle-triangle
	■—◆$\overset{4}{—}$◇	d_2^3	v_0^1	6	rectangle	vertices
$(a,b,0)$	□—□$\overset{4}{—}$◇	d_0	v_2	24	vertices	triangle
	□—◆$\overset{4}{—}$□	d_1^2	v_1^1	24	hexagon-rectangle	triangle-triangle
	◆—□$\overset{4}{—}$◇	d_1^1	v_1^2	12	hexagon-hexagon	triangle-triangle
	◆—◆$\overset{4}{—}$□	d_2^1	v_0^2	8	hexagon	vertices
	□—◆$\overset{4}{—}$◆	d_2^2	v_0^1	6	rectangle	vertices
$(a,0,c)$	□—◇$\overset{4}{—}$□	d_0	v_2	24	vertices	kite
	◆—□$\overset{4}{—}$□	d_1^1	v_1^2	24	triangle-rectangle	kite-kite
	□—□$\overset{4}{—}$◆	d_1^2	v_1^1	24	rectangle-rectangle	kite-kite
	◆—◆$\overset{4}{—}$□	d_2^1	v_0^3	8	triangle	vertices
	◆—□$\overset{4}{—}$◆	d_2^2	v_0^2	12	rectangle	vertices
	□—◆$\overset{4}{—}$◆	d_2^3	v_0^1	6	rectangle	vertices
$(0,b,c)$	◇—□$\overset{4}{—}$□	d_0	v_2	24	vertices	triangle
	□—◆$\overset{4}{—}$□	d_1^1	v_1	24	triangle-octagon	triangle-triangle
	◇—□$\overset{4}{—}$◆	d_1^2	v_1	12	octagon-octagon	triangle-triangle
	◆—◆$\overset{4}{—}$□	d_2^1	v_0^2	8	triangle	vertices
	□—◆$\overset{4}{—}$◆	d_2^2	v_0^1	6	octagon	vertices
(a,b,c)	□—□$\overset{4}{—}$□	d_0	v_2	48	vertices	triangle
	◆—□$\overset{4}{—}$□	d_1^1	v_1^3	24	hexagon-rectangle	triangle-triangle
	□—◆$\overset{4}{—}$□	d_1^2	v_1^2	24	hexagon-octagon	triangle-triangle
	□—□$\overset{4}{—}$◆	d_1^3	v_1^1	24	octagon-rectangle	triangle-triangle
	◆—◆$\overset{4}{—}$□	d_2^1	v_0^3	8	hexagon	vertices
	◆—□$\overset{4}{—}$◆	d_2^2	v_0^2	12	rectangle	vertices
	□—◆$\overset{4}{—}$◆	d_2^3	v_0^1	6	octagon	vertices

Table 5.5. Decorations of the Coxeter–Dynkin diagrams of B_3 and C_3 are presented for dominant points λ, namely $(0,b,0)$, $(a,b,0)$, $(a,0,c)$, $(0,b,c)$ and (a,b,c). The faces d_k and v_{2-k}, $k \in \{0,1,2\}$ correspond to the faces of $\mathcal{D}(\lambda)$ and $\mathcal{V}(\lambda)$, respectively. The polygon-polygon notation corresponds to the types of edges shared by the two-dimensional faces of a polytope. The number of faces $N(d_k)$ and $N(v_{2-k})$ is denoted by N.

- the lengths of the edges of $\mathcal{V}_{B_3}(\lambda)-$polytope are determined as

$$\begin{aligned}
&|\omega_1' - r_1\omega_1'| = |2\omega_1' - \omega_2'| = |2c_1\omega_1 - c_2\omega_2|,\\
&|\omega_2' - r_2\omega_2'| = |-\omega_1' + 2\omega_2' - 2\omega_3'| = |-c_1\omega_1 + 2c_2\omega_2 - 2c_3\omega_3|,\\
&|\omega_2' - r_3\omega_3'| = |-\omega_2' + 2\omega_3'| = |-c_2\omega_2 - 2c_3\omega_3|;
\end{aligned}$$

- the lengths of the edges of $\mathcal{V}_{C_3}(\lambda)-$polytope are determined as

$$\begin{aligned}
&|\omega_1' - r_1\omega_1'| = |2\omega_1' - \omega_2'| = |2c_1\omega_1 - c_2\omega_2|,\\
&|\omega_2' - r_2\omega_2'| = |-\omega_1' + 2\omega_2' - \omega_3'| = |-c_1\omega_1 + 2c_2\omega_2 - c_3\omega_3|,\\
&|\omega_2' - r_3\omega_3'| = |-2\omega_2' + 2\omega_3'| = |-2c_2\omega_2 - 2c_3\omega_3|.
\end{aligned}$$

5.4. The orbits of $\mathcal{V}_W(\lambda)-$polytopes

For the Coxeter–Dynkin diagrams (Figure 5.3), the decoration rules yield up three differently decorated diagrams at the last step of the recursive procedure. Such diagrams correspond to the orbits providing the vertices of $\mathcal{V}_W(\lambda)-$polytopes. Therefore, depending on a seed point λ, a dual polytope of the crystallographic group W may contain up to three generic orbits within its structure, i.e. the orbits obtained by the action of W on the points $(a', 0, 0)$, $(0, b', 0)$ and $(0, 0, c')$ (see Table 4.3).

The generic orbits of the crystallographic group A_3 are explicitly provided by the sets of points as

$$\begin{aligned}
O_{A_3}(a,0,0) &= \{(a,0,0), (-a,a,0), (0,-a,a), (0,0,-a)\};\\
O_{A_3}(0,b,0) &= \{\pm(0,b,0), \pm(b,-b,b), \pm(-b,0,b)\};\\
O_{A_3}(0,0,c) &= \{(0,0,c), (0,c,-c), (c,-c,0), (-c,0,0)\}.
\end{aligned}$$

The generic orbits of the crystallographic group B_3 are explicitly provided by the sets of points as

$$\begin{aligned}
&O_{B_3}(a,0,0) = \{(a,0,0), \pm(-a,a,0), \pm(0,-a,2a), (0,0,-a)\};\\
&O_{B_3}(0,b,0) = \{\pm(0,b,0), \pm(b,-b,2b), \pm(-b,0,2b), \pm(b,b,-2b), \pm(-b,2b,-2b), \pm(2b,-b,0)\};\\
&O_{B_3}(0,0,c) = \{\pm(0,0,c), \pm(0,c,-c), \pm(c,-c,c), \pm(-c,0,c)\}.
\end{aligned}$$

The generic orbits of the crystallographic group C_3 are explicitly provided by the sets of points as

$$\begin{aligned}
&O_{C_3}(a,0,0) = \{(a,0,0), \pm(-a,a,0), \pm(0,-a,a), (-a,0,0)\};\\
&O_{C_3}(0,b,0) = \{\pm(0,b,0), \pm(b,-b,b), \pm(-b,0,b), \pm(b,b,-b), \pm(-b,2b,-b), \pm(2b,-b,0)\};\\
&O_{C_3}(0,0,c) = \{\pm(0,0,c), \pm(0,2c,-c), \pm(2c,-2c,c), \pm(-2c,0,c)\}.
\end{aligned}$$

5.5. Orbit decompositions

The symmetry breaking of $V_W(\lambda)-$polytopes can be achieved by using a technique introduced in (Bodner *et al.* [**13**]). Employing the branching rules defined in (Larouche and Patera [**87**]; Larouche *et al.* [**88**]), the symmetry of the crystallographic group W can be reduced to the symmetry of its two-dimensional subgroups W', i.e., $W \to W' \times A_1$. The symmetry reduction allows us to decompose the vertices of a polytope of W into circular/polygonal orbits with $W'-$symmetry. Such set of two-dimensional orbits yields the 'pancake'-structure of a polytope.

In order to achieve an orbit decomposition of a polytope, we consider the coordinates of its vertices in the mixed basis. The orbit points governed by the $W'-$symmetry are found on the plane spanned by two vectors of the $\omega-$basis that, from the duality relation (5.1.4), are orthogonal to one of the simple roots of $\alpha-$basis. The spacing between the two-dimensional orbits of a polytope is obtained by projecting any point of each such orbit onto the direction, say l, provided by the corresponding simple root.

Applying the approach developed in (Bodner *et al.* [**13**]) to the $\mathcal{V}_{A_3}(\lambda)-$, $\mathcal{V}_{B_3}(\lambda)-$ and $\mathcal{V}_{C_3}(\lambda)-$polytopes, we can obtain orbit decompositions for each considered polytope. For the crystallographic groups A_3, B_3 and C_3, the subgroups W' are listed in Table 5.2. Using the mixed bases and the quadratic form matrices (Table 5.1), we construct the transformation matrices. Any transformation matrix takes the form of the identity matrix, for which one of the columns is replaced by the corresponding column of C_W^{-1}.

For the crystallographic group A_3, the transformation matrices are

$$A_2: \qquad (a,b,c)\begin{pmatrix} \frac{3}{4} & 0 & 0 \\ \frac{1}{2} & 1 & 0 \\ \frac{1}{4} & 0 & 1 \end{pmatrix} = \left(\tfrac{3}{4}a + \tfrac{1}{2}b + \tfrac{1}{4}c, b, c\right);$$

$$A_1 \times A_1: \qquad (a,b,c)\begin{pmatrix} 1 & \frac{1}{2} & 0 \\ 0 & 1 & 0 \\ 0 & \frac{1}{2} & 1 \end{pmatrix} = \left(a, \tfrac{1}{2}a + b + \tfrac{1}{2}c, c\right);$$

$$A_2: \qquad (a,b,c)\begin{pmatrix} 1 & 0 & \frac{1}{4} \\ 0 & 1 & \frac{1}{2} \\ 0 & 0 & \frac{3}{4} \end{pmatrix} = \left(a, b, \tfrac{1}{4}a + \tfrac{1}{2}b + \tfrac{3}{4}c\right).$$

For the crystallographic group B_3, the transformation matrices are

$$B_2: \qquad (a,b,c)\begin{pmatrix}1 & 0 & 0\\ 1 & 1 & 0\\ \frac{1}{2} & 0 & 1\end{pmatrix} = \frac{1}{2}\left(2a+2b+c, b, c\right);$$

$$A_1\times A_1: \qquad (a,b,c)\begin{pmatrix}1 & 1 & 0\\ 0 & 2 & 0\\ 0 & 1 & 1\end{pmatrix} = (a, a+2b+c, c);$$

$$A_2: \qquad (a,b,c)\begin{pmatrix}1 & 0 & 1\\ 0 & 1 & 2\\ 0 & 0 & \frac{3}{2}\end{pmatrix} = \frac{1}{2}\left(a, b, 2a+4b+3c\right).$$

For the crystallographic group C_3, the transformation matrices are

$$C_2: \qquad (a,b,c)\begin{pmatrix}1 & 0 & 0\\ 1 & 1 & 0\\ 1 & 0 & 1\end{pmatrix} = (a+b+c, b, c);$$

$$A_1\times A_1: \qquad (a,b,c)\begin{pmatrix}1 & 1 & 0\\ 0 & 2 & 0\\ 0 & 2 & 1\end{pmatrix} = (a, a+2b+2c, c);$$

$$A_2: \qquad (a,b,c)\begin{pmatrix}1 & 0 & \frac{1}{2}\\ 0 & 1 & 1\\ 0 & 0 & \frac{3}{2}\end{pmatrix} = \frac{1}{2}\left(a, b, a+2b+3c\right).$$

Acting with such matrices on the orbit points provided in the $\omega-$basis, we obtain the points with their coordinates in the mixed basis. After the transformation has been completed, the points are sorted depending on the signs of their coordinates corresponding to the $\omega-$vectors in the mixed bases as

(*i*) for the subgroups A_2 of A_3, B_2 of B_3 and C_2 of C_3, the second and third coordinates have to be non-negative;

(*ii*) for the subgroup A_1 of A_3, B_3 and C_3, the first and third coordinates have to be non-negative;

(*iii*) for the subgroup A_2 of A_3, B_3 and C_3, the first and second coordinates have to be non-negative.

Therefore, points with the indicated non-negative coordinates provide the dominant points μ of the two-dimensional orbits found within the structure of a polytope. In Subsections 5.5.1–5.5.3, we consider the orbit decompositions of the vertices of $\mathcal{V}_{A_3}(\lambda)-$, $\mathcal{V}_{B_3}(\lambda)-$ and $\mathcal{V}_{C_3}(\lambda)-$polytopes for each type of seed point λ, respectively. For simplicity, we choose

λ	$\lvert O_\lambda(A_2)\rvert$	$\lvert O_\lambda(B_2)\rvert$	$\lvert O_\lambda(C_2)\rvert$	$\lvert O_\lambda(A_1\times A_1)\rvert$
$(0,0)$	1	1	1	1
$(a,0)$	3	4	4	2
$(0,b)$	3	4	4	2
(a,b)	6	8	8	4

Table 5.6. The sizes of two-dimensional orbits of the crystallographic reflection groups A_2, B_2, C_2 and $A_1 \times A_1$ are provided for each type of dominant point λ with $a, b \in \mathbb{R}^{>0}$.

the coordinates of λ to be equal 0 or 1. The numbers of points that belong to the two-dimensional orbits of each considered polytope (see Table 5.6) are indicated under each point determining such orbits in $\mathbb{R}^3$. The illustrations of the 'pancake'-structures for the families of $\mathcal{V}_{A_3}(\lambda)-$ and $\mathcal{V}_{B_3}(\lambda)-$polytopes are provided in Appendices C and D, respectively. For the families of $\mathcal{V}_W(\lambda)-$polytopes, the numbers of orbits and 'pancakes' are provided in Tables 5.7–5.9.

5.5.1. Orbit decompositions of the $\mathcal{V}_{A_3}(\lambda)-$polytopes

The polytope $\mathcal{V}_{A_3}(1,0,0)$. The structure of the $\mathcal{V}_{A_3}(1,0,0)-$polytope contains 4 vertices that can be decomposed into

- two orbits with the A_2-symmetry:

$$\{\alpha_1,\omega_2,\omega_3\}:\quad \underset{1}{\Big(-\frac{9}{4},0,0\Big)},\ \underset{3}{\Big(\frac{3}{4},0,3\Big)};$$

- two orbits with the $A_1\times A_1-$symmetry:

$$\{\omega_1,\alpha_2,\omega_3\}:\quad \underset{2}{\Big(3,-\frac{3}{2},0\Big)},\ \underset{2}{\Big(0,\frac{3}{2},3\Big)};$$

- two orbits with the A_2-symmetry:

$$\{\omega_1,\omega_2,\alpha_3\}:\quad \underset{3}{\Big(0,3,-\frac{3}{4}\Big)},\ \underset{1}{\Big(0,0,\frac{9}{4}\Big)}.$$

The polytope $\mathcal{V}_{A_3}(0,1,0)$. The structure of the $\mathcal{V}_{A_3}(0,1,0)-$polytope contains 8 vertices that can be decomposed into

- four orbits with the A_2-symmetry:

$$\{\alpha_1,\omega_2,\omega_3\}:\quad \underset{1}{\Big(-\frac{3}{4},0,0\Big)},\ \underset{3}{\Big(-\frac{1}{4},1,0\Big)},\ \underset{3}{\Big(\frac{1}{4},0,1\Big)},\ \underset{1}{\Big(\frac{3}{4},0,0\Big)};$$

- four orbits with the $A_1 \times A_1-$symmetry:

$$\{\omega_1, \alpha_2, \omega_3\}: \quad \left(1, -\frac{1}{2}, 0\right)_2, \left(0, -\frac{1}{2}, 1\right)_2, \left(0, \frac{1}{2}, 1\right)_2, \left(1, \frac{1}{2}, 0\right)_2;$$

- four orbits with the A_2-symmetry:

$$\{\omega_1, \omega_2, \alpha_3\}: \quad \left(0, 0, -\frac{3}{4}\right)_1, \left(0, 1, -\frac{1}{4}\right)_3, \left(1, 0, \frac{1}{4}\right)_3, \left(0, 0, \frac{3}{4}\right)_1.$$

The polytope $\mathcal{V}_{A_3}(0,0,1)$. The structure of the $\mathcal{V}_{A_3}(0,0,1)-$polytope contains 4 vertices that can be decomposed into

- two orbits with the A_2-symmetry:

$$\{\alpha_1, \omega_2, \omega_3\}: \quad \left(-\frac{1}{4}, 1, 0\right)_3, \left(\frac{3}{4}, 0, 0\right)_1;$$

- two orbits with the $A_1 \times A_1-$symmetry:

$$\{\omega_1, \alpha_2, \omega_3\}: \quad \left(0, -\frac{1}{2}, 1\right)_2, \left(1, \frac{1}{2}, 0\right)_2;$$

- two orbits with the A_2-symmetry:

$$\{\omega_1, \omega_2, \alpha_3\}: \quad \left(0, 0, -\frac{3}{4}\right)_1, \left(1, 0, \frac{1}{4}\right)_3.$$

The polytope $\mathcal{V}_{A_3}(1,1,0)$. The structure of the $\mathcal{V}_{A_3}(1,1,0)-$polytope contains 8 vertices that can be decomposed into

- four orbits with the A_2-symmetry:

$$\{\alpha_1, \omega_2, \omega_3\}: \quad \left(-\frac{5}{4}, 0, 0\right)_1, \left(-\frac{1}{4}, 1, 0\right)_3, \left(\frac{5}{12}, 0, \frac{5}{3}\right)_3, \left(\frac{3}{4}, 0, 0\right)_1;$$

- four orbits with the $A_1 \times A_1-$symmetry:

$$\{\omega_1, \alpha_2, \omega_3\}: \quad \left(\frac{5}{3}, -\frac{5}{6}, 0\right)_2, \left(0, -\frac{1}{2}, 1\right)_2, \left(1, \frac{1}{2}, 0\right)_2, \left(0, \frac{5}{6}, \frac{5}{3}\right)_2;$$

- four orbits with the A_2-symmetry:

$$\{\omega_1, \omega_2, \alpha_3\}: \quad \left(0, 0, -\frac{3}{4}\right)_1, \left(0, \frac{5}{3}, -\frac{5}{12}\right)_3, \left(1, 0, \frac{1}{4}\right)_3, \left(0, 0, \frac{5}{4}\right)_1.$$

The polytope $\mathcal{V}_{A_3}(1,0,1)$. The structure of the $\mathcal{V}_{A_3}(1,0,1)-$polytope contains 14 vertices that can be decomposed into

- six orbits with the A_2-symmetry:

$$\{\alpha_1, \omega_2, \omega_3\}: \quad \left(-\frac{3}{4}, 0, 0\right)_1, \left(-\frac{1}{2}, 0, 1\right)_3, \left(-\frac{1}{4}, 1, 0\right)_3, \left(\frac{1}{4}, 0, 1\right)_3, \left(\frac{1}{2}, 1, 0\right)_3, \left(\frac{3}{4}, 0, 0\right)_1;$$

- seven orbits with the $A_1 \times A_1$−symmetry:

$$\{\omega_1, \alpha_2, \omega_3\}: \quad \underset{1}{(0,-1,0)}, \underset{2}{\left(1,-\frac{1}{2},0\right)}, \underset{2}{\left(0,-\frac{1}{2},1\right)}, \underset{4}{(1,0,1)}, \underset{2}{\left(0,\frac{1}{2},1\right)}, \underset{2}{\left(1,\frac{1}{2},0\right)}, \underset{1}{(0,1,0)};$$

- six orbits with the A_2−symmetry:

$$\{\omega_1, \omega_2, \alpha_3\}: \quad \underset{1}{\left(0,0,-\frac{3}{4}\right)}, \underset{3}{\left(1,0,-\frac{1}{2}\right)}, \underset{3}{\left(0,1,-\frac{1}{4}\right)}, \underset{3}{\left(1,0,\frac{1}{4}\right)}, \underset{3}{\left(0,1,\frac{1}{2}\right)}, \underset{1}{\left(0,0,\frac{3}{4}\right)}.$$

The polytope $\mathcal{V}_{A_3}(0,1,1)$. The structure of the $\mathcal{V}_{A_3}(0,1,1)$−polytope contains 8 vertices that can be decomposed into

- four orbits with the A_2−symmetry:

$$\{\alpha_1, \omega_2, \omega_3\}: \quad \underset{1}{\left(-\frac{9}{20},0,0\right)}, \underset{3}{\left(-\frac{1}{4},1,0\right)}, \underset{3}{\left(\frac{3}{20},0,\frac{3}{5}\right)}, \underset{1}{\left(\frac{3}{4},0,0\right)};$$

- four orbits with the $A_1 \times A_1$−symmetry:

$$\{\omega_1, \alpha_2, \omega_3\}: \quad \underset{2}{\left(0,-\frac{1}{2},1\right)}, \underset{2}{\left(\frac{3}{5},-\frac{3}{10},0\right)}, \underset{2}{\left(0,\frac{3}{10},\frac{3}{5}\right)}, \underset{2}{\left(1,\frac{1}{2},0\right)};$$

- four orbits with the A_2−symmetry:

$$\{\omega_1, \omega_2, \alpha_3\}: \quad \underset{1}{\left(0,0,-\frac{3}{4}\right)}, \underset{3}{\left(0,\frac{3}{5},-\frac{3}{20}\right)}, \underset{3}{\left(1,0,\frac{1}{4}\right)}, \underset{1}{\left(0,0,\frac{9}{20}\right)}.$$

The polytope $\mathcal{V}_{A_3}(1,1,1)$. The structure of the $\mathcal{V}_{A_3}(1,1,1)$−polytope contains 14 vertices that can be decomposed into

- six orbits with the A_2−symmetry:

$$\{\alpha_1, \omega_2, \omega_3\}: \quad \underset{1}{\left(-\frac{3}{4},0,0\right)}, \underset{3}{\left(-\frac{3}{8},0,\frac{3}{4}\right)}, \underset{3}{\left(-\frac{1}{4},1,0\right)}, \underset{3}{\left(\frac{1}{4},0,1\right)}, \underset{3}{\left(\frac{3}{8},\frac{3}{4},0\right)}, \underset{1}{\left(\frac{3}{4},0,0\right)};$$

- seven orbits with the $A_1 \times A_1$−symmetry:

$$\{\omega_1, \alpha_2, \omega_3\}: \quad \underset{2}{\left(0,-\frac{3}{4},0\right)}, \underset{2}{\left(1,-\frac{1}{2},0\right)}, \underset{2}{\left(0,-\frac{1}{2},1\right)}, \underset{2}{\left(\frac{3}{4},0,\frac{3}{4}\right)}, \underset{2}{\left(0,\frac{1}{2},1\right)}, \underset{2}{\left(1,\frac{1}{2},0\right)}, \underset{2}{\left(0,\frac{3}{4},0\right)};$$

- six orbits with the A_2−symmetry:

$$\{\omega_1, \omega_2, \alpha_3\}: \quad \underset{1}{\left(0,0,-\frac{3}{4}\right)}, \underset{3}{\left(\frac{3}{4},0,-\frac{3}{8}\right)}, \underset{3}{\left(0,1,-\frac{1}{4}\right)}, \underset{3}{\left(1,0,\frac{1}{4}\right)}, \underset{3}{\left(0,\frac{3}{4},\frac{3}{8}\right)}, \underset{1}{\left(0,0,\frac{3}{4}\right)}.$$

	A_2		$A_1 \times A_1$		A_2	
λ	*Orbits*	*'Pancakes'*	*Orbits*	*'Pancakes'*	*Orbits*	*'Pancakes'*
$(a,0,0)$	2	2	2	2	2	2
$(0,b,0)$	4	4	4	2	4	4
$(0,0,c)$	2	2	2	2	2	2
$(a,b,0)$	4	4	4	4	4	4
$(a,0,c)$	6	6	7	5	6	6
$(0,b,c)$	4	4	4	4	4	4
(a,b,c)	6	6	7	5	6	6

Table 5.7. The numbers of orbits and 'pancakes' are provided for $\mathcal{V}_{A_3}(\lambda)-$polytopes. The dominant points λ with the coordinates $a = b = c$ are considered.

5.5.2. Orbit decompositions of the $\mathcal{V}_{B_3}(\lambda)-$polytopes

The polytope $\mathcal{V}_{B_3}(1,0,0)$. The structure of the $\mathcal{V}_{B_3}(1,0,0)-$polytope contains 8 vertices that can be decomposed into

- two orbits with the B_2-symmetry:

$$\{\alpha_1,\omega_2,\omega_3\}: \quad (-1,\underset{4}{0},2),(1,\underset{4}{0},2);$$

- three orbits with the $A_1 \times A_1-$symmetry:

$$\{\omega_1,\alpha_2,\omega_3\}: \quad (0,\underset{2}{-2},2),(2,\underset{4}{0},2),(0,\underset{2}{2},2);$$

- four orbits with the A_2-symmetry:

$$\{\omega_1,\omega_2,\alpha_3\}: \quad (0,\underset{1}{0},-3),(2,\underset{3}{0},-1),(0,\underset{3}{2},1),(0,\underset{1}{0},3)\,.$$

The polytope $\mathcal{V}_{B_3}(0,1,0)$. The structure of the $\mathcal{V}_{B_3}(0,1,0)-$polytope contains 14 vertices that can be decomposed into

- five orbits with the B_2-symmetry:

$$\{\alpha_1,\omega_2,\omega_3\}: \quad (-1,\underset{1}{0},0),\Big(-\frac{1}{2},\underset{4}{0},1\Big),(0,\underset{4}{1},0),\Big(\frac{1}{2},\underset{4}{0},1\Big),(1,\underset{1}{0},0);$$

- six orbits with the $A_1 \times A_1-$symmetry:

$$\{\omega_1,\alpha_2,\omega_3\}: \quad (0,\underset{2}{-1},1),(1,\underset{2}{-1},0),(1,\underset{4}{0},1),(0,\underset{2}{0},2),(0,\underset{2}{1},1),(1,\underset{2}{1},0);$$

- six orbits with the A_2-symmetry:

$$\{\omega_1,\omega_2,\alpha_3\}: \quad \underset{1}{\left(0,0,-\frac{3}{2}\right)}, \underset{3}{(0,1,-1)}, \underset{3}{\left(1,0,-\frac{1}{2}\right)}, \underset{3}{\left(0,1,\frac{1}{2}\right)}, \underset{3}{(1,0,1)}, \underset{1}{\left(0,0,\frac{3}{2}\right)}.$$

The polytope $\mathcal{V}_{B_3}(0,0,1)$. The structure of the $\mathcal{V}_{B_3}(0,0,1)-$polytope contains 6 vertices that can be decomposed into

- three orbits with the B_2-symmetry:

$$\{\alpha_1,\omega_2,\omega_3\}: \quad \underset{1}{(-1,0,0)}, \underset{4}{(0,1,0)}, \underset{1}{(1,0,0)};$$

- three orbits with the $A_1\times A_1-$symmetry:

$$\{\omega_1,\alpha_2,\omega_3\}: \quad \underset{2}{(1,-1,0)}, \underset{2}{(0,0,2)}, \underset{2}{(1,1,0)};$$

- two orbits with the A_2-symmetry:

$$\{\omega_1,\omega_2,\alpha_3\}: \quad \underset{3}{(0,1,-1)}, \underset{3}{(1,0,1)}.$$

The polytope $\mathcal{V}_{B_3}(1,1,0)$. The structure of the $\mathcal{V}_{B_3}(1,1,0)-$polytope contains 14 vertices that can be decomposed into

- five orbits with the B_2-symmetry:

$$\{\alpha_1,\omega_2,\omega_3\}: \quad \underset{1}{(-1,0,0)}, \underset{4}{\left(-\frac{2}{3},0,\frac{4}{3}\right)}, \underset{4}{(0,1,0)}, \underset{4}{\left(\frac{2}{3},0,\frac{4}{3}\right)}, \underset{1}{(1,0,0)};$$

- six orbits with the $A_1\times A_1-$symmetry:

$$\{\omega_1,\alpha_2,\omega_3\}: \quad \underset{2}{\left(0,-\frac{4}{3},\frac{4}{3}\right)}, \underset{2}{(1,-1,0)}, \underset{4}{\left(\frac{4}{3},0,\frac{4}{3}\right)}, \underset{2}{(0,0,2)}, \underset{2}{(1,1,0)}, \underset{2}{\left(0,\frac{4}{3},\frac{4}{3}\right)};$$

- six orbits with the A_2-symmetry:

$$\{\omega_1,\omega_2,\alpha_3\}: \quad \underset{1}{(0,0,-2)}, \underset{3}{(0,1,-1)}, \underset{3}{\left(\frac{4}{3},0,-\frac{2}{3}\right)}, \underset{3}{\left(0,\frac{4}{3},\frac{2}{3}\right)}, \underset{3}{(1,0,1)}, \underset{1}{(0,0,2)};$$

The polytope $\mathcal{V}_{B_3}(1,0,1)$. The structure of the $\mathcal{V}_{B_3}(1,0,1)-$polytope contains 26 vertices that can be decomposed into

- eight orbits with the B_2-symmetry:

$$\{\alpha_1,\omega_2,\omega_3\}: \quad \underset{1}{(-1,0,0)}, \underset{4}{\left(-\frac{2}{3},\frac{2}{3},0\right)}, \underset{4}{\left(-\frac{1}{2},0,1\right)}, \underset{4}{\left(0,0,\frac{4}{3}\right)}, \underset{4}{(0,1,0)}, \underset{4}{\left(\frac{1}{2},0,1\right)},$$
$$\underset{4}{\left(\frac{2}{3},\frac{2}{3},0\right)}, \underset{1}{(1,0,0)};$$

- eleven orbits with the $A_1 \times A_1-$symmetry:

$$\{\omega_1, \alpha_2, \omega_3\}: \quad \underset{1}{\left(0,-\frac{4}{3},0\right)}, \underset{2}{(0,-1,1)}, \underset{2}{(1,-1,0)}, \underset{4}{\left(\frac{2}{3},-\frac{2}{3},\frac{4}{3}\right)}, \underset{2}{\left(\frac{4}{3},0,0\right)}, \underset{4}{(1,0,1)},$$
$$\underset{2}{(0,0,2)}, \underset{4}{\left(\frac{2}{3},\frac{2}{3},\frac{4}{3}\right)}, \underset{2}{(0,1,1)}, \underset{2}{(1,1,0)}, \underset{1}{\left(0,\frac{4}{3},0\right)};$$

- nine orbits with the A_2-symmetry:

$$\{\omega_1, \omega_2, \alpha_3\}: \quad \underset{1}{\left(0,0,-\frac{3}{2}\right)}, \underset{3}{\left(\frac{2}{3},0,-\frac{4}{3}\right)}, \underset{3}{(0,1,-1)}, \underset{3}{\left(1,0,-\frac{1}{2}\right)}, \underset{6}{\left(\frac{2}{3},\frac{2}{3},0\right)}, \underset{3}{\left(0,1,\frac{1}{2}\right)},$$
$$\underset{3}{(1,0,1)}, \underset{3}{\left(0,\frac{2}{3},\frac{4}{3}\right)}, \underset{1}{\left(0,0,\frac{3}{2}\right)};$$

The polytope $\mathcal{V}_{B_3}(0,1,1)$. The structure of the $\mathcal{V}_{B_3}(0,1,1)-$polytope contains 14 vertices that can be decomposed into

- five orbits with the B_2-symmetry:

$$\{\alpha_1, \omega_2, \omega_3\}: \quad \underset{1}{(-1,0,0)}, \underset{4}{\left(-\frac{2}{5},0,\frac{4}{5}\right)}, \underset{4}{(0,1,0)}, \underset{4}{\left(\frac{2}{5},0,\frac{4}{5}\right)}, \underset{1}{(1,0,0)};$$

- six orbits with the $A_1 \times A_1-$symmetry:

$$\{\omega_1, \alpha_2, \omega_3\}: \quad \underset{2}{(1,-1,0)}, \underset{2}{\left(0,-\frac{4}{5},\frac{4}{5}\right)}, \underset{4}{\left(\frac{4}{5},0,\frac{4}{5}\right)}, \underset{2}{(0,0,2)}, \underset{2}{\left(0,\frac{4}{5},\frac{4}{5}\right)}, \underset{2}{(1,1,0)};$$

- six orbits with the A_2-symmetry:

$$\{\omega_1, \omega_2, \alpha_3\}: \quad \underset{1}{\left(0,0,-\frac{6}{5}\right)}, \underset{3}{(0,1,-1)}, \underset{3}{\left(\frac{4}{5},0,-\frac{2}{5}\right)}, \underset{3}{\left(0,\frac{4}{5},\frac{2}{5}\right)}, \underset{3}{(1,0,1)}, \underset{1}{\left(0,0,\frac{6}{5}\right)}.$$

The polytope $\mathcal{V}_{B_3}(1,1,1)$. The structure of the $\mathcal{V}_{B_3}(1,1,1)-$polytope contains 26 vertices that can be decomposed into

- eight orbits with the B_2-symmetry:

$$\{\alpha_1, \omega_2, \omega_3\}: \quad \underset{1}{(-1,0,0)}, \underset{4}{\left(-\frac{3}{5},\frac{3}{5},0\right)}, \underset{4}{\left(-\frac{1}{2},0,1\right)}, \underset{4}{\left(0,0,\frac{6}{5}\right)}, \underset{4}{(0,1,0)}, \underset{4}{\left(\frac{1}{2},0,1\right)},$$
$$\underset{4}{\left(\frac{3}{5},\frac{3}{5},0\right)}, \underset{1}{(1,0,0)};$$

- eleven orbits with the $A_1 \times A_1-$symmetry:

$$\{\omega_1, \alpha_2, \omega_3\}: \quad \underset{1}{\left(0,-\frac{6}{5},0\right)}, \underset{2}{(0,-1,1)}, \underset{2}{(1,-1,0)}, \underset{4}{\left(\frac{3}{5},-\frac{3}{5},\frac{6}{5}\right)}, \underset{2}{\left(\frac{6}{5},0,0\right)}, \underset{4}{(1,0,1)},$$
$$\underset{2}{(0,0,2)}, \underset{4}{\left(\frac{3}{5},\frac{3}{5},\frac{6}{5}\right)}, \underset{2}{(0,1,1)}, \underset{2}{(1,1,0)}, \underset{1}{\left(0,\frac{6}{5},0\right)};$$

λ	B_2		$A_1 \times A_1$		A_2	
	Orbits	*'Pancakes'*	*Orbits*	*'Pancakes'*	*Orbits*	*'Pancakes'*
$(a,0,0)$	2	2	3	3	4	4
$(0,b,0)$	5	5	6	3	6	6
$(0,0,c)$	3	3	3	3	2	2
$(a,b,0)$	5	5	6	5	6	6
$(a,0,c)$	8	7	11	7	9	9
$(0,b,c)$	5	5	6	5	6	6
(a,b,c)	8	7	11	7	9	9

Table 5.8. The numbers of orbits and 'pancakes' are provided for $\mathcal{V}_{B_3}(\lambda)-$polytopes. The dominant points λ with the coordinates $a = b = c$ are considered.

- nine orbits with the A_2-symmetry:

$$\{\omega_1, \omega_2, \alpha_3\}: \quad \left(0, \underset{1}{0}, -\frac{3}{2}\right), \left(\frac{3}{5}, \underset{3}{0}, -\frac{6}{5}\right), (0, \underset{3}{1}, -1), \left(1, \underset{3}{0}, -\frac{1}{2}\right), \left(\frac{3}{5}, \underset{6}{\frac{3}{5}}, 0\right), \left(0, \underset{3}{1}, \frac{1}{2}\right), \\ (1, \underset{3}{0}, 1), \left(0, \underset{3}{\frac{3}{5}}, \frac{6}{5}\right), \left(0, \underset{1}{0}, \frac{3}{2}\right).$$

5.5.3. Orbit decompositions of the $\mathcal{V}_{C_3}(\lambda)-$polytopes

The polytope $\mathcal{V}_{C_3}(1,0,0)$. The structure of the $\mathcal{V}_{C_3}(1,0,0)-$polytope contains 8 vertices that can be decomposed into

- two orbits with the C_2-symmetry:

$$\{\alpha_1, \omega_2, \omega_3\}: \quad (-2, \underset{4}{0}, 2), (2, \underset{4}{0}, 2);$$

- three orbits with the $A_1 \times A_1-$symmetry:

$$\{\omega_1, \alpha_2, \omega_3\}: \quad (0, \underset{2}{-4}, 2), (4, \underset{4}{0}, 2), (0, \underset{2}{4}, 2);$$

- four orbits with the A_2-symmetry:

$$\{\omega_1, \omega_2, \alpha_3\}: \quad (0, \underset{1}{0}, -3), (4, \underset{3}{0}, -1), (0, \underset{3}{4}, 1), (0, \underset{1}{0}, 3).$$

The polytope $\mathcal{V}_{C_3}(0,1,0)$. The structure of the $\mathcal{V}_{C_3}(0,1,0)-$polytope contains 14 vertices that can be decomposed into

- five orbits with the C_2-symmetry:

$$\{\alpha_1, \omega_2, \omega_3\}: \quad (-1, \underset{1}{0}, 0), \left(-\frac{1}{2}, \underset{4}{0}, \frac{1}{2}\right), (0, \underset{4}{1}, 0), \left(\frac{1}{2}, \underset{4}{0}, \frac{1}{2}\right), (1, \underset{1}{0}, 0);$$

- six orbits with the $A_1 \times A_1$−symmetry:

$$\{\omega_1, \alpha_2, \omega_3\}: \quad \underset{2}{\left(0,-1,\frac{1}{2}\right)}, \underset{2}{(1,-1,0)}, \underset{4}{\left(1,0,\frac{1}{2}\right)}, \underset{2}{(0,0,1)}, \underset{2}{\left(0,1,\frac{1}{2}\right)}, \underset{2}{(1,1,0)};$$

- six orbits with the A_2−symmetry:

$$\{\omega_1, \omega_2, \alpha_3\}: \quad \underset{1}{\left(0,0,-\frac{3}{4}\right)}, \underset{3}{\left(0,1,-\frac{1}{2}\right)}, \underset{3}{\left(1,0,-\frac{1}{4}\right)}, \underset{3}{\left(0,1,\frac{1}{4}\right)}, \underset{3}{\left(1,0,\frac{1}{2}\right)}, \underset{1}{\left(0,0,\frac{3}{4}\right)}.$$

The polytope $\mathcal{V}_{C_3}(0,0,1)$. The structure of the $\mathcal{V}_{C_3}(0,0,1)$−polytope contains 6 vertices that can be decomposed into

- three orbits with the C_2−symmetry:

$$\{\alpha_1, \omega_2, \omega_3\}: \quad \underset{1}{(-1,0,0)}, \underset{4}{(0,1,0)}, \underset{1}{(1,0,0)};$$

- three orbits with the $A_1 \times A_1$−symmetry:

$$\{\omega_1, \alpha_2, \omega_3\}: \quad \underset{2}{(1,-1,0)}, \underset{2}{(0,0,1)}, \underset{2}{(1,1,0)};$$

- two orbits with the A_2−symmetry:

$$\{\omega_1, \omega_2, \alpha_3\}: \quad \underset{3}{\left(0,1,-\frac{1}{2}\right)}, \underset{3}{\left(1,0,\frac{1}{2}\right)}.$$

The polytope $\mathcal{V}_{C_3}(1,1,0)$. The structure of the $\mathcal{V}_{C_3}(1,1,0)$−polytope contains 14 vertices that can be decomposed into

- five orbits with the C_2−symmetry:

$$\{\alpha_1, \omega_2, \omega_3\}: \quad \underset{1}{(-1,0,0)}, \underset{4}{\left(-\frac{4}{5},0,\frac{4}{5}\right)}, \underset{4}{(0,1,0)}, \underset{4}{\left(\frac{4}{5},0,\frac{4}{5}\right)}, \underset{1}{(1,0,0)};$$

- six orbits with the $A_1 \times A_1$−symmetry:

$$\{\omega_1, \alpha_2, \omega_3\}: \quad \underset{2}{\left(0,-\frac{8}{5},\frac{4}{5}\right)}, \underset{2}{(1,-1,0)}, \underset{4}{\left(\frac{8}{5},0,\frac{4}{5}\right)}, \underset{2}{(0,0,1)}, \underset{2}{(1,1,0)}, \underset{2}{\left(0,\frac{8}{5},\frac{4}{5}\right)};$$

- six orbits with the A_2−symmetry:

$$\{\omega_1, \omega_2, \alpha_3\}: \quad \underset{1}{\left(0,0,-\frac{6}{5}\right)}, \underset{3}{\left(0,1,-\frac{1}{2}\right)}, \underset{3}{\left(\frac{8}{5},0,-\frac{2}{5}\right)}, \underset{3}{\left(0,\frac{8}{5},\frac{2}{5}\right)}, \underset{3}{\left(1,0,\frac{1}{2}\right)}, \underset{1}{\left(0,0,\frac{6}{5}\right)}.$$

The polytope $\mathcal{V}_{C_3}(1,0,1)$. The structure of the $\mathcal{V}_{C_3}(1,0,1)$−polytope contains 26 vertices that can be decomposed into

- eight orbits with the C_2−symmetry:

$$\{\alpha_1,\omega_2,\omega_3\}:\quad \underset{1}{(-1,0,0)}, \underset{4}{\left(-\frac{3}{4},0,\frac{3}{4}\right)}, \underset{4}{\left(-\frac{3}{5},0,\frac{3}{5}\right)}, \underset{4}{\left(0,0,\frac{3}{4}\right)}, \underset{4}{(0,1,0)}, \underset{4}{\left(\frac{3}{5},0,\frac{3}{5}\right)}, \underset{4}{\left(\frac{3}{4},\frac{3}{4},0\right)}, \underset{1}{(1,0,0)};$$

- eleven orbits with the $A_1 \times A_1$−symmetry:

$$\{\omega_1,\alpha_2,\omega_3\}:\quad \underset{1}{\left(0,-\frac{3}{2},0\right)}, \underset{2}{\left(0,-\frac{6}{5},\frac{3}{5}\right)}, \underset{2}{(1,-1,0)}, \underset{4}{\left(\frac{3}{4},-\frac{3}{4},\frac{3}{4}\right)}, \underset{2}{\left(\frac{3}{2},0,0\right)}, \underset{4}{\left(\frac{6}{5},0,\frac{3}{5}\right)}, \underset{2}{(0,0,1)}, \underset{4}{\left(\frac{3}{4},\frac{3}{4},\frac{3}{4}\right)}, \underset{2}{(1,1,0)}, \underset{2}{\left(0,\frac{6}{5},\frac{3}{5}\right)}, \underset{1}{\left(0,\frac{3}{2},0\right)};$$

- nine orbits with the A_2−symmetry:

$$\{\omega_1,\omega_2,\alpha_3\}:\quad \underset{1}{\left(0,0,-\frac{9}{10}\right)}, \underset{3}{\left(\frac{3}{4},0,-\frac{3}{4}\right)}, \underset{3}{\left(0,1,-\frac{1}{2}\right)}, \underset{3}{\left(\frac{6}{5},0,-\frac{3}{10}\right)}, \underset{6}{\left(\frac{3}{4},\frac{3}{4},0\right)}, \underset{3}{\left(0,\frac{6}{5},\frac{3}{10}\right)}, \underset{3}{\left(1,0,\frac{1}{2}\right)}, \underset{3}{\left(0,\frac{3}{4},\frac{3}{4}\right)}, \underset{1}{\left(0,0,\frac{9}{10}\right)}.$$

The polytope $\mathcal{V}_{C_3}(0,1,1)$. The structure of the $\mathcal{V}_{C_3}(0,1,1)$−polytope contains 14 vertices that can be decomposed into

- five orbits with the C_2−symmetry:

$$\{\alpha_1,\omega_2,\omega_3\}:\quad \underset{1}{(-1,0,0)}, \underset{4}{\left(-\frac{3}{7},0,\frac{3}{7}\right)}, \underset{4}{(0,1,0)}, \underset{4}{\left(\frac{3}{7},0,\frac{3}{7}\right)}, \underset{1}{(1,0,0)};$$

- six orbits with the $A_1 \times A_1$−symmetry:

$$\{\omega_1,\alpha_2,\omega_3\}:\quad \underset{2}{(1,-1,0)}, \underset{2}{\left(0,-\frac{6}{7},\frac{3}{7}\right)}, \underset{4}{\left(\frac{6}{7},0,\frac{3}{7}\right)}, \underset{2}{(0,0,1)}, \underset{2}{\left(0,\frac{6}{7},\frac{3}{7}\right)}, \underset{2}{(1,1,0)};$$

- six orbits with the A_2−symmetry:

$$\{\omega_1,\omega_2,\alpha_3\}:\quad \underset{1}{\left(0,0,-\frac{9}{14}\right)}, \underset{3}{\left(0,1,-\frac{1}{2}\right)}, \underset{3}{\left(\frac{6}{7},0,-\frac{3}{14}\right)}, \underset{3}{\left(0,\frac{6}{7},\frac{3}{14}\right)}, \underset{3}{\left(1,0,\frac{1}{2}\right)}, \underset{1}{\left(0,0,\frac{9}{14}\right)};$$

The polytope $\mathcal{V}_{C_3}(1,1,1)$. The structure of the $\mathcal{V}_{C_3}(1,1,1)$−polytope contains 26 vertices that can be decomposed into

- eight orbits with the C_2−symmetry:

$$\{\alpha_1,\omega_2,\omega_3\}:\quad \underset{1}{(-1,0,0)}, \underset{4}{\left(-\frac{5}{8},\frac{5}{8},0\right)}, \underset{4}{\left(-\frac{5}{9},0,\frac{5}{9}\right)}, \underset{4}{\left(0,0,\frac{5}{8}\right)}, \underset{4}{(0,1,0)}, \underset{4}{\left(\frac{5}{9},0,\frac{5}{9}\right)}, \underset{4}{\left(\frac{5}{8},\frac{5}{8},0\right)}, \underset{1}{(1,0,0)};$$

	C_2		$A_1 \times A_1$		A_2	
λ	*Orbits*	*'Pancakes'*	*Orbits*	*'Pancakes'*	*Orbits*	*'Pancakes'*
$(a,0,0)$	2	2	3	3	4	4
$(0,b,0)$	5	5	6	3	6	6
$(0,0,c)$	3	3	3	3	2	2
$(a,b,0)$	5	5	6	5	6	6
$(a,0,c)$	8	5	11	7	9	9
$(0,b,c)$	5	5	6	5	6	6
(a,b,c)	8	5	11	7	9	9

Table 5.9. The numbers of orbits and 'pancakes' are provided for $\mathcal{V}_{C_3}(\lambda)-$polytopes. The dominant points λ with the coordinates $a = b = c$ are considered.

- eleven orbits with the $A_1 \times A_1-$symmetry:

$$\{\omega_1, \alpha_2, \omega_3\}: \quad \underset{1}{\left(0,-\frac{5}{4},0\right)}, \underset{2}{\left(0,-\frac{10}{9},\frac{5}{9}\right)}, \underset{2}{(1,-1,0)}, \underset{4}{\left(\frac{5}{8},-\frac{5}{8},\frac{5}{8}\right)}, \underset{2}{\left(\frac{5}{4},0,0\right)}, \underset{4}{\left(\frac{10}{9},0,\frac{5}{9}\right)},$$
$$\underset{2}{(0,0,1)}, \underset{4}{\left(\frac{5}{8},\frac{5}{8},\frac{5}{8}\right)}, \underset{2}{(1,1,0)}\ \underset{2}{\left(0,\frac{10}{9},\frac{5}{9}\right)}, \underset{1}{\left(0,\frac{5}{4},0\right)};$$

- nine orbits with the A_2-symmetry:

$$\{\omega_1, \omega_2, \alpha_3\}: \quad \underset{1}{\left(0,0,-\frac{5}{6}\right)}, \underset{3}{\left(\frac{5}{8},0,-\frac{5}{8}\right)}, \underset{3}{\left(0,1,-\frac{1}{2}\right)}, \underset{3}{\left(\frac{10}{9},0,-\frac{5}{18}\right)}, \underset{6}{\left(\frac{5}{8},\frac{5}{8},0\right)}, \underset{3}{\left(0,\frac{10}{9},\frac{5}{18}\right)},$$
$$\underset{3}{\left(1,0,\frac{1}{2}\right)}, \underset{3}{\left(0,\frac{5}{8},\frac{5}{8}\right)}, \underset{1}{\left(0,0,\frac{5}{6}\right)}.$$

5.6. Symmetry breaking of $\mathcal{V}_W(\lambda)$ and related tubes

In this section, we follow a symmetry-breaking procedure described in Section 4.9. However, for simplicity, the two-dimensional faces involved in a symmetry-breaking mechanism are not colored. Several examples of the nanotubes constructed from broken-in-half polytopes of the $\mathcal{V}_{A_3}(\lambda)-$ and $\mathcal{V}_{B_3}(\lambda)-$families are considered in Figures 5.4–5.9, where the ordering depends on the number of orbits contained within a corresponding polytope. Since this manuscript is currently in preparation, the nanotubes from the other polytopes of the crystallographic groups A_3 and B_3 are planned to be presented later.

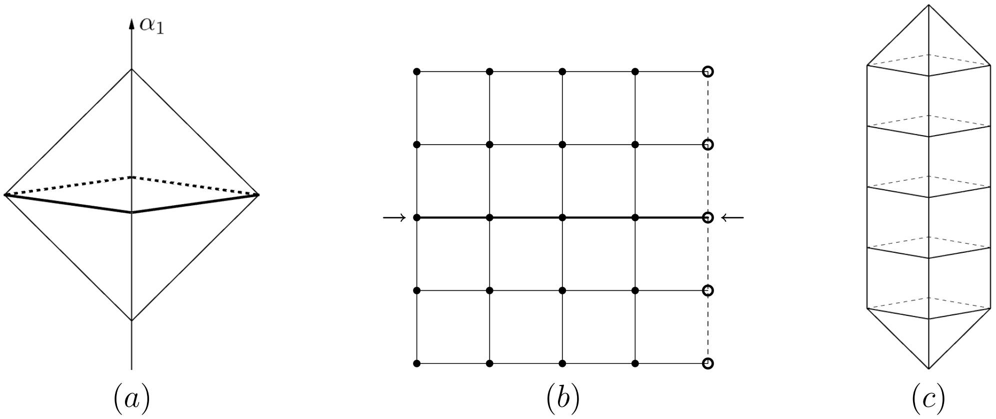

Fig. 5.4. (a) The polytope $\mathcal{V}_{B_3}(0,0,1)$ is oriented in the α_1-direction. The symmetry-breaking path is indicated by bold black edges. (b) The insert for $\mathcal{V}_{B_3}(0,0,1)$. (c) The nanotube obtained by inserting four extra orbits into the structure of $\mathcal{V}_{B_3}(0,0,1)$.

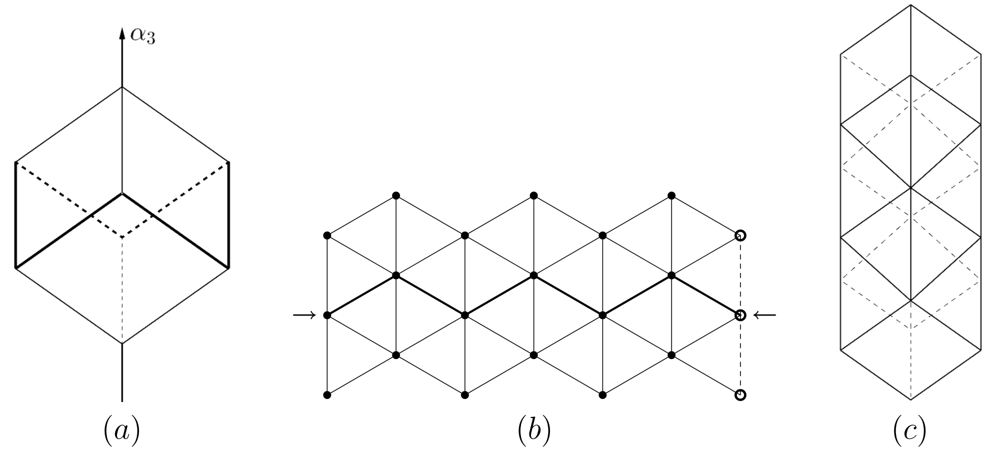

Fig. 5.5. (a) The polytope $\mathcal{V}_{B_3}(1,0,0)$ is oriented in the α_3-direction. The symmetry-breaking path is indicated by bold black edges. (b) The insert for $\mathcal{V}_{B_3}(1,0,0)$. (c) The nanotube obtained by inserting four extra orbits into the structure of $\mathcal{V}_{B_3}(1,0,0)$.

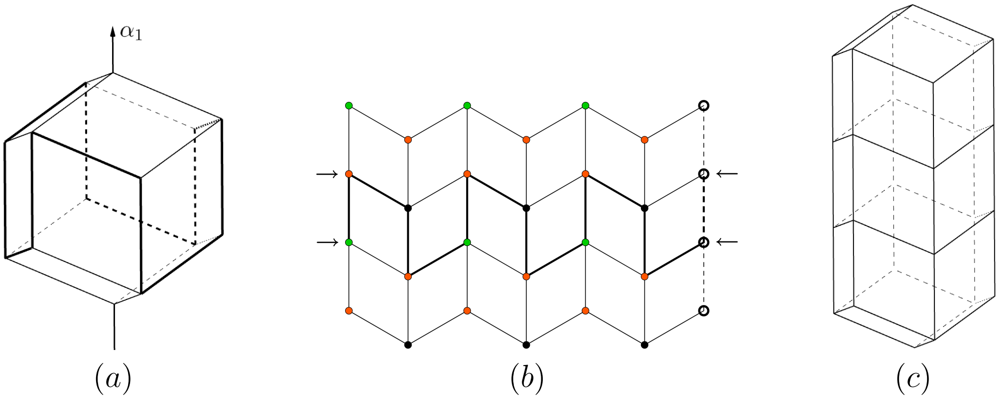

Fig. 5.6. (a) The polytope $\mathcal{V}_{A_3}(1,0,1)$ is oriented in the α_1-direction. The symmetry-breaking path is indicated by bold black edges. (b) The insert for $\mathcal{V}_{A_3}(1,0,1)$. (c) The nanotube obtained by inserting four extra orbits into the structure of $\mathcal{V}_{A_3}(1,0,1)$.

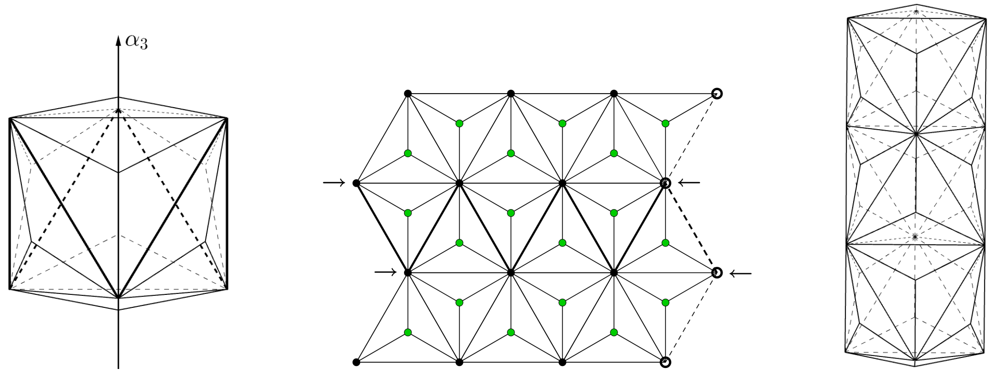

(*a*) (*b*) (*c*)

Fig. 5.7. (*a*) The polytope $\mathcal{V}_{B_3}(0,1,1)$ is oriented in the α_3-direction. The symmetry-breaking path is indicated by bold black edges. (*b*) The insert for $\mathcal{V}_{B_3}(0,1,1)$. (*c*) The nanotube obtained by inserting six extra orbits into the structure of $\mathcal{V}_{B_3}(0,1,1)$.

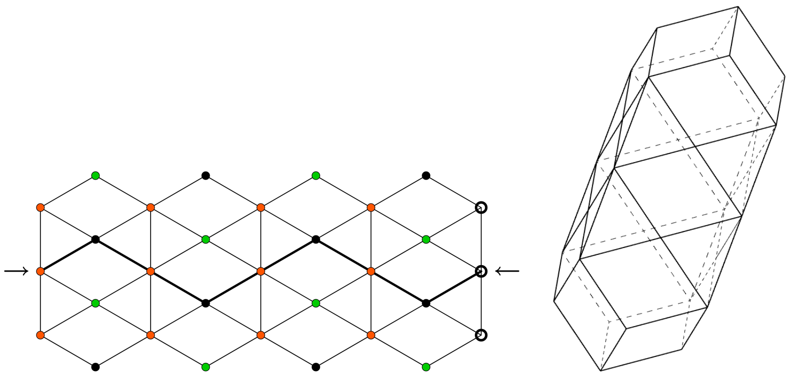

(*a*) (*b*) (*c*)

Fig. 5.8. (*a*) The polytope $\mathcal{V}_{A_3}(1,0,1)$ is oriented in the α_2-direction. The symmetry-breaking path is indicated by bold black edges. (*b*) The insert for $\mathcal{V}_{A_3}(1,0,1)$. (*c*) The nanotube obtained by inserting six extra orbits into the structure of $\mathcal{V}_{A_3}(1,0,1)$.

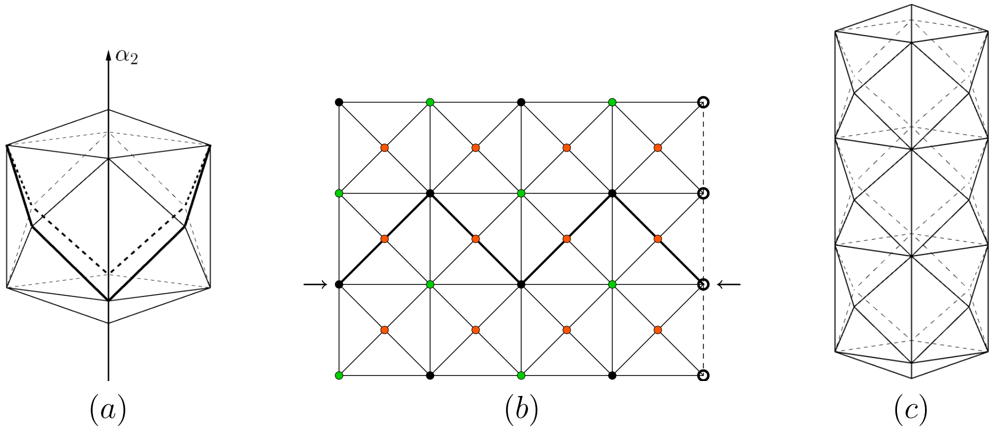

(*a*) (*b*) (*c*)

Fig. 5.9. (*a*) The polytope $\mathcal{V}_{A_3}(1,1,1)$ is oriented in the α_2-direction. The symmetry-breaking path is indicated by bold black edges. (*b*) The insert for $\mathcal{V}_{A_3}(1,1,1)$. (*c*) The nanotube obtained by inserting six extra orbit into the structure of $\mathcal{V}_{A_3}(1,1,1)$.

Conclusion

The goal of this work was to explore the applications of finite Coxeter groups to Fourier-like analysis provided on the weight lattice of the crystallographic reflection group A_2 (Hrivnák *et al.* [**1**]), as well as to the construction of nanotube-like structures (Myronova [**3**]). The latter are obtained using a well-known symmetry-breaking technique applied to the family of dual polyhedra of the non-crystallographic group H_3. Since such polytopes may contain up to three orbits within their structures, we have demonstrated the construction of the corresponding stellated polytopes. Since the structure of the fullerene C_{20} is provided by the dodecahedron, we have extended this fullerene into carbon nanotubes of armchair C_{20+6N} and zig-zag C_{20+10N} types. In addition, we have considered the orbit-decompositions of dual polytopes constructed using the crystallographic groups A_3, B_3 and C_3. We have also investigated the relevance of the non-crystallographic groups with 5-fold symmetry to determining the indices of orbits (Myronova *et al.* [**2**]). In the geometric interpretation, the algorithm that yields the lower orbits of polytopes, i.e., the orbits of smaller radii comparing to an initial one, provides the structures of nested polytopes.

Despite the fact that finite reflection groups are relevant to numerous scientific areas, their possible applications have not been explored fully yet. In this section, we list the unsolved problems that are considered as future research but have not appeared in the concluding remarks of Chapters 2–4. More precisely,

- A symmetry-breaking mechanism applied to the polytopes generated by the finite reflection groups in the four-dimensional Euclidean space is an open problem. It is an interesting task to determine the orbit-decompositions of polytopes obtained by the action of the crystallographic groups A_4, B_4, C_4, F_4, D_4 and the non-crystallographic group H_4. For example, using the Coxeter–Dynkin diagram of the non-crystallographic group H_4 (Figure 1.3), its symmetry can be reduced as $H_4 \to A_1 \times H_3$, $H_4 \to A_1 \times H_2 \times A_1$, $H_4 \to A_2 \times A_1 \times A_1$ and $H_4 \to A_3 \times A_1$. In this case, instead of circular/polygonal orbits in the decomposition, we expect to have spherical/polyhedral ones. The geometric visualization of polytopes provided by the there-dimensional subgroups of H_4 remains an open problem. Moreover, in recent studies (Dechant [**35**]), the construction of the four-dimensional root system

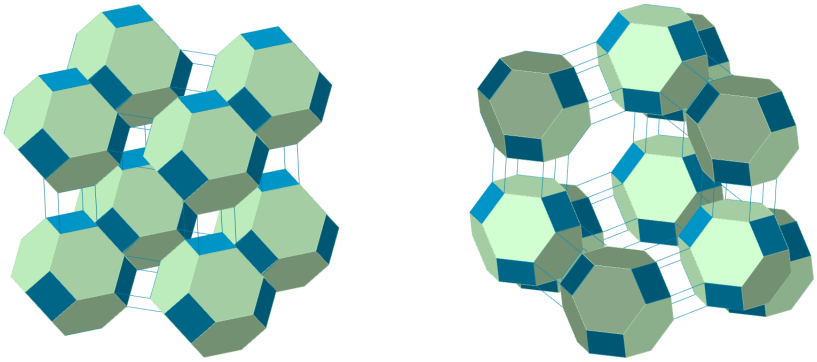
(a) (b)

Fig. 5.10. (a) The structure of Zeolite A is constituted by the polytopes $\mathcal{D}_{A_3}(1,1,1)$ (truncated octahedron) and $\mathcal{D}_{B_3}(1,0,0)$ (cube). (b) The structure of faujasite-type zeolites X and Y is constituted by the polytopes $\mathcal{D}_{A_3}(1,1,1)$ (truncated octahedron) and $\mathcal{D}_{A_2\times A_1}(1,1,1)$ (hexagonal prism).

from the corresponding three-dimensional one has been described in detail for the icosahedral case $H_3 \to H_4$.

- In Chapter 5, we demonstrate the orbit-decompositions of dual polytopes obtained by the actions of the Weyl groups A_3, B_3 and C_3 on each type of dominant point λ. However, the construction of related nanotube-like structures for the considered polytopes has not been determined for each case yet. As well, it would be useful to establish a connection between such nanotubes and the chemical compounds that impose the physical constraints permitting the existence of such tube-like structures.
- Another interesting task is the construction of hierarchical non-crystalline structures, biocrystals and modular structures described in detail in (Bulienkov [**25**]) by using group-theoretical methods.
- The construction of multi-shell nanostructures (Diudea *et al.* [**45**]) and porous nanomaterials (Lutz [**94**]) (for example, see Figure 5.10) is considered as future work. For such structures, three-dimensional polytopes of the crystallographic and non-crystallographic types constitute building blocks. Since the polytopes obtained by the actions of the groups $A_1\times A_1\times A_1$, $A_2\times A_1$, $B_2\times A_1$, $C_2\times A_1$, $G_2\times A_1$ and $H_2\times A_1$, together with their duals, play an important role in the construction of such nanomaterials (as they provide the structures of prisms and bipyramids), their orbit decompositions should be considered independently.

Moreover, the generic realizations of conformal and de Sitter algebras have been formulated in (Myronova and Nesterenko [**4**]), and the orthogonal systems of functions on lattices of $SU(n+1)$, $n<\infty$ have been investigated in (Myronova and Szajewska [**5**]). Therefore, we plan to continue our research in these areas as well.

References

---

[1] Hrivnák, J.; Myronova, M.; Patera, J. (2020) Central splitting of A_2 discrete Fourier–Weyl transforms. *Symmetry*, **12**, 1828, doi:10.3390/sym12111828.

[2] Myronova, M.; Patera, J.; Szajewska, M. (2020) Nested polyhedra and indices of orbits of Coxeter groups of non-crystallographic type. *Symmetry*, **12**, 1737, doi:10.3390/sym12101737.

[3] Myronova, M. (2020) On symmetry breaking of dual polyhedra of the non-crystallographic group H_3. accepted in *Acta Cryst. A*.

[4] Myronova, M.; Nesterenko, M. (2019) Generic realizations of conformal and de Sitter algebras. *TRIM*, **16**, 100–112.

[5] Myronova, M.; Szajewska, M. (2019) The orthogonal systems of functions on lattices of $SU(n+1)$, $n<\infty$. In Proceedings of XXXVII Workshop 2018 on Geometric Methods in Physics, Białowieża, Poland, 2018, Jul 1–7; Trends in Mathematics; *Springer: Basel, Switzerland*, 195–203.

[6] Andrews, R.; Jacques, D.; Qian, D.; Rantell, T. (2002) Multiwall carbon nanotubes: synthesis and application. *Acc. Chem. Res.*, **35**, 1008–1017, doi:10.1021/ar010151m.

[7] Atiyah, M.; Sutcliffe, P. (2003) Polyhedra in Physics, Chemistry and Geometry. *Milan J. Math.*, **71**, 33–58.

[8] Atoyan, A.; Patera, J. (2004) Properties of continuous Fourier extension of the discrete cosine transform and its multidimensional generalization. *J. Math. Phys.*, **45**, 2468–2491, doi:10.1063/1.1738187.

[9] Aznar, M.; Luque, A.; Reguera, D. (2012) Relevance of capsid structure in the buckling and maturation of spherical viruses. *Phys. Biol.*, **9**, 036003, doi:10.1088/1478-3975/9/3/036003.

[10] Baake, M.; Grimm, U. (2013) Aperiodic Order, Volume 1: A Mathematical Invitation. *Cambridge University Press: Cambridge, UK*; ISBN 97805218699911.

[11] Balandin, A. (2011) Thermal properties of graphene and nanostructured carbon materials. *Nat. Mater*, **10**, 569–581, doi:10.1038/nmat3064.

[12] Bianco, A.; Kostarelos, K.; Prato, M. (2005) Applications of carbon nanotubes in drug delivery. *Curr. Opin. Chem. Biol.*, **9**, doi:10.1016/j.cbpa.2005.10.005.

[13] Bodner, M.; Patera, J.; Szajewska, M. (2013) C_{70}, C_{80}, C_{90} and carbon nanotubes by breaking of the icosahedral symmetry of C_{60}. *Acta Cryst. A*, **69**, 583–591, doi:10.1107/s0108767313021375.

[14] Bodner, M.; Bourret, E.; Patera, J.; Szajewska, M. (2014) Icosahedral symmetry breaking: C_{60} to C_{78}, C_{96} and to related nanotubes. *Acta Cryst. A*, **70**, 650–655, doi:10.1107/S2053273314017215.

[15] Bodner, M.; Bourret, E.; Patera, J.; Szajewska, M. (2015) Icosahedral symmetry breaking: C_{60} to C_{84}, C_{108} and to related nanotubes. *Acta Cryst. A*, **71**, 297–300, doi:10.1107/S2053273315003824.

[16] Bodner, M.; Patera, J.; Szajewska, M. (2017) Decomposition matrices for the special case of data on the triangular lattice of $SU(3)$. *Appl. Comput. Harmon. Anal.*, **43**, 346–353, doi:10.1016/j.acha.2016.07.001.

[17] Bourbaki, N. (1968) *Groupes et algèbres de Lie, Chapiters IV, V, VI.* Hermann: Paris, France.

[18] Bourret, E.; Grabowiecka, Z. (2019) The polytopes of the H_3 group with 60 vertices and their orbit decompositions. *Acta Cryst. A*, **75**, 541–550, doi:10.1107/S2053273319000640.

[19] Braden, H.W. (1991) Integral pairings and Dynkin indices. *J. London Math. Soc.*, **s2-43**, 313–323, doi:10.1112/jlms/s2-43.2.313.

[20] Bremner, M.R. (1986) Fast computation of weight multiplicities. *J. Symb. Comput.*, **2**, 357–362, doi:10.1016/S0747-7171(86)80003-7.

[21] Bremner, M.R.; Moody R.V.; Patera, J. (1985) Tables of Dominant Weight Multiplicities for Representations of Simple Lie Algebras. *Marcel Dekker, Inc.: New York, NY, USA*; ISBN 0824772709.

[22] Brinkmann, G.; Dress, A.W.M. (1997) A constructive enumeration of fullerenes. *J. Algorithms*, **23**, 345–358, doi:10.1006/jagm.1996.0806.

[23] Brinkmann, G.; Goedgebeur, J.; McKay, B.D. (2012) The Generation of Fullerenes. *J. Chem. Inf. Model.*, **52**, 2910–2918, doi:10.1021/ci3003107.

[24] Britanak, V.; Rao, K.; Yip, P. (2007) Discrete Cosine and Sine Transforms: General Properties, Fast Algorithms and Integer Approximations. *Elsevier/Academic Press: Amsterdam, The Netherlands*; ISBN 9780123736246.

[25] Bulienkov, N.A. (1998) Three Possible Branches of Determinate Modular Generalization of Crystallography. *Quasicrystals and Discrete Geometry*, ed. J. Patera (Amer. Math. Soc.), *Fields Institute Monograph Series*, **10**, 67–134.

[26] Carter, J.B.; Saunders, V.A. (2007) Virology Principles and Applications. *John Wiley & Sons, Ltd.: Chichester, UK*; ISBN 9780470023860.

[27] Caspar, D.L.D.; Klug, A. (1962) Physical Principles in the Construction of Regular Viruses. *Cold. Spring. Harb. Symp Quant. Biol.*, **27**, 1–24, doi:10.1101/sqb.1962.027.001.005.

[28] Chen, L.; Moody, R.V.; Patera, J. (1998) Noncrystallographic root systems. *Quasicrystals and Discrete Geometry*, ed. J. Patera (Amer. Math. Soc.), *Fields Institute Monograph Series*, **10**, 135–178.

[29] Champagne, B.; Kjiri, M.; Patera, J.; Sharp, R.T. (1995) Description of reflection-generated polytopes using decorated Coxeter diagrams. *Can. J. Phys.*, **73**, 566–584, doi:10.1139/p95-084.

[30] Cooley, J.W.; Tukey, J.W. (1965) An Algorithm for the Machine Calculation of Complex Fourier Series. *Math. Comput.*, **19**, 297–301, doi:10.2307/2003354.

[31] Coxeter, H.S.M. (1934) Discrete groups generated by reflections. *Annals of Math.*, **35**, 588–621, doi:10.2307/1968753.

[32] Coxeter, H.S.M. (1971) A Spectrum of Mathematics; Essays Presented to H.G. Forder. *Oxford University Press: Oxford, UK*; 98–107.

[33] Coxeter, H.S.M. (1973) Regular Polytopes, 3rd ed. *Dover Publications, Inc.: New York, NY, USA*; ISBN 0486614808.

[34] Czyżycki, T.; Hrivnák, J.; Motlochová, L. (2020) Generalized Dual-Root Lattice Transforms of Affine Weyl Groups. *Symmetry*, **12**, 1018, doi:10.3390/sym12061018.

[35] Dechant, P.-P. (2021) Clifford spinors and root system induction: H_4 and the Grand Antiprism. *arXiv:2103.07817v2*.

[36] Dechant, P.-P.; Bœhm, C.; Twarock, R. (2012) Novel Kac-Moody-type affine extensions of non-crystallographic Coxeter groups. *J. Phys. A Math. Theor.*, **45**, 285202, doi:10.1088/1751-8113/45/28/285202.

[37] Dechant, P.-P.; Bœhm, C.; Twarock, R. (2013) Affine extensions of non-crystallographic Coxeter groups induced by projection. *J. Math. Phys.*, **54**, 093508, doi:10.1063/1.4820441.

[38] Dechant, P.-P.; Wardman, J.; Keef, T.; Twarock, R. (2014) Viruses and fullerenes – symmetry as a common thread? *Acta Cryst. A*, **70**, 162–167, doi:10.1107/S2053273313034220.

[39] Dechant, P.-P.; Twarock, R. (2021) Models of viral capsid symmetry as a driver of discovery in virology and nanotechnology. *Biochem (Lond)*, **43**, 20–24, doi:10.1042/bio_2020_102.

[40] Degiorgi, L. (1998) Fullerenes and carbon derivatives: from insulators to superconductors. *Adv. Phys.*, **47**, 207–316, doi:10.1080/000187398243555.

[41] Deodhar, V.V. (1982) On the root system of a Coxeter group. *Communications in Algebra*, **10**, 611–630, doi:10.1080/00927878208822738.

[42] Diederich, F.; Whetten, R.L. (1992) Beyond C_{60}: the higher fullerenes. *Acc. Chem. Res.*, **25**, 119–126, doi:10.1021/ar00015a004.

[43] Devi, P.; Saini, S.; Kim, K.-H. (2019) The advanced role of carbon quantum dots in nanomedical applications. *Biosens. Bioelectron.*, **141**, 111158, doi:10.1016/j.bios.2019.02.059.

[44] Dirican, M.; Yanilmaz, M.; Zhang, X. (2014) Free-standing polyaniline – porous carbon nanofiber electrodes for symmetric and asymmetric supercapacitors. *RSC Adv.*, **4**, 59427–59435, doi:10.1039/C4RA09103E.

[45] Diudea, M.V.; Bende, A.; Nagy, C.L. (2014) Carbon multi-shell cages *Phys. Chem. Chem. Phys.*, **16**, 5260–5269, doi:10.1039/C3CP55309D.

[46] Dresselhaus, M.S.; Dresselhaus, G.; Eklund, P.C. (1996) Science of fullerenes and carbon nanotubes. *Academic Press, Inc.: New York, NY, USA*; ISBN 9780080540771.

[47] Dresselhaus, M.S; Dresselhaus, G.; Saito, R. (1995) Physics of carbon nanotubes. *Carbon*, **33**, 883–891, doi:10.1016/0008-6223(95)00017-8.

[48] Dynkin, E.B. (1957) Semisimple subalgebras of semisimple Lie algebras. *Trans. Am. Math. Soc.*, **6**, 111–244, doi:10.1090/trans2/006.

[49] Eletskii, A.V.; Smirnov, B.M. (1995) Fullerenes and carbon structures. *Phys.-Uspekhi*, **38**, 935–964, doi:10.3367/UFNr.0165.199509a.0977.

[50] Eletskii, A.V. (2007) Mechanical properties of carbon nanostructures and related materials. *Phys.-Uspekhi*, **50**, 225–261, doi:0.1070/PU2007v050n03ABEH006188.

[51] Flamant, J.; Le Bihan, N.; Chainais, P. (2019) Time frequency analysis of bivariate signals. *Appl. Comput. Harmon. Anal.*, **46**, 351–383, doi:10.1016/j.acha.2017.05.007.

[52] Fowler, P.W.; Manolopoulos, D.E. (2006) An Atlas of Fullerenes. *Dover Publications, Inc.: Mineola, NY, USA*; ISBN 9780486453620.

[53] Geim, A.; Novoselov, K. (2007) The rise of graphene. *Nat. Mater*, **6**, 183–191, doi:10.1038/nmat1849.

[54] Grabowiecka, Z.; Patera, J.; Szajewska, M. (2018) Reduction of orbits of finite Coxeter groups of non-crystallographic type. *J. Math. Phys.*, **59**, 101705, doi:10.1063/1.5032210.

[55] Grünbaum, B.; Shephard, G.C. (1987) Tilings and patterns. *W. H. Freeman & Company: New York, NY, USA*; ISBN 0716711931.

[56] Gupta, P.; Tsai, K.; Ruhunage, C.K.; Gupta, V.K.; Rahm, C.E.; Jiang, D.; Alvarez, N.T. (2020) True picomolar neurotransmitter sensor based on open-ended carbon nanotubes. *Anal. Chem.*, **92**, 8536–8545, doi:10.1021/acs.analchem.0c01363.

[57] Háková L.; Larouche, M.; Patera, J. (2008) The rings of n-dimensional polytopes. *J. Phys. A*, **41**, 495202, doi:10.1088/1751-8113/41/49/495202.

[58] Hernández, J.R.; Amado, M.; Pérez-González, F. (2000) DCT-domain watermarking techniques for still images: detector performance analysis and a new structure. *IEEE Trans. Image Process.*, **9**, 55–68, doi:10.1109/83.817598.

[59] Hrivnák, J.; Motlochová, L.; Patera, J. (2012) On discretization of tori of compact simple Lie groups II. *J. Phys. A*, **45**, 255201, doi:10.1088/1751-8113/45/25/255201.

[60] Hrivnák, J.; Juránek, M. (2017) On $E-$discretization of tori of compact simple Lie groups. II. *J. Math. Phys.*, **58**, 103504, doi:10.1063/1.4997520.

[61] Hrivnák, J.; Motlochová, L. (2018) Discrete cosine and sine transforms generalized to honeycomb lattice. *J. Math. Phys.*, **59**, 063503, doi:10.1063/1.5027101.

[62] Hrivnák, J.; Motlochová, L. (2019) Dual-root lattice discretization of Weyl orbit functions. *J. Fourier Anal. Appl.*, **25**, 2521–2569, doi:10.1007/s00041-019-09673-1.

[63] Hrivnák, J.; Patera, J. (2009) On discretization of tori of compact simple Lie groups. *J. Phys. A Math. Theor.*, **42**, 385208, doi:10.1088/1751-8113/42/38/385208.

[64] Hrivnák, J.; Patera, J. (2010) On $E-$discretization of tori of compact simple Lie groups. *J. Phys. A Math. Theor.*, **43**, 165206, doi:10.1088/1751-8113/43/16/165206.

[65] Hrivnák, J.; Walton, M.A. (2016) Weight-lattice discretization of Weyl-orbit functions. *J. Math. Phys.*, **57**, 083512, doi:10.1063/1.4961154.

[66] Humphreys, J.E. (1980) Introduction to Lie algebras and representation theory. Graduate Texts in Mathematics, Vol. 9; *Springer-Verlag: New York, NY, USA*; Third printing, revised; ISBN 0387900527.

[67] Humphreys, J.E. (1990) Reflection groups and Coxeter groups. *Cambridge Studies in Advanced Mathematics, Vol. 29*; Cambridge University Press: Cambridge, UK, doi:10.1017/CBO9780511623646.

[68] Indelicato, G.; Cermelli, P.; Salthouse, D.G.; Racca, S.; Zanzotto G.; Twarock, R. (2011) A crystallographic approach to structural transitions in icosahedral viruses. *J. Math. Biol.*, **64**, 745–773; doi:10.1007/s00285-011-0425-5.

[69] Irarrazaval, P.; Lizama, C.; Parot, V.; Sing-Long, C.; Tejos, C. (2011) The fractional Fourier transform and quadratic field magnetic resonance imaging. *Comput. Math. Appl.*, **62**, 1576–1590, doi:10.1016/j.camwa.2011.03.027.

[70] Janner, A. (2014) Alternative approaches to onion-like icosahedral fullerenes. *Acta Cryst. A*, **70**, 168–180, doi:10.1107/S2053273313034219.

[71] Kahlessenane, F.; Khaldi, A.; Euschi, S. (2020) A robust blind color image watermarking based on Fourier transform domain. *Optik*, **208**, 164562, doi:10.1016/j.ijleo.2020.164562.

[72] Kane, R. (2001) Reflection groups and invariant theory. CMS Books in Mathematics/Ouvrages de Mathématiques de la SMC, Vol. 5; *Springer-Verlag: New York, NY, USA*; ISBN 038798979X.

[73] Kazemzadeh, H.; Mozafari, M. (2019) Fullerene-based delivery systems. *Drug Discov. Today*, **24**, 898–905, doi:10.1016/j.drudis.2019.01.013.

[74] Keef, T.; Twarock, R. (2009) Affine extensions of the icosahedral group with applications to the three-dimensional organisation of simple viruses. *J. Math. Biol.*, **59**, 287–313, doi:10.1007/s00285-008-0228-5.

[75] Keef T.; Taormina A.; Twarock R. (2005) Assembly models for Papovaviridae based on tiling theory. *Phys Biol.*, **2**, 175–188. doi: 10.1088/1478-3975/2/3/005.

[76] Kerner, R. (2014) Discrete Groups and Internal Symmetries of Icosahedral Viral Capsids. *Mol. Based Math. Biol.*, **2**, 1–18, doi:10.2478/mlbmb-2014-0001.

[77] Kirillov, A., Jr. (2008) An introduction to Lie groups and Lie algebras. *Cambridge University Press: Cambridge, UK*; ISBN 9780511755156.

[78] Klimyk, A.U.; Patera, J. (2006) Orbit functions. *SIGMA*, **2**, 006, doi:10.3842/SIGMA.2006.006.

[79] Klimyk, A.U.; Patera, J. (2007) Antisymmetric orbit functions. *SIGMA*, **3**, 023, doi:10.3842/SIGMA.2007.023.

[80] Klimyk, A.U.; Patera, J. (2008) $E-$orbit functions. *SIGMA*, **4**, 002, doi:10.3842/SIGMA.2008.002.

[81] Klimyk, A.U.; Patera, J. (2007) (Anti)symmetric multivariate trigonometric functions and corresponding Fourier transforms. *J. Math. Phys.*, **48**, 093504, doi:10.1063/1.277976848.

[82] Knupfer, M. (2001) Electronic properties of carbon nanostructures. *Surf. Sci. Rep.*, **42**, 1–74, doi:10.1016/S0167-5729(00)00012-1.

[83] Koca, N.O.; Koca, M. (2017) Regular and irregular chiral polyhedra from Coxeter diagrams via quaternions. *Symmetry*, **9**, 148, doi:10.3390/sym9080148.

[84] Kroto, H.W.; Heath, J.R.; O'Brien, S.C. & Curl, R. F. & Smalley, R.E. (1985) C_{60}: Buckminsterfullerene. *Nature* **318**, 162–163, doi:10.1038/318162a0.

[85] Kuo, K.H.; Deng D.W (2002) Hierarchic multishell structures with icosahedral symmetry. *J. Alloys Compd.*, **342**, 174–179, doi:10.1016/S0925-8388(02)00167-6.

[86] Lahav, A.; Chernyakova, T.; Eldar, Y.C. (2017) FoCUS: Fourier-Based Coded Ultrasound. *IEEE Trans. Ultrason. Ferroelectr. Freq. Control*, **64**, 1828–1839, doi:10.1109/TUFFC.2017.2760359.

[87] Larouche M.; Patera, J. (2011) Branching rules for Weyl group orbits of simple Lie algebras B_n, C_n and D_n. *J. Phys. A*, **44**, 115203, doi:10.1088/1751-8113/44/11/115203.

[88] Larouche M.; Nesterenko, M.; Patera J. (2009) Branching rules for the Weyl group orbits of the Lie algebra A_n. *J. Phys. A*, **42**, 485203; doi:10.1088/1751-8113/42/48/485203.

[89] Levitov, L.S.; Rhyner, J. (1988) Crystallography of quasicrystals; application to icosahedral symmetry. *J. Phys. France*, **49**, 1835–1849, doi:10.1051/jphys:0198800490110183500.

[90] Li, H.; Sun, J.; Xu, Y. (2008) Discrete Fourier analysis, cubature and interpolation on a hexagon and a triangle. *SIAM J. Numer. Anal.*, **46**, 1653–1681, doi:10.1137/060671851.

[91] Li, H.; Xu, Y. (2010) Discrete Fourier analysis on fundamental domain and simplex of A_d lattice in d-variables. *J. Fourier Anal. Appl.*, **16**, 383–433, doi:10.1007/s00041-009-9106-9.

[92] Lin, Y.; Cai, W.; Shao, X. (2006) Fullerenes connected nanotubes: An approach to build multidimensional carbon nanocomposites. *Chem. Phys.*, **331**, 85–91, doi:10.1016/j.chemphys.2006.09.031.

[93] Liu, S.; Guo, C.; Sheridan, J.T. (2014) A review of optical image encryption techniques. *Opt. Laser Technol.*, **57**, 327–342, doi:10.1016/j.optlastec.2013.05.023.

[94] Lutz, W. (2014) Zeolite Y: Synthesis, Modification, and Properties?A Case Revisited. *Adv. Mater. Sci. Eng.*, **2014**, 724248, doi:10.1155/2014/724248.

[95] Manolopoulos, D.E.; May, J.C.; Down, S.E. (1991) Theoretical studies of the fullerenes: C_{34} to C_{70}. *Chem. Phys. Lett.*, **181**, 105–111, doi:10.1016/0009-2614(91)90340-F.

[96] Mar, N.; Sansores, L.E.; Muhl, S.; Ramos, E.; Salcedo, R. (2015) Symmetric nested complexes of fullerenes. *J. Mol. Model.*, **21**, 101, doi:10.1007/s00894-015-2646-9.

[97] McKay, W.G.; Patera, J. (1981) Tables of Dimensions, Indices, and Branching Rules for Representations of Simple Lie Algebras. *Marcel Dekker, Inc.: New York, NY, USA*; ISBN 0824712277.

[98] Moody, R.V.; Nesterenko, M.; Patera, J. (2008) Computing with almost periodic functions. *Acta Cryst. A*, **64**, 654–669, doi:10.1107/S0108767308025440.

[99] Moody, R.V.; Motlochová, L.; Patera, J. (2014) Gaussian cubature arising from hybrid characters of simple Lie groups. *J. Fourier Anal. Appl.*, **20**, 1257–1290, doi:10.1007/s00041-014-9355-0.

[100] Moody, R.V.; Patera, J. (1982) Fast recursion formula for weight multiplicities. *Bull. Am. Math. Soc.*, **7**, 237–242, doi:0.1090/S0273-0979-1982-15021-2.

[101] Moody, R.V.; Patera, J. (1984) Characters of elements of finite order in simple Lie groups. *SIAM. J. Algebr. Discret. Methods*, **5**, 359–383, doi:10.1137/0605037.

[102] Moody, R.V.; Patera, J. (1987) Computation of character decompositions of class functions on compact semisimple Lie groups. *Math. Comp.*, **48**, 799–827, doi:10.1090/S0025-5718-1987-0878707-3.

[103] Moody, R.V.; Patera, J. (1992) Voronoi and Delaunay cells of root lattices: classification of their faces and facets by Coxeter-Dynkin diagrams. *J. Phys. A Math. Theor*, **25**, 5089–5134, doi:10.1088/0305-4470/25/19/020.

[104] Moody, R.V.; Patera, J. (1993) Quasicrystals and icosians. *J. Phys. A Math. Theor*, **26**, 2829–2853, doi:10.1088/0305-4470/26/12/022.

[105] Moody, R.V.; Patera, J. (2006) Orthogonality within the families of $C-$, $S-$, and $E-$functions of any compact semisimple Lie group. *SIGMA*, **2**, 076, doi:10.3842/SIGMA.2006.076.

[106] Nespolo, M.; Souvignier, B.; Litvin, D. (2008) About the concept and definition of noncrystallographic symmetry. *Z. Kristallogr. Cryst. Mater.*, **223**, 605–606, doi:10.1524/zkri.2008.1137.

[107] Nesterenko, M.; Patera, J. (2008) Three dimensional $C-$, $S-$, and $E-$transforms. *J. Phys. A*, **41**, 475205, doi:10.1088/1751-8113/41/47/475205.

[108] Okubo, S. (1977) Gauge groups without triangular anomaly. *Phys. Rev. D*, **16**, 3528–3534, doi:10.1103/PhysRevD.16.3528.

[109] Okubo, S. (1985) Branching index sum rules for simple Lie algebras. *J. Math. Phys.*, **26**, 2127–2137, doi:10.1063/1.526835.

[110] Okubo, S.; Patera, J. (1983) General indices of simple Lie algebras and symmetrized product representations. *J. Math. Phys.*, **24**, 2722–2733, doi:10.1063/1.525670.

[111] Okubo, S.; Patera, J. (1984) General indices of representations and Casimir invariants. *J. Math. Phys.*, **25**, 219–227, doi:10.1063/1.526143.

[112] Okubo, S.; Patera, J. (1985) Cancellation of higher-order anomalies. *Phys. Rev. D*, **31**, 2669–2671; doi:10.1103/PhysRevD.31.2669.

[113] Pandolfo, A.G.; Hollenkamp, A.F. (2006) Carbon properties and their role in supercapacitors. *J. Power Sources*, **157**, 11–27, doi:10.1016/j.jpowsour.2006.02.065.

[114] Panyushev, D.I. (2009) On the Dynkin index of a principal sl_2-subalgebra. *Adv. Math.*, **221**, 1115–1121; doi:10.1016/j.aim.2009.01.015.

[115] Patera, J.; Sharp, R.T. (1981) On the triangle anomaly number of $SU(n)$ representations. *J. Math. Phys.*, **22**, 2352–2356, doi:10.1063/1.524815.

[116] Patera, J.; Sharp, R.T.; Winternitz, P. (1976) Higher indices of group representations. *J. Math. Phys.*, **17**, 1972–1979, doi:10.1063/1.522836.

[117] Patera, J.; Zaratsyan, A. (2005) Discrete and continuous cosine transform generalized to Lie groups $SU(2) \times SU(2)$ and $O(5)$. *J. Math. Phys.*, **46**, 053514, doi:10.1063/1.1897143.

[118] Patera, J.; Zaratsyan, A. (2005) Discrete and continuous cosine transform generalized to Lie groups $SU(3)$ and $G(2)$. *J. Math. Phys.*, **46**, 113506, doi:10.1063/1.2109707.

[119] Patera, J.; Zaratsyan, A. (2006) Discrete and continuous sine transform generalized to the semisimple Lie groups of rank two. *J. Math. Phys.*, **47**, 043512, doi:10.1063/1.2191361.

[120] Plonka, G.; Tasche, M. (2005) Fast and numerically stable algorithms for discrete cosine transforms. *Linear Algebra Appl.*, **394**, 309–345, doi:1 0.1016/j.laa.2004.07.015.

[121] Popov, V. (2004) Carbon nanotubes: properties and application. *Mater. Sci. Eng. R Rep.*, **43**, 61–102, doi:10.1016/j.mser.2003.10.001.

[122] Prasad, B.V.V.; Schmid, M.F. (2011) Principle of virus structural organization. In Rossmann M., Rao V., Viral Molecular Machines, *Adv. Exp. Med. Biol.*, **726**, 17–47, doi:10.1007/978-1-4614-0980-9.

[123] Püschel, M. (2003) Cooley-Tukey FFT like algorithms for the DCT. In Proceedings of the 2003 IEEE International Conference on Acoustics, Speech, and Signal Processing (ICASSP '03), Hong Kong, China, 6–10 April 2003, 501–504, doi:10.1109/ICASSP.2003.1202413.

[124] Püschel, M.; Moura, J.M.F. (2003) The Algebraic Approach to the Discrete Cosine and Sine Transforms and Their Fast Algorithms. *SIAM J. Comput.*, **32**, 1280–1316, doi:10.1137/S009753970139272X.

[125] Püschel, M.; Moura, J.M.F. (2008) Algebraic signal processing theory: Foundation and 1-D time. *IEEE Trans. Signal Process.*, **56**, 3572–3585, doi:10.1109/TSP.2008.925261.

[126] Ramond, P. (2010) Group Theory: A Physicist's Survey. *Cambridge University Press: Cambridge, UK*; ISBN 9780521896030.

[127] Rasheed, M.H.; Salih, O.M.; Siddeq, M.M.; Rodrigues, M.A. (2020) Image compression based on 2D discrete Fourier transform and matrix minimization algorithm. *Array*, **6**, 100024, doi:10.1016/j.array.2020.100024.

[128] Rols, S.; Johnson, M.R.; Zeppenfeld, P.; Bienfait, M.; Vilches, O.E.; Schneble, J. (2005) Argon adsorption in open-ended single-wall carbon nanotubes. *Phys. Rev. B*, **71**, 155411, doi:10.1103/PhysRevB.71.155411.

[129] Ravanbakhsh, H.; Bao, G.; Latifi, N.; Mongeau, L.G. (2019) Carbon nanotube composite hydrogels for vocal fold tissue engineering: biocompatibility, rheology, and porosity. *Mater. Sci. Eng. C*, **103**, 109861, doi:10.1016/j.msec.2019.109861.

[130] Salthouse, D.G.; Indelicato, G.; Cermelli, P.; Keef, T.; Twarock, R. (2015) Approximation of virus structure by icosahedral tilings. *Acta Cryst. A* **71**, 410–422, doi:10.1107/S2053273315006701.

[131] Shcherbak, O.P. (1988) Wavefronts and reflection groups. *Russ. Math. Surv.*, **43**, 149–194, doi:10.1070/rm1988v043n03abeh001741.

[132] Shephard, G.C. (2000) Icosahedral deltahedra. *Period. Math. Hung.*, **39**, 88–106, doi:10.1023/A:1004838806529.

[133] Szajewska, M. (2012) Faces of platonic solids in all dimensions. *arXiv:1204.1875.*

[134] Szajewska, M. (2014) Faces of platonic solids in all dimensions. *Acta Cryst. A*, **70**, 358–363, doi:10.1107/S205327331400638X.

[135] Talis, A.L.; Kraposhin, V.S.; Kondrat'ev, S.Y.; Nikolaichik, V.I.; Svyatysheva, E.V.; Everstov, A.A. (2017) Non-crystallographic symmetry of liquid metal, flat crystallographic faults and polymorph transformation of the M_7C_3 carbide. *Acta Cryst. A*, **73**, 209–217, doi:10.1107/S2053273317000936.

[136] Taylor, E.E.; Garman K.; Stadie N.P. (2020) Atomistic Structures of Zeolite-Templated Carbon. *Chem. Mater.*, **32**, 2742–2752, doi:10.1021/acs.chemmater.0c00535.

[137] Taylor, R.; Walton, D.R.M. (1993) The chemistry of fullerenes. *Nature*, **363**, 685–693, doi:10.1038/363685a0.

[138] Terwilliger, T.C. (2013) Finding non-crystallographic symmetry in density maps of macromolecular structures. *J. Struct. Funct. Genomics*, **14**, 91–95, doi:10.1007/s10969-013-9157-7.

[139] Thomas, B.G.; Twarock, R.; Valiunas, M.; Zappa, E. (2015) Nested polytopes with non-crystallographic symmetry induced by projection. In Proceedings of Bridges on Mathematical Connections in Art, Music and Science 2015, Baltimore, MD, USA, 29 July–02 August 2015; *Tessellations Publishing: Phoenix, AZ, USA*, 167–174.

[140] Twarock, R. (2004) A tiling approach to virus capsid assembly explaining a structural puzzle in virology. *J. Theor. Biol*, **226**, 477–482, doi:10.1016/j.jtbi.2003.10.006.

[141] Twarock, R. (2004) Mathematical models for tubular structures in the family of Papovaviridae. *Bull Math Biol.*, **67**, 973–987, doi:10.1016/j.bulm.2004.11.005.

[142] Twarock, R. (2006) Mathematical virology: a novel approach to the structure and assembly of viruses. *Phil. Trans. R. Soc. A.*, **364**, 3357–3373, doi:10.1098/rsta.2006.1900.

[143] Twarock, R.; Luque, A. (2019) Structural puzzles in virology solved with an overarching icosahedral design principle. *Nat. Commun.*, **10**, 4414–4414, doi:10.1038/s41467-019-12367-3.

[144] Tzeng, S-S.; Hung, K-H.; Ko, T-H. (2006) Growth of carbon nanofibers on activated carbon fiber fabrics. *Carbon*, **44**, 859–865, doi:10.1016/j.carbon.2005.10.033.

[145] Wang, Z.; Ke, X.; Zhu, Z.; Zhu, F.; Ruan, M. & Chen, H. & Huang, R. & Zheng, L. (2001) A new carbon solid made of the world's smallest caged fullerene C_{20}. *Phys. Lett. A*, **280**, 351–356, doi:10.1016/S0375-9601(00)00847-1.

[146] Yadav, D.; Amini, F.; Ehrmann, A. (2020) Recent advances in carbon nanofibers and their applications – A review. *Eur. Polym. J.*, **138**, 109963, doi:10.1016/j.eurpolymj.2020.109963.

[147] Yang, N.; Chen, X.; Ren, T.; Zhang P.; Yang, D. (2015) Carbon nanotube based biosensors. *Sens. Actuators B Chem.*, **207**, 690–715, doi:10.1016/j.snb.2014.10.040.

[148] Yoshida, M.; Osawa, E. (1995) Formalized drawing of fullerene nets. 1. Algorithm and exhaustive generation of isomeric structures. *Bull. Chem. Soc. Jpn.*, **68**, 2073–2081, doi:10.1246/BCSJ.68.2073.

[149] Zappa, E. (2015) *New group theoretical methods for applications in virology and quasicrystals*, Ph.D. thesis, University of York, York, United Kingdom.

[150] Zelevinsky, A. (2006) Nested complexes and their polyhedral realizations. *Pure Appl. Math. Q.*, **2**, 655–671, doi:10.4310/PAMQ.2006.v2.n3.a3.

[151] Zhang, H.; Okubo S.; Tosa,Y. (1988) Global gauge anomaly for simple Lie algebras. *Phys. Rev. D.*, **37**, 2946–2957, doi:10.1103/physrevd.37.2946.

[152] Zhang, J.; Terrones, M.; Park, C.R.; Mukherjee, R.; Monthioux, M.; Koratkar, N.; Kim, Y.S.; Hurt, R.; Frackowiak, E.; Enoki, T.; Chen, Y.; Chen, Y.; Bianco, A. (2016) Carbon science in 2016: Status, challenges and perspectives. *Carbon*, **98**, 708–732, doi:10.1016/j.carbon.2015.11.060.

[153] Zheng, Y.; Guo, B.; Chen, Z.; Li, C. (2019) A Fourier descriptor of 2D shapes based on multiscale centroid contour distances used in object recognition in remote sensing images. *Sensors*, **19**, 486, doi:10.3390/s19030486.

Appendix A

The 'pancake'-structures of $\mathcal{V}_{H_3}(\lambda)-$polytopes

In Figures A.1−A.7, the polytopes $\mathcal{V}_{H_3}(\lambda)$ are viewed from the direction orthogonal to the simple roots α_k, $k \in \{1,2,3\}$. The polytopes of $\mathcal{V}_{H_3}(\lambda)$ are presented in the top row. The corresponding 'pancake'-structures with respect to each $G' \subset H_3$ are shown in the bottom row. The numbers on the left of each 'pancake' stand for the numbers of points of the two-dimensional orbits. The values on the right correspond to the α_k-coordinates that provide the spacing between the 'pancakes'. For clarity, the points of generic orbits are depicted by black, green and orange colors. The bold segments indicate the symmetry-breaking path for a considered $\mathcal{V}_{H_3}(\lambda)-$polytope.

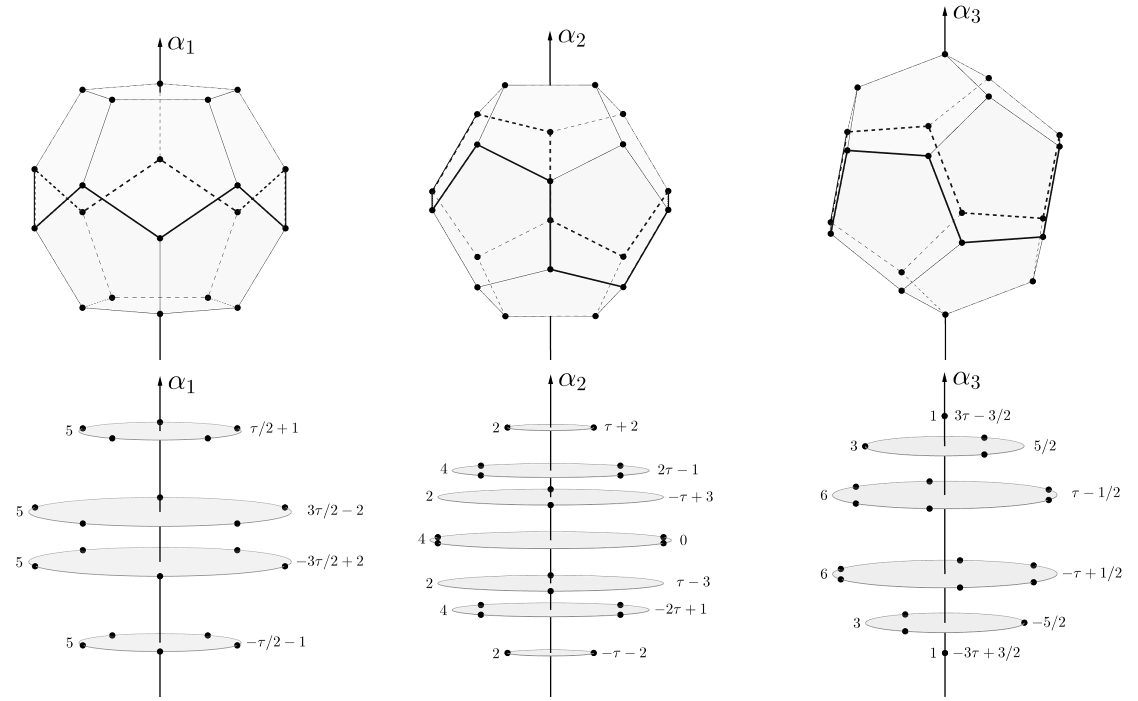
α_1
α_2
α_3
α_1
5
$\tau/2+1$
5
$3\tau/2-2$
5
$-3\tau/2+2$
5
$-\tau/2-1$
α_2
2
$\tau+2$
4
$2\tau-1$
2
$-\tau+3$
4
0
2
$\tau-3$
4
$-2\tau+1$
2
$-\tau-2$
α_3
1
$3\tau-3/2$
3
$5/2$
6
$\tau-1/2$
6
$-\tau+1/2$
3
$-5/2$
1
$-3\tau+3/2$

Fig. A.1. The polytope $\mathcal{V}_{H_3}(1,0,0)$ is oriented in the direction of the simple roots α_1, α_2 and α_3. The points of the orbits $O_{H_3}(0,0,c')$ are depicted by black color.

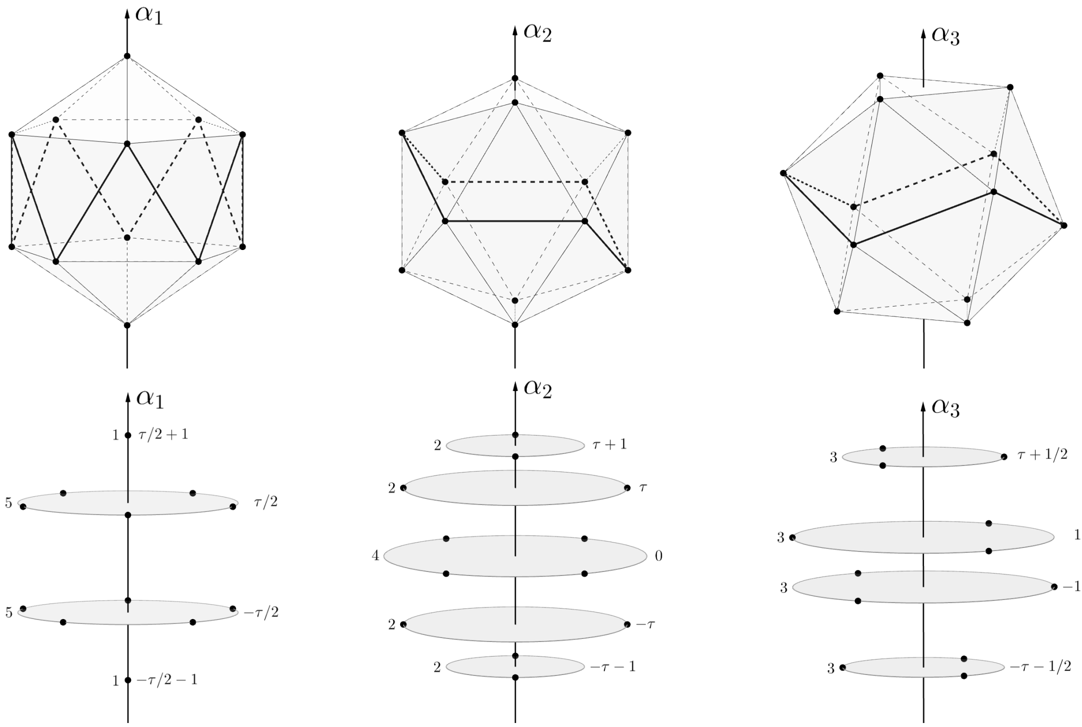
α_1
α_2
α_3
1 $\tau/2+1$
5 $\tau/2$
5 $-\tau/2$
1 $-\tau/2-1$
2 $\tau+1$
2 τ
4 0
2 $-\tau$
2 $-\tau-1$
3 $\tau+1/2$
3 1/2
3 $-1/2$
3 $-\tau-1/2$

Fig. A.2. The polytope $\mathcal{V}_{H_3}(0,0,1)$ is oriented in the direction of the simple roots α_1, α_2 and α_3. The points of the orbits $O_{H_3}(a',0,0)$ are depicted by black color.

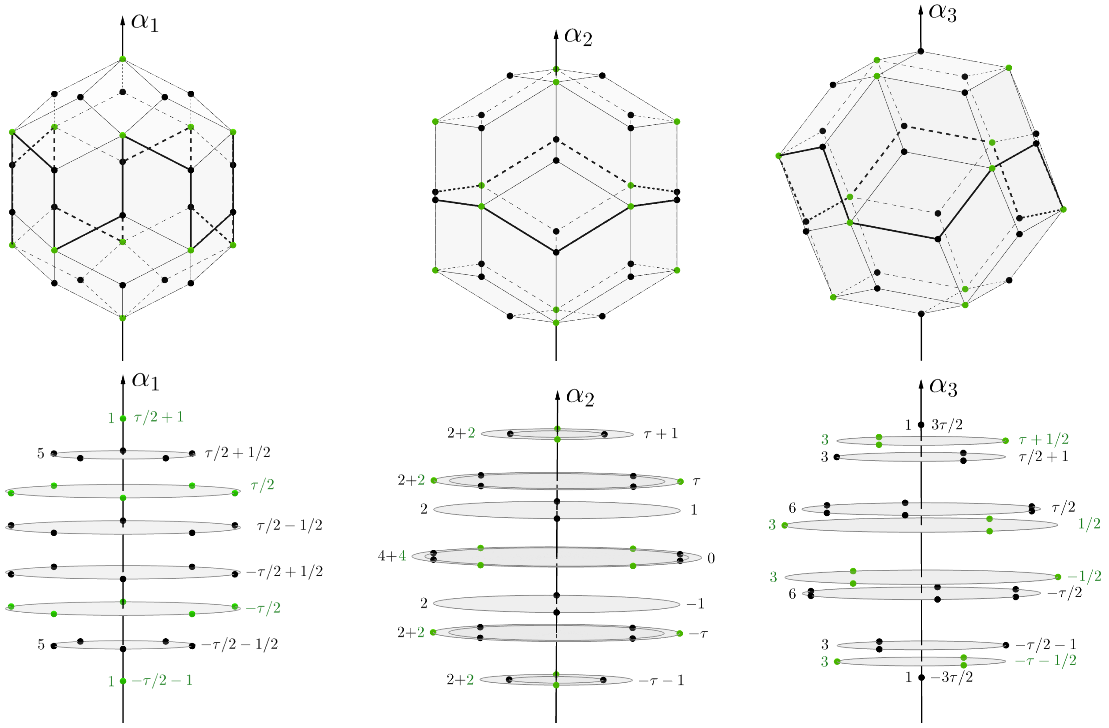
α_1
α_2
α_3
1 $\tau/2+1$
5 $\tau/2+1/2$
5 $\tau/2$
5 $\tau/2-1/2$
5 $-\tau/2+1/2$
5 $-\tau/2$
5 $-\tau/2-1/2$
1 $-\tau/2-1$
2+2 $\tau+1$
2+2 τ
2 1
4+4 0
2 -1
2+2 $-\tau$
2+2 $-\tau-1$
1 $3\tau/2$
3 $\tau+1/2$
3 $\tau/2+1$
6 $\tau/2$
3 1/2
3 $-1/2$
6 $-\tau/2$
3 $-\tau/2-1$
3 $-\tau-1/2$
1 $-3\tau/2$

Fig. A.3. The polytope $\mathcal{V}_{H_3}(0,1,0)$ is oriented in the direction of the simple roots α_1, α_2 and α_3. The points of the orbits $O_{H_3}(a',0,0)$ and $O_{H_3}(0,0,c')$ are depicted by green and black colors, respectively.

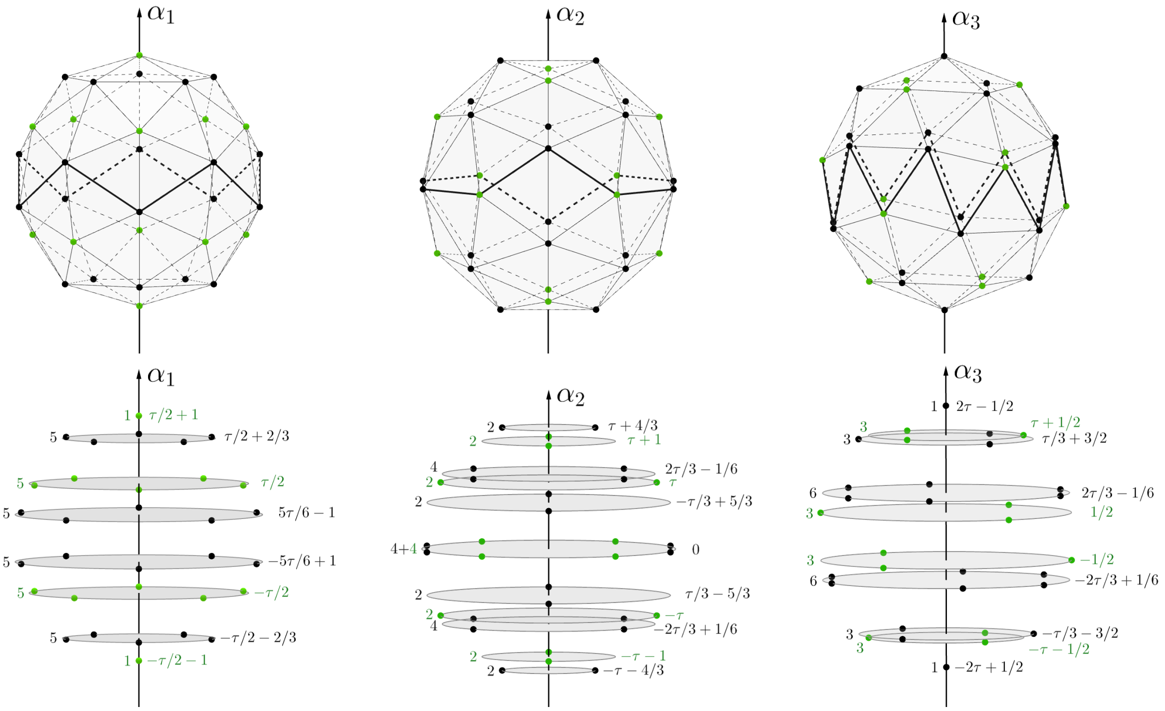
α_1
α_2
α_3
1 $\tau/2+1$
5 $\tau/2+2/3$
5 $\tau/2$
5 $5\tau/6-1$
5 $-5\tau/6+1$
5 $-\tau/2$
5 $-\tau/2-2/3$
1 $-\tau/2-1$
2 $\tau+4/3$
2 $\tau+1$
4 $2\tau/3-1/6$
2 τ
2 $-\tau/3+5/3$
4+4 0
2 $\tau/3-5/3$
2 $-\tau$
4 $-2\tau/3+1/6$
2 $-\tau-1$
2 $-\tau-4/3$
1 $2\tau-1/2$
3 $\tau+1/2$
3 $\tau/3+3/2$
6 $2\tau/3-1/6$
3 $1/2$
3 $-1/2$
6 $-2\tau/3+1/6$
3 $-\tau/3-3/2$
3 $-\tau-1/2$
1 $-2\tau+1/2$

Fig. A.4. The polytope $\mathcal{V}_{H_3}(1,1,0)$ is oriented in the direction of the simple roots α_1, α_2 and α_3. The points of the orbits $O_{H_3}(a',0,0)$ and $O_{H_3}(0,0,c')$ are depicted by green and black colors, respectively.

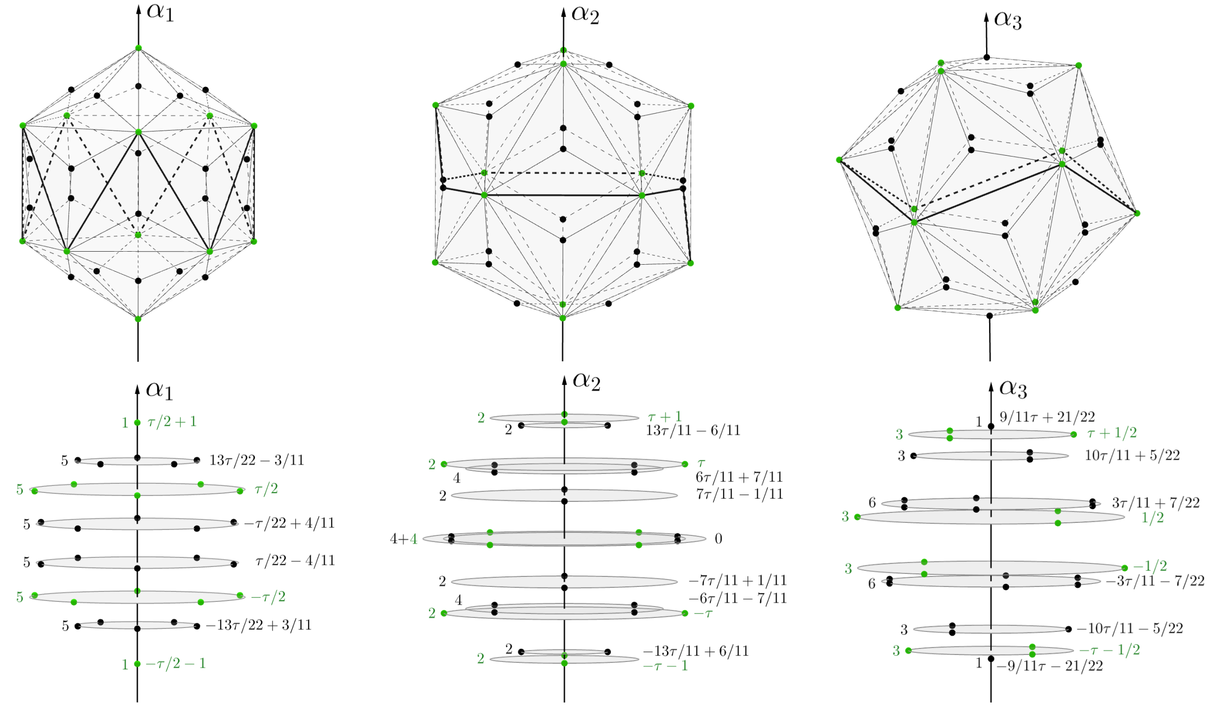
α_1
α_2
α_3
1 $\tau/2+1$
5 $13\tau/22-3/11$
5 $\tau/2$
5 $-\tau/22+4/11$
5 $\tau/22-4/11$
5 $-\tau/2$
5 $-13\tau/22+3/11$
1 $-\tau/2-1$
2 $\tau+1$
2 $13\tau/11-6/11$
2 τ
4 $6\tau/11+7/11$
2 $7\tau/11-1/11$
4+4 0
2 $-7\tau/11+1/11$
4 $-6\tau/11-7/11$
2 $-\tau$
2 $-13\tau/11+6/11$
2 $-\tau-1$
1 $9/11\tau+21/22$
3 $\tau+1/2$
3 $10\tau/11+5/22$
6 $3\tau/11+7/22$
3 $1/2$
3 $-1/2$
6 $-3\tau/11-7/22$
3 $-10\tau/11-5/22$
3 $-\tau-1/2$
1 $-9/11\tau-21/22$

Fig. A.5. The polytope $\mathcal{V}_{H_3}(0,1,1)$ is oriented in the direction of the simple roots α_1, α_2 and α_3. The points of the orbits $O_{H_3}(a',0,0)$ and $O_{H_3}(0,0,c')$ are depicted by green and black colors, respectively.

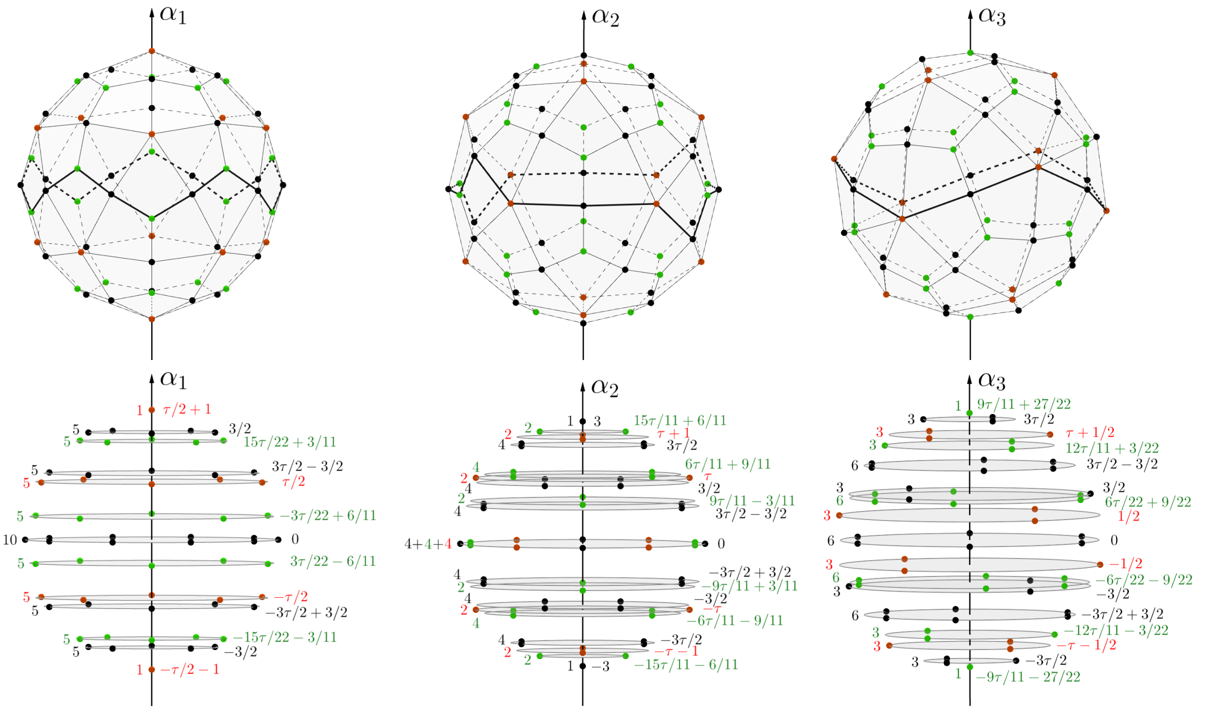
α_1
α_2
α_3
1 $\tau/2+1$
5 $3/2$
5 $15\tau/22+3/11$
5 $3\tau/2-3/2$
5 $\tau/2$
5 $-3\tau/22+6/11$
10 0
5 $3\tau/22-6/11$
5 $-\tau/2$
5 $-3\tau/2+3/2$
5 $-15\tau/22-3/11$
5 $-3/2$
1 $-\tau/2-1$
1 3
2 $15\tau/11+6/11$
2 $\tau+1$
4 $3\tau/2$
4 $6\tau/11+9/11$
2 τ
4 $3/2$
2 $9\tau/11-3/11$
4 $3\tau/2-3/2$
4+4+4 0
4 $-3\tau/2+3/2$
2 $-9\tau/11+3/11$
4 $-3/2$
2 $-\tau$
4 $-6\tau/11-9/11$
4 $-3\tau/2$
2 $-\tau-1$
2 $-15\tau/11-6/11$
1 -3
1 $9\tau/11+27/22$
3 $3\tau/2$
3 $\tau+1/2$
3 $12\tau/11+3/22$
6 $3\tau/2-3/2$
3 $3/2$
6 $6\tau/22+9/22$
3 $1/2$
6 0
3 $-1/2$
6 $-6\tau/22-9/22$
3 $-3/2$
6 $-3\tau/2+3/2$
3 $-12\tau/11-3/22$
3 $-\tau-1/2$
3 $-3\tau/2$
1 $-9\tau/11-27/22$

Fig. A.6. The polytope $\mathcal{V}_{H_3}(1,0,1)$ is oriented in the direction of the simple roots α_1, α_2 and α_3. The points of the orbits $O_{H_3}(a',0,0)$, $O_{H_3}(0,b',0)$ and $O_{H_3}(0,0,c')$ are depicted by orange, black and green colors, respectively.

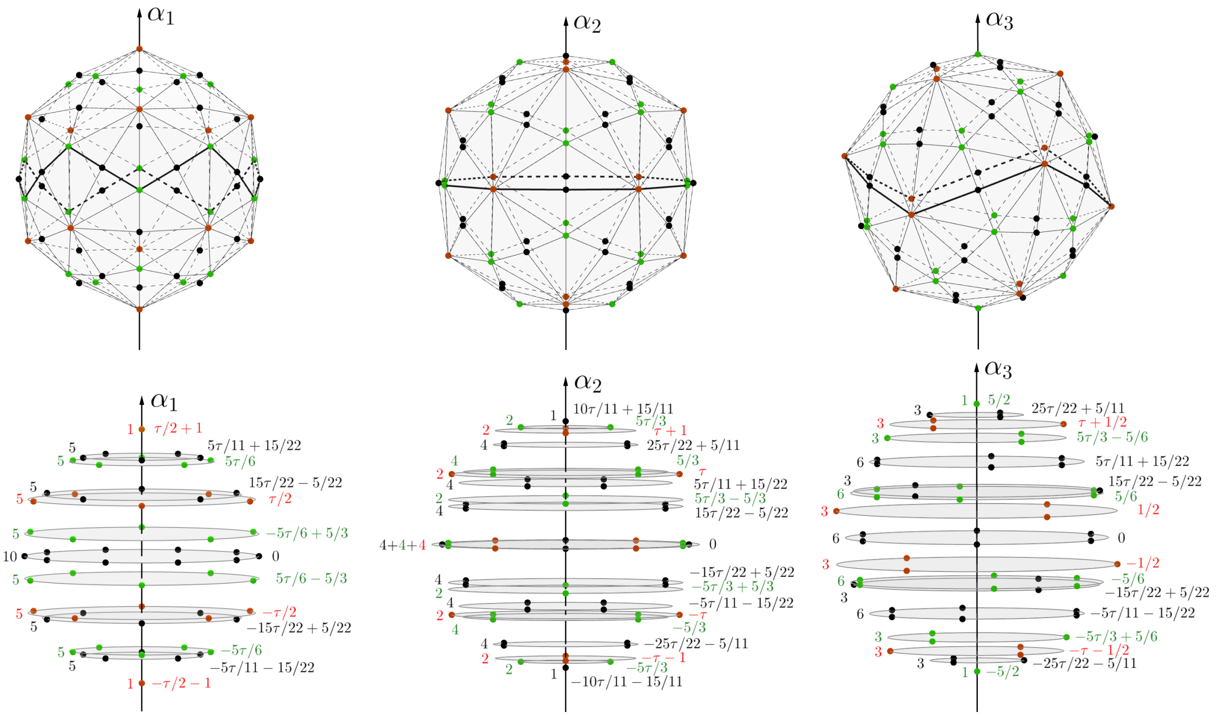
α_1
α_2
α_3
1 $\tau/2+1$
5 $5\tau/11+15/22$
5 $5\tau/6$
5 $15\tau/22-5/22$
5 $\tau/2$
5 $-5\tau/6+5/3$
10 0
5 $5\tau/6-5/3$
5 $-\tau/2$
5 $-15\tau/22+5/22$
5 $-5\tau/6$
5 $-5\tau/11-15/22$
1 $-\tau/2-1$
1 $10\tau/11+15/11$
2 $5\tau/3$
2 $\tau+1$
4 $25\tau/22+5/11$
4 $5/3$
2 τ
4 $5\tau/11+15/22$
2 $5\tau/3-5/3$
4 $15\tau/22-5/22$
4+4+4 0
4 $-15\tau/22+5/22$
2 $-5\tau/3+5/3$
4 $-5\tau/11-15/22$
2 $-\tau$
4 $-5/3$
4 $-25\tau/22-5/11$
2 $-\tau-1$
2 $-5\tau/3$
1 $-10\tau/11-15/11$
1 $5/2$
3 $25\tau/22+5/11$
3 $\tau+1/2$
3 $5\tau/3-5/6$
6 $5\tau/11+15/22$
3 $15\tau/22-5/22$
6 $5/6$
3 $1/2$
6 0
3 $-1/2$
6 $-5/6$
3 $-15\tau/22+5/22$
6 $-5\tau/11-15/22$
3 $-5\tau/3+5/6$
3 $-\tau-1/2$
3 $-25\tau/22-5/11$
1 $-5/2$

Fig. A.7. The polytope $\mathcal{V}_{H_3}(1,1,1)$ is oriented in the direction of the simple roots α_1, α_2 and α_3. The points of the orbits $O_{H_3}(a',0,0)$, $O_{H_3}(0,b',0)$ and $O_{H_3}(0,0,c')$ are depicted by orange, black and green colors, respectively.

Appendix B

Tables of orbit decompositions of $\mathcal{V}_{H_3}(\lambda)$−polytopes

The orbit decompositions of $\mathcal{V}_{H_3}(\lambda)$ with respect to the two-dimensional subgroups H_2, $A_1 \times A_1$ and A_2 of the Coxeter group H_3 are presented in Tables B.1−B.7. A point $\mu \in \mathbb{R}^3$ determines each two-dimensional orbit within the structure of $\mathcal{V}_{H_3}(\lambda)$, and its coordinates are provided in the mixed basis (Subsection 4.2.4). The squared radius of each orbit $O_{G'}(\mu')$ is denoted by $R^2(\mu')$, and it is provided in terms of τ (see expression (4.2.2)); the numerical value of the squared radius is denoted by $N[R^2(\mu')]$. The number of points of each orbit $O_{G'}(\mu')$ is denoted by N_p. Since the orbit with the dominant point $c_1(1,0,0)$, where $c_1 = 1$, is the same for each polytope containing it within its structure, we do not repeat it.

	$\mathcal{V}_{H_3}(1,0,0)$			
	Orbit $c_3(0,0,1)$			
G'	μ	$R^2(\mu')$	$N[R^2(\mu')]$	N_p
H_2	$(\frac{\tau}{2}+1,0,3\tau-4)$	$36.2-21.7\tau$	1.056	5
	$(\frac{3\tau}{2}-2,0,3-\tau)$	$14.5-7.2\tau$	2.764	5
	$(2-\frac{3\tau}{2},3-\tau,0)$	$14.5-7.2\tau$	2.764	5
	$(-\frac{\tau}{2}-1,3\tau-4,0)$	$36.2-21.7\tau$	1.056	5
$A_1 \times A_1$	$(0,2+\tau,3\tau-4)$	$12.5-7.5\tau$	0.365	2
	$(3-\tau,2\tau-1,3-\tau)$	$10-5\tau$	1.910	4
	$(2\tau-1,3-\tau,0)$	2.5	2.5	2
	$(3\tau-4,0,2\tau-1)$	$15-7.5\tau$	2.865	4
	$(2\tau-1,\tau-3,0)$	2.5	2.5	2
	$(3-\tau,1-2\tau,3-\tau)$	$10-5\tau$	1.910	4
	$(0,-2-\tau,3\tau-4)$	$12.5-7.5\tau$	0.365	2
A_2	$(0,0,3\tau-\frac{3}{2})$	0	0	1
	$(0,3-\tau,\frac{5}{2})$	$6.7-3.3\tau$	1.273	3
	$(3-\tau,3\tau-4,\tau-\frac{1}{2})$	$13.3-6.7\tau$	2.546	6
	$(3\tau-4,3-\tau,\frac{1}{2}-\tau)$	$13.3-6.7\tau$	2.546	6
	$(3-\tau,0,-\frac{5}{2})$	$6.7-3.3\tau$	2.764	3
	$(0,0,\frac{3}{2}-3\tau)$	0	0	1

Table B.1. The orbit decomposition of the polytope $\mathcal{V}_{H_3}(1,0,0)$.

	$\mathcal{V}_{H_3}(0,0,1)$			
	Orbit $c_1(1,0,0)$			
G'	μ	$R^2(\mu')$	$N[R^2(\mu')]$	N_p
H_2	$(1+\frac{\tau}{2},0,0)$	0	0	1
	$(\frac{\tau}{2},1,0)$	1.45	1.45	5
	$(-\frac{\tau}{2},0,1)$	1.45	1.45	5
	$(-1-\frac{\tau}{2},0,0)$	0	0	1
$A_1\times A_1$	$(1,\tau+1,0)$	0.5	0.5	2
	$(0,\tau,\tau)$	$0.5+0.5\tau$	1.309	2
	$(\tau,0,1)$	$1+0.5\tau$	1.809	4
	$(0,-\tau,\tau)$	$0.5+0.5\tau$	1.309	2
	$(1,-\tau-1,0)$	0.5	0.5	2
A_2	$(1,0,\tau+\frac{1}{2})$	0.667	0.667	3
	$(0,\tau,\frac{1}{2})$	$0.7+0.7\tau$	1.735	3
	$(\tau,0,-\frac{1}{2})$	$0.7+0.7\tau$	1.735	3
	$(0,1,-\tau-\frac{1}{2})$	0.667	0.667	3

Table B.2. The orbit decomposition of the polytope $\mathcal{V}_{H_3}(0,0,1)$.

	$\mathcal{V}_{H_3}(0,1,0)$			
	Orbit $c_3(0,0,1)$			
G'	μ	$R^2(\mu')$	$N[R^2(\mu')]$	N_p
H_2	$(\frac{\tau}{2}+\frac{1}{2},0,\tau-1)$	$2.9-1.5\tau$	0.553	5
	$(\frac{\tau}{2}-\frac{1}{2},0,1)$	1.45	1.45	5
	$(\frac{\tau}{2}-\frac{1}{2},1,0)$	1.45	1.45	5
	$(-\frac{\tau}{2}-\frac{1}{2},\tau-1,0)$	$2.9-1.5\tau$	0.553	5
$A_1\times A_1$	$(0,1+\tau,\tau-1)$	$1-0.5\tau$	0.191	2
	$(1,\tau,1)$	1	1	4
	$(\tau,1,0)$	$0.5+0.5\tau$	1.309	2
	$(\tau-1,0,\tau)$	1.5	1.5	4
	$(\tau,-1,0)$	$0.5+0.5\tau$	1.309	2
	$(1,-\tau,1)$	1	1	4
	$(0,-1-\tau,\tau-1)$	$1-0.5\tau$	1.309	2
A_2	$(0,0,\frac{3}{2}\tau)$	0	0	3
	$(0,1,\tau+\frac{1}{2})$	0.667	0.667	3
	$(1,\tau-1,\frac{\tau}{2})$	1.333	1.333	6
	$(\tau-1,1,-\frac{\tau}{2})$	1.333	1.333	6
	$(1,0,-\frac{\tau}{2}-1)$	0.667	0.667	3
	$(0,0,-\frac{3}{2}\tau)$	0	0	3

Table B.3. The orbit decomposition of the polytope $\mathcal{V}_{H_3}(0,1,0)$.

	$\mathcal{V}_{H_3}(1,1,0)$			
	Orbit $c_3(0,0,1)$			
G'	μ	$R^2(\mu')$	$N[R^2(\mu')]$	N_p
H_2	$\frac{1}{6}(3\tau+4,0,10\tau-12)$	$9.8-5.6\tau$	0.702	5
	$\frac{1}{6}(5\tau-6,0,10-6\tau)$	$4.2-1.45\tau$	1.839	5
	$\frac{1}{6}(6-5\tau,10-6\tau,0)$	$4.2-1.45\tau$	1.839	5
	$\frac{1}{6}(-3\tau-4,10\tau-12,0)$	$9.8-5.6\tau$	0.702	5
$A_1\times A_1$	$\frac{1}{3}(0,3\tau+4,5\tau-6)$	$3.4-1.9\tau$	0.243	2
	$\frac{1}{3}(5-\tau,4\tau-3,5-\tau)$	$2.9-\tau$	1.271	4
	$\frac{1}{3}(4\tau-1,5-\tau,0)$	$0.9+0.4\tau$	1.664	2
	$\frac{1}{3}(5\tau-6,0,4\tau-1)$	$4.3-1.5\tau$	1.906	4
	$\frac{1}{3}(4\tau-1,\tau-5,0)$	$0.9+0.4\tau$	1.664	2
	$\frac{1}{3}(5-\tau,3-4\tau,5-\tau)$	$2.9-\tau$	1.271	4
	$\frac{1}{3}(0,-3\tau-4,5\tau-6)$	$3.4-1.9\tau$	0.243	2
A_2	$\frac{1}{6}(0,0,12\tau-3)$	0	0	3
	$\frac{1}{6}(0,10-2\tau,2\tau+9)$	$1.9-0.7\tau$	0.847	3
	$\frac{1}{6}(10-2\tau,10\tau-12,4\tau-1)$	$3.9-1.3\tau$	1.695	6
	$\frac{1}{6}(10\tau-12,10-2\tau,1-4\tau)$	$3.9-1.3\tau$	1.695	6
	$\frac{1}{6}(10-2\tau,0,-2\tau-9)$	$1.9-0.7\tau$	0.847	3
	$\frac{1}{6}(0,0,3-12\tau)$	0	0	3

Table B.4. The orbit decomposition of the polytope $\mathcal{V}_{H_3}(1,1,0)$.

	$\mathcal{V}_{H_3}(0,1,1)$			
	Orbit $c_3(0,0,1)$			
G'	μ	$R^2(\mu')$	$N[R^2(\mu')]$	N_p
H_2	$\frac{1}{11}(\frac{13\tau}{2}+3,0,8-\tau)$	$0.8-0.2\tau$	0.487	5
	$\frac{1}{11}(4-\frac{\tau}{2},0,7\tau-1)$	$0.6+0.4\tau$	1.275	5
	$\frac{1}{11}(\frac{\tau}{2}-4,0,7\tau-1)$	$0.6+0.4\tau$	1.275	5
	$\frac{1}{11}(-\frac{13\tau}{2}-3,0,8-\tau)$	$0.8-0.2\tau$	0.487	5
$A_1\times A_1$	$\frac{1}{11}(13\tau+6,0,8-\tau)$	$0.3-0.1\tau$	0.168	4
	$\frac{1}{11}(6\tau+7,7\tau-1,7\tau-1)$	$0.4+0.3\tau$	0.881	4
	$\frac{1}{11}(7\tau+1,6\tau+7,0)$	$0.4+0.5\tau$	1.154	2
	$\frac{1}{11}(0,8-\tau,7+6\tau)$	$0.6+0.4\tau$	1.322	2
	$\frac{1}{11}(-7\tau-1,6\tau+7,0)$	$0.4+0.5\tau$	1.154	2
	$\frac{1}{11}(-6\tau-7,7\tau-1,7\tau-1)$	$0.4+0.3\tau$	0.881	4
	$(\frac{1}{11}(-13\tau-6,0,8-\tau))$	$0.3-0.1\tau$	0.168	4
A_2	$\frac{9}{22}(0,0,18\tau+21)$	0	0	1
	$\frac{1}{11}(0,7\tau-1,10+8\tau)$	$0.3+0.2\tau$	0.588	3
	$\frac{1}{11}(7\tau-1,8-\tau,12\tau+14)$	$0.6+0.4\tau$	1.175	6
	$\frac{1}{11}(7\tau-1,8-\tau,-12\tau-14)$	$0.6+0.4\tau$	1.175	6
	$\frac{1}{11}(0,7\tau-1,-10-8\tau)$	$0.3+0.2\tau$	0.588	3
	$\frac{9}{22}(0,0,-18\tau-21)$	0	0	1

Table B.5. The orbit decomposition of the polytope $\mathcal{V}_{H_3}(0,1,1)$.

	$\mathcal{V}_{H_3}(1,0,1)$			
	Orbit $c_2(0,1,0)$			
G'	μ	$R^2(\mu')$	$N[R^2(\mu')]$	N_p
H_2	$\frac{3}{2}(1,2-\tau,0)$	$16.3-9.8\tau$	0.475	5
	$\frac{3}{2}(\tau-1,0,\tau-1)$	$6.5-3.3\tau$	1.244	5
	$\frac{3}{2}(0,2-\tau,2-\tau)$	$29-16.8\tau$	1.719	10
	$\frac{3}{2}(1-\tau,\tau-1,0)$	$6.5-3.3\tau$	1.244	5
	$\frac{3}{2}(-1,0,2-\tau)$	$16.3-9.8\tau$	0.475	5
$A_1\times A_1$	$\frac{3}{2}(0,2,0)$	0	0	1
	$\frac{3}{2}(2-\tau,\tau,\tau-1)$	$7.9-4.5\tau$	0.594	4
	$\frac{3}{2}(1,1,2-\tau)$	$6.8-3.4\tau$	1.289	4
	$\frac{3}{2}(\tau-1,\tau-1,1)$	$3.4-1.1\tau$	1.555	4
	$\frac{3}{2}(2\tau-2,0,0)$	$9-4.5\tau$	1.719	2
	$\frac{3}{2}(0,0,2\tau-2)$	$9-4.5\tau$	1.719	2
	$\frac{3}{2}(\tau-1,1-\tau,1)$	$3.4-1.1\tau$	1.555	4
	$\frac{3}{2}(1,-1,2-\tau)$	$6.8-3.4\tau$	1.289	4
	$\frac{3}{2}(2-\tau,-\tau,-2)$	$7.9-4.5\tau$	0.594	4
	$\frac{3}{2}(0,-2,0)$	0	0	2
A_2	$\frac{3}{2}(0,2-\tau,\tau)$	$7.5-4.5\tau$	0.219	3
	$\frac{3}{2}(2-\tau,\tau-1,1)$	$6-3\tau$	1.459	6
	$\frac{3}{2}(1,0,\tau-1)$	1.5	1.5	3
	$\frac{3}{2}(\tau-1,\tau-1,0)$	$9-4.5\tau$	1.719	6
	$\frac{3}{2}(0,1,1-\tau)$	1.5	1.5	3
	$\frac{3}{2}(\tau-1,2-\tau,-1)$	$6-3\tau$	1.459	6
	$\frac{3}{2}(2-\tau,0,-\tau)$	$7.5-4.5\tau$	0.219	3
	Orbit $c_3(0,0,1)$			
H_2	$\frac{3}{22}(2+5\tau,0,8-2\tau)$	$1.8-0.8\tau$	0.612	5
	$\frac{3}{22}(4-\tau,0,6\tau-2)$	$1.1-0.3\tau$	1.599	5
	$\frac{3}{22}(\tau-4,6\tau-2,0)$	$1.1-0.3\tau$	1.599	5
	$\frac{3}{22}(-2-5\tau,8-2\tau,0)$	$1.8-0.8\tau$	0.612	5
$A_1\times A_1$	$\frac{3}{11}(0,2+5\tau,4-\tau)$	$0.6-0.3\tau$	0.211	2
	$\frac{3}{11}(3\tau-1,3+2\tau,3\tau-1)$	$0.7+0.2\tau$	1.105	4
	$\frac{3}{11}(3+2\tau,3\tau-1,0)$	$0.5+0.6\tau$	1.446	2
	$\frac{3}{11}(4-\tau,0,3+2\tau)$	$1.1+0.3\tau$	1.657	4
	$\frac{3}{11}(3+2\tau,1-3\tau,0)$	$0.5+0.6\tau$	1.446	2
	$\frac{3}{11}(3\tau-1,-3-2\tau,3\tau-1)$	$0.7+0.2\tau$	1.105	4
	$\frac{3}{11}(0,-2-5\tau,4-\tau)$	$0.6-0.3\tau$	0.211	2
A_2	$\frac{3}{22}(0,0,9+6\tau)$	0	0	1
	$\frac{3}{22}(0,6\tau-2,1+8\tau)$	$0.5+0.1\tau$	0.737	3
	$\frac{3}{22}(6\tau-2,8-2\tau,3+2\tau)$	$1+0.3\tau$	1.473	6
	$\frac{3}{22}(8-2\tau,-2+6\tau,-3-2\tau)$	$1+0.3\tau$	1.473	6
	$\frac{3}{22}(6\tau-2,0,-1-8\tau)$	$0.5+0.1\tau$	0.737	3
	$\frac{3}{22}(0,0,-9-6\tau)$	0	0	1

Table B.6. The orbit decomposition of the polytope $\mathcal{V}_{H_3}(1,0,1)$.

	$\mathcal{V}_{H_3}(1,1,1)$			
	Orbit $c_2(0,1,0)$			
G'	μ	$R^2(\mu')$	$N[R^2(\mu')]$	N_p
H_2	$\frac{1}{22}(10\tau+15, 20-5\tau, 0)$	$1.3-0.5\tau$	0.424	5
	$\frac{1}{22}(15\tau-5, 0, 15\tau-5)$	$0.8+0.2\tau$	1.110	5
	$\frac{1}{22}(0, 20\tau-5, 20\tau-5)$	$2.5-0.6\tau$	1.535	10
	$\frac{1}{22}(5-15\tau, 15\tau-5, 0)$	$0.8+0.2\tau$	1.110	5
	$\frac{1}{22}(-10\tau-15, 0, 20-5\tau)$	$1.3-0.5\tau$	0.424	5
$A_1\times A_1$	$\frac{1}{22}(0, 30+20\tau, 0)$	0	0	1
	$\frac{1}{22}(20-5\tau, 25\tau+10, 15\tau-5)$	$0.7+0.1\tau$	0.530	4
	$\frac{1}{22}(10\tau+15, 10\tau+15, 20-5\tau)$	$0.8+0.2\tau$	1.151	4
	$\frac{1}{22}(15\tau-5, 15\tau-5, 10\tau+15)$	$0.6+0.5\tau$	1.388	4
	$\frac{1}{22}(30\tau-10, 0, 0)$	$1+0.3\tau$	1.535	2
	$\frac{1}{22}(0, 0, 30\tau-10)$	$1+0.3\tau$	1.535	2
	$\frac{1}{22}(15\tau-5, 5-15\tau, 10\tau+15)$	$0.6+0.5\tau$	1.388	4
	$\frac{1}{22}(10\tau+15, 10\tau-15, 20-5\tau)$	$0.8+0.2\tau$	1.151	4
	$\frac{1}{22}(20-5\tau, -10-25\tau, 15\tau-5)$	$0.7+0.1\tau$	0.530	4
	$\frac{1}{22}(0, -30-20\tau, 0)$	0	0	1
A_2	$\frac{1}{22}(0, 20-5\tau, 25\tau+10)$	$0.6-0.2\tau$	0.195	3
	$\frac{1}{22}(20-5\tau, 15\tau-5, 10\tau+15)$	$0.7+0.2\tau$	1.023	6
	$\frac{1}{22}(10\tau+15, 0, 15\tau-5)$	$0.4+0.6\tau$	1.339	3
	$\frac{1}{22}(15\tau-5, 15\tau-5, 0)$	$1+0.3\tau$	1.535	6
	$\frac{1}{22}(0, 10\tau+15, 5-15\tau)$	$0.4+0.6\tau$	1.339	3
	$\frac{1}{22}(15\tau-5, 20-5\tau, -10\tau-15)$	$0.7+0.2\tau$	1.023	6
	$\frac{1}{22}(20-5\tau, 0, -25\tau-10)$	$0.6-0.2\tau$	0.195	3
	Orbit $c_3(0,0,1)$			
H_2	$\frac{1}{6}(10-\tau, 0, 10\tau-10)$	$8-4\tau$	1.536	5
	$\frac{1}{6}(5\tau, 0, 20-10\tau)$	$20.1-12.1\tau$	0.587	5
	$\frac{1}{6}(5\tau-10, 10\tau-10, 0)$	$8-4\tau$	1.536	5
	$\frac{1}{6}(-5\tau, 20-10\tau, 0)$	$20.1-12.1\tau$	0.587	5
$A_1\times A_1$	$\frac{1}{3}(0, 5\tau, 10-5\tau)$	$6.9-4.2\tau$	0.203	2
	$\frac{1}{3}(5\tau-5, 5, 5\tau-5)$	$5.6-2.8\tau$	1.061	4
	$\frac{1}{3}(5, 5\tau-5, 0)$	1.389	1.389	2
	$\frac{1}{3}(10-5\tau, 0, 5)$	$8.3-4.2\tau$	1.592	4
	$\frac{1}{3}(5, 5-5\tau, 0)$	1.389	1.389	2
	$\frac{1}{3}(5\tau-5, -5, 5\tau-5)$	$5.6-2.8\tau$	1.061	4
	$\frac{1}{3}(0, -5\tau, 10-5\tau)$	$6.9-4.2\tau$	0.203	2
A_2	$\frac{1}{6}(0, 0, 15)$	0	0	1
	$\frac{1}{6}(0, 10\tau-10, 10\tau-5)$	$3.7-1.9\tau$	0.707	3
	$\frac{1}{6}(10\tau-10, 20\tau-10, 5)$	$7.4-3.7\tau$	1.415	6
	$\frac{1}{6}(20-10\tau, 10\tau-10, -5)$	$7.4-3.7\tau$	1.415	6
	$\frac{1}{6}(10\tau-10, 0, 5-10\tau)$	$3.7-1.9\tau$	0.707	3
	$\frac{1}{6}(0, 0, -15)$	0	0	1

Table B.7. The orbit decomposition of the polytope $\mathcal{V}_{H_3}(1,1,1)$.

Appendix C

The ‘pancake’-structures of $\mathcal{V}_{A_3}(\lambda)-$polytopes

In Figures C.1−C.7, the polytopes $\mathcal{V}_{A_3}(\lambda)$ are viewed from the direction orthogonal to the simple roots α_k, $k \in \{1,2,3\}$. The polytopes of $\mathcal{V}_{A_3}(\lambda)$ are presented in the top row. The corresponding ‘pancake’-structures with respect to each $W' \subset A_3$ are shown in the bottom row. The numbers on the left of each ‘pancake’ stand for the numbers of points of the two-dimensional orbits. The values on the right correspond to the α_k-coordinates that provide the spacing between the ‘pancakes’. For clarity, the points of generic orbits are depicted by black, green and orange colors. The bold segments indicate the symmetry-breaking path for a considered $\mathcal{V}_{A_3}(\lambda)-$polytope.

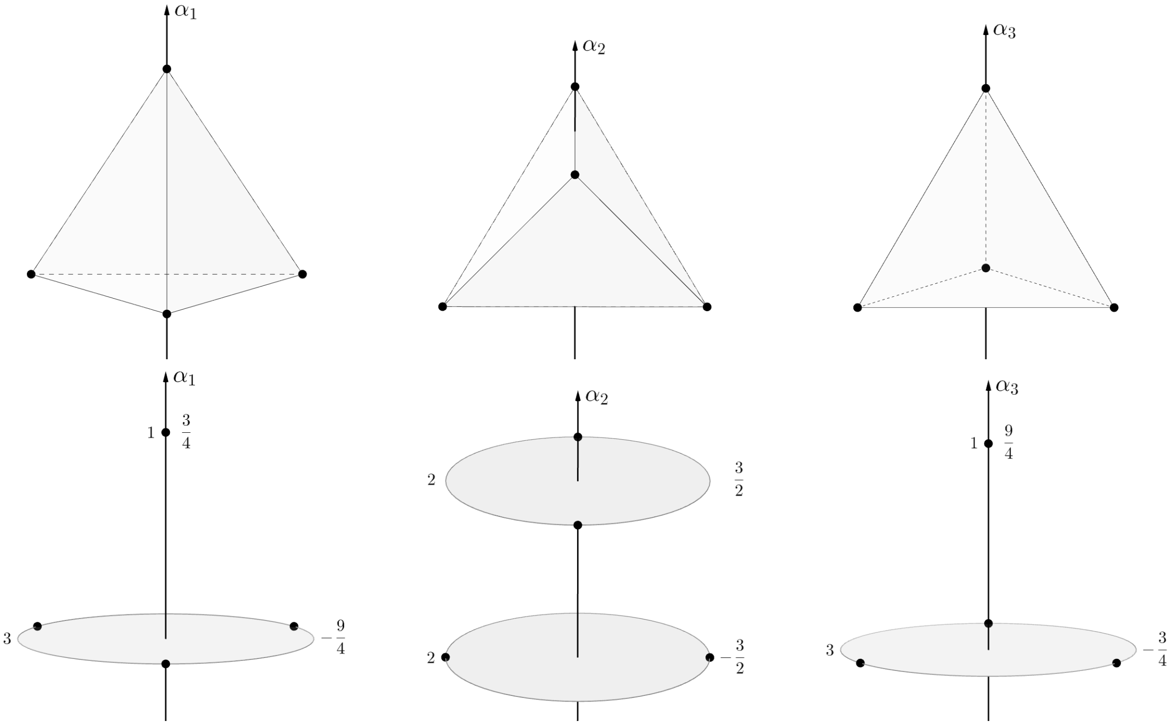

Fig. C.1. The polytope $\mathcal{V}_{A_3}(1,0,0)$ is oriented in the direction of the simple roots α_1, α_2 and α_3. The points of the orbit $O_{A_3}(0,0,c')$ are depicted by black color.

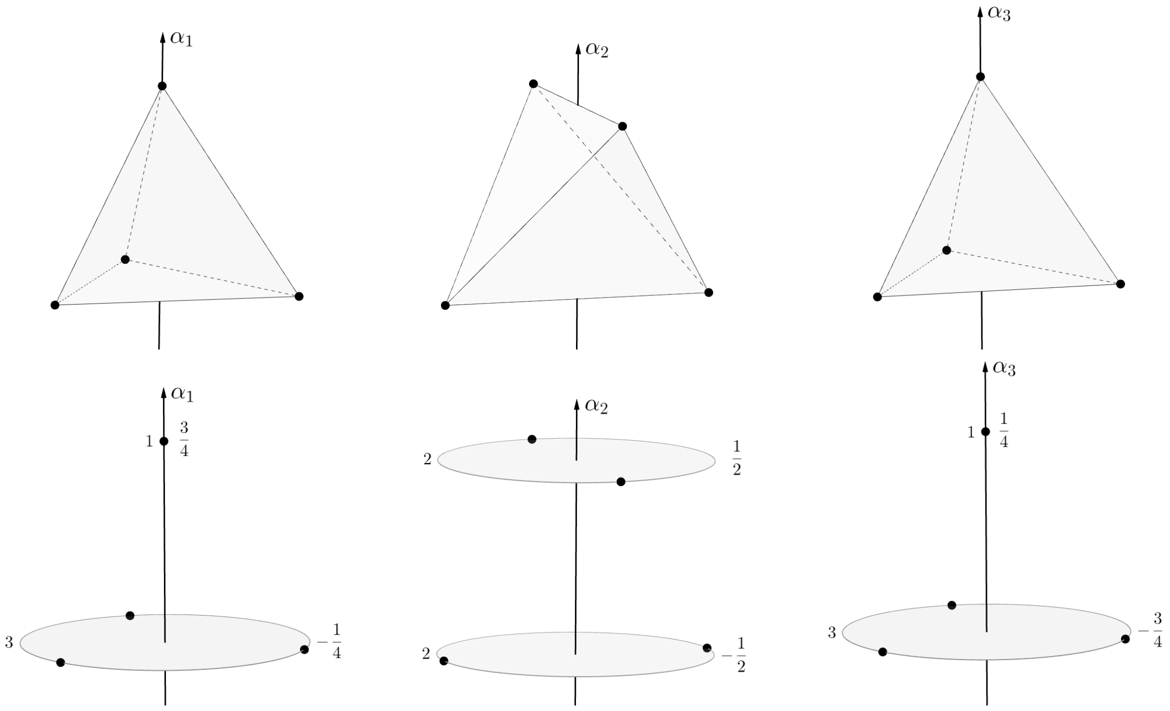
α_1
α_2
α_3
α_1
1
$\frac{3}{4}$
3
$-\frac{1}{4}$
α_2
2
$\frac{1}{2}$
2
$-\frac{1}{2}$
α_3
1
$\frac{1}{4}$
3
$-\frac{3}{4}$

Fig. C.2. The polytope $\mathcal{V}_{A_3}(0,0,1)$ is oriented in the direction of the simple roots α_1, α_2 and α_3. The points of the orbit $O_{A_3}(a',0,0)$ are depicted by black color.

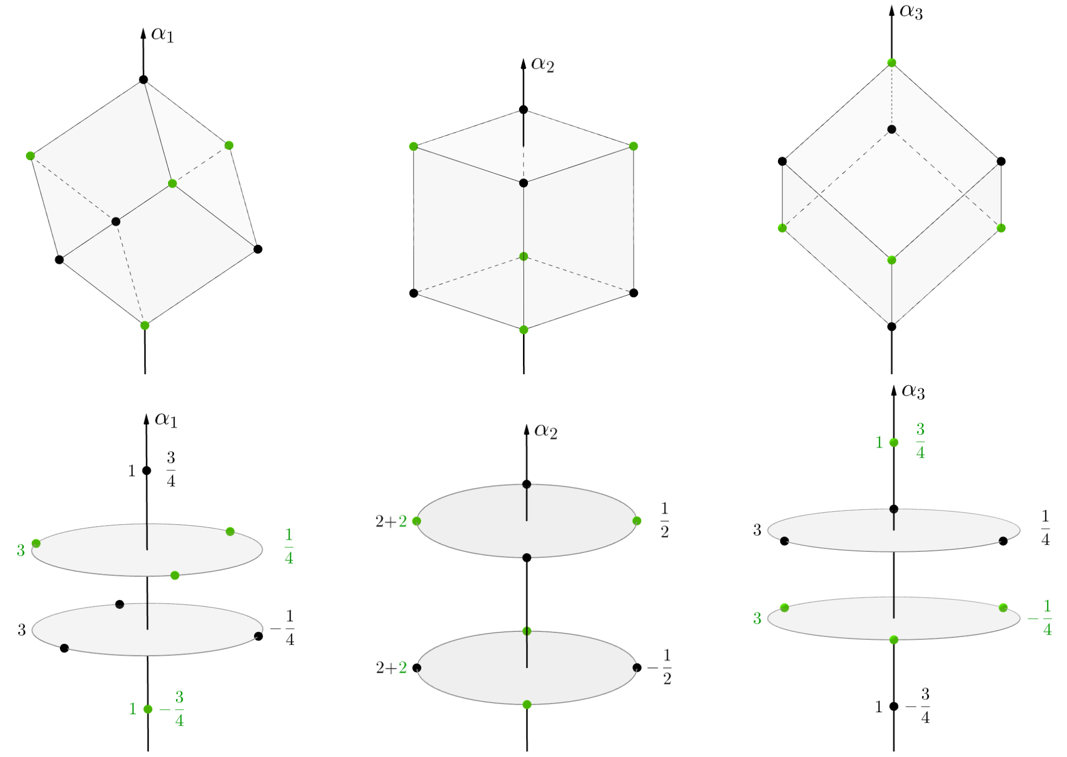
α_1
α_2
α_3
α_1
1
$\frac{3}{4}$
3
$\frac{1}{4}$
3
$-\frac{1}{4}$
1
$-\frac{3}{4}$
α_2
2+2
$\frac{1}{2}$
2+2
$-\frac{1}{2}$
α_3
1
$\frac{3}{4}$
3
$\frac{1}{4}$
3
$-\frac{1}{4}$
1
$-\frac{3}{4}$

Fig. C.3. The polytope $\mathcal{V}_{A_3}(0,1,0)$ is oriented in the direction of the simple roots α_1, α_2 and α_3. The points of the orbits $O_{A_3}(a',0,0)$ and $O_{A_3}(0,0,c')$ are depicted by green and black colors, respectively.

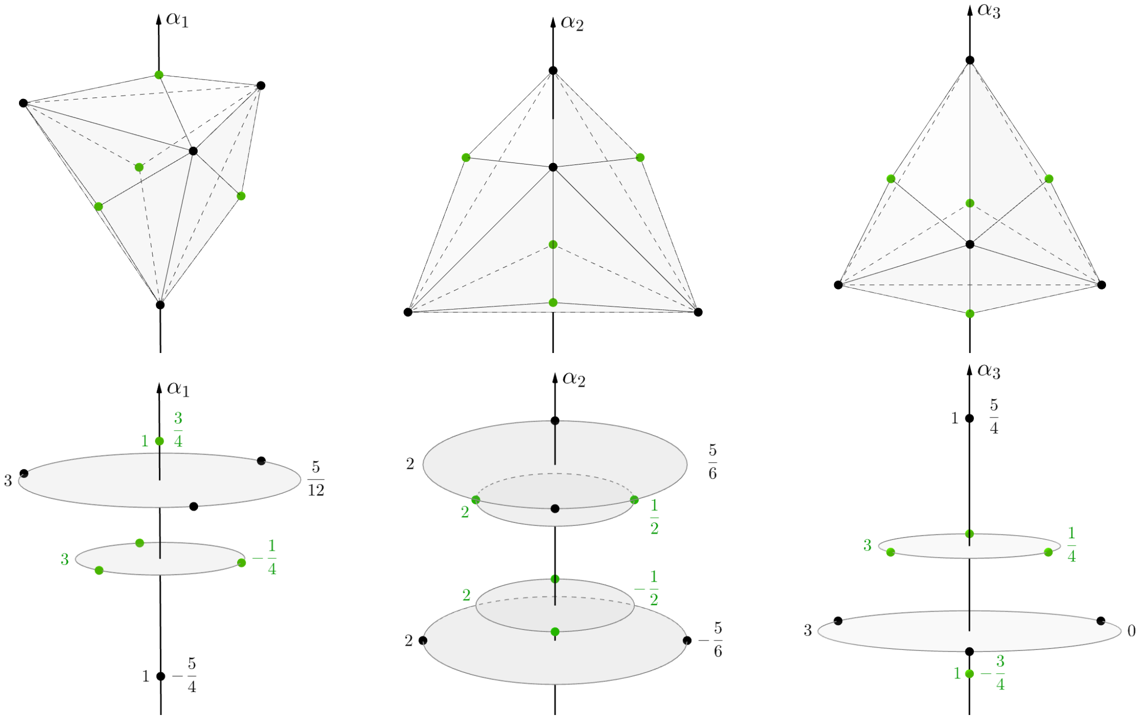
α_1
α_2
α_3
α_1
1 $\frac{3}{4}$
3 $\frac{5}{12}$
3 $-\frac{1}{4}$
1 $-\frac{5}{4}$
α_2
2 $\frac{5}{6}$
2 $\frac{1}{2}$
2 $-\frac{1}{2}$
2 $-\frac{5}{6}$
α_3
1 $\frac{5}{4}$
3 $\frac{1}{4}$
3 0
1 $-\frac{3}{4}$

Fig. C.4. The polytope $\mathcal{V}_{A_3}(1,1,0)$ is oriented in the direction of the simple roots α_1, α_2 and α_3. The points of the orbits $O_{A_3}(a',0,0)$ and $O_{A_3}(0,0,c')$ are depicted by green and black colors, respectively.

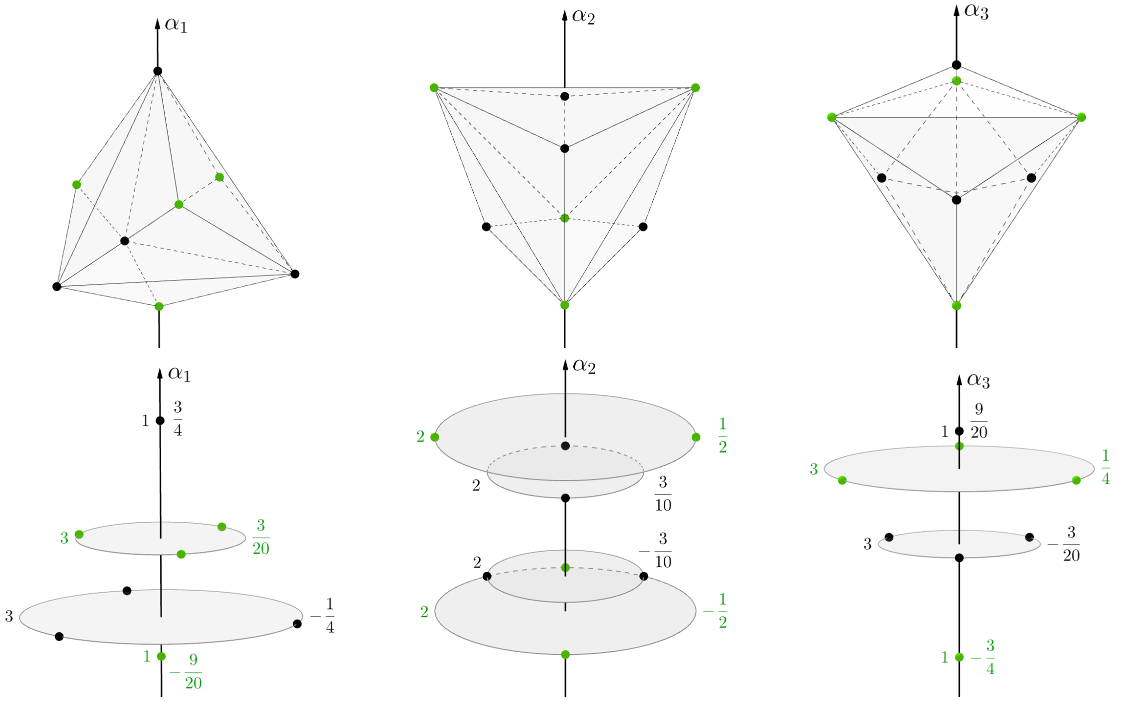
α_1
α_2
α_3
α_1
1 $\frac{3}{4}$
3 $\frac{3}{20}$
3 $-\frac{1}{4}$
1 $-\frac{9}{20}$
α_2
2 $\frac{1}{2}$
2 $\frac{3}{10}$
2 $-\frac{3}{10}$
2 $-\frac{1}{2}$
α_3
1 $\frac{9}{20}$
3 $\frac{1}{4}$
3 $-\frac{3}{20}$
1 $-\frac{3}{4}$

Fig. C.5. The polytope $\mathcal{V}_{A_3}(0,1,1)$ is oriented in the direction of the simple roots α_1, α_2 and α_3. The points of the orbits $O_{A_3}(a',0,0)$ and $O_{A_3}(0,0,c')$ are depicted by green and black colors, respectively.

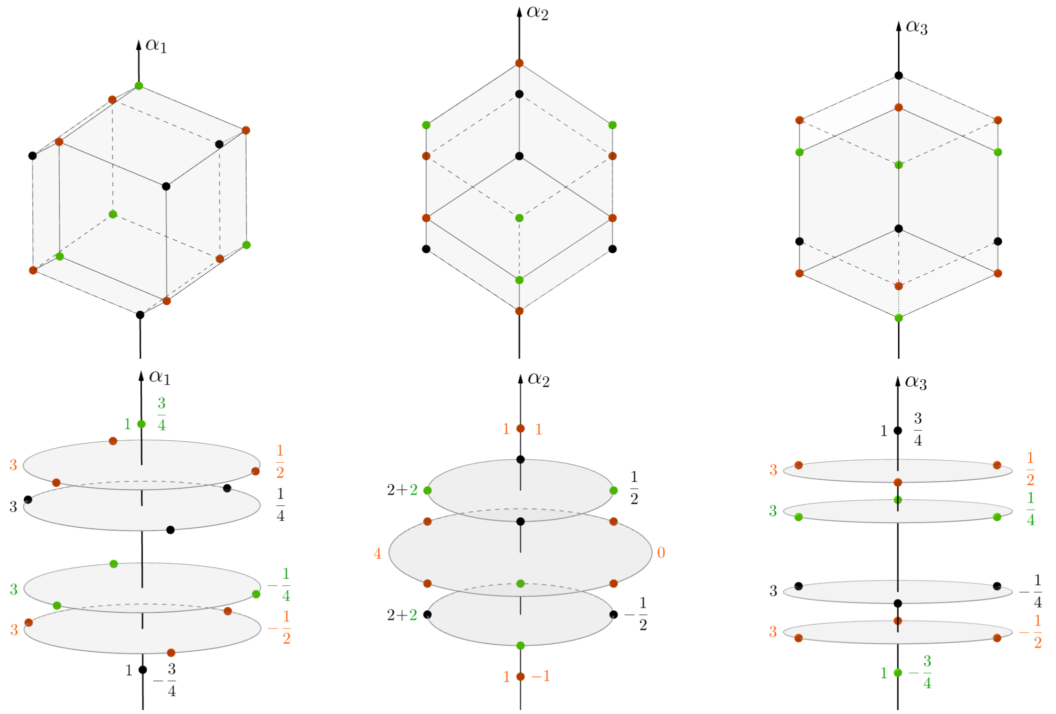

α_1
α_2
α_3
α_1
1 $\frac{3}{4}$
3 $\frac{1}{2}$
3 $\frac{1}{4}$
3 $-\frac{1}{4}$
3 $-\frac{1}{2}$
1 $-\frac{3}{4}$
α_2
1 1
2+2 $\frac{1}{2}$
4 0
2+2 $-\frac{1}{2}$
1 −1
α_3
1 $\frac{3}{4}$
3 $\frac{1}{2}$
3 $\frac{1}{4}$
3 $-\frac{1}{4}$
3 $-\frac{1}{2}$
1 $-\frac{3}{4}$

Fig. C.6. The polytope $\mathcal{V}_{A_3}(1,0,1)$ is oriented in the direction of the simple roots α_1, α_2 and α_3. The points of the orbits $O_{A_3}(a',0,0)$, $O_{A_3}(0,b',0)$ and $O_{A_3}(0,0,c')$ are depicted by green, orange and black colors, respectively.

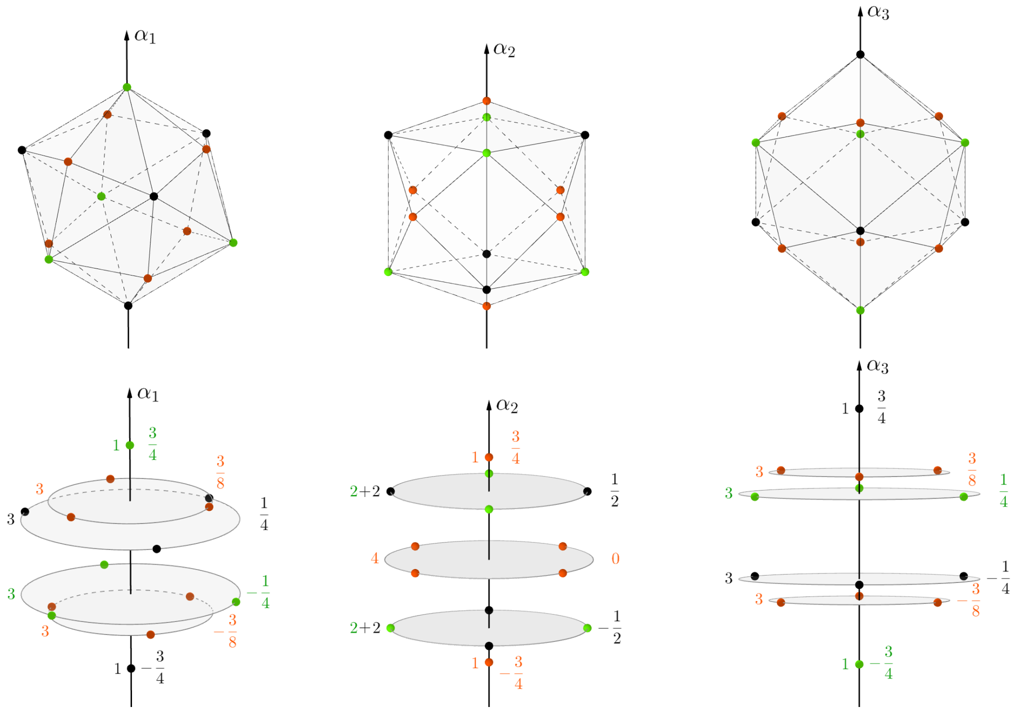

α_1
α_2
α_3
α_1
1 $\frac{3}{4}$
3 $\frac{3}{8}$
3 $\frac{1}{4}$
3 $-\frac{1}{4}$
3 $-\frac{3}{8}$
1 $-\frac{3}{4}$
α_2
1 $\frac{3}{4}$
2+2 $\frac{1}{2}$
4 0
2+2 $-\frac{1}{2}$
1 $-\frac{3}{4}$
α_3
1 $\frac{3}{4}$
3 $\frac{3}{8}$
3 $\frac{1}{4}$
3 $-\frac{1}{4}$
3 $-\frac{3}{8}$
1 $-\frac{3}{4}$

Fig. C.7. The polytope $\mathcal{V}_{A_3}(1,1,1)$ is oriented in the direction of the simple roots α_1, α_2 and α_3. The points of the orbits $O_{A_3}(a',0,0)$, $O_{A_3}(0,b',0)$ and $O_{A_3}(0,0,c')$ are depicted by green, orange and black colors, respectively.

Appendix D

The ‘pancake’-structures of $\mathcal{V}_{B_3}(\lambda)-$polytopes

In Figures D.1−D.7, the polytopes $\mathcal{V}_{B_3}(\lambda)$ are viewed from the direction orthogonal to the simple roots α_k, $k \in \{1, 2, 3\}$. The polytopes of $\mathcal{V}_{B_3}(\lambda)$ are presented in the top row. The corresponding ‘pancake’-structures with respect to each $W' \subset B_3$ are shown in the bottom row. The numbers on the left of each ‘pancake’ stand for the numbers of points of the two-dimensional orbits. The values on the right correspond to the α_k-coordinates that provide the spacing between the ‘pancakes’. For clarity, the points of generic orbits are depicted by black, green and orange colors. The bold segments indicate the symmetry-breaking path for a considered $\mathcal{V}_{B_3}(\lambda)-$polytope.

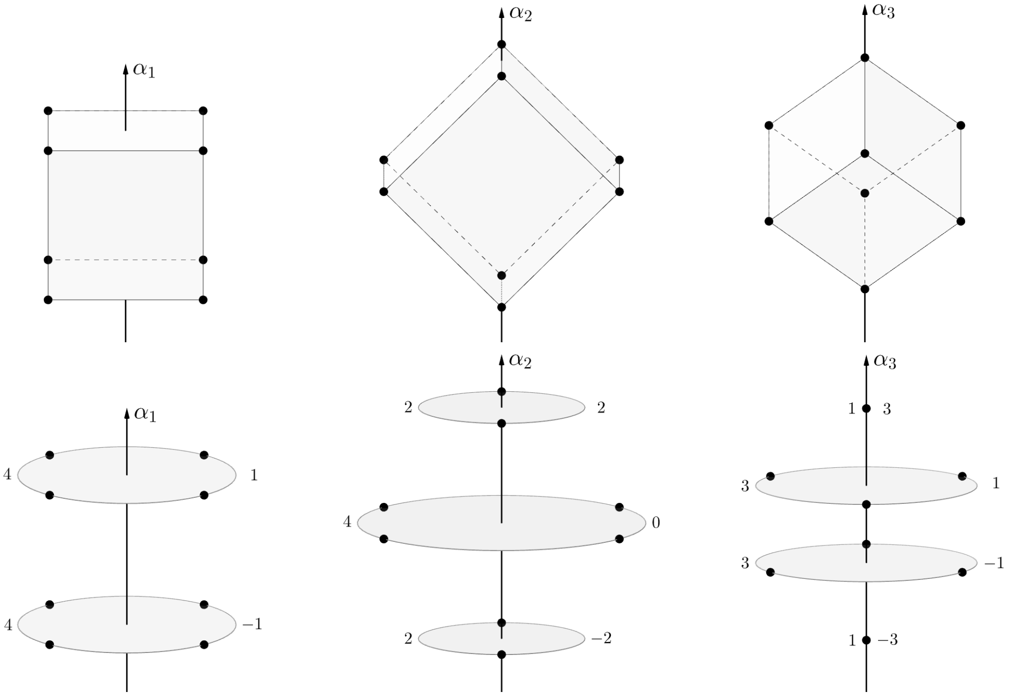

Fig. D.1. The polytope $\mathcal{V}_{B_3}(1, 0, 0)$ is oriented in the direction of the simple roots α_1, α_2 and α_3. The points of the orbit $O_{B_3}(c', 0, 0)$ are depicted by black color.

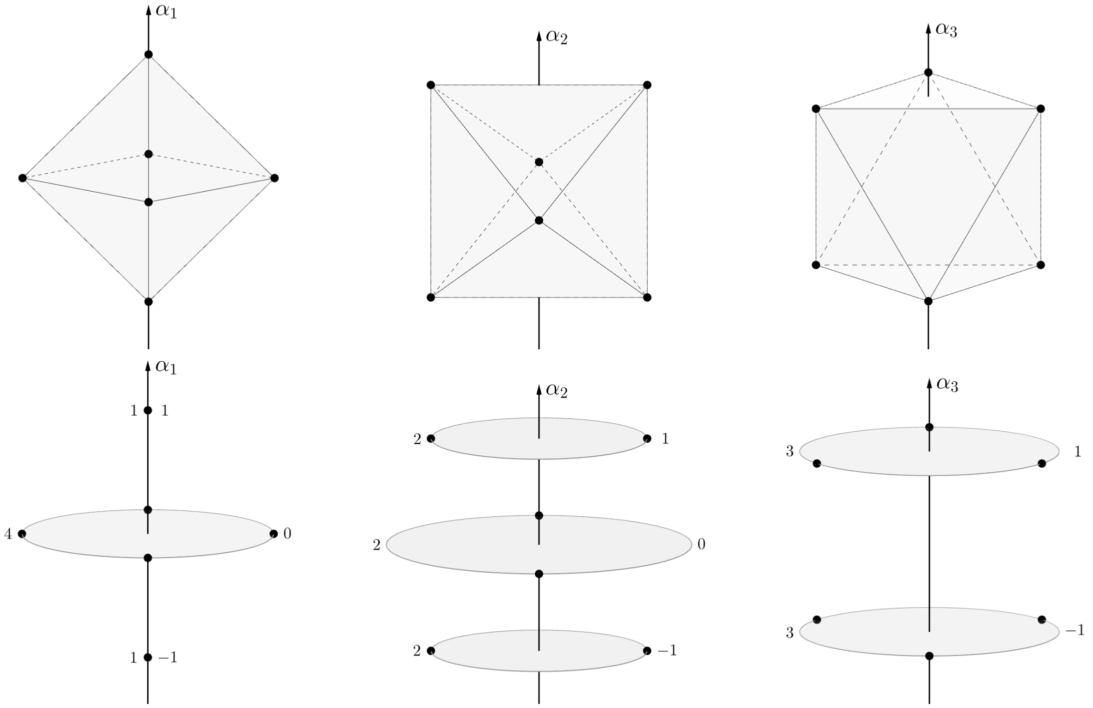
α_1
α_2
α_3
α_1
1 1
4 0
1 −1
α_2
2 1
2 0
2 −1
α_3
3 1
3 −1

Fig. D.2. The polytope $\mathcal{V}_{B_3}(0,0,1)$ is oriented in the direction of the simple roots α_1, α_2 and α_3. The points of the orbit $O_{B_3}(0,0,a')$ are depicted by black color.

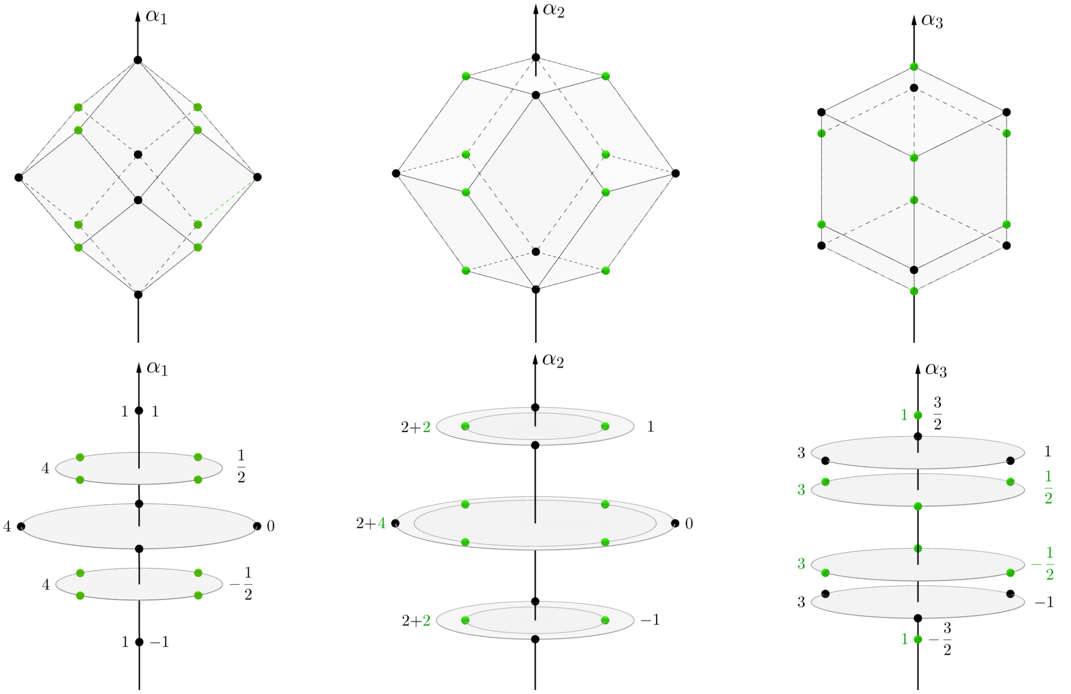
α_1
α_2
α_3
α_1
1 1
4 $\frac{1}{2}$
4 0
4 $-\frac{1}{2}$
1 −1
α_2
2+2 1
2+4 0
2+2 −1
α_3
1 $\frac{3}{2}$
3 1
3 $\frac{1}{2}$
3 $-\frac{1}{2}$
3 −1
1 $-\frac{3}{2}$

Fig. D.3. The polytope $\mathcal{V}_{B_3}(0,1,0)$ is oriented in the direction of the simple roots α_1, α_2 and α_3. The points of the orbits $O_{B_3}(a',0,0)$ and $O_{B_3}(0,0,c')$ are depicted by black and green colors, respectively.

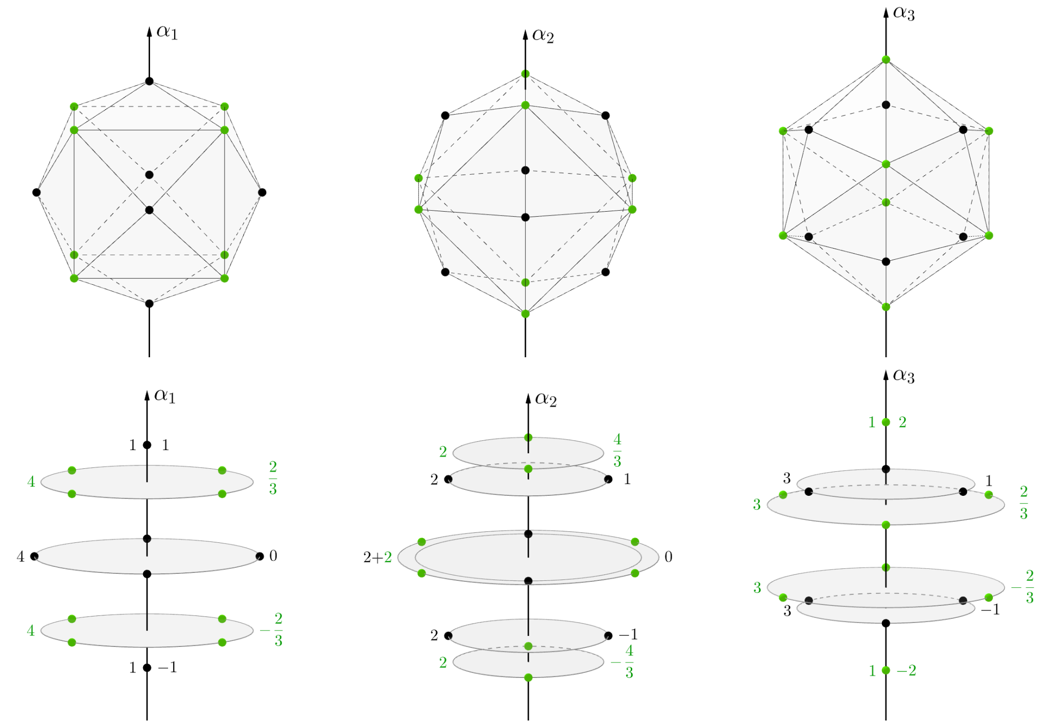
α_1
α_2
α_3
α_1
1
1
4
$\frac{2}{3}$
4
0
4
$-\frac{2}{3}$
1
-1
α_2
2
$\frac{4}{3}$
2
1
2+2
0
2
-1
2
$-\frac{4}{3}$
α_3
1
2
3
1
3
$\frac{2}{3}$
3
$-\frac{2}{3}$
3
-1
1
-2

Fig. D.4. The polytope $\mathcal{V}_{B_3}(1,1,0)$ is oriented in the direction of the simple roots α_1, α_2 and α_3. The points of the orbits $O_{B_3}(a',0,0)$ and $O_{B_3}(0,0,c')$ are depicted by black and green colors, respectively.

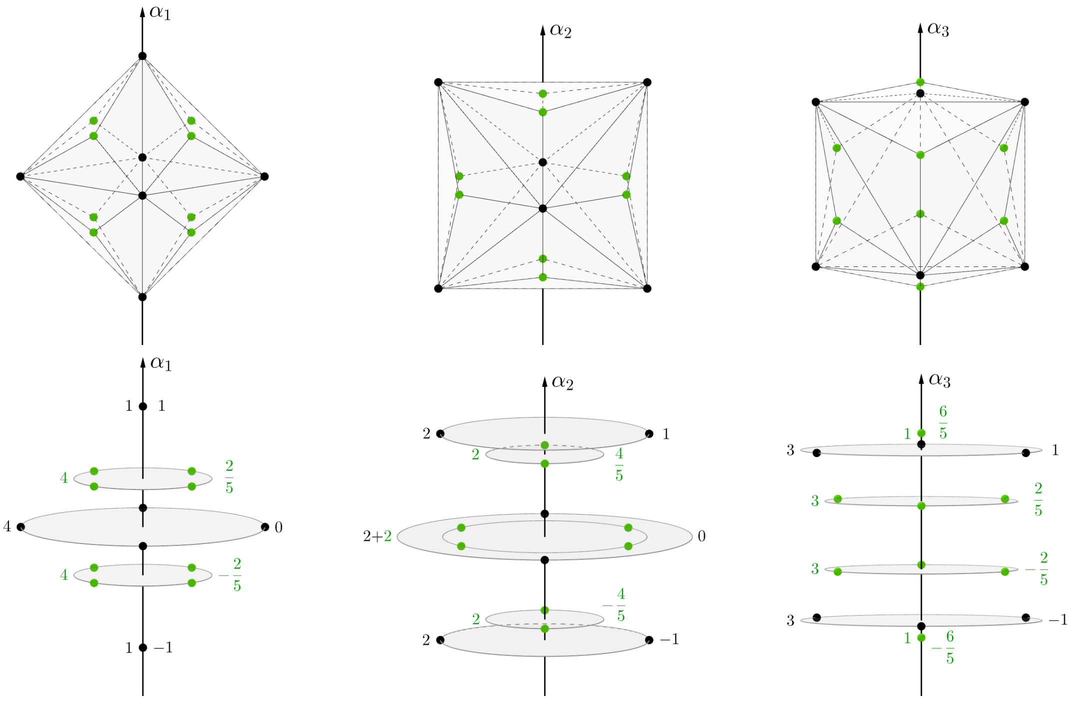
α_1
α_2
α_3
α_1
1
1
4
$\frac{2}{5}$
4
0
4
$-\frac{2}{5}$
1
-1
α_2
2
1
2
$\frac{4}{5}$
2+2
0
2
$-\frac{4}{5}$
2
-1
α_3
1
$\frac{6}{5}$
3
1
3
$\frac{2}{5}$
3
$-\frac{2}{5}$
3
-1
1
$-\frac{6}{5}$

Fig. D.5. The polytope $\mathcal{V}_{B_3}(0,1,1)$ is oriented in the direction of the simple roots α_1, α_2 and α_3. The points of the orbits $O_{B_3}(a',0,0)$ and $O_{B_3}(0,0,c')$ are depicted by black and green colors, respectively.

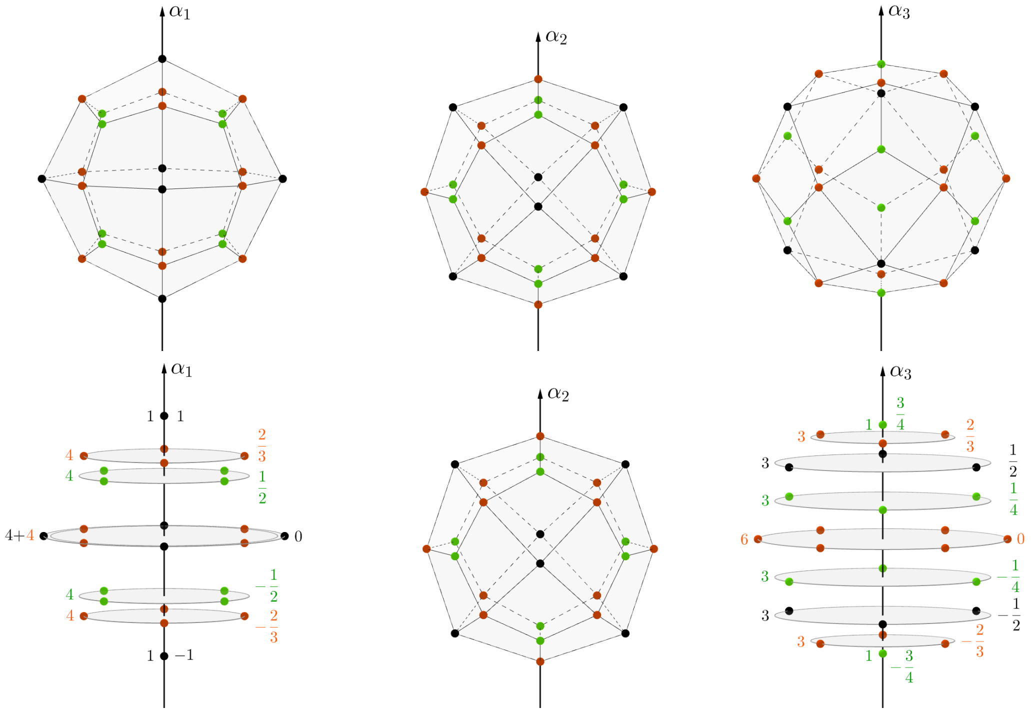
α_1
α_2
α_3
α_1
1 1
4 $\frac{2}{3}$
4 $\frac{1}{2}$
4+4 0
4 $-\frac{1}{2}$
4 $-\frac{2}{3}$
1 -1
α_2
α_3
1 $\frac{3}{4}$
3 $\frac{2}{3}$
3 $\frac{1}{2}$
3 $\frac{1}{4}$
6 0
3 $-\frac{1}{4}$
3 $-\frac{1}{2}$
3 $-\frac{2}{3}$
1 $-\frac{3}{4}$

Fig. D.6. The polytope $\mathcal{V}_{B_3}(1,0,1)$ is oriented in the direction of the simple roots α_1, α_2 and α_3. The points of the orbits $O_{B_3}(a',0,0)$, $O_{B_3}(0,b',0)$ and $O_{B_3}(0,0,c')$ are depicted by green, orange and black colors, respectively.

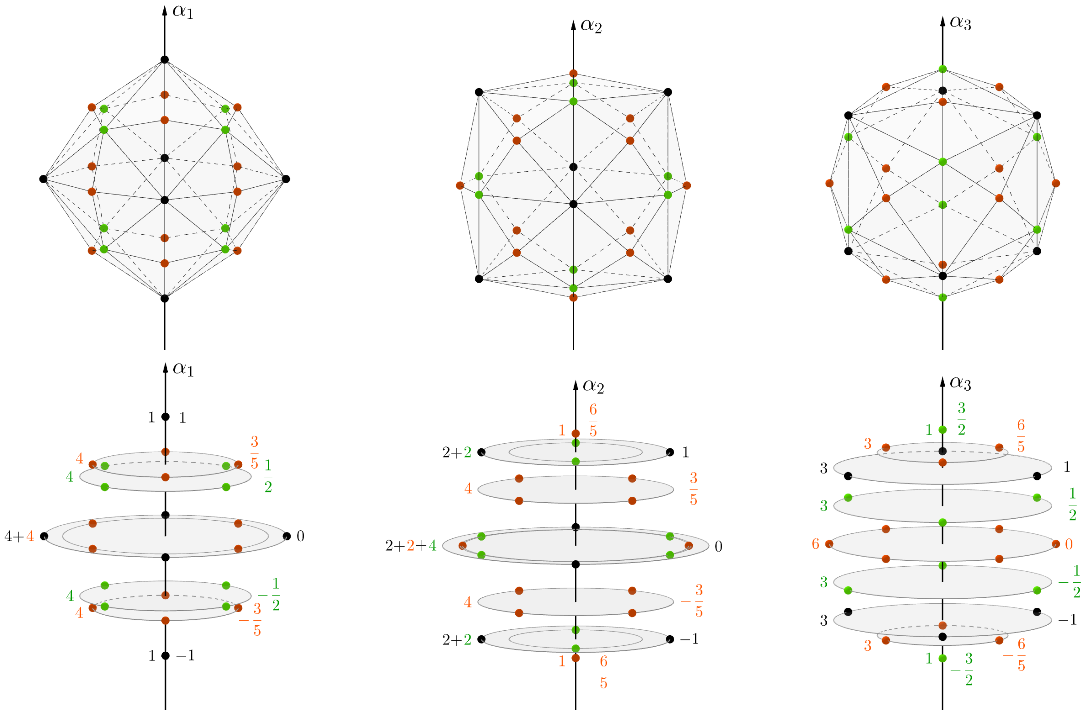
α_1
α_2
α_3
α_1
1 1
4 $\frac{3}{5}$
4 $\frac{1}{2}$
4+4 0
4 $-\frac{1}{2}$
4 $-\frac{3}{5}$
1 -1
α_2
1 $\frac{6}{5}$
2+2 1
4 $\frac{3}{5}$
2+2+4 0
4 $-\frac{3}{5}$
2+2 -1
1 $-\frac{6}{5}$
α_3
1 $\frac{3}{2}$
3 $\frac{6}{5}$
3 1
3 $\frac{1}{2}$
6 0
3 $-\frac{1}{2}$
3 -1
3 $-\frac{6}{5}$
1 $-\frac{3}{2}$

Fig. D.7. The polytope $\mathcal{V}_{B_3}(1,1,1)$ is oriented in the direction of the simple roots α_1, α_2 and α_3. The points of the orbits $O_{B_3}(a',0,0)$, $O_{B_3}(0,b',0)$ and $O_{B_3}(0,0,c')$ are depicted by green, orange and black colors, respectively.

Appendix E

Interpolation by splitting transforms (Mathematica code)

In Chapter 2, the figures for Example 6 (Interpolation by splitting transforms) have been produced using Wolfram Mathematica software (Version Number: 12.0.0.0). We present the code used to produce the graphics (see Figures 2.4–2.7). For simplicity, we only consider the interpolating function $\mathrm{I}[f]_M^{(0)}$ (2.3.33). This code can be used for any $M \in \mathbb{N}$, and it can be copied and pasted directly in the Mathematica notebook.

For example, let us choose $M = 7$,

```
In[1]:=    M = 7;
```

Then, we input the vectors of the $\omega-$basis of A_2 as

```
In[2]:=    om1 = {1, 0};
           om2 = {0, 1};
```

For producing graphics, we use the orthonormal basis of A_2. The fundamental weights expressed using the orthonormal basis correspond to the input

```
In[3]:=    om11 = {1/Sqrt[2], 1/Sqrt[6]};
           om22 = {0, Sqrt[2/3]};
```

For any label $\lambda = (\lambda_1, \lambda_2)$ and any point $x = (x_1, x_2)$, the scalar product (2.2.7) corresponds to the input

```
In[4]:=    ScalProd[{la1_ , la2_}, {x1_ , x2_}] :=
           2/3la1*x1 + 1/3la2*x1 + 1/3la1*x2 + 2/3la2*x2;
```

Next, we input the $C-$function (2.3.5) as follows

```
In[5]:=  Cfunc[{la1_ , la2_ , x1_ , x2_}] :=
         Exp[2*Pi*I*ScalProd[{la1, la2}, {x1, x2}]] +
         Exp[2*Pi*I*ScalProd[{-la1, la1 + la2}, {x1, x2}]] +
         Exp[2*Pi*I*ScalProd[{la1 + la2, -la2}, {x1, x2}]] +
         Exp[2*Pi*I*ScalProd[{la2, -la1 - la2}, {x1, x2}]] +
         Exp[2*Pi*I*ScalProd[{-la1 - la2, la1}, {x1, x2}]] +
         Exp[2*Pi*I*ScalProd[{-la2, -la1}, {x1, x2}]];
```

We input the values of the discrete functions $h_M(\lambda)$ (2.2.39), $\varepsilon(s)$ (2.2.65) and $d(s)$ (2.2.67). For $h_M(\lambda)$, we have the following input

```
In[6]:=  hM[{la0_, la1_, la2_}] := 1 /; la0 != 0 && la1 != 0 && la2 != 0;
         hM[{la0_, la1_, la2_}] := 2 /; la0 != 0 && la1 == 0 && la2 != 0;
         hM[{la0_, la1_, la2_}] := 2 /; la0 != 0 && la1 != 0 && la2 == 0;
         hM[{la0_, la1_, la2_}] := 2 /; la0 == 0 && la1 != 0 && la2 != 0;
         hM[{la0_, la1_, la2_}] := 6 /; la0 != 0 && la1 == 0 && la2 == 0;
         hM[{la0_, la1_, la2_}] := 6 /; la0 == 0 && la1 != 0 && la2 == 0;
         hM[{la0_, la1_, la2_}] := 6 /; la0 == 0 && la1 == 0 && la2 != 0;
```

For the discrete function $\varepsilon(s)$, we have the following input

```
In[7]:=  eps[{s0_, s1_, s2_}] := 6 /; s0 != 0 && s1 != 0 && s2 != 0;
         eps[{s0_, s1_, s2_}] := 3 /; s0 != 0 && s1 == 0 && s2 != 0;
         eps[{s0_, s1_, s2_}] := 3 /; s0 != 0 && s1 != 0 && s2 == 0;
         eps[{s0_, s1_, s2_}] := 3 /; s0 == 0 && s1 != 0 && s2 != 0;
         eps[{s0_, s1_, s2_}] := 1 /; s0 != 0 && s1 == 0 && s2 == 0;
         eps[{s0_, s1_, s2_}] := 1 /; s0 == 0 && s1 != 0 && s2 == 0;
         eps[{s0_, s1_, s2_}] := 1 /; s0 == 0 && s1 == 0 && s2 != 0;
```

For the discrete function $d(s)$, we have the following input

```
In[8]:=  ds[{s0_, s1_, s2_}] := 3 /; s0 != 0 && s1 != 0 && s2 != 0 &&
         s0 == s1 == s2;
         ds[{s0_, s1_, s2_}] := 1 /; s0 != 0 && s1 != 0 && s2 != 0;
         ds[{s0_, s1_, s2_}] := 1 /; s0 == 0 && s1 != 0 && s2 != 0;
         ds[{s0_, s1_, s2_}] := 1 /; s0 != 0 && s1 == 0 && s2 != 0;
         ds[{s0_, s1_, s2_}] := 1 /; s0 != 0 && s1 != 0 && s2 == 0;
         ds[{s0_, s1_, s2_}] := 1 /; s0 == 0 && s1 == 0 && s2 != 0;
         ds[{s0_, s1_, s2_}] := 1 /; s0 == 0 && s1 != 0 && s2 == 0;
         ds[{s0_, s1_, s2_}] := 1 /; s0 != 0 && s1 == 0 && s2 == 0;
```

In order to construct the splitting weight set $\Lambda_M^{(0)}$ (2.2.27) and splitting point set $F_M^{(0)}$ (2.2.53), the following functions are employed

```
In[9]:=   v[{x_ , y_ , z_}] := {x, y, z};
          w[{x_ , y_ , z_}] := {y, z};
          i[{x_ , y_ , z_}] := {y/M, z/M};
```

The elements $\lambda = [\lambda_0, \lambda_1, \lambda_2]$ (2.2.22) of the splitting weight set $\Lambda_M^{(0)}$ are provided as

```
In[10]:=  La0v = Map[v,Cases[Flatten[Table[{x, y, z}, {x, 0, M, 1},
          {y, 0, M, 1}, {z, 0, M, 1}],2], {a_ , b_ , c_} /;
          a + b + c == M && Mod[b + 2c, 3] == 0]];
```

Therefore, the elements of the splitting weight set $\Lambda_7^{(0)}$ are provided in Kac coordinates as

```
Out[10]=  {{0, 2, 5}, {0, 5, 2}, {1, 0, 6}, {1, 3, 3}, {1, 6, 0}, {2, 1, 4},
          {2, 4, 1}, {3, 2, 2}, {4, 0, 3}, {4, 3, 0}, {5, 1, 1}, {7, 0, 0}}
```

The labels $\lambda = (\lambda_1, \lambda_2)$ provided by the splitting weight set $\Lambda_M^{(0)}$ are given by

```
In[11]:=  La0w = Map[w,Cases[Flatten[Table[{x, y, z}, {x, 0, M, 1},
          {y, 0, M, 1}, {z, 0, M, 1}], 2], {a_ , b_ ,c_} /;
          a + b + c == M && Mod[b + 2c, 3] == 0]];
```

Therefore, the labels of the splitting weight set $\Lambda_7^{(0)}$ are listed as

```
Out[11]=  {{2, 5}, {5, 2}, {0, 6}, {3, 3}, {6, 0}, {1, 4}, {4, 1}, {2, 2},
          {0, 3}, {3, 0}, {1, 1}, {0, 0}}
```

The elements $s = [s_0, s_1, s_2]$ (2.2.50) of the splitting point set $F_M^{(0)}$ are provided as

```
In[12]:=  FM0h =  Map[v,Cases[Flatten[Table[{x, y, z}, {x, 0, M, 1},
          {y, 0, M, 1}, {z, 0, M, 1}], 2], {a_ , b_ , c_} /;
          (a + b + c == M && a > b && a > c) || (a + b + c == M &&
          a == b && b >= c)]];
```

Therefore, the elements of the splitting point set $F_7^{(0)}$ are provided in Kac coordinates as

```
Out[12]=  {{3, 2, 2}, {3, 3, 1}, {4, 0, 3}, {4, 1, 2}, {4, 2, 1}, {4, 3, 0},
          {5, 0, 2}, {5, 1, 1}, {5, 2, 0}, {6, 0, 1}, {6, 1, 0}, {7, 0, 0}}
```

To illustrate the points at the final step, we consider the points $s = (\frac{s_1}{M}, \frac{s_2}{M})$ provided by the splitting point set $F_M^{(0)}$

```
In[13]:=  FM0i =  Map[i,Cases[Flatten[Table[{x, y, z}, {x, 0, M, 1},
          {y, 0, M, 1}, {z, 0, M, 1}], 2], {a_ , b_ , c_} /;
          (a + b + c == M && a > b && a > c) || (a + b + c == M &&
          a == b && b >= c)]];
```

For $M = 7$, we have the following output

```
Out[13]=  {{2/7, 2/7}, {3/7, 1/7}, {0, 3/7}, {1/7, 2/7}, {2/7, 1/7}, {3/7, 0},
          {0, 2/7}, {1/7, 1/7}, {2/7, 0}, {0, 1/7}, {1/7, 0}, {0, 0}}
```

For the $C-$functions, we use the cartesian product to generate a list of input containing the elements of the form $\{\lambda_1, \lambda_2, x_1, x_2\}$. More precisely,

```
In[14]:=  CartProd[A_ , B_] :=  Module[{l, i, j}, l = {};
             For[i = 1, i <= Length[A], i++,
                For[j = 1, j <= Length[B], j++,
                   AppendTo[l, {A[[i]], B[[j]]}]]]; l];
```

Therefore, a list of input for $C-$functions is provided by

```
In[15]:=  InpC = Simplify[Partition[Partition[Flatten[
          CartProd[La0w, FM0i]], 4], Length[La0w]]];
```

For $M = 7$, as an example, we present a list of input containing only one sublist. The total number of sublists is equal to M.

```
Out[15]=  {{{2, 5, 2/7, 2/7}, {2, 5, 3/7, 1/7}, {2, 5, 0, 3/7},
          {2, 5, 1/7, 2/7}, {2, 5, 2/7, 1/7}, {2, 5, 3/7, 0},
          {2, 5, 0, 2/7}, {2, 5, 1/7, 1/7}, {2, 5, 2/7, 0},
          {2, 5, 0, 1/7}, {2, 5, 1/7, 0}, {2, 5, 0, 0}},
          {...}, {...},..., {...}}
```

For the interpolation test, we chose the function that has a pick in the middle of the kite-shaped region F_P (2.3.39) and depends on the value of the parameter σ (see Figure 2.3). More precisely,

```
In[16]:=  sigma = 0.065;

          F[x_ , y_] := 0.4 Exp[-((x - 1/6)^2 + 1/3(x + 2y - 1/2)^2)/sigma^2];
```

The spectrum coefficients $c_\lambda[f]_M$ (2.3.37) are calculated using the following input

```
In[17]:=  SpecCoef = FullSimplify[
             Table[Sum[(eps[FM0h[[u]]]/ds[FM0h[[u]]])*Apply[F,FM0i[[u]]]*
             Conjugate[Cfunc[InpC[[r, u]]]]/(6*M^2*hM[La0v[[r]]]),
             {u, 1, Length[La0v]}], {r, 1, Length[La0v]}]];
```

The real part of the interpolating function $\mathrm{I}[f]_M^{(0)}$ (2.3.33) is given by

```
In[18]:=  IntFM0Re[{x_ , y_}] := Re[Sum[SpecCoef[[u]]*Cfunc[Join[La0w[[u]],
          {x, y}]], {u, 1, Length[La0w]}]];
```

For the color options that differ from those already defined in Mathematica, we chose to work with the palette of the hexadecimal colors. The function that converts a color format from the hexadecimal to decimal one is given by

```
In[19]:=    HexToRGB :=
            RGBColor@@(IntegerDigits[
                ToExpression@StringReplace[#, "#" -> "16^^"], 256, 3]/255.) &;
```

We can visualize the interpolating function $\mathrm{I}^{(0)}[f]_M$ by generating its 3D plot over a kite-shaped region using the $\omega-$basis,

```
In[20]:=    InterpPlot = Plot3D[IntFMORe[{x, y}], Element[{x, y},
            Polygon[{{0, 0}, om1/2, (om1 + om2)/3, om2/2, {0, 0}}]],
            Background -> None, Mesh -> None, Axes -> False, Boxed -> False,
            PlotRange -> Full, BoundaryStyle -> None,
            PlotPoints -> 100, ImageSize -> 2000,
            ColorFunction -> (Blend[{HexToRGB["#6581d0"], HexToRGB["#a1b8e6"],
            HexToRGB["#b8d4ef"]}, #3] &), Lighting -> "Neutral"]
```

Out[20]=

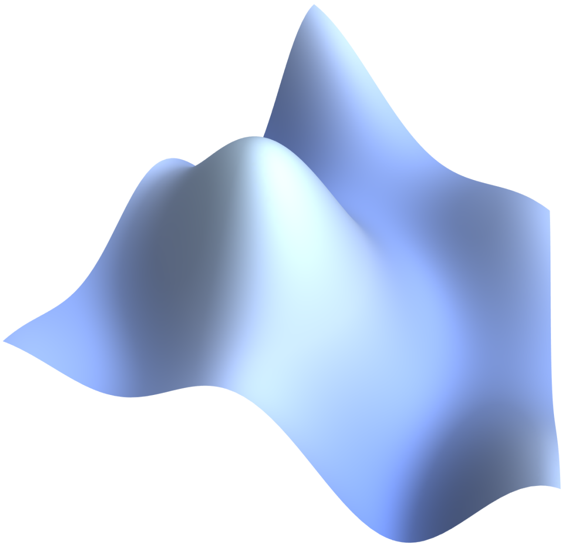

To switch from the $\omega-$basis to the orthonormal basis, we use the following code,

```
In[21]:=    DiscGraph = DiscretizeGraphics@First@Normal@InterpPlot;
            (* generates the discretized 3D plot of InterPlot *)
            ListPt = MeshCoordinates@DiscGraph; (* generates a list of the
            coordinates of InterPlot with the elements of the form (x, y, z) *)
            Step1 = Dot[Drop[ListPt, None, {3}], {om11, om22}];
            (* generates a list with the elements of the form (x', y') given in
            the orthonormal basis *)
```

```
Step2 = Drop[ListPt, None, {1, 2}]; (* generates a list containing
the z-coordinate of each element of ListPt *)
ListPtPlot = Table[Flatten[Join[Step1[[n]], Step2[[n]]]],
{n, 1, Length[ListPt]}]; (* generates a new list containing the
elements of the form (x', y', z)*)
```

Therefore, the interpolating function $\mathrm{I}^{(0)}[f]_M$ can be plotted in 3D as

```
In[22]:=  InterpPlotOrt = ListPlot3D[ListPtPlot, Background -> None,
          Mesh -> None, Axes -> False, Boxed -> False, PlotRange -> Full,
          BoundaryStyle -> None, MaxPlotPoints -> 100,
          InterpolationOrder -> 3, ImageSize -> 2000,
          ColorFunction -> (Blend[{HexToRGB["#6581d0"], HexToRGB["#a1b8e6"],
          HexToRGB["#b8d4ef"]}, #3] &), Lighting -> "Neutral"]
```

Out[22]=

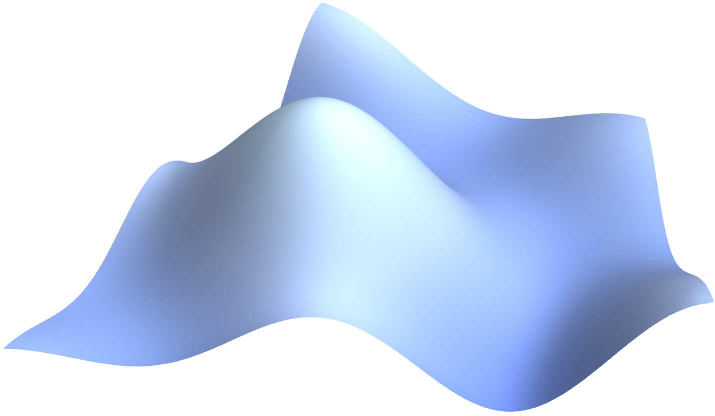

To produce a contour plot of the constructed 3D function, we use the following code,

```
In[23]:=  InterpContourPlot = ListContourPlot[ListPtPlot, Background -> None,
          Mesh -> None, Axes -> False, Frame -> False,
          PlotRange -> {{-0.03, 0.5}, {-0.03, 0.5}, Full},
          PlotRangePadding -> 0, Contours -> 10,
          MaxPlotPoints -> 300, InterpolationOrder -> 3, ImageSize -> 2000,
          ColorFunction -> (Blend[{HexToRGB["#6581d0"], HexToRGB["#a1b8e6"],
          HexToRGB["#cbe2f6"], HexToRGB["#ceeffa"], HexToRGB["#d1fffe"],
          HexToRGB["#d4ffea"], HexToRGB["#efffee"]}, #1] &),
          ContourStyle -> Directive[AbsoluteThickness[10],
          HexToRGB["#3e528b"], Opacity[0.8]]];
```

Finally, to graphically represent the points of the splitting point set $F_M^{(0)}$ together with the contour plot of $\mathrm{I}^{(0)}[f]_M$, we use the following lines of code,

```
In[24]:=    Points = ListPlot[Dot[FM0i, {om11, om22}],
            PlotStyle -> HexToRGB["#044583"] (*dark blue*),
            PlotMarkers -> {"●", 150}, Axes -> False];

            FinalContourPlot = Show[InterpContourPlot, Points]
```

For $M = 7$, the contour plot of $\mathrm{I}^{(0)}[f]_7$ together with the points of $F_7^{(0)}$ are presented as

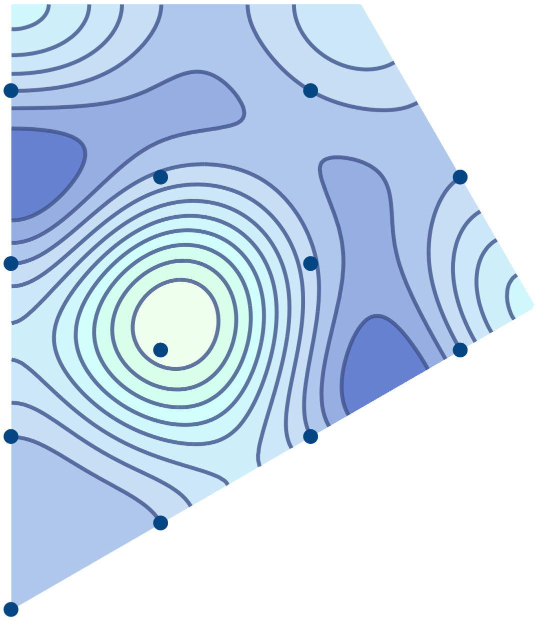Out[24]=